EXERGY METHODS FOR COMMERCIAL AIRCRAFT

Cranfield University
Centre for Aeronautics

EXERGY METHODS FOR COMMERCIAL AIRCRAFT

INTEGRATING THE LAWS OF THERMODYNAMICS INTO ALL DISCIPLINES OF AIRCRAFT DESIGN

DAVID J. R. HAYES

SUPERVISORS

Dr Mudassir Lone

Dr James F Whidborne

Dr Etienne Coetzee

DOCTORATE THESIS

July 2018

David J. R. Hayes: *Exergy Methods for Commercial Aircraft: Integrating the Laws of Thermodynamics into all Disciplines of Aircraft Design*, Doctorate Thesis, Cranfield University, United Kingdom, © July 2018

"The law that entropy always increases
the second law of thermodynamics
holds I think, the supreme position among the laws of Nature.

If someone points out to you that your pet theory of the universe
is in disagreement with Maxwell's equations
then so much worse for Maxwell equations.

If it is found to be contradicted by observation
well these experimentalists do bungle things sometimes.

But if your theory is found to be against the second law of thermodynamics
I can give you no hope
there is nothing for it but to collapse in deepest humiliation."

Sir Arthur Eddington
The Nature of the Physical World
1928

ABSTRACT

As a consequence of practicalities, work share and difficulties in designing complex aerospace systems, there has been historical segregation of sub-systems in aircraft design. This methodology has proved successful for conventional swept wing aircraft configurations, as the sub-systems are only loosely integrated with one another. This results in discipline-specific performance, loss and optimization metrics being developed at sub-system level, which are not clearly linked to the overall system performance or objective. To meet social, economic and environmental needs, the next generation of aircraft require revolutionary concepts, which tend to be far more integrated, similar to military vehicles. Thus, performance, loss and optimization metrics need to be considered at system level, in order to account for the interactions between competing engineering disciplines.

This thesis advocates an alternative systems engineering approach to developing future commercial aircraft, where the universal thermodynamic metrics energy and entropy are coupled to provide a holistic performance, loss and optimization metric for all aircraft disciplines. The method known as *exergy analysis* has been applied in the development of propulsion systems, but is sparsely applied in other aerospace disciplines. Applying the laws of thermodynamics to all aircraft sub-systems can seem obscure, especially in mature disciplines such as aerodynamics where energy may only be considered implicitly.

Along with conventional configurations, this thesis studies a conceptual highly integrated High Aspect Ratio Wing (HARW) aircraft with morphing wing-tips, where the extended wingspan improves aerodynamic performance but as a consequence the wings have greater flexibility. Morphing is not a widely proliferated technology primarily due to the conservative approach to civil aircraft design, but original equipment manufacturers also struggle to demonstrate how the morphing effectiveness on a scale model can be scaled up to a full size aircraft.

This thesis shows a clear contribution to knowledge in extending the current exergy methodology by investigating flight dynamic exergy analysis, and its application to morphing technologies for large commercial aircraft, evaluating the aerodynamic and aeroelastic contribution to an aircraft's overall exergy use. To achieve this, each node of the Collar's triangle [27] is evaluated using the exergy metric. In the absence of an open-source code, a non-linear structural code designated the Beam Reduction (BEAR) model, has been written to study the structural dynamics of an airframe written in MSC Nastran format within a MATLAB® / Simulink® environment. To facilitate the study of flight dynamics, a bespoke Prandtl-Glauert aerodynamics model with an exergy post-processing script has been developed. Static and dynamic aeroelastic effects were studied through a coupling of the aforementioned structure and aerodynamic exergy based models.

One of the main barriers to applying exergy analysis to commercial aircraft is gaining acceptance of a novel methodology in disciplines with entrenched practices. An example being in aerodynamic design, where the force balance approach is the established analysis method, yet exergy analysis requires the engineer to consider an alternative view of the aerodynamics as a system that uses and converts energy. To counter this, the thesis shows the capability and benefits of exergy analysis over conventional analysis techniques. This is emphasised in the comparison of using

exergy based methods or the Breguet Range Equation for assessing the performance benefit of morphing wing extensions, where both methods provide the same top level conclusion, but exergy provides additional insight into the system the Breguet analysis can not.

ACKNOWLEDGMENTS

I would like to thank my academic supervisors, Dr Mudassir Lone and Dr James Whidborne, for their support and novel insights throughout this research programme. I would also like to express my thanks to my industrial supervisor, Dr Etienne Coetzee, who's enthusiasm and interest in the topic laid the foundations for this work. I wish to thank and acknowledge Dr Jose Camberos of the United States Air Force Research Laboratory (US AFRL) for the multiple transatlantic exergy based discussions and co-authoring of the journal paper. Finally I would like to thank the Engineering and Physical Sciences Research Council (EPSRC) and Airbus Group for providing funding for me to undertake this PhD.

This work was supported by the United Kingdom Engineering and Physical Sciences Research Council (EPSRC) Industrial Cooperative Award in Science & Technology (CASE) grant EP/M507374/1 for the Cranfield University, Centre for Aeronautics, in collaboration with Airbus Group.

AIRBUS

CONTENTS

NOMENCLATURE

ROMAN LETTERS (REGULAR AND CALLIGRAPHIC)

A	Area $[m^2]$
b	Wing span $[m]$
c	Wing chord dimension $[m]$
c_p	Specific heat capacity at constant pressure $\left[\frac{J}{mol.K}\right]$
c_v	Specific heat capacity at constant volume $\left[\frac{J}{mol.K}\right]$
c_T	Thrust Specific Fuel Consumption (TSFC) $\left[\frac{kg}{N/s}\right]$
C	Capacitance $[F]$
C	Structural damping $[\frac{kg}{s}]$
C_D	Drag coefficient $[-]$
C_L	Lift coefficient $[-]$
C_X	Exergy coefficient $[-]$
D	Aerodynamic Drag Force $[N]$
D_r	Rayleigh dissipation function $[W]$
e	Oswald efficiency factor $[-]$
E	Energy $[J]$
E	Elastic (Young's) modulus $[Pa]$
E_i	Energy Intensity $\left[\frac{J}{pp.km}\right]$
F	Helmholtz free energy $[J]$
F	General force $[N]$
g	Gravity $\left[\frac{m}{s^2}\right]$
G	Gibbs free energy $[J]$
G	Bulk (shear) modulus $[Pa]$
h	Enthalpy (mass specific) $\left[\frac{J}{kg}\right]$
h	Height (in reference to potential energy) $[m]$
H	Enthalpy $[J]$
I	Second moment of area $[m^4]$
I	Identity matrix $[-]$
J	Polar moment of inertia $[m^4]$
J	Cost function
k_B	Boltzmann constant $\left[\frac{J}{K}\right]$
K	Structural stiffness $[\frac{N}{m}]$
L	Aerodynamic Lift Force $[N]$
L	Lagrangian $[J]$
m	Mass $[kg]$
M	Moment $[Nm]$
M	Structural mass $[kg]$
n	Quantity of gas $[mol]$
p	Pressure $[Pa]$
P	Force $[N]$
q	Fluid dynamic pressure $[Pa]$
q	Structural displacement state vector $[m, m, m, rad, rad, rad]$
$\dot{q}$	Structural velocity state vector $\left[\frac{m}{s}, \frac{m}{s}, \frac{m}{s}, \frac{rad}{s}, \frac{rad}{s}, \frac{rad}{s}\right]$

$\ddot{q}$	Structural acceleration state vector $\left[\frac{m}{s^2}, \frac{m}{s^2}, \frac{m}{s^2}, \frac{rad}{s^2}, \frac{rad}{s^2}, \frac{rad}{s^2}\right]$
Q	Energy transfer via heat $[J]$
Q	Hermitian matrix $[-]$
R	Range $[km]$
R	Universal gas constant $\left[\frac{J}{mol.K}\right]$
s	Entropy (mass specific) $\left[\frac{J}{K.kg}\right]$
S	Entropy $\left[\frac{J}{K}\right]$
S	Wing reference area (planform) $[m^2]$
t	Time $[s]$
T	Tempature $[K]$
T	Kinetic energy $[J]$
T	Thrust (force) $[N]$
u	Internal energy (mass specific) $\left[\frac{J}{kg}\right]$
u	Displacement (translation) (Cartesian X axis) $[m]$
u	Velocity (fluid) $\left[\frac{m}{s}\right]$
$\dot{u}_\infty$	Freestream velocity $\left[\frac{m}{s}\right]$
U	Internal energy $[J]$
v	Volume (mass specific) $= \frac{1}{\rho}$ $\left[\frac{m^3}{kg}\right]$
v	Displacement (translation)(translation) (Cartesian Y axis) $[m]$
V	Volume $[m^3]$
V	Potential energy $[J]$
w	Displacement (translation) (Cartesian Z axis) $[m]$
W	Energy transfer via work $[J]$
$\mathcal{W}$	Structural weight $[N]$
x	Direction on Cartesian co-ordinate system
X_{sys}	System exergy$[J]$
X_U	Thermal exergy$[J]$
X_T	Kinetic exergy$[J]$
X_V	Potential exergy$[J]$
X_{Ch}	Chemical exergy$[J]$
X_D	Destroyed exergy$[J]$
y	Direction on Cartesian co-ordinate system
z	Direction on Cartesian co-ordinate system

GREEK LETTERS

α	Angle of attack $[rad]$
Γ	Circulation $\left[\frac{m^2}{s}\right]$
ϵ	Carnot efficiency $[-]$
ζ	Structural damping coefficient $[-]$
η	Rayleigh damping coefficient $[-]$
η_I	First law (thermodynamics) efficiency $[-]$
η_{II}	Second law (thermodynamics) efficiency $[-]$
η_p	propulsion efficiency $[-]$
η_a	aerodynamic efficiency $[-]$
η_s	structural efficiency $[-]$
η_x	exergetic efficiency $[-]$
θ	Displacement (rotational) (Cartesian Y axis) $[rad]$
κ	Timoshenko shear coefficient $[-]$

λ	Rayleigh damping coefficient $[-]$
λ	Taper ratio $[-]$
Λ	Sweep angle (wing) $[rad]$
μ	Fluid dynamic viscosity $[Pa.s]$
ν	Poisson ratio $[-]$
ρ	Density $\left[\frac{kg}{m^3}\right]$
ϕ	Exergy (mass specific) $\left[\frac{j}{kg}\right]$
ϕ	Displacement (rotational) (Cartesian X axis) $[rad]$
ψ	Flow exergy $\left[\frac{J}{s}\right]$
ψ	Displacement (rotational) (Cartesian Z axis) $[rad]$
ω	Eigenvalue $\left[\frac{1}{s}\right]$
Ω	number of system microstates $[-]$
Υ	Electrical potential $[V]$

SUBSCRIPTS

$(\,)_0$	Initial condition
$(\,)_1$	Final condition
$(\,)_\infty$	Environment (reference state)

LIST OF FIGURES

LIST OF TABLES

Part I

INTRODUCTION

"Any method involving the notion of entropy, the very existence of which depends on the second law of thermodynamics, will doubtless seem to many far-fetched, and may repel beginners as obscure and difficult of comprehension"

Willard Gibbs
Graphical Methods in the Thermodynamics of Fluids
1873

1

OVERVIEW

There is a need for the next generation of commercial aircraft to have revolutionary configurations, in order to meet the economic and environmental challenges of the coming decades. The Airbus/Rolls Royce E-Thrust aircraft concept (Figure 1.1) is one such example, which provides a hybrid/electrical distributed propulsion system integrated into a modified version of Airbus' future vision Concept Plane (see Figure 1.4a). The E-Thurst aircraft is an illustration of one of many proposed concepts from leading Original Equipment Manufacturers (OEMs) that can be defined as a highly integrated system.

Consider, the Chief Design Engineer (CDE) of the aircraft has aerodynamics, propulsion and fuselage engineers competing for resources to improve the performance of their respective discipline, be it an improved lift-to-drag ratio, lower specific impulse or a lighter structure. For conventional design, methods such as Breguet's range equation exist to see which of these improvements will bring the most benefit to the aircrafts performance. This is possible as conventional in service aircraft can be considered loosely integrated, in that the disciplines can be designed and assessed independently, as there is little interaction between the competing subsystems. Conversely, integrated concepts see significant discipline interaction, in that changes to one discipline design will impact others performance, thus the discipline specific design process used for conventional aircraft is no longer suitable. Furthermore, performance analysis developed for turbofan engines are not read across to that of electric propulsion, so how does one measure the merits of incorporating electric propulsion in place of a next generation turbofan? It is not as simple as seeing the performance of the engine, one must consider that an electric propulsion concept is likely to require some form of electricity storage, be it a capacitor or battery, which unlike jet fuel is not burnt off during flight, and thus adds to the weight of the aircraft, impacting the structural design and aerodynamic requirements.

Figure 1.1: Airbus and Rolls-Royce E-Thrust

Thus a design and analysis methodology is required, where integrated disciplines can be analysed and compared under a common metric. In the framework of physics today, the two universal metrics any system or system transfer can be defined within, are energy and entropy, from the first and second laws of thermodynamics. This thesis advocates the use of integrating the laws of thermodynamics into all areas of aircraft design, to provide a design methodology that allows multi-disciplinary design and analysis of all aircraft systems.

This chapter outlines why there is a need for revolutionary concepts, and how integrated thermodynamic analysis may provide a solution for performance assessment. The chapter concludes with the research objectives of this thesis and how they will be met.

1.1 THE NEED FOR REVOLUTIONARY CONCEPTS

Since the development of the Boeing 247 in 1933 and the first commercial jet liner the de Havilland Comet in 1949, the *energy intensity*[1], E_i,

$$E_i = \frac{\text{fuel consumed}(MJ)}{\text{no. of passengers} \times \text{distance travelled}(km)}$$

for each aircraft evolution has reduced, see Figure 1.2. The Advisory Council for Aviation Research and Innovation in Europe (ACARE) [1] attributes this reduction to five major challenges sought after for every future aircraft; (1) to meet market and societal needs, (2) to maintain and extend industrial leadership, (3) to protect the environment and the energy supply, (4) to ensure safety and security and (5) to prioritise research, test capabilities and education.

The *market driven needs* of airlines encourage the delivery of lower energy intensity aircraft, as a reduction allows for lower more competitive air fares and a higher profit margin as a result of the lower fuel costs. *To protect the environment and the energy supply*[2], the European Commission has outlined an acceptable pace for emissions reduction in *Flightpath 2050* [63]. In response, ACARE have laid out a set of targets[3] that will enable the aims of Flightpath 2050 to be achieved. One of these targets states that relative to the capabilities in 2000, by 2050

> *"CO2 emissions per passenger kilometre [are to be] reduced by 75%, NOx emissions by 90% and perceived noise by 65%"*
>
> - ACARE [1]

Traditionally, when considering options for improving aircraft design, there has been historical segregation of component and sub-system design and analysis into various disciplines, due to the difficulties and practicalities in designing complex aerospace systems. An example is aircraft performance measured as the *range*, calculated using the Breguet Range Equation [9] for steady cruise. Here the propulsion, aerodynamics and structures disciplines each have different performance, loss and optimization metrics, however the Breguet Range Equation non-dimensionalises these using contrasting methods to provide a function for the aircraft range. Jupp [90] and Lee [96] use the Breguet Range Equation , where the product of three non-dimensionalised

1 *Energy Intensity* is a measure of aircraft fuel economy
2 To counter the contribution of aviation to global warming
3 Replicated worldwide with targets from the Air Transport Action Group (ATAG) [2].

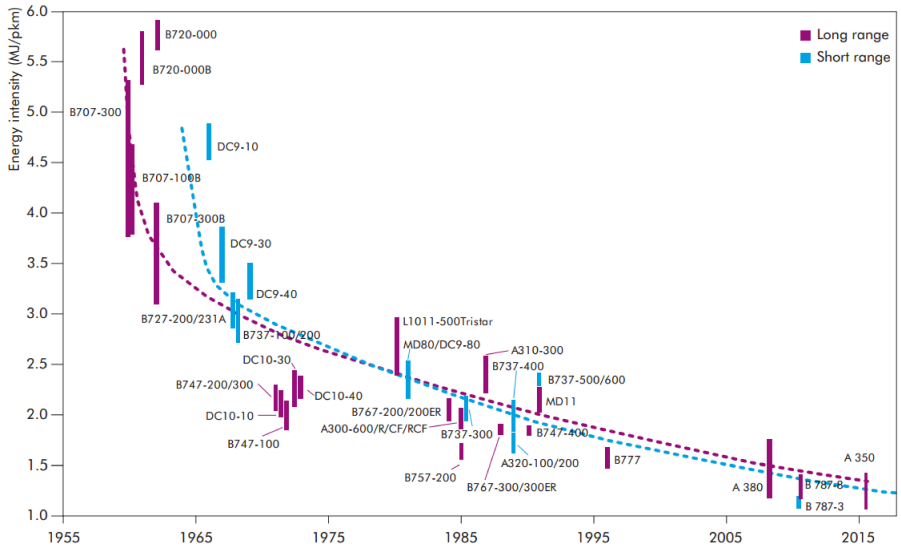

Figure 1.2: Evolution of aircraft energy intensity [84]

relationships, the propulsion efficiency[4] (η_p), the aerodynamic efficiency[5] (η_a) and the structural efficiency[6] (η_s), are optimised to maximise the aircraft range (R) as

$$R = \left(\frac{LCV}{g}\right) \underbrace{\left(\frac{V}{LCV \times SFC}\right)}_{\eta_p} \underbrace{\left(\frac{L}{D\,(M)}\right)}_{\eta_a} \underbrace{\ln \frac{\mathcal{W}_1}{\mathcal{W}_0}}_{\eta_s} \tag{1.1}$$

Note that the propulsion efficiency is stated as a function of Specific Fuel Consumption (SFC) and Lower Calorific Value (LCV) as to non-dimensionalise the propulsion efficiency. The drag components of the aerodynamic efficiency is stated as a function of the Mach number as to highlight that dependent on the Mach number of flight different components contribute to the total drag. This thesis deals primarily with aircraft travelling below $0.6M$, as such form and induced drag are considered, however for transonic flight wave drag would need to be included as is a major contributor to entropy generation.

Recent improvements in propulsion efficiency are evident in the Airbus A320 NEO (New Engine Option) where the development of Geared Turbofan (GTF) engines offers a 15% reduction in fuel burn [90]. The enhancement of the aerodynamic efficiency was the driver for the introduction of span extension technologies of the folding wingtips on the Boeing 777X. Advances in structural efficiency are noticeable in the increased use of composites from 15% of the structure weight being composite at the end of the 20th century [90], to 50% in the Boeing 787 and Airbus A350 XWB.

These evolutionary improvements to conventional configurations have contributed to aircraft now being 70% more fuel efficient per seat kilometre than the de Havilland Comet [2]. This reduction is also stated by the European Environment Agency who note

> *"the environmental performance of European transport is slowly improving, but there is still some way to go in decreasing oil consumption in transport"*
>
> - European Environment Agency [64]

Thus, to meet the environmental targets OEMs need to commit to keeping the trend in efficiency improvements that is evident in the latest generation of aircraft. How-

4 Function of thrust specific fuel consumption (c_T)
5 Function of aircraft Lift (L) and total Drag (D)
6 Function of initial aircraft weight $(\mathcal{W}_1)$ and final post fuel burn weight $(\mathcal{W}_0)$

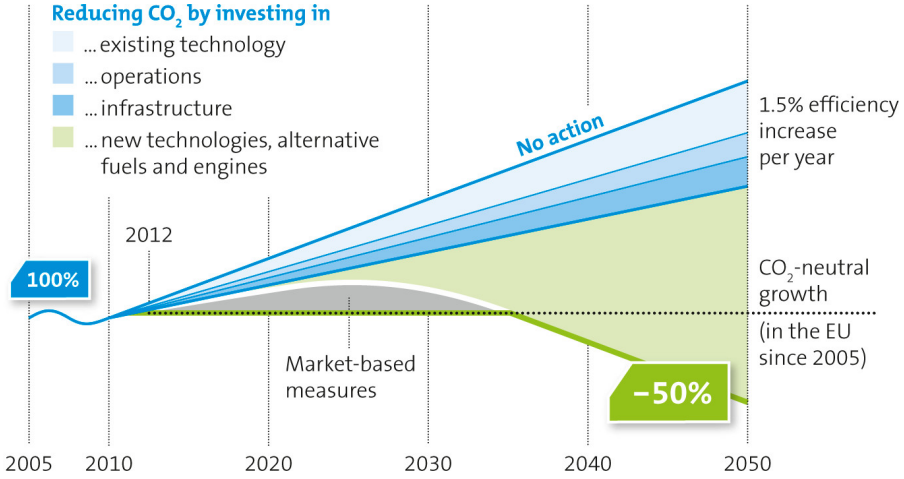

Figure 1.3: Predictions of measures to be taken to reduce carbon emissions [2]

(a) Airbus Concept Plane

(b) Airbus BLADE

Figure 1.4: Future Aircraft Configurations of Airbus

ever, air transport is currently experiencing the fastest growth of any mode of transport [97], and by 2035 it is estimated that the required number of passenger aircraft will increase by 109% from 2015 levels [3]. In addition, the International Energy Agency [84] has highlighted a trend that conventional aircraft configurations are near *optimised*, demonstrated by the plateauing improvements in *energy intensity* seen in Figure 1.2.

Giurgiutiu [71] anticipates that research issues for future aircraft will be focused on

> *"disruptive new and revolutionary structural concepts and unprecedented flight configurations"*
>
> - Victor Giurgiutiu [71]

This premise is verified by ATAG [2] with the forecast that evolutionary improvements to current technology will account for less than 10% of the reduction in carbon emissions (see Figure 1.3), with the majority of reductions expected from biofuels and *additional new-generation technology*.

Hence aircraft manufacturers are researching technologies and configurations that may provide the required performance improvements. Propulsion efficiency improvements are expected from next generation turbofan development as well as new concepts of open rotor engines and hybrid turbofan-electric propulsion as seen in the conceptual Airbus E-Thrust aircraft (Figure 1.1). Future aerodynamic efficiencies move away from the conventional swept aircraft configuration to High Aspect Ratio Wing (HARW), such as the Airbus Concept Plane (Figure 1.4a), which reduce vortex drag. Alternative aerodynamic improvements can be found in blended wing body

concepts to minimise aircraft surface area, thus parasitic drag and also laminar flow wing technology seen in the BLADE (Breakthrough Laminar Aircraft Demonstrator in Europe) project [90] (Figure 1.4b). Structural mass will continue to be reduced with further composites use and novel manufacturing methods, such as 3D printing. However, there is no way of comparing these discipline specific performance improvements to one another, except using a top level metric such as range.

1.2 THERMODYNAMIC PERFORMANCE MODELLING

From a systems engineer's perspective, the role at top level system design is to make trades between competing disciplines and sources of loss to arrive at a vehicle design with the least possible *cost*[7]. The Breguet methodology does not provide a systematic way to trade performance metrics across disciplines, as such there is no guarantee that individually optimised sub-systems will form an optimal system when bought together at top level and sub-system interactions occur (see Figure 1.5a). Yet for for conventional swept wing aircraft configurations the Breguet methodology has proved successful, as the sub-system disciplines are only loosely integrated with one another.

However, the commercial aircraft revolutionary concepts shown in Figure 1.4 are more integrated vehicles, similar to what we see in current generation military aircraft, which need to be designed with no prior flight experience, thus requiring a more rigorous analytical process to supplement the lack of in-service performance information. Hence, in order to facilitate these highly integrated configurations, the systems engineer has a need for a loss accounting method that enables systematic analysis of inefficiencies/loss where system wide consequences of design trades can be evaluated. Hence, performance optimisation needs to be considered at the top level, in order to account for the interactions between competing engineering disciplines. A critical part of this is the development of a decomposition strategy where all the subsystem components can be optimized to a system-level common metric in a common mathematical framework (see Figure 1.5b). In order to facilitate this integrated approach, a universal metric is required that can be used in the analysis of all aerospace disciplines.

The only universal properties in physics are *energy* from the first law of thermodynamics and *entropy* from the second law of thermodynamics. Both energy and entropy are recognised as important in all natural processes including physics-based machines. Thus, using either of these metrics would provide the necessary integrated approach, as all aircraft systems operate using energy from a common fuel source and will generate entropy through their inefficiencies. Any system design evolution works on the theory of allowing energy to transfer through a sub system *more easily*, by minimising the entropy production. Throughout the history of thermodynamics, the focus has been on heat engines and power generation technology with the aim to reducing the gap between actual operation and operation in the reversible cycle. As energy is the basic currency of all physical events, energy analysis based on fuel burn, derived from Newtonian mechanics and the first law of thermodynamics, is commonly used in the design of aerospace systems.

Traditional first law design optimisation methods such as the Breguet equation tend to consider energy implicitly. It is not atypical to view an aircraft as a system that converts chemical energy (fuel) into useful work to accomplish its mission, treating energy flows into and out of a system along paths of mass flow, heat transfer, and work. In this case energy is conserved, not destroyed, the statement made by the first

7 Typically in-flight fuel burn for a commercial aircraft

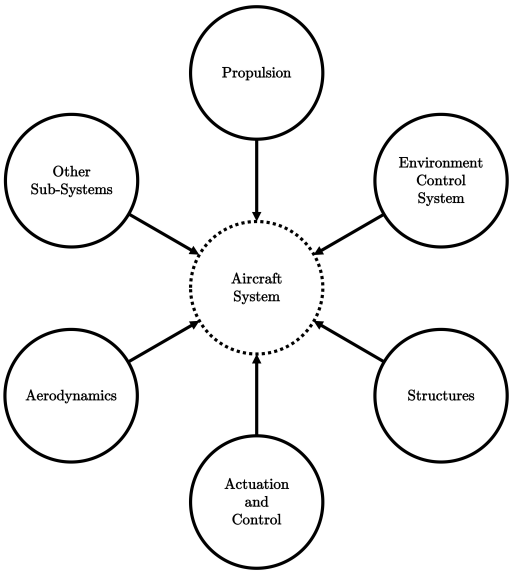

(a) Traditional discipline specific

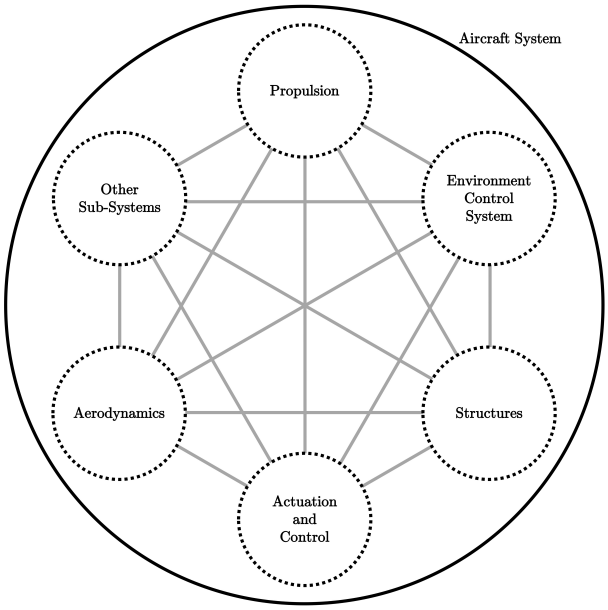

(b) Integrated system based

Figure 1.5: Aircraft Optimisation Methodologies

law of thermodynamics. However, when we perform an energy study of a system such as an aircraft we are not only interested in the conversion of energy from one form to another, but also the conditions and limitations on such a conversion. This is where the application of the second law can provide beneficial insight; as to whether the achieved final solution is near the optimal case or whether the solution is in fact feasible.

This thesis advocates an alternative thermodynamics based systems engineering approach to developing future commercial aircraft, where entropy and energy are coupled to provide additional design insight where traditional methods are restricted, through a method known as *exergy analysis*. A general introduction to the use of exergy within aerospace systems can be found in Doty [54, 55] as well as the published textbook by Camberos and Moorhouse [40], where the primary focus is that of military and hypersonic systems.

Thermodynamic analysis methods, were developed to improve system efficiency of traditional heat driven systems such as ground based power plants and aircraft propulsion systems. However, given thermodynamics is the study of energy content and transfer, and all systems and processes use energy in some form, thermodynamic analysis provides an integrated approach to aircraft optimisation, suitable for all disciplines in aerospace design. Work to date is focused in the military domain based on highly simplified structures, but such a method could be shown to have benefit to the highly conservative and risk averse commercial aerospace sector. Applying thermodynamic design and analysis methods to an aircraft discipline such as aerodynamics, can seem obscure given the widely applied traditional force balance approach. Yet, applying such a method may facilitate the development of aerodynamic concepts that are highly integrated to the propulsion, an application where the force-balance approach is limited, a thought echoed by Camberos

> *"Such capability may allow the development of new and innovative concepts that do not just marginally improve performance but may enable the realization of entire new regimes of performance and operability, especially for high-speed aerospace vehicles"*
>
> - José Camberos [39]

1.3 EXERGY AS A TOOL FOR AEROSPACE DESIGN

Environmental regulation and economic pressures on OEMs are driving a revolution in the architecture of commercial aircraft. There is a trend in proposed future concepts away form the conventional discipline specific tube fuselage with swept wings, where the propulsion system, aerodynamics and other sub-systems can be designed independently of one another. Disruptive new configurations are being proposed by academia and OEMs, such as the HARW configuration discussed in the thesis, where aircraft sub-systems are more highly integrated. As such for a systems engineer, the aircraft needs to be viewed as a system of systems, where design trade-off can be done between conventionally dissimilar technology, providing a more integrated approach to aircraft design. To facilitate this, a universal metric must be used that can be used for performance analysis of any sub-system. This thesis proposes the use of the exergy metric, which tracks the useful work through the system, and how energy's usefulness can be destroyed, through entropy generating processes. The thesis has primarily focused on modelling aeroelastic systems using the common metric, by modelling all aspects of Collar's triangle using exergy analysis. The application to top level aircraft has been shown at the end of the thesis, where a holistic thermo-

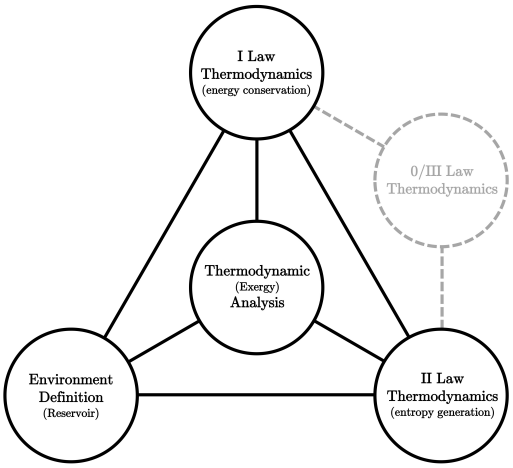

Figure 1.6: Discipline relation triangle for thermodynamic (exergy) analysis

dynamic loss management model has been presented which can include all aircraft sub-systems at the required fidelity.

If the thesis is to be believed and that future aircraft configurations can only be *optimised* through using a process such as exergy analysis, the fundamental issue with exergy analysis must be overcome, which is the acceptance of a new methodology in areas of aircraft design with well established design practices.

Exergy is a concept discussed in thermodynamics at masters level, and as such remains unknown to the majority of engineers outside of the propulsion discipline. So, when discussing exergy within engineering disciplines not aware of the subject, there can be an adverse reaction to its use. Given exergy analysis is simply an extension of explicit first law methods most engineers use, it can be questioned, as to whether the term of exergy needs to exist, or is it just a word to make a novel method sound profound? Enthalpy, energy and entropy are all fundamentally different concepts, and whilst understanding these terms can be confusing, a knowledge of all is needed to describe an energy transfer system. However, exergy is not a different concept, it is an analysis method which couples first law (energy) and second law (entropy) analysis methods with a defined environment (enthalpy) (see Figure 1.6), so fundamentally exergy analysis is nothing new, it is just the application of all laws of thermodynamics to an analysis, thus the term *integrated thermodynamic analysis* would in the authors opinion be more palatable to engineers, as all engineers will understand the basic laws of thermodynamics.

Thus in place of discussing *exergy transfer*, a simpler understanding would come from stating all the analysis method is doing is three things:

- Tracking the flow of energy through the aircraft between different sub-systems (First law of thermodynamics)
- Highlighting system inefficiencies in energy transfer where entropy is produced (Second law of thermodynamics)
- Undertaking the above within a defined external state which limits the maximum amount of energy that can be transferred between systems (Carnot Efficiencies)

Understanding the above methodology leads the engineer to see that exergy analysis, or integrated thermodynamic analysis, is focused on design improvement by allowing the transfer and conversion of energy between systems without losing useful energy in the process through entropy generation. Once this premise is understood,

the challenge is to convince potential users that thermodynamic analysis is not limited to heat driven systems and can in fact be applied to any system or process.

Exergy is commonly referred to as a *second law* analysis method, in contrast to the *first law* energy method. But it is not. Exergy analysis is an extension of energy analysis, where in place of applying just the first law to a system, all four laws of thermodynamics are applied. This lends itself to the discussion that exergy analysis is not aiming to discredit any other methodology, first law based or not (e.g. Breguet is first law based), it is aiming to provide additional insight into the analysis.

1.4 RESEARCH OBJECTIVES

This thesis applies integrated thermodynamic analysis to conventional swept wing aircraft, to show the benefits of the methodology in comparison to traditional discipline design approaches. The thesis then extends the implementation to a conceptual highly integrated High Aspect Ratio Wing (HARW) aircraft[8] with morphing wingtips, where the extended wingspan improves aerodynamic performance but as a consequence the wings have greater flexibility. The launch of the Boeing 777X is the first modern application of ground based morphing on commercial aircraft, yet the technology has found no other commercial application, primarily due to the conservative approach to civil aircraft design, but OEMs also struggle to demonstrate how the morphing effectiveness on a scale model can be scaled up to a full size aircraft.

This thesis develops existing exergy methodology practices by investigating flight dynamic exergy analysis and its application to morphing technologies for large commercial aircraft, evaluating the aerodynamic and aeroelastic contribution to an aircrafts overall exergy use. To achieve this each node of Collar's triangle [27] is evaluated using the exergy metric.

The majority of exergy studies focus on steady-state performance analysis and adopt simplified models for flight dynamics and morphing, and estimate the exergetic cost of such devices in global performance terms such as weight and fuel burn penalties. As a result, the primary research challenge is seen to be the definition, calculation and analysis of dynamic exergy for flexible aircraft; where the effects of variables such as wing flexibility on stored strain energy and consequently exergy destruction will be explicitly studied.

Thus, this thesis challenges and highlights the limitations of traditional design methodologies, and proposes an alternative global viewpoint of energy balance, by tracking the exergy flow and entropy generation in the system. This aims to lay the foundations for a novel physics based Multi-Disciplinary Optimisation (MDO) method to enable the development and realisation of next generation commercial aircraft and technologies, where systems are highly coupled. This thesis proposes the following research questions:

1. Does applying second law exergy analysis provide insights into future concept aircraft designs that were not previously obtainable through other in-practice MDO methods?
2. Can exergy analysis be used as a design tool with capability to compare and justify the integration of different morphing technologies on future concept aircraft?
3. Is exergy analysis consistent with a scaled model when applied to a high fidelity real world problem?

8 for HARW aircraft aerodynamics and structures are highly integrated

4. Can wing aeroelastic phenomena of a highly flexible aircraft be integrated into the exergy analysis to assess the impact of elastic stored energy and wing flexibility on the aircraft exergy usage?

1.5 CHAPTER SUMMARY

To meet the environmental and economic challenges for aviation in the near future, there is a clear need for revolutionary concepts in aircraft design, that move away from the iterative progression of the conventional tube with swept wings. In order to develop such a concept a new analysis and performance metric is needed that can be used to assess all aircraft subsystems, which this thesis advocates should be done using an integrated thermodynamic analysis method. To provide insight into this by answering the above research questions, the thesis is structured into four *parts*;

I An introduction to the project, the theory of exergy analysis and a review of literature for current usage of the method in aerospace

II The theoretical development of the exergy method for use in fluid-structure interaction models, through the study of exergy analysis in aeroelastics

III Provides applications for the developed exergy methodology, in direct response to the research questions above

IV Conclusions and further work discussion

2

TECHNICAL FOUNDATION AND FORMULAE

This chapter aims to provide the basics to the thermodynamics behind exergy analysis. By building upon concepts all engineers have an understanding of, such as the first law of thermodynamics, to the less known concept of exergy and its transfer and destruction. Basic concepts such as the *fundamental thermodynamic relation* are then expanded to provide an *exergetic thermodynamic relation*.

In studying energy transfers and conversion, the principles are taken from the laws of thermodynamics.

∅ *Zeroth Law.* If two bodies are in thermal equilibrium wih a third body, they are also in thermal equilibrium with each other

I *First Law.* Energy can be neither created of destroyed during a process; it can only change forms (principle of conservation of energy)

II *Second Law.* It is impossible for any device that operates on a cycle to receive heat from a single reservoir and produce a net amount of work (Kelvin-Planck statement)

III *Third Law.* The entropy of a pure crystalline substance at absolute zero temperature is zero, since there is no uncertainty about the state of the molecules at that instant

For the purposes of this work the four laws will be regarded as self-evidently true, thus the axioms of the thesis. Basic knowledge of the laws of thermodynamics is assumed, so a detailed overview is omitted.

2.1 FIRST LAW OF THERMODYNAMICS

Energy is an abstract concept, given it can only be observed through its effects on matter and electromagnetic radiation. Energy is not the *ability of a system to perform work*[1], more accurately, energy is the extensive, conserved quantity that is inter-changeable with heat and work. The first law of thermodynamics, the *conservation of energy*, is a mathematical principle that states there is a quantity in the universe (or any closed system) that will always sum to a constant numerical quantity, no matter what process or conversion it goes through, and this quantity is known as energy. Feynman summarises the postulated energy theory by noting:

> *"It is important to realize that in physics today, we have no knowledge of what energy is. We do not have a picture that energy comes in little blobs of a definite amount. It is not that way. However, there are formulas for calculating some numerical quantity, and when we add it all together it gives "28"*[2]*, always the same number. It is an abstract thing in that it does not tell us the mechanism or the reasons for the various formulas."*
>
> - Richard Feynman [65]

1 The ability of a system to perform work will later be defined as *available energy* or *exergy*

2 This pun is in reference to Feynmans' *Dennis the Mennis* analogy on Energy Conservation, which is worth a read for the reader still puzzled by the concept of energy

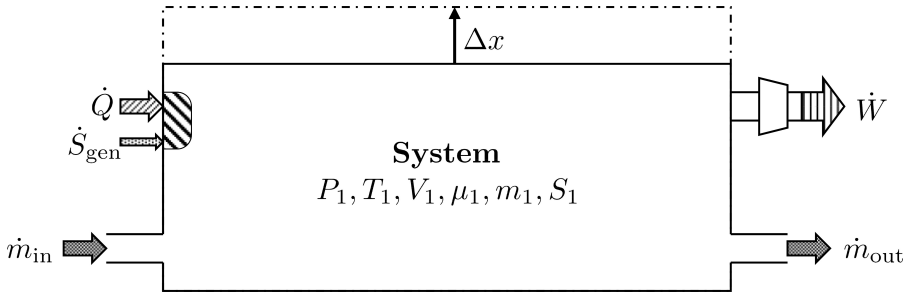

Figure 2.1: Energy transfers for an open system

Energy (E) can be neither created nor destroyed during a process; it can only change forms

$$\sum E = \text{constant}$$

Energy can be sub divided into two major forms, that of *kinetic energy* and *potential energy*. Kinetic energy is the energy associated with movement, be it the motion of waves, electrons, atoms, molecules or substances, thus a function of velocity or rate change of a state. Potential energy is the energy of state (e.g. position, chemical composition...), where the system has a disparity in some form to its environment which enables it to do or receive work, thus a function of position or state. On a microscopic level all energy can be described as either kinetic or potential, however in engineering it is simpler and clearer to discuss energy as a macroscopic term, where energy can sub-divide into other forms with their own mathematical expressions.

- Kinetic
  - Radiant (electromagnetic) Energy
  - Thermal Energy
  - Mechanical Energy (objects in motion)
  - Electrical Energy
  - Sound Energy
  - Magnetic Energy
- Potential
  - Chemical Energy
  - Nuclear Energy
  - Stored Mechanical (elastic) Energy
  - Gravitational Energy

In this research any form of energy that is discussed can be described by one of the above sub-categories[3].

2.1.1 *Energy Conservation and Transfers*

The first law of thermodynamics for a closed system allows energy to be transfered via work (W) and heat (Q), using the sign convention given in Figure 2.1

$$\Delta E_{sys} = \int Q dt - \int W dt$$

3 There is one final form of energy discovered by Einstein, which is the energy of an object for just having mass ($E = mc^2$), known as *mass energy*. This is associated with the theory of relativity and beyond the limitations of this study, as such will not be discussed further in this research.

which is derived by defining the Joule proportionality constant as the equivalence of work and heat, with the total sum of the energy remaining constant, such that energy is never created nor destroyed

$$\dot{E}_{sys} = \dot{E}_{in} - \dot{E}_{out}$$

This can be extended for an open system where the system energy can be varied through mass transfer, which can be in the forms of enthalpy ($h = u + pv$), kinetic and potential energy.

$$\frac{\delta E}{\delta t} = \dot{Q} - \dot{W} + \sum_{in} \dot{m} \left(h + \frac{1}{2}\dot{q}^2 + gq \right) - \sum_{out} \dot{m} \left(h + \frac{1}{2}\dot{q}^2 + gq \right) \tag{2.1}$$

2.1.2 *First Law Thermodynamic Analysis*

Energy analysis is based purely on Newtonian mechanics and the first law of thermodynamics, treating energy flows into and out of a system along paths of mass flow, heat transfer, and work; where energy is always conserved, not destroyed. Yet, understanding how a system converts energy from one form to another does not fully describe the conversion process, in addition the conditions and limitations on such a conversion need to be known. The drawbacks of a first law analysis method can be highlighted by the *coffee cup* thought experiment.

EXAMPLE 1

A cup of coffee, initially at temperature, T_1, is placed into a room at lower temperature, T_∞. Abiding by the first law of thermodynamics, the coffee could cool by transferring thermal energy to the environment via heat, with the sum of the energies in the cup and environment remaining constant.

However, the reverse process also adheres to the first law where the room transfers thermal energy via heat into the cup to increase the coffee temperature. But, observation shows heat only travels unidirectionally from a *hot* source to a *cooler* source, thus the coffee can only reduce in temperature to the point of thermal equilibrium with the room ($T_1 = T_\infty$).

This thought experiment shows the first law of thermodynamics analysis method does not inform about:

- *Feasibility.* The constraint of the first law, is that if a process satisfies the first law it is not to say it is feasible, just that if it is feasible the first law must be satisfied.
- *Irreversibility (directionality).* The first law of thermodynamics states that a system's energy is constant unless energy is transferred via work or heat, and that no energy is lost in transfer.
- *Availability.* The first law shows the *quantity* of energy used by each system and not the *quality* (availability of energy to be converted into work) of energy flow through the entire system.
- *Optimal efficiency.* Boundaries of real systems tell us that the efficiency cannot exceed 100%, but even if irreversibility were removed the heat engine first law efficiency would not approach this.

2.2 SECOND LAW OF THERMODYNAMICS

The application of the second law of thermodynamics can provide beneficial insight to an analysis on top of that generated by the first law analysis method, a thought summarised again by Feynman.

> *"With regard to the conservation of energy, we should note that available energy is another matter there is a lot of jiggling around in the atoms of the water of the sea, because the sea has a certain temperature, but it is impossible to get them herded into a definite motion without taking energy from somewhere else. That is, although we know for a fact that energy is conserved, the energy available for human utility is not conserved so easily. The laws which govern how much energy is available are called the laws of thermodynamics and involve a concept called entropy for irreversible thermodynamic processes."*
>
> - Richard Feynman [65]

Entropy (S) can be defined as the extensive system property that describes the number of ways a thermodynamic system can be arranged, thus a measure of the systems disorder, calculated as the product of the Boltzmann constant (k_B) and the natural log of the number of microstates the system can be in (Ω)

$$S = k_B \ln \Omega$$

However, defining a systems entropy at any given time is not overly useful with an unknown maximum entropy. Thus, typically of more interest is the change in entropy of a system.

2.2.1 *Entropy Generation and Transfer*

If the process undergoes a thermodynamic transfer the combined entropy of the system and the environment will either increase or remain the same. The latter case is known as a reversible process, where energy is transferred along a defined thermodynamic path cyclically such that the system returns to its initial state without any change, the so-called Carnot cycle for a frictionless heat engine. However a reversible process is an ideal case, as all real processes have irreversibilities, be it friction, expansion of gas, chemical reaction, diffusion of gases etc. Clausius' second law of thermodynamics, states that real processes are irreversible and proceed only in one particular sense. The directionality of a process can be defined in terms of the positive entropy generation, S_{gen} as a function of the systems pre, S_0, and post, S_1, entropy state, and that generated through heat transfer, Q, at a given temperature, T

$$S_{gen} = S_1 - S_0 - \int \frac{\delta Q}{T} \geq 0$$

> *"It is impossible to construct a system which will operate in a cycle and transfer heat from a cooler to a hotter body without work being done on the system by the surroundings."*
>
> - Clausius' Theorem [153]

The concept of entropy transfer, makes the distinction between heat transfer and work transfer as parallel forms of energy transfer as it is only the transfer of energy as heat that is accompanied by entropy transfer, for example through frictional losses. A systems total entropy, S_{sys}, can be defined as

$$\dot{S}_{sys} = \dot{S}_{in} - \dot{S}_{out} + \dot{S}_{gen}$$

Given entropy can only be generated, the second law builds on the understanding of a system given by the first law by applying a directionality to the energy transfer through the introduction of a system property known as *entropy*.

Allowing for mass flow in an open system, the entropy statement can be given from the second law of thermodynamics as:

$$\frac{\delta S}{\delta t} \geq \sum_{in} \dot{m}s - \sum_{out} \dot{m}s + \frac{\dot{Q}}{T}$$

or as a function of entropy generation:

$$\dot{S}_{gen} = \frac{\delta S}{\delta t} - \frac{\dot{Q}}{T} + \sum_{out} \dot{m}s - \sum_{in} \dot{m}s \geq 0 \tag{2.2}$$

Whilst the second law cannot in itself be proven, no experiment has been conducted that contradicts the second law (in either Kelvin-Planck and Clausius statements form, see [44]) thus the definition can be accepted as true.

2.2.2 *Second Law Thermodynamic Analysis*

All real world processes are irreversible. Auditing a design with the entropy approach will highlight where available energy is being used throughout the system, showing areas of unavoidable irreversibilities such as combustion losses as well as those irreversibilities with avoidable waste, as to direct the designers attention to those areas. The second law approach is focused on identifying irreversibilties where entropy is produced with the aim to optimize the structure as to minimize this production. Some common examples of system generic irreversibilities are given by Smith [166] as:

- Mixing objects or fluids
- Heat transfer (through a finite temperature difference)
- Friction as a result of relative motion of objects or fluids
- Chemical reactions
- Inelastic deformation of solids
- Electric resistance
- Drag (vortex and parasitic)
- Sudden compressions such as shock waves

Using the coffee cup analogy from the example in Section 2.1.2, in order for the combined entropy of the coffee cup system and the environment to increase, thermal energy may be transferred out of the cup via heat. This is because the entropy of the coffee cup system decreases during cooling, yet the sum of the system and environmental entropy increases, thus entropy generation in line with the second law. Meaning the premise of thermal energy being transferred into the cup is not possible, as would result in negative entropy generation. The second law therefore provides additional insight to the first law analysis, in the following areas:

- *Feasibility.* The second law states a system moves to become more disordered and that entropy, a measure of disorder, can only ever increase in a real system, thus can only be positive when energy is transferred to a cooler source. This is an important distinction, because the first law does not distinguish between heat and work transfer.
- *Irreversibility.* The wastes or losses can be quantified by entropy generation. The increasing entropy in a system marks the approach to thermodynamic equilibrium, the point of maximum entropy. As such entropy is a measure of the unavailability of work potential.

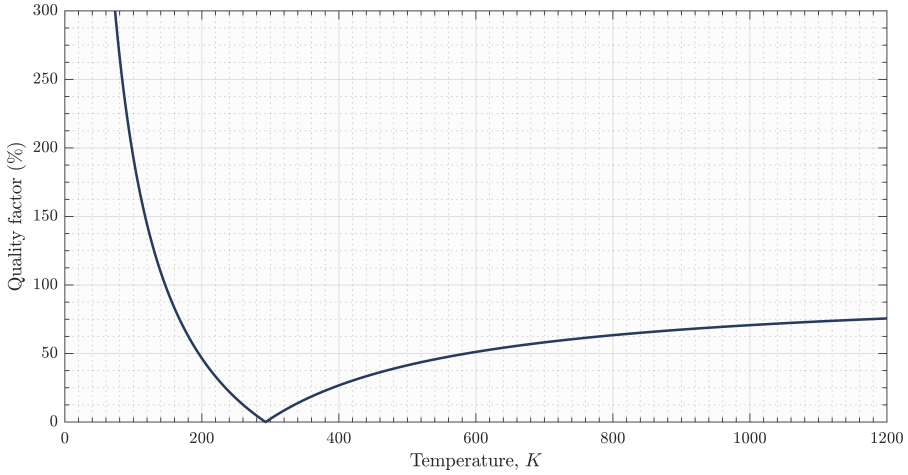

Figure 2.2: Energy Quality as a function of its temperature

- *Availability.* The energy quality can be seen as the absolute inverse of the Carnot efficiency (ϵ) an expression for the maximum amount of work that can be taken from the coffee cup as a function of the coffee temperature, T_1, and the room environment temperature, T_0

  $$\text{Energy Quality} = \left|\frac{1}{\epsilon}\right| = \left|\frac{T_1 - T_0}{T_1}\right|$$

  Plotting the absolute inverse of this function gives the quality factor, a measure of the *quality* or available energy (exergy) in a system, see Figure 2.2. This shows the farther the system is from thermodynamic equilibrium (higher temperature) the more available the system energy. Another interesting implication is that the exergy of a very cold body far exceeds its low energy content as heat is taken from the environment. Thus, the amount of available work is high, as work is done on the body.

- *Optimal Efficiency.* Taking the internal combustion engine as an example, the standard first law efficiency of such an engine is usually around 20% [15]. This first law efficiency (η_I) can be calculated as

  $$\eta_I = \frac{W_{out} - W_{in}}{Q_{hot}}$$

  The idealized (Carnot) process provides the tools to provide a more accurate obtainable efficiency. A reversible process never occurs in nature, but can still be used in *thought experiments* to provide a theoretical upper limit for the performance of a device, through a second law efficiency which informs how well the process could ever do compared to the reversible cycle efficiency ($\eta_{Reversible}$)

  $$\eta_{II} = \frac{(\eta_I)_{Irreversible}}{\eta_{Reversible}} \tag{2.3}$$

2.3 INTEGRATED THERMODYNAMIC ANALYSIS

It can be postulated that when applied individually energy or entropy analysis are incomplete. Undertaking a first or second law analysis in isolation provides insight into the thermodynamic process behaviour, however neither describe the system processes completely. The application of the first and second law together, outside propulsion, is sometimes considered an abstract concept as energy and entropy are thought to be separate state properties. However, the contrary is true, where a synthesised application allows the energy transfers of a system to be described with the

first law, and the second law providing insight into the feasibility, directionality and the losses of useful energy with each of these energy transfers.

2.3.1 *Coupling the Laws of Thermodynamics*

The first mathematical synthesis of the first and second laws of thermodynamics was defined as *available energy* which was posed by Gibbs in 1873, defining the term *enthalpy* ($H = U + pV$) as a measure of the total energy of a system, the sum of the internal energy (U) and the product of pressure (p) and volume (V). The Gibbs Free Energy (G) is a theoretical value that defines the maximum work that can be obtained from a closed system undergoing a reversible, isothermal (constant temperature) and isobaric (constant pressure) process

$$G(p,T) = \underbrace{U + pV}_{\text{I Law}} - \underbrace{TS}_{\text{II Law}} \tag{2.4}$$

It will become evident that exergy is conceptually related to Gibbs Free Energy, and as such a suitable starting point to define exergy is to understand what is meant by Gibbs Free Energy.

> ***Gibbs Free Energy*** *is a thermodynamic potential that indicates the amount of work obtainable from a system undergoing an isothermal and isobaric process*

A similar formulation is that of Helmholtz free energy (F), which defines the maximum work that can be obtained from a closed system reversibly through a isothermal and isochoric (constant volume) process.

$$F(T,V) = U - TS$$

2.3.2 *Closed System Exergy*

Exergy can be viewed as an extension of Gibbs and Helmholtz Free Energy where the available energy is not dependent on whether or not it is an isothermal, isobaric or isochoric process, however it is dependent on the unconstrained environment in which it resides. Ayres [15] highlights the similarity and difference of exergy to these two forms of free energy, as:

> *"The most general of all thermodynamic potentials of course is exergy, defined as the maximum amount of work that can be extracted from a system without any constraints on volume, pressure, temperature or composition."*
>
> - Robert Ayres [15]

Understanding the two fundamental principles of thermodynamics, a combined definition from Sciubba [162], Bejan [20], Naterer [118] and Ayres [15] can propose a synthesised statement of the first and second laws.

> *The maximum theoretical useful work obtained if a system is brought into thermodynamic equilibrium with the environment by means of processes in which the system interacts only with this environment. Exergy is a measure of the departure of the given state from the environmental state (distance from thermodynamic equilibrium), the larger the departure, the greater the potential for doing work. It is not a conserved quantity (like energy) but it is possible to construct an exergy balance for any energy or materials transformation process, accounting for inputs, process losses, useful products and wastes.*

Thus analysis using the simultaneous application of the laws of thermodynamics within a defined environment is defined as *integrated thermodynamic analysis*, where

exergy is the metric. The environment in which a system resides is more commonly known as a *reference state*, which is defined by thermodynamic variables of reference temperature (T_∞), reference pressure (P_∞) and reference chemical potential of species 'k' (μ_{k_∞}), see Figure 2.3a. In practice an environment is defined by any environmental state, so for an aircraft system the environment is stated as a temperature, pressure, velocity, chemical composition and position as shown in Figure 2.3c. However whilst all are required for exergy analysis the temperature is the most important as thermal energy transferred via heat is the least available form of energy, and the transfer associated with entropy generation (Figure 2.3b).

The exergy or available energy of an independent system residing in a given environment is defined by the *system exergy* (X_{sys}). This can be easier understood by subdividing the total system exergy into contributing parts. Note the difference to subdivision given in Section 2.1, where the exergy terms are not subdivided into just kinetic and potential terms. Kinetic, X_T, and potential, X_V, exergies can only be transfered via work and are ideally converted, however the thermal, X_U, and chemical exergies, X_{Ch}, are transfered via work and heat (not ideally) so are quantified separately. Thus

$$X_{sys} = X_U + X_T + X_V + X_{Ch} \tag{2.5}$$

with the sub-exergies being defined as:

- Thermal exergy (X_U)
  - Internal exergy (closed system)
  - Enthalpy exergy (open system)
- Kinetic Exergy (X_T)
  - Mechanical (objects in motion)
  - Radiant (electromagnetic)
  - Sound
- Potential Exergy (X_V)
  - Gravitational
  - Stored mechanical (elastic)
  - Nuclear
  - Electrical
  - Magnetic
- Chemical Exergy (X_{Ch})

The *thermal exergy* is defined as the work obtainable by taking the system through a process such as compression, expansion or heat exchange, to the temperature and pressure states of the environment [15]. For a closed system (non mass transfer) the *thermal exergy* can be simplified to the internal exergy of the system

$$X_U = (U - U_\infty) + P_\infty (\mathcal{V} - \mathcal{V}_\infty) - T_\infty (S - S_\infty)$$

where the maximum work that can be output is a function of the internal energy (U), volume ($\mathcal{V}$), entropy (S), the environment temperature (T_∞) and pressure (P_∞). However in an open system, the exergy of mass flow must be accounted for, as given in the enthalpy exergy

$$X_U = \underbrace{(U + PV) - (U_\infty + P_\infty \mathcal{V}_\infty)}_{(h - h_\infty)} - T_\infty (S - S_\infty)$$

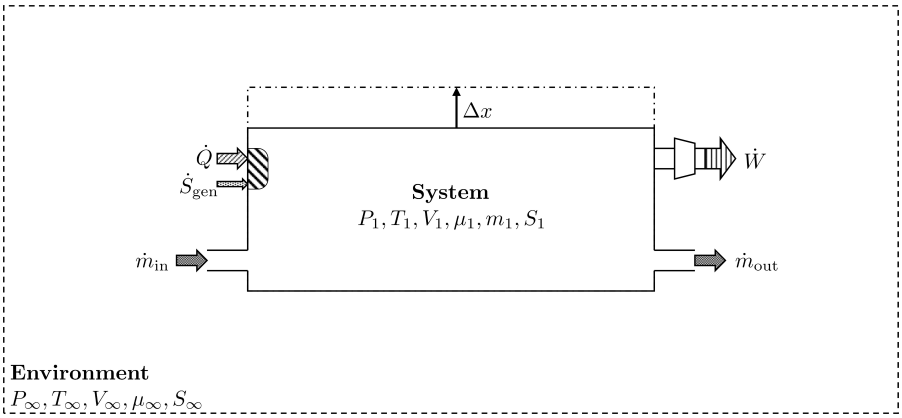

(a) Open thermodynamic system and its interactions with the environment

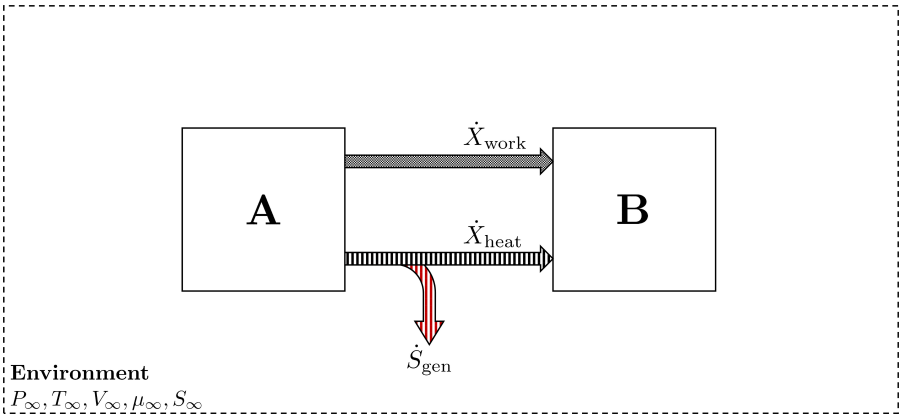

(b) Thermodynamic system transfer for energy

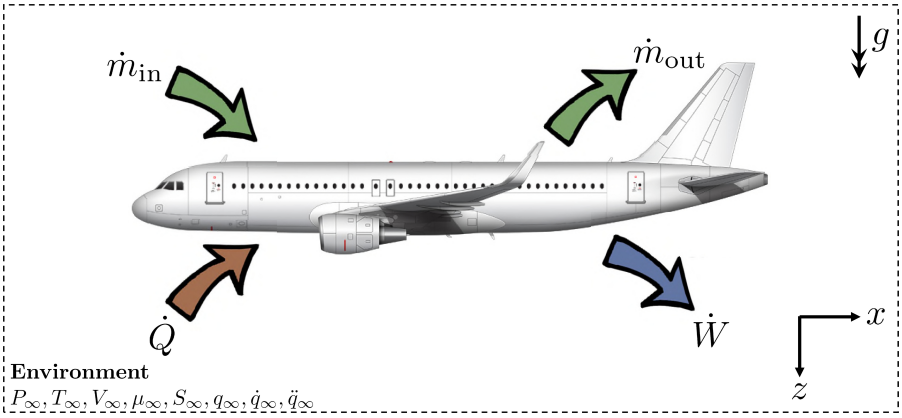

(c) Open thermodynamic system and its interactions with the environment of an aircraft

Figure 2.3: Thermodynamic Systems

where a clear resemblance to Gibbs Free Energy (equation 2.4) can be seen, however in this case for a fully defined unconstrained environment.

The *kinetic exergy* is defined as the work obtainable from movement, be it the motion of waves, electronics, atoms, molecules or substances.

$$X_T = \underbrace{\frac{1}{2} m \left(V - V_\infty\right)^2}_{\text{Mechanical}}$$

The *potential exergy* is defined as the work obtainable from system state (e.g. position, chemical composition, etc.), where the system has a disparity in some form to its environment which enables it to do or receive work.

$$X_V = \underbrace{mg\left(q - q_\infty\right)}_{\text{Gravitational}} + \underbrace{\frac{k\left(q - q_\infty\right)^2}{2}}_{\text{Stored mechanical}} + \underbrace{\frac{C(\mathrm{Y} - \mathrm{Y}_\infty)^2}{2}}_{\text{Electrical (capacitor)}}$$

In practice kinetic and potential exergy are both *perfect forms* of exergy, in that they can be completely converted to work, given a null reference state.

The *chemical exergy* is defined as the maximum amount of work obtainable by taking a system reversibly to the same chemical composition as the environment, with environmental temperature and pressure conditions. Camberos [40] formulates a mass derived chemical exergy (equal to the mole derived function) as given by

$$X_{Ch} = \sum_i^n y_i \left(\mu_{i_1} - \mu_{i_\infty}\right) \tag{2.6}$$

where the exergy is a function of the chemical potential (μ_k) and mass ratio (y_i) as opposed to alternative stoichiometric mole ratio ($v_{i,j}/v_j$) relationships of Simpson [164].

Whilst this is a form of potential exergy, it cannot be perfectly converted to work. In addition to the exergy losses through heat generation (entropy production) found in reactions such as combustion, irreversibility is generated as gaseous compounds are released to the environment at dead state chemical potential, for example carbon dioxide and water vapour.

2.3.3 *Exergy Transfer*

Exergy (as with energy) can be transferred into and removed from a systems control volume through three means; mass flow, heat and work. Considering a closed system, exergy can only be transferred by heat or work.

The flow exergy, ψ, can be used to define the exergy of the mass flow into and out of the system

$$\dot{m}\psi = \dot{X}_{sys} = \dot{X}_U + \dot{X}_T + \dot{X}_V + \dot{X}_{Ch} \tag{2.7}$$

The flow exergy can be used to define the exergy of the mass flow into and out of the system, as mass contains exergy as well as energy and entropy, and the exergy, energy and entropy contents of a system are proportional to mass.

The second law tells us that the maximum work that can be obtained from energy transfer between a system temperature, T, and environment temperature, T_0, is through the Carnot cycle heat engine. As such the Carnot efficiency describes the fraction of heat that can be transferred, and ultimately the total amount of useful work, known as the exergy transfer by heat.

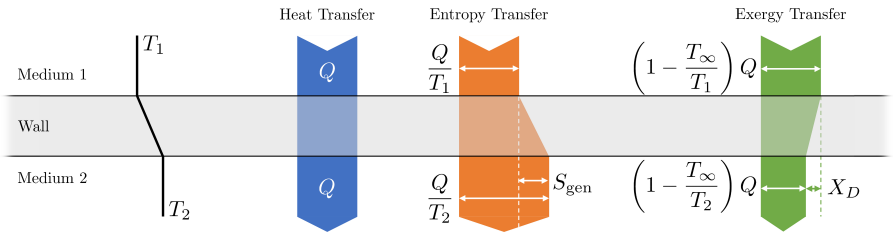

Figure 2.4: Comparison between energy, entropy and exergy transfer through a medium

Assume that the system temperature is not constant over the location of the heat transfer, the *exergy transfer by heat* is given by the integration:

$$X_{\text{heat}} = \int \left(1 - \frac{T_\infty}{T}\right) \delta Q \tag{2.8}$$

Exergy transferred by work is equal to the work input or output itself

$$X_{work} = W$$

However in the case where work is done by or on surrounding atmospheric pressure a loss in useful work output must be accounted for. Take a weightless and frictionless piston as an example, work must be done on the atmospheric air to move the piston as work is input into the system and the pressure rises. Thus the exergy transfer due to work becomes

$$X_{work} = W - P_\infty(V_1 - V_0) \tag{2.9}$$

The exergy balance is used to identify the change in exergy of a system given a specific exergy transfer. Coupling the equations for mass transfer, heat transfer and work transfer with the exergy destruction principle leads to an expression for the balance of exergy equation representing a synthesis of the first and second laws. For a closed system the exergy difference is dependent only on heat and work transfer as no mass transfer is allowed. Combining equations 2.8 and 2.9 the expression for exergy change is given as

$$X_2 - X_1 = \int \left(1 - \frac{T_\infty}{T}\right) Q dt - \left[\int W dt + P_\infty \left(V_\infty - V_1\right)\right] - T_\infty S_{gen}$$

Given as a rate change in system exergy as:

$$\frac{dX_{cv}}{dt} = \sum \left(1 - \frac{T_\infty}{T_k}\right) \dot{Q}_k - \left\{\dot{W} - P_\infty \frac{dV_{cv}}{dt}\right\} - T_\infty \dot{S}_{gen}$$

The open system is an extension of the closed system, yet in this case exergy changes are allowed through mass transfer. Substituting Equation 2.7 gives,

$$X_2 - X_1 = \sum \left(1 - \frac{T_\infty}{T_k}\right) Q_k - \{W - P_\infty(V_1 - V_\infty)\} + \sum_{in} \dot{m}\psi - \sum_{out} \dot{m}\psi - X_D \tag{2.10}$$

Given as a rate change in system exergy as:

$$\begin{aligned}\frac{dX_{cv}}{dt} = &\underbrace{\sum \left(1 - \frac{T_\infty}{T_k}\right) \dot{Q}_k}_{\text{Heat Transfer}} - \underbrace{\left\{\dot{W} - P_\infty \frac{dV_{cv}}{dt}\right\}}_{\text{Work Transfer}} \\ &+ \underbrace{\sum_{in} \dot{m}\psi - \sum_{out} \dot{m}\psi}_{\text{Mass Transfer}} - \dot{X}_D\end{aligned} \tag{2.11}$$

A thought experiment is provided in Appendix A to clarify the difference between energy, entropy and exergy.

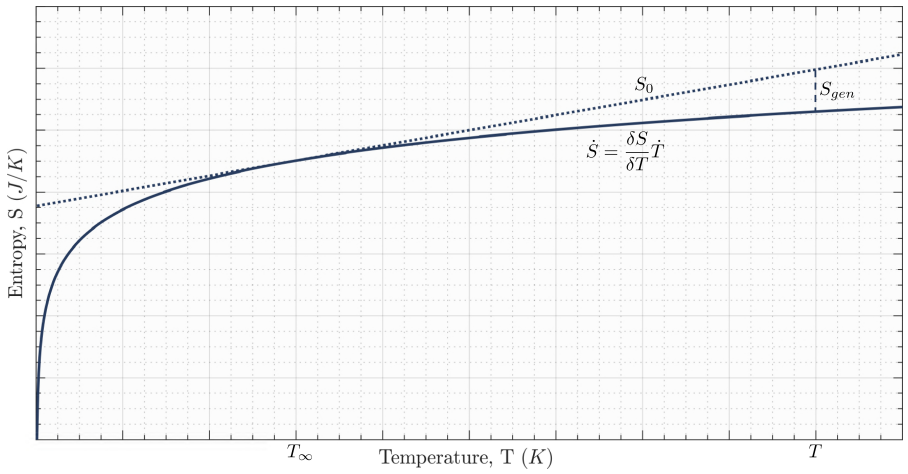

Figure 2.5: Geometric definition of a concave entropy function [37]

2.4 DERIVED PROPERTIES OF ENTROPY AND EXERGY

2.4.1 *Concavity of Entropy*

Entropy is an abstract principle that is hard to understand due to the inability to measure the property. If a systems entropy could be known, the number is inconsequential unless the maximum value is also known. Thus, Naterer [118] and Camberos [37] show it is the generation of entropy that is significant in the design process, with the knowledge that entropy is always increasing to an eventual maximum value. This leads to one of the fundamental principles of entropy in that it has a concave geometric profile, which is critical when understanding the non-negative nature of entropy generation. Previously it was defined that entropy is only associated with energy transfer through heat currents and not work, thus for simplicity a system only allowing heat transfer is considered for this derivation. The first (equation 2.1) and second (equation 2.2) law of thermodynamics can be substituted and expressed together as

$$S_{gen} = S_\infty - S - \frac{1}{T_\infty}\delta U$$

Introducing specific heat, $c_v = \frac{\delta U}{\delta T}$

$$S_{gen} = S_\infty - S - \frac{c_v}{T_\infty}(T_\infty - T)$$

This expresses entropy generation as a function of temperature, using the specific heat capacity at constant volume, c_v $(J/mol.K)$. Taking this concept one stage further and introducing the thermodynamic relation for specific heat and entropy ($\frac{c_v}{T} = \frac{\delta S}{\delta T}$)

$$S_{gen} = S_\infty - S - \left.\frac{\delta S}{\delta T}\right|_\infty (T_\infty - T)$$

Plotting this function for entropy against temperature as in Figure 2.5, it can be noted that the entropy generation function is concave, as such entropy is always increasing asymptotically to a maximum value, the point at which available energy is zero.

2.4.2 *Guoy-Stodola Identity*

Gouy [74] and Stodola [170] derived an expression for entropy such that it was in terms of useful energy (exergy) and thus easier to quantify in energy units of Joules, and understand the energy lost due to entropy generation. The derivation comes from an upper bound work transfer out of the unsteady open system, where the

first and second law are expressed as equation 2.1 and equation 2.2 respectively. Simplifying to remove heat transfer

$$\begin{aligned}\dot{W}_{max} = &\sum_{in} \dot{m} \left(h + \frac{1}{2}\dot{q}^2 + gq + Ts \right) \\ &- \sum_{out} \dot{m} \left(h + \frac{1}{2}\dot{q}^2 + gq + Ts \right) \\ &- \frac{d}{dt}(E - T_\infty S)\end{aligned}$$

Of engineering significance is the difference between the maximum work output and the actual work output. In this treatment it is recognized that this quantity is the lost available work (destroyed exergy) and on a unit time basis, lost available power, or rate of exergy destruction associated with the degree of irreversibility

$$\dot{X}_D = \dot{W}_{max} - \dot{W}$$

The destroyed exergy is zero when the system operates reversibly, while in the irreversible cases destroyed exergy is always positive. The fact that destroyed exergy is always positive has nothing to do with the sign convention adopted for work transfer. The lost available work (destroyed exergy) is not an energy transfer interaction system-environment, such as work and heat transfer. Lost available work is a measure of the inequality sign in the second law, a measure of the degree of thermodynamic irreversibility. By merging equations with the first law an important relationship between destroyed exergy and entropy generation is derived

$$\dot{X}_D = T_\infty \left(\frac{\delta S}{\delta t} - \frac{\dot{Q}}{T_\infty} - \sum_{in} \dot{m}s + \sum_{out} \dot{m}s \right)$$

By simplifying with the expression for entropy generation as in Equation 2.2, the Gouy-Stobola identity for an environmental temperature is defined as

$$\dot{X}_D = T_\infty \dot{S}_{gen} \tag{2.12}$$

The Gouy-Stobola theorem is actually defined as a direct proportionality between entropy generation and exergy destruction. In the above case the constant is the environmental dead state temperature, however this could be a different constant dependent on the system being analysed, so

$$\dot{X}_D \propto \dot{S}_{gen}$$

> *"The sum of the entropies of all the bodies taking part in any [real] process whatever is at the end of the process greater than at its beginning... For irreversible processes of any nature (also chemical), the useful work suffers a reduction equal to the product of the resulting increase of entropy in all the bodies taking part in the process and the temperature of the heat-abstracting reservoir, that is, the environment."*
>
> - Aurel Stodola [170]

2.4.3 *Convexity of Exergy*

Above it was defined that destroyed exergy is always positive as it is a measure of the inequality sign in the second law, which is a measure of the degree of thermodynamic irreversibility. Thus it is possible to show that unlike the geometric concavity of entropy, exergy is in fact geometrically convex, see Naterer [118] and Camberos

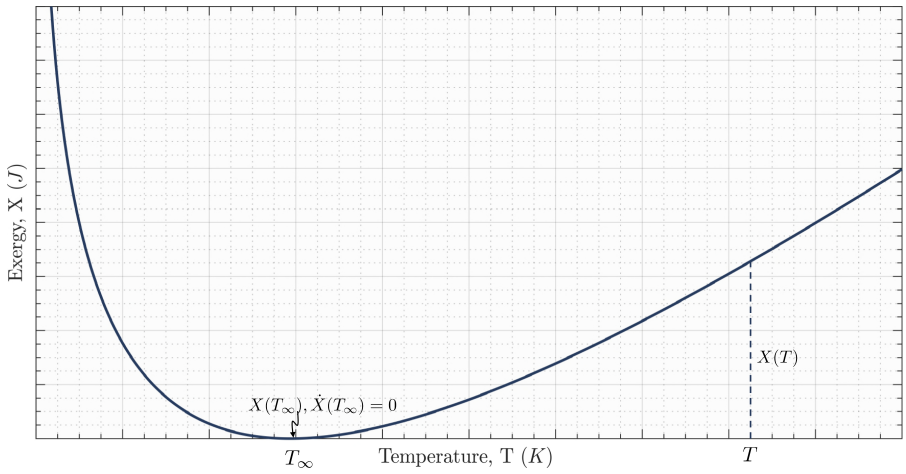

Figure 2.6: Geometric definition of a convex exergy function

[37]. To derive this, it is assumed a system has only thermal exergy as defined in Equation 2.11 formed with the specific heat capacity,

$$\dot{X} = c_v \dot{T} + P_\infty \dot{V} - T_\infty \dot{S}$$
$$\dot{S} = \dot{S}_{gen} + \frac{\delta S}{\delta T}\dot{T} + \frac{\delta S}{\delta V}\dot{V}$$

Combining these equations along with the thermodynamic relations $\frac{\delta S}{\delta U} = \frac{1}{T}$ and $\frac{\delta S}{\delta V} = \frac{P}{T}$

$$\dot{X} = c_v \dot{T} + P_\infty \dot{V} - T_\infty \left(\dot{S}_{gen} + \frac{\delta S}{\delta T}\dot{T} + \frac{\delta S}{\delta V}\dot{V} \right)$$
$$\dot{X} - \left(1 - \frac{T_\infty}{T}\right) c_v \dot{T} - \left(P_\infty - T_\infty \frac{P}{T}\right) \dot{V} = -T_\infty \dot{S}_{gen}$$

From the second law of thermodynamics (Equation 2.2) it can thus be stated that

$$\dot{X} - \left(1 - \frac{T_\infty}{T}\right) c_v \dot{T} - \left(P_\infty - T_\infty \frac{P}{T}\right) \dot{V} \leq 0$$

This result proves the geometric property of convexity for exergy. Thus the geometric properties of concavity and convexity for entropy and exergy respectively are equivalent. An example function plotted for exergy vs temperature can be seen in Figure 2.6.

A further example can be found in Appendix A calculating the exergy of a stream of gas.

2.4.4 *The Exergetic Thermodynamic Relation*

The *fundamental thermodynamic relation* is a coupling of the laws of thermodynamics, to describe a closed system allowing rate changes in the internal energy through entropy and volume variations assuming an uniform temperature and pressure at constant chemical composition, given as

$$dU = TdS - \underbrace{PdV}_{\delta W}$$

Here the work transfer is work done by pressure for given volume changes. In the same way exergy can be viewed as an unconstrained Gibbs Free Energy, the fundamental thermodynamic relation can be expanded to include exergy terms, to form

the *exergetic thermodynamic relation* for an open system, accounting for the aircraft environment of volume (V_∞) and free stream velocity (u_∞)

$$\delta W = \int_{\infty}^{1} P dV = \underbrace{P_\infty \left(V_1 - V_\infty\right)}_{X_M}$$

The mechanical work done can be defined in terms of Gibbs Free Energy enthalpy, Equation 2.4, as

$$\begin{aligned}\left(H_1 - H_\infty\right) + P_\infty V_1 &= \left\{\left(U_1 - U_\infty\right) + P_1 V_1 - P_\infty V_\infty\right\} + P_\infty V_1 \\ P_\infty \left(V_1 - V_\infty\right) &= \left(H_1 - H_\infty\right) - \left(U_1 - U_\infty\right) - V_1 \left(P_1 - P_\infty\right)\end{aligned}$$

Substituting this into the work equation

$$\delta W = \left(H_1 - H_\infty\right) - \left(U_1 - U_\infty\right) - V_1 \left(P_1 - P_\infty\right)$$

Coupling with Equations 2.1, 2.2 and 2.7

$$\begin{aligned}\left(U_1 - U_\infty\right) =& T \left(S_1 - S_\infty\right) \\ &- \left\{\left(H_1 - H_\infty\right) - \left(U_1 - U_\infty\right) - V_1 \left(P_1 - P_\infty\right)\right\} \\ &+ \sum_{in} m \left(\psi + S\right) - \sum_{out} m \left(\psi + S\right)\end{aligned}$$

Simplifying and putting in terms of mass specific exergy, ψ

$$\left(p_1 - p_\infty\right) = \rho \left(h_1 - h_\infty\right) - \rho T \left(s_1 - s_\infty\right) - \sum_{in} \rho \left(\psi + S\right) + \sum_{out} \rho \left(\psi + S\right) \qquad (2.13)$$

Equation 2.13 defines the amount of system exergy (ψ_{sys}) that can be extracted from a system taken into pressure equilibrium with the environment for a given exergy destruction (ψ_D) due to irreversibilities. This relation can be used in further derivations as a fundamental relation from the coupling of the first and second laws of thermodynamics.

2.5 CHAPTER SUMMARY

This chapter provides the technical foundation behind exergy analysis on any system, from the first and second laws of thermodynamics, Equations 2.1 and 2.2 respectively, through to the coupled formulation in the exergy transfer equation (Equation 2.9). A clear distinction between the terms energy, entropy and exergy has been made, with relationships such as the Guoy-Stodola identity (Equation 2.12) showing how concepts such as entropy and exergy are related through the destruction of useful work or exergy. As mentioned in Chapter 1 for aviation design, first law methodologies based on energy have been applied through fuel burn analysis, however using a coupled first and second law approach such as exergy analysis has not been applied within industry except for the design of propulsion systems.

Exergy analysis results can be obtained by simply understanding how the components and their interactions are connected. Detailed information on the performance of a sub-system is not typically required, making it a useful tool from the preliminary design phase and through production. Exergy analysis provides

> *"a consistent framework within which losses can be compared within machines, between machines of different types for the same job and with perfection in the form of the completely reversible machine."*
>
> - Clarke & Horlock [47]

Thus it is feasible to formulate a set of vehicle design requirements stated in terms of the total energy use of the system, as an alternative view to that of discipline specific optimisation (see Figure 1.5a). All systems over the flight mission can therefore be modelled in terms of the fuel energy used and exergy destruction losses. One of the convenient properties of exergy analysis is that exergy is more easily interpreted than entropy, as exergy has the same units as energy (Joules), and as such in an economic analysis (also referred to as thermoeconomics in texts [19], [140] [141]) as a monetary value can be assigned to the loss of exergy in terms of energy cost, based on the cost of fuel per Joule for example. Then a simple comparison of every system can be made under the metric of exergy destruction in terms of fuel use.

Chapter 3 will show how the methodology detailed in this chapter has been applied to academic work in aerospace systems.

3

EXERGY ANALYSIS IN AEROSPACE - A REVIEW

From 2001 to 2009, the Air Force Office of Scientific Research funded research into *exergy based methods for aerospace vehicle design* [71]. Camberos and Moorhouse have summarised much of this US Department of Defense funded research in *Exergy Analysis and Design Optimization for Aerospace Vehicles and Systems* [40]. The international research community applying exergy analysis to aerospace systems appears to be quite small, with Camberos and Moorhouse being involved (and leading) any US based research through various institutions including University of Dayton, Virginia Polytechnic Institute, Clemson University and Missouri University of Science and Technology, all of which have sizeable research groups working on exergy analysis. However there is plenty of interest in the topic outside of the US, with ONERA in France [11–14], Anadolu University in Turkey [61, 168, 178], Canadian National Research Council [135],University of Sao Paulo in Brazil [50, 51, 68, 69], Cranfield University [79, 80] and Bath University [24] in UK to name just a few.

The significance of exergy analysis research is shown by Giurgiutiu [71] who cites the studies of Moorhouse and collaborators at the Air Force Research Laboratory (AFRL) into exergy-based multidisciplinary design as one of eight fundamental research projects for future flight structures. One of critical outputs from Moorhouse's work is

> *"[changing the] analysis/design paradigm from energy-based to exergy-based (specifically, minimum exergy destruction). This shift in methodology is even more critical in exploratory research and development where previous experience may not be available to provide guidance."*
>
> - David Moorhouse [54]

This leads to the conclusion that the exergy-based conceptual framework enables the design of truly energy-efficient, integrated systems, subject to constraints. This chapter will therefore provide a summary of how exergy analysis has been applied to aerospace systems to date and discuss the limitations to the application and how it can be expanded for further use. Many of the insights drawn in this chapter can be seen in [78].

3.1 COMPARING EXERGY ANALYSIS TO CONVENTIONAL ANALYSIS

Periannan [131–133] applied exergy-based analysis and optimization methods to the synthesis/design and operation of aircraft systems to show the advantages of such a method over first law methods. This was done by comparing different objective functions to the same design; minimizing take-off gross weight, maximizing thrust efficiency, maximization of thermodynamic effectiveness, and minimizing exergy destruction. Periannan stated

> *"As long as the constraint space is the same, an energy-based objective produces the same optimum as that of the exergy-based objective provided that they are equivalent forms of the same thing, for example, fuel consumption"*
>
> - Vijayamand Periannan [131]

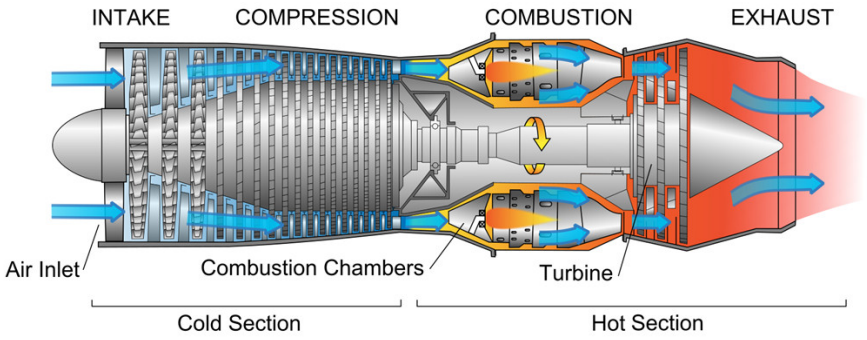

(a) Illustration of the turbojet used in Doty Analysis [55]

System 1: Combustor	***System 2:*** Duct	***System 3:*** Turbine
		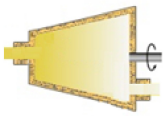

(b) Schematic of the simplified turbojet system used for exergy analysis[55]

Figure 3.1: Doty Geometry for comparison of 1st Law and Exergy Analysis

When this analysis was extended beyond propulsion and Environmental Control System (ECS) to include the aerodynamics (by definition not an energy system in the traditional sense), Periannan showed the equivalence between the energy and exergy objectives no longer holds. The need for a common currency points generally to the need for exergy as the basis for both analysis and optimization [132].

Doty [54] [56] [55] takes a similar comparison exercise, in this case a complex turbo-jet engine (Figure 3.1a) is simplified into interacting thermodynamic systems (Figure 3.1b); in this simplification of a complex engine *system 1* represents energy production (compression, mixing, combustion), *system 2* represents energy transfer (duct or pipe), and *system 3* represents energy conversion (work-extraction via turbine device). The paper aims to compare the same system process from an energy based first law method

$$\dot{Q} - \dot{W}_s - \dot{W}_{shear} - W_{other} = \frac{\partial}{\partial t}\int_{CV} e\rho dV + \int_{CS}(e + pv)\,\rho\vec{V}d\vec{A}$$

as previously given in equation 2.1 and an exergy based second law method

$$\frac{dX_{CV}}{dt} = \int_{CS}\left(1 - \frac{T_0}{T_k}\right)\delta\dot{Q} - \left(\dot{W} - P_0\frac{dV_{CV}}{dt}\right) + \int_{CS}\psi\rho\vec{V}\left(d\vec{A}\right) - \dot{X}_D$$

for the exergy transfer in an open system as in equation 2.11.

Three main conclusions are drawn from this comparison, which shows the advantages of the second law approach over the traditional first law methods [54]

- Second Law analysis provides physical limits on performance that the first law analysis does not
- First law energy analysis yields operating conditions that are not feasible, thus cannot exist. In the body of work, 40 % of the results obtained from the first law analysis were not feasible.
- The exergy destruction focus provides a consistent accounting for all forms of losses regardless of point of origin

These examples have shown exergy analysis to be an excellent tool for optimising individual sub systems, however the true potential of exergy analysis is the integration of the different technical disciplines, under a complete system of energy systems [39]. Optimization based on minimum exergy destruction can be used as a MDO technique required for the analysis of aerospace vehicles in terms of the efficient use of on-board energy [39]. This style of analysis could be done at any stage of design on high or low fidelity models where the whole system is modelled and mapped over the entire mission profile and all locations of exergy destruction highlighted.

3.2 EXERGY ANALYSIS APPLICATION TO PROPULSION SYSTEMS

Thermodynamic methods, such as exergy analysis, can provide a means for accounting for resources and wastes in a systematic uniform way. However application of these methods have been limited in application mainly to design optimisation of classical thermodynamics-based disciplines, and have not seen much usage in other areas. Early exergy analyses were concerned with extracting the maximum exergy from a hot gaseous stream which is discharged into the environment, as in an aircraft engine [19]. One of the reasons exergy research has focused heavily on thermodynamic dominant propulsion systems is the view that in comparison to exergy destroyed due to propulsion, all other forms of irreversibility are essentially negligible, thus the focus for reduction through optimisation is on the engine [154]. It should however be noted that reducing the aerodynamic drag will result in a lower thrust requirement from the engine, lowering the energy use.

From an exergy perspective, conventional turbofan engines convert chemical exergy into mechanical and electrical exergy for use by other aircraft systems. At the beginning of a flight the source of exergy for transport aircraft is defined by the quantity of fuel and the chemical exergy contained within. Chemical exergy arises when there is a disequilibrium between the resource and environment leading to a chemical potential. This could be a potential created by a concentration gradient of compounds freely available in the environment, such as oxygen, carbon dioxide and methane. Or exergy arises from a non-environmental compounds, a typical example being fuels. In both scenarios work can be extracted as the resource and environment are bought into chemical equilibrium.

Applying exergy analysis to aerospace systems is not a novel concept, with work dating back to the 1970s. The application of exergy analysis is applied to *steady state* propulsion systems, a clear extension to the previous applications of exergy to thermodynamic systems such as power stations.

> *"In time, the engines of nature acquire configurations that flow more easily, and this means that they evolve toward less entropy generation, and more production of motive power per unit of useful energy (exergy) used."*
>
> - Adrian Bejan [22]

Examples of this work can be found in Sciubba [162], Glansdorff [72], Bauer [17], Maltry [104], Clarke & Horlock [47], Lewis [99], Li & Qiu [102], all of which undertook early optimisation analysis of aeronautic propulsive systems. This area is still under development today, with huge potential for improvement in efficiency of aircraft engines.

More recent approaches to applying exergy principles to the optimisation of propulsion systems, include Dincer [52], Clarke [47], Marley [107] and Ehyaei [61] in turbojet engines and Doty [56], Roth [156] [155] [158] and Riggins [147][150][148] in turbofan engines for commercial aircraft.

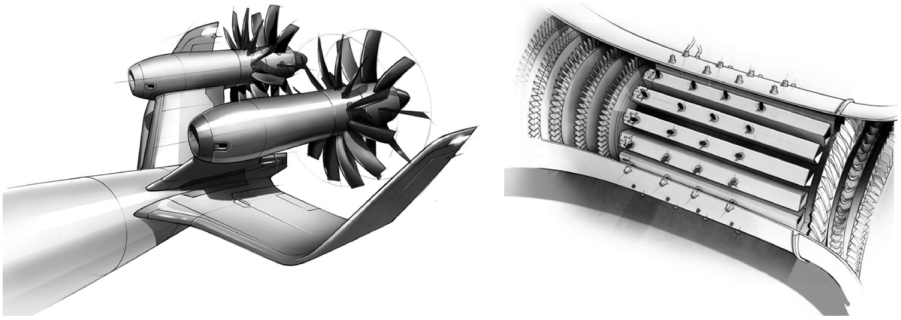

Figure 3.2: Chalmers University open rotor (left), pulse detonation core (right) [76]

Noticing the lack of diversity in exergy analysis application beyond turbojets and turbofans, Grönstedt [76] included other potential future engines, using an assumed future 2050 optimised turbofan configuration as the baseline. Grönstedt performed an exergy analysis on an (futuristic) open rotor engine from Chalmers University, an intercooled recuperated engine and an engine working with a pulse detonation combustion core, which are the three alternative configurations he saw as the future of aircraft propulsion (see Figure 3.2). Whilst Grönstedt showed the alternatives proposed provided a valid alternative to the turbofan configuration from an exergy perspective, what is more interesting are the conclusions on the use of the exergy metric, which were

> *"A striking strength of the analysis is that it establishes a common currency for comparing losses originating from very different physical sources of irreversibility. This substantially reduces the complexity of analyzing and comparing losses in aero engines. In particular, the analysis sheds new light on how the intercooled recuperated engine establishes its performance benefits... As part of analyzing the computational results it has become evident that exergy analysis is also quite rewarding when a comparative analysis of different engine architectures is carried out."*
>
> - Tomas Grönstedt [76]

An area for which exergy analysis may prove highly beneficial is in providing evidence for the integration of electric engines, an area of research gaining increasing focus for future aircraft. Schmitz [161] initially shows the shortcomings of traditional analysis methods, and then demonstrates how the *unified figures of merit* provided by exergy are useful in allowing for consistent comparisons between electric and conventional engines. Schmitz's work is concluded with a detailed comparison between a conventional turbofan, a parallel-hybrid turbofan, a novel integrated-hybrid turbofan concept, and an entirely electrical fan concept [161].

One should be mindful that individual sub-systems (such as propulsion) optimised separately to the complete system are unlikely to be an optimised system as different sub-systems will have adverse effects on each other. So whilst use of exergy methods has been used for propulsion sub system optimisation, unless this is integrated into the complete system, an optimised result will not be achieved. Justification for this top level systems approach can be seen from the analyses and optimisation of hypersonic vehicles (ramjet and scramjet) through exergy analysis by Brilliant [33], Markell [105] [106] and Tang [172]. What this work showed is that to fully realise the benefits of exergy analysis, what is needed is extension past just modelling the propulsion system to include the full system being mapped for its exergy uses, including application to the airframe and its losses through irreversibilities, providing a more holistic approach to the design process [161].

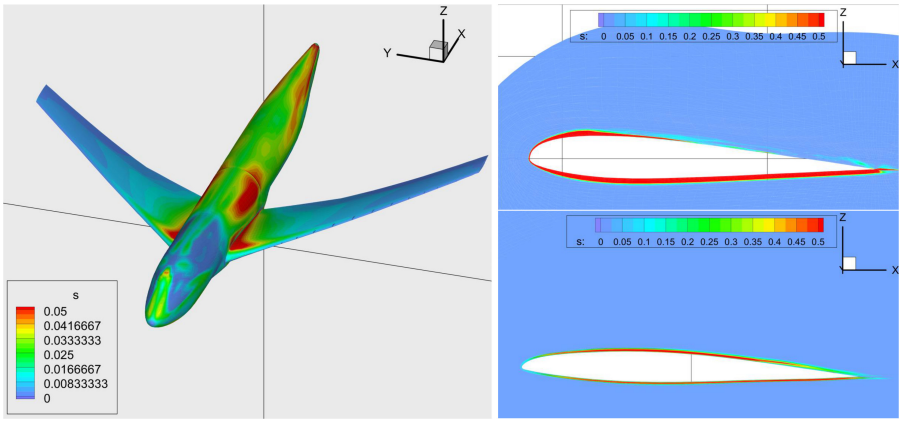

Figure 3.3: Entropy generation around the B747-200 aircraft and wing sections [5]

3.3 AERODYNAMIC AND STRUCTURAL OPTIMISATION USING EXERGY

Entropy generation or exergy destruction due to aircraft aerodynamics are usually far smaller than the exergy destruction within the propulsion system. This does not however mean there is no purpose to optimise aircraft aerodynamics, as it may be the case reducing exergy destruction due to drag is more cost effective than reducing total engine exergy destruction. Exergy analysis also proves to be a useful tool for wing optimisation when the aerodynamics are considered in isolation from the rest of the aircraft.

Significant resources have been put into optimising aerofoil shape and wing lift distribution to maximise lift to drag ratio, with these activities continuing to date for all new aircraft. Exergy analysis can be of benefit in improving the thermodynamic performance of the system by highlighting the mechanisms generating entropy and allowing the designer to pinpoint areas for improvement, or help dump unwanted energy from the system in landing or gust events.

Given the wide adoption of Computational Fluid Dynamics (CFD) in the design of aerodynamic systems, integration of exergy analysis into CFD solvers or as a post processor is an important step to make exergy analysis fully versatile. The constitutive form of entropy generation, which is mathematically equivalent to the transport equation for entropy, is given by Alabi [4–8] as

$$\dot{S}_{gen} = \frac{1}{T}\tau_{ij}\frac{\partial u_i}{\partial x_j} - \frac{q_k}{T^2}\frac{\partial T}{\partial x_k} \tag{3.1}$$

which is used by Alabi to calculate the entropy in the flow over the airframe subsystem aerodynamics (AFS-A) of a Boeing 747-200, cruising at Mach 0.855. Alabi ran the simulation with both inviscid and viscous flows, and showed that given the low temperature gradients the entropy production was dominated by the viscous dissipation, as such only the viscous flow simulation modelled entropy production (negligible amount of entropy were generated using the inviscid flow due to minor contribution from temperature gradients). Examples of the output entropy generation are given in Figure 3.3. Alabi validated this work using Prandtl-Glauret airfoil theory for a lumped parameter model [4, 5].

Focusing on the Blended Wing Body NASA N3-X configuration, Arntz [11–13], showed the same conclusion as Alabi in that viscous dissipation dominates entropy generation in drag. This is as one would expect given the viscous dissipation is the dominant factor from turbulence and the lift-induced drag. Arntz's work also investigated the exergy analysis of a blended wing boundary layer ingestion (BLI) system,

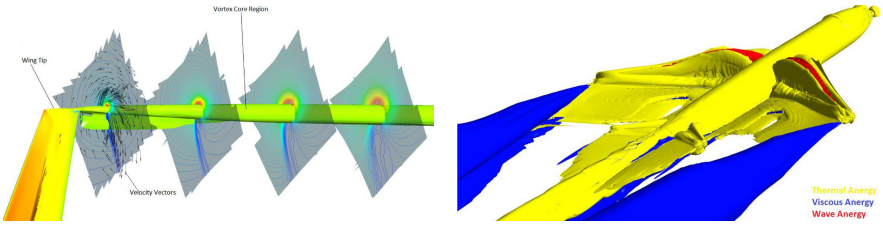

(a) Wing tip vortex of NASA CRM [111] (b) Entropy generation CRM plot [111]

Figure 3.4: Output from McGuire CFD analysis on NASA CRM

and identified components of recoverable exergy in the wake/jet of the aircraft that could be recovered using BLI methods.

Using a FORTRAN Reynolds-averaged Navier Stokes flow solution, Arntz [14] computed the entropy generation around the NASA Common Research Model (CRM) configuration travelling at transonic speed, thus as well as the parasitic and vortex drag components of entropy generation, Arntz was able to show the entropy generated in shock waves. Replicating and extending the work of Arntz at ONERA [14] McGuire [111] used the NASA Common Research Model (CRM) to calculate the entropy and exergy destruction in the induced, parasitic and wave drag, calculating the power loss (exergy destruction rate) for the CRM cruising at transonic speeds. Some examples of the results from McGuire are given in Figure 3.4.

Memon [112] provides a more detailed study for the exergy destruction in vortex drag, through experiments in a water tunnel at Institute of Aerospace Systems, focusing on the exergy distribution in the vortex for a variable angle of attack. When considering aerodynamics in energy terms, the point of minimum exergy state is assumed to correspond to the maximum lift-to-drag ratio angle of attack. What Memon showed is that this is not the case, and that it is related to where the wing-tip vortex changes from a wakelike to jetlike vortex[1]. This is in agreement with the work of Lee [98], who showed that at the point where the vortex changes from wakelike to jetlike is the point of maximum lift-to-drag ratio. Thus Memon concludes

> *"the exergy method holds promise as a metric for the improvement of aircraft performance through the reduction of lift- induced [drag]."*
>
> - Muhammad Memon [112]

3.4 MULTI-DISCIPLINARY OPTIMISATION USING THE EXERGY METRIC

Multi-disciplinary integrated design is where the system is considered as the complete collection of sub-systems interacting with one another and the optimisation of this system. As previously commented, this removes the issues with designing sub-systems in isolation where a sub-optimal design is usually the outcome.

Conventional Multi-Disciplinary Optimisation uses normalized coefficients to local variable dimensions, as seen in the Breguet equation (equation 1.1) with the aerodynamic, propulsion and structure non-dimensionalised factors. However, such a method cannot account for essential differences between the aerodynamic, propulsion and structural, and the magnitude of sensitivities can mislead the direction of optimization. Riggins [40] summarised this thought as

1 Jetlike vortices encase a pocket of axial fluid flow in the vortex that is at a velocity greater than the freestream [98]

> *"In current Multi-Disciplinary Optimisation and Analysis efforts, the various components and subsystems are still generally evaluated or analysed in terms of their traditional and unique loss and performance metrics... the characteristic, property, or quantity being used as the metric for loss minimization at all levels of system, sub-system, and component design/evaluation should be the same as or at least explicitly related to the system-level performance objective itself."*
>
> - David Riggins [40]

There is no end point with the evolution of aerospace vehicles where one would say we have a perfect design, but what exergy offers is a tool to be used to highlight areas of designs that waste useful energy and thus could be improved to as near optimisation as feasible, summarised by Bejan as:

> *"Thermodyanmic optimisation (or entropy generation minimisation) brings the design as closely as permissible to the theoretical limit."*
>
> - Adrian Bejan [21]

Camberos defines some of the key advantages of the exergy true *common currency* objective function for MDO as:

- Sensitivities are normalized according to global dimensions
- The magnitude of these sensitivities will be a better indication as to best direction for system optimization
- Opens viable (excluding physically infeasible) possibilities for revolutionary design
- Provide a clear picture of total system integration

By devising ways to avoid the destruction of exergy, better use can be made of fuels. By accounting for all the exergy streams of the system it is possible to determine the second law (exergetic) efficiency. By performing exergy accounting at higher and higher fidelities, a map can be drawn of how the destruction of exergy is distributed over the engineering system of interest. In this way the components and mechanisms (processes) that destroy exergy the most can be identified. It is then by repeating the exergy analysis on the improved system that one can evaluate the thermodynamic improvements made due to the second law implementation.

An example of multi-disciplinary integrated design with the use of an empirical exergy model, Doty [53] showed a surrogate model for a wing and turbo-fan engine, provided benefits from an exergy destruction point of view when compared to individually optimised sub-systems. Doty also compared the results of a first law analysis against that of a second law exergy analysis, commenting that the second law approach showed which optimisations were actually feasible (the concept of building directionality into the method).

The conclusions made by Doty [53] regarding the optimisation of integrated systems, echo those of Riggins [151] [152] who performed integrated system exergy analysis mainly on hypersonic vehicles. Riggins was also involved with the work of Marley [107] who took a lumped parameter model of a single-spool turbojet engine. The work highlighted under what conditions the steady exergy analysis methods can be applied to the transient operation of a turbojet engine. Marley [107] concluded that the engine thrust calculated by steady exergy analysis, tracked the actual thrust during transient manoeuvres, through two analyses on a full aircraft and engine in different control volumes as seen in Figure 3.5.

Riggins' [149] work on hypersonics is also documented in Camberos' textbook [40], where Riggins discusses how exergy analysis and optimisation provides significant

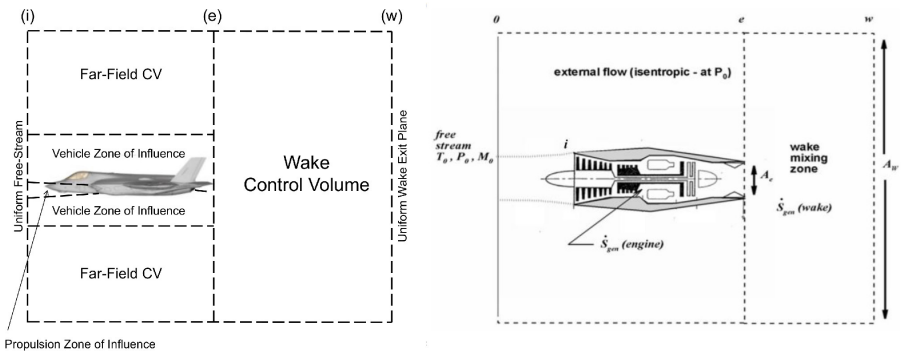

Figure 3.5: Control volume definition for Marley study [107]

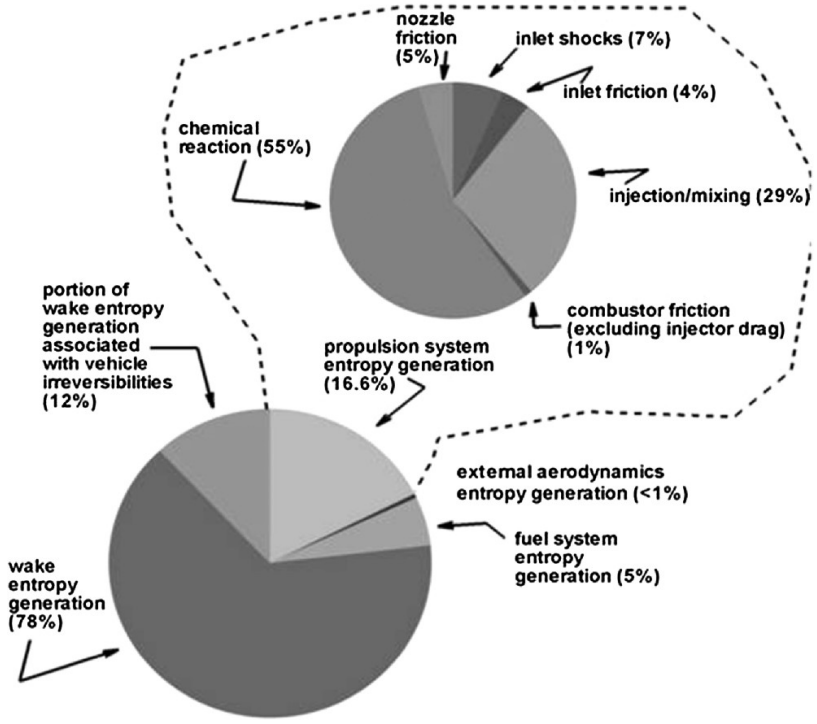

Figure 3.6: Detailed breakdown of instantaneous exergy losses [149]

advances in aerospace vehicle design, especially of hypersonic flight, where there is a demand for a thorough and systematic integration of all sub-systems. In this work, Riggins compared the output of two entropy based optimisation routines for the vehicle against a known set of design variables that yielded a maximum vehicle performance. The two entropy based method were (1) inclusive of the vehicle only availability and (2) included (1) but with the far field wake entropy generation. Riggins showed using a simple academic example (Figure 3.6) that for hypersonic vehicles the wake entropy generation can be three to five times larger than entropy generation associated with the vehicle itself, thus the far-field volume must always be included in analysis.

3.5 FULL VEHICLE EXERGY ANALYSIS

Complete aircraft optimisation is the process of performing an exergy analysis over the complete flight profile and assessing the exergy flow and use throughout the system, to the point of total exergy destruction. A widely published and referenced body of work detailing an application of complete aircraft exergy analysis is the

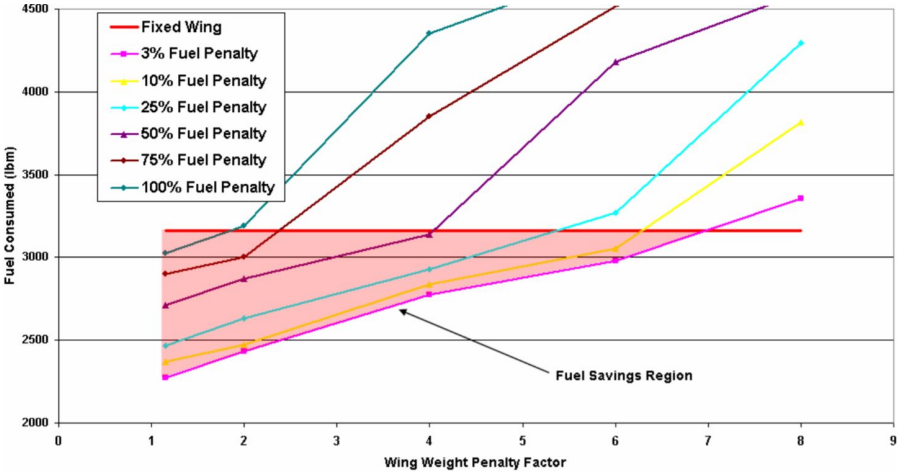

Figure 3.7: Sensitivity analysis of morphing wing effectiveness, Butt [35]

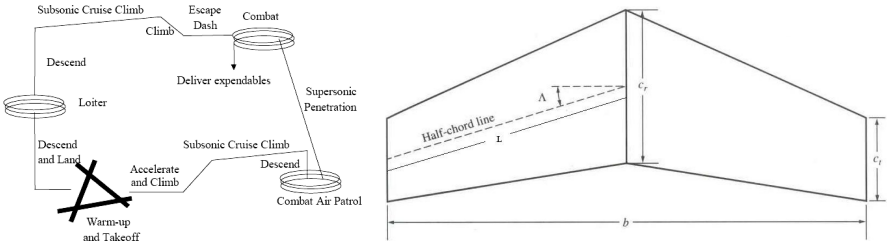

(a) Flight Envelope for Smith study

(b) Geometry of morphing dimensions

Figure 3.8: Advanced Air-to-Air Fighter Exergy Study [166]

morphing wing optimisation of a future advanced air to air fighter (AAF) [32, 35, 105, 116, 117, 130–133, 135, 140, 141, 166, 167, 179]. This is an example of a widely applied application of exergy analysis where it is coupled with large-scale optimisation of a system, the principles of which are the same as discussed in previous sections.

The initial study into the AAF by Von Spakovsky [179] simplified the AAF into two sub-systems, the propulsion and airframe. The aim of the study, based on the DARPA morphing aircraft structures programme, was to perform optimisation studies on the AAF airframe at different flight phases where the wing sweep, length, root chord length and tip chord length were the parameters to be optimised. An empirical exergy analysis was undertaken on these different configurations by Butt [35] with fuel consumption as the comparable output. A standard fixed wing fighter jet was also included for comparison. The model does not include actual morphing technologies, just the geometries they would create. Therefore to account for the additional components Butt [35] applies fuel and wing weight penalties as shown in Figure 3.7.

The conclusion to this work was that if the morphing technology had a weight and fuel usage that lay in the shaded region of Figure 3.7 the morphing wing provided a benefit in terms of total fuel consumption, as derived from an exergy perspective.

This work was extended by another masters student of Von Spakovsky, Smith [166], who took the same model of the AAF propulsion and airframe, but increased the complexity by including other exergy consuming devices such as the ECS, fuel loop system, vapour compression loop system, electrical systems, central hydraulics systems, oil loop system and flight control systems.

3.6 MAPPING EXERGY OVER THE VARIABLE FLIGHT ENVELOPE

Ground based systems, such as power stations, which are typical subjects of exergy analysis have a relatively consistent external environment, so can be assumed to have a constant reference state. The majority of exergy analysis applied to aerospace vehicles makes the same assumption, whether this be a ground based propulsion system or assuming the complete vehicle operates only in the dominant cruise phase of flight. It is accepted that the maximum thrust obtainable from combustion is dependent on the composition of the environment in which the system operates, exergy analysis broadens this to any transfer of heat or work being dependent on the environment. In such a way, when exergy analysis is extended for use in aerospace applications it is evident that the external environment should be far from constant through the mission profile. The thermodynamic variables of temperature and pressure will significantly vary at sea level when compared to aircraft cruising altitude.

The reference state difficulty associated with aerospace exergy analysis has been studied by both Dincer [52] and Berg [23] [24] [25].

At a more fundamental level, Sciubba [162] states in relation to chemical exergy *selecting a set of reference substances and determining their average concentration in the earths crust. These reference substances are the basis for the calculation of the exergy of the individual chemicals. The problem of how to identify a convenient "average composition" of the lito- hydro- and lower atmosphere was debated. Small differences in the reference elements produce substantial differences in the exergy values for most practical metals and fuels. At present, in practice all exergy calculations are based on the reference environment published by Szargut [171]*

Gandolfi [68] mapped a complete flight mission of a commercial aircraft, identifying exergy destruction at different phases of flight. Figure 3.9 shows the results Gandolfi found for the distribution of irreversibilities among flight phases, where whilst cruise (assumed to be 40 minutes) is the largest destroyer of exergy, it does not overshadow the other phases as to make them negligible. A development of Gandolfi's work would be to evaluate the actual flight missions of airlines, because each aircraft can be used for a variety of different missions, often being used for missions the aircraft was not primarily designed for.

Dincer [52] adapted the work of Clarke [47] on theoretical analysis of aircraft turbojet power plants to include a variable reference state, which Dincer compared against constant reference states at sea level and cruise altitude. The chosen comparison metric was the *cumulative rational efficiency*

$$\psi_{cum} = \frac{\int_0^t P_T\,(t)\,dt}{\int_0^t X_{in}\,(t)\,dt}$$

a function of the thrust power extracted, P_T and the input exergy from fuel, X_{in}. Dincer defined this because he found that irregularities in the instantaneous efficiencies with flight distance are put into better perspective in terms of their impact on engine efficiency over an entire flight by weighting them by this ratio. Thus, short phases of flight such as take off, where the turbojet is running at a higher efficiency does not overwhelm the dominant phase of cruise flight.

Figure 3.10 displays the compared variable reference state and two constant states at sea level and cruise altitude. The sea level reference state can be seen to overestimate the efficiency of the turbojet when compared to the variable model, as well as having an inverse increase in efficiency during climb. This increase of efficiency during climb is an illusion of negative exergy in the incoming airflow, which occurs due to the growing discrepancy between the modelled sea level state and the actual

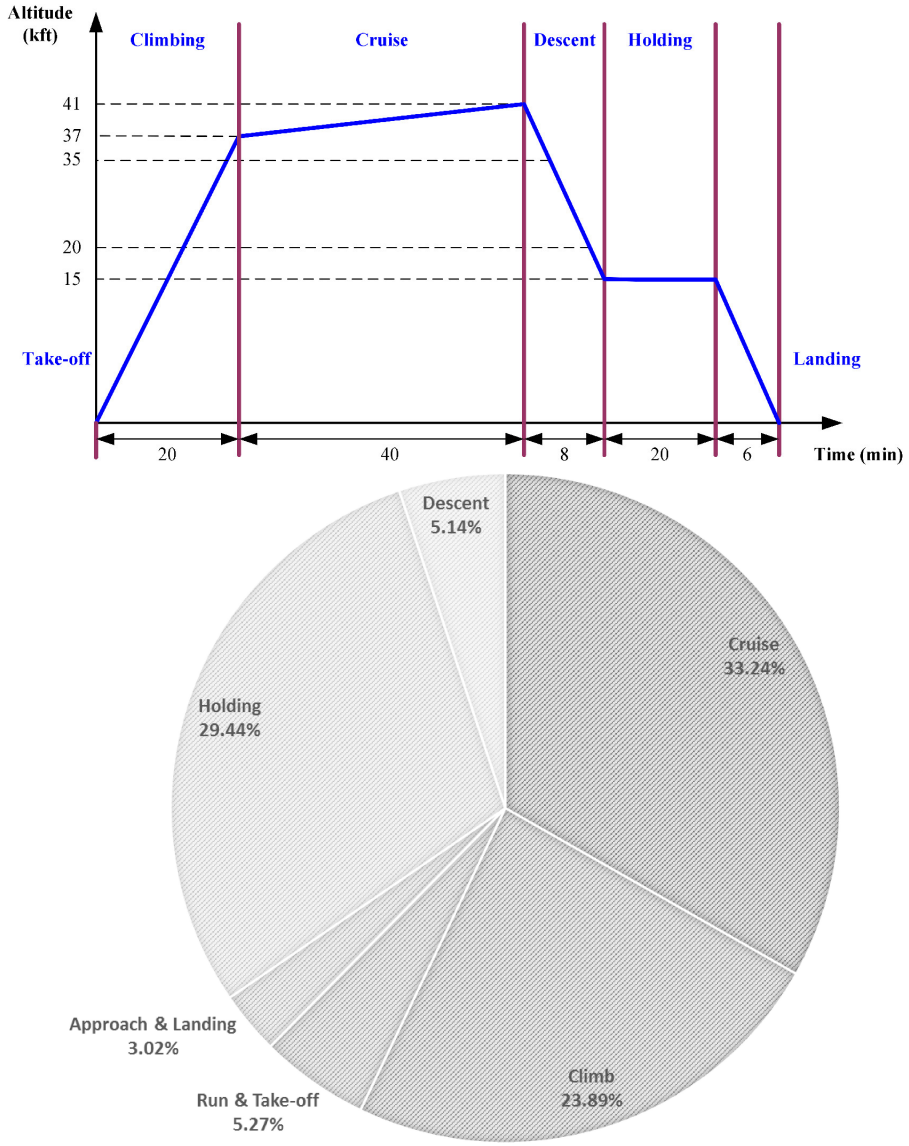

Figure 3.9: Distribution of losses as a percentage of exergy in different phases of flight as stated by Gandolfi [68]

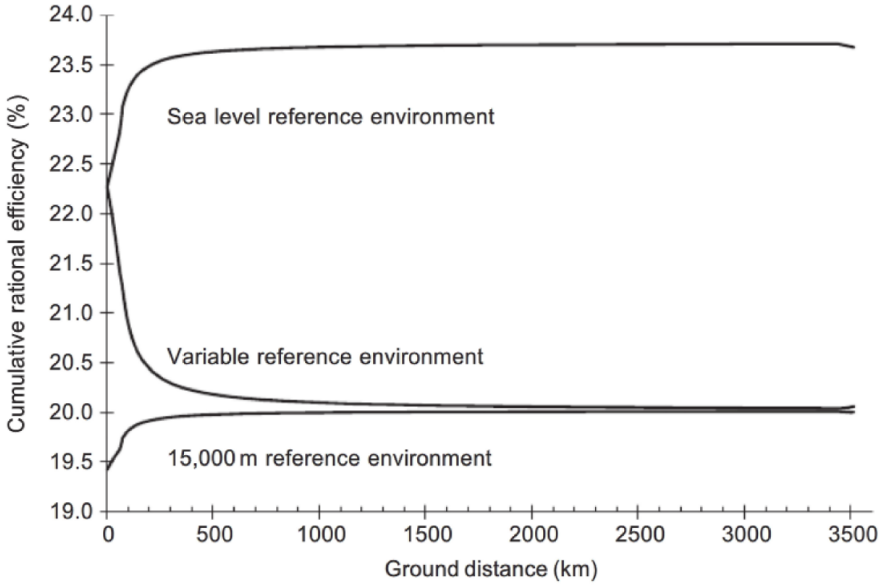

Figure 3.10: (a) Turbojet cumulative rational efficiency for various reference states [52]

state at altitude. The cruise altitude reference state creates a positive *illusion* of exergy during the climb phase, starting from a fictitiously low engine efficiency. However because the flight mission is dominated by cruise the plateau efficiency is close to that of the variable reference environment. Dincer [52] concludes that the variable reference state should be used for aerospace power unit applications, with a cruise altitude constant reference state only being used where there is suitable justification to not model the variable reference state.

Dincer modelled a flight mission dominated by the cruise phase of flight, which may be suitable for commercial flights. For a military flight mission there is typically no dominating flight phase as such the only option would be to use a variable reference state, or else errors in both numerical accuracy and predicted trends would be more evident with the constant state model.

Etele [62] conducted a similar analysis to Dincer on varying reference states (T_0,P_0) by taking a turbojet engine and modelling the sensitivity of exergy efficiencies to the reference environment. Etele undertook an analysis that compared reference states based at ground level, cruise altitude and one that varies the conditions based on flight phase. In contrast to the conclusions of Dincer, Etele was able to show that the exergy efficiency of a simplistic approach (ground level or cruise reference) gave a similar result to that of the complex variable reference state. However, the work of Berg [23] [25] on time-variant exergy analysis concluded that for a complete system mapping the vehicle exergy must allow for time variant analysis. Such an analysis allows for temporary storage of exergy. Berg undertook a time-variant analysis in a similar method to that of Gandolfi [68] [69], where the phases of flight are broken down, and reference environment parameters are obtained for each of the phases. Unlike Gandolfi, Berg is able to validate his results against a simple UAV model [23] and then through a more complex commercial aircraft mapping [25].

The initial exergy reserves are calculated by the exergy of the jet fuel and/or batteries on board the aircraft. The exergy of these sources is then mapped through each conversion process with the exergy destruction highlighted at each stage, to the point of complete exergy destruction.

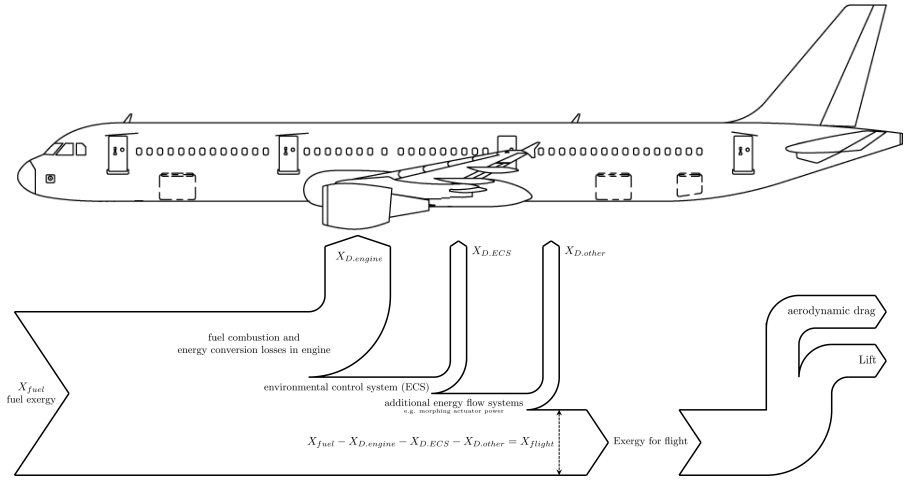

Figure 3.11: Grassmann diagram for the exergy flow through an aircraft, highlighting irreversibility locations

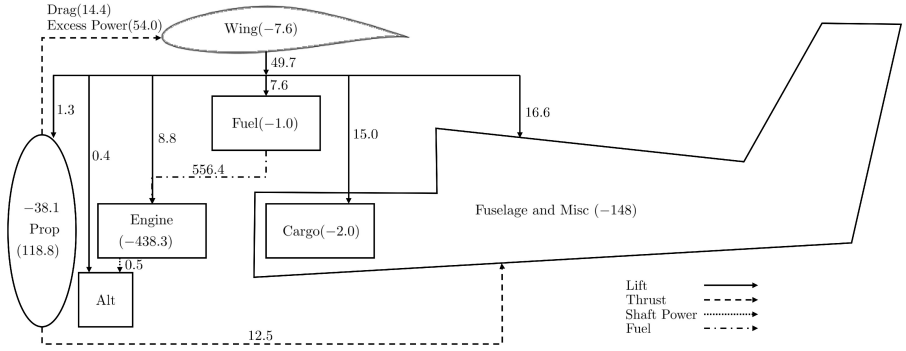

Figure 3.12: Exergy Flow Diagram of a light aircraft [128] [129]

3.7 VISUALISING EXERGY USE

Due to the complex nature of aircraft systems, many authors have commented on the difficulty in visualising exergy flow through an entire system. Two methods have been proposed, the use of *exergy flow diagrams* from the work of Paulus [128] [129] and *Grassmann diagrams* by De Oliveira [50] and Berg [23].

Figure 3.12 shows an example exergy flow diagram from the work of Paulus. The diagram represents the interactions between different sub systems through which exergy can flow. One concern with this style of diagram is that with a more complex system such as a commercial aircraft (see Figure 3.13) the diagram will quickly become cluttered with multiple interactions, making it difficult to decipher.

It is also easy to visualise the exergy flow through a system, using a similer graph to that of a Sankey Diagram[2], known as a Grassmann diagram, where the exergy source (typically fuel) is mapped throughout the flight mission to highlight areas of exergy destruction. The same exergy flow as in Figure 3.13 can be shown for an A340 as an entropy flow diagram in Figure 3.14 (equivalent to Figure 3.12) and a Grassmann diagram in Figure 3.11, where the horizontal arrow represents the flow of exergy, and the vertical arrows represent entropy production or exergy destroyed through various energy conversion processes, such as combustion, the Environmental Control System (ECS) and in the generation of drag [54].

2 A Sankey diagram is a flow diagram, where the width of the arrows is shown proportionally to the flow quantity, commonly used in heat engine design

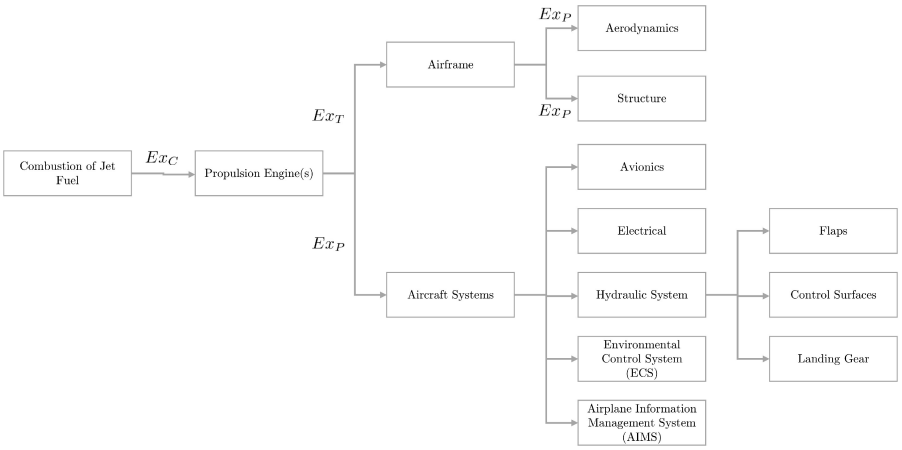

Figure 3.13: Exergy Flow through a generic commercial aircraft

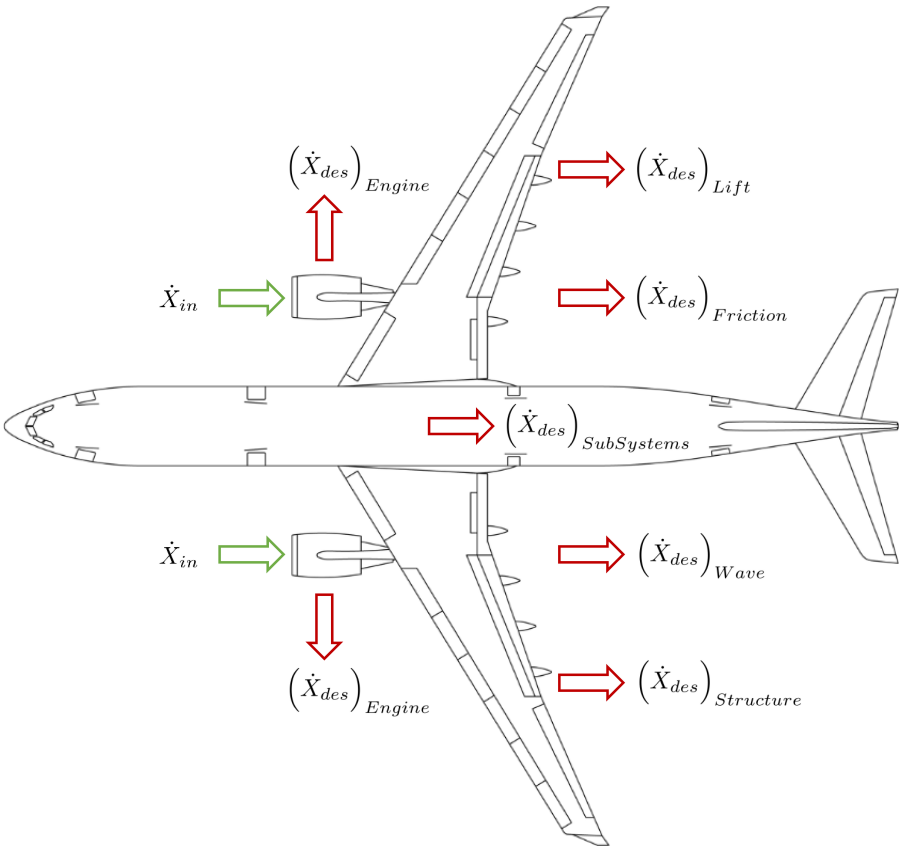

Figure 3.14: Exergy Flow Diagram of a generic commercial aircraft

3.8 THE SLOW ADOPTION OF EXERGY ANALYSIS

Since the first use of the term *available work* by Gibbs [15], areas where exergy analysis has seen wide adoption are those processes dominated by thermodynamics, such as heat engines and power generation technology (internal combustion gas engines, steam power cycles, gas turbine cycles and renewable energy cycles), heat exchanges and heat networking, air conditioning systems, cryogenics and chemical processes. Direct references for these are not given as beyond the scope of this paper, but a comprehensive review of these technologies is provided by Sciubba [162] and Ayres [15].

Much of the work in the aerospace sector on exergy analysis is sub-system specific, focused in the propulsion community, given the traditional thermodynamic nature of the system, and as such read across from earlier uses of exergy analysis. However in the aerospace community, outside of propulsion, there has been a slow adoption of thermodynamic optimisation and the exergy method [162].

Ayres [15] gives the reason for the slow adoption of exergy being due to confusion and misunderstanding associated with thermodynamics, which essentially is generated due to many of the variables not being physical variables people can measure, including entropy, enthalpy, internal energy, heat, Gibbs free energy and exergy, whilst these are mathematically proven within the theory, they cannot be physically visualised. Noting the difficulty in explaining the concept of exergy, Zabihian [183] presented a paper purely focused on how to comprehend the concept of exergy and teach it to students, focusing on a more global understanding of the methodology rather than to just one application as many authors focus.

Edwards [60] argues that the adoption of exergy methods has been slow in the field of combustion as exergies are approximately equal to the respective lower heating values, thus providing little benefit in real calculations.

A further obstacle is a consistent definition of exergy, which is exacerbated by the fact different authors have used various terms to refer to exergy and the term exergy for slight different purposes. Sciubba [162] and Ayres [15] provide examples of this including; available energy, Arbeitsfähigkeit (translated from German as working capacity), exergie (German), availability, available work, available useful work, useful energy, distinguishability and essergy (an abbreviation of essence of energy). Sciubba [162] states the accepted terminology is now exergy (with a few American authors still using the term availability). Justified by the definition of such work being based on *energy* meaning internal work, from the Greek *en* and *ergon*, and then changing the prefix to the Greek *ex* suggesting external application to work.

Working with an exergy metric would also require significant change to the design practice, as typically aircraft sub-systems are optimised for their individual requirements to the optimal operating conditions, irrespective to the top level optimisation and efficiency of the complete system. A critical part of implementing an exergy based approach is the development of a decomposition strategy where all the sub-system components can be optimized to a system-level common metric. This would be no easy task, as major sub-systems of aircraft are designed by different companies and incorporated at a higher level, such as the Airbus and engine suppliers relationship.

3.9 FUTURE WORK IN EXERGY BASED AIRCRAFT DESIGN

The majority of exergy studies focus on steady-state performance analysis and adopt simplified models for flight dynamics and morphing, and estimate the exergetic cost

of such devices in global performance terms such as weight and fuel burn penalties. As a result, the future direction for the development of exergy is the definition, calculation and analysis of dynamic exergy for flexible aircraft; where the effects of variables such as wing flexibility on stored strain energy and consequently exergy destruction will be explicitly studied. Developing a method for selecting the appropriate reference state will be another area of interest. The selection of a reference state is straight forward for steady-state analysis, however, in a dynamic scenario the exergetic content of the atmosphere over the course of a time-domain simulation must be considered to accurately account for a varying reference frame.

Furthermore, novel technologies that will allow the realisation of future greener aircraft are typically being developed in isolation in the academic community. For example, toe-steering for composites (aeroelastic tailoring), morphing devices, loads control and flutter suppression, all as individual technologies are required for future aircraft design, but if they are not designed under a common mathematical framework (like that of exergy), the implementation of such technology on the dynamics, structural weight penalties, aerodynamic benefits and other system complexities will not be realised.

3.10 CHAPTER SUMMARY

One of the common themes throughout the review is the fact that the work has been completed within the academic community on highly simplified examples. This is useful for proving the theoretical foundation of exergy analysis, but unless the method can be proven for more complex real world systems it is unlikely to be adopted into industry. Numerous studies have been conducted into optimisation of specific aircraft sub-systems with exergy, such as the Environmental Control System (ECS), propulsion and wing/aerofoil geometry. The concept of complete aircraft mapping has been attempted by a few authors to show exergy destruction variation over different stages of aircraft flight.

There are many areas in which exergy analysis could be studied for the purposes of doctorate research and making a contribution to knowledge, thus it is important that this thesis focuses only on those areas which facilitate answering the research questions. The focus on this research is therefore into the aeroelastics (aerodynamics and structures) of exergy analysis, an area little research has been conducted on from an exergy perspective.

Part II

EXERGY ANALYSIS OF AEROELASTIC SYSTEMS

"A theory is the more impressive the greater the simplicity of its premises, the more different kinds of things it relates, and the more extended its area of applicability. Therefore the deep impression that classical thermodynamics made upon me. It is the only physical theory of universal content which I am convinced will never be overthrown, within the framework of applicability of its basic concepts"

Albert Einstein
Einstein: The Formative Years, 1879-1909

4

EXERGY ANALYSIS OF STRUCTURAL DYNAMICS

Consider an aircraft in trimmed cruise configuration, the generated lift force deforms the wing[1]. There is strain energy in the deformed wing, however this is not energy that can be extracted to perform work, thus the wing is considered to have zero available energy or exergy. Under environmental loading, such as a gust event, energy is put into the structure over a period of time causing it to oscillate. Assuming the aircraft does not harvest this energy, the system needs to dissipate the additional energy back into the environment, in order to return to the trimmed cruise structural configuration. Exergy analysis allows the quantification of the additional environmentally induced energy and aids understanding in how entropy is generated and thus how exergy is dissipated from the system. This scenario is the case study used in Chapter 8. But in order to undertake such a study initially the theory behind structural exergy analysis must be discussed, and to support this several *toy* examples are used.

This thesis aims to apply exergy analysis methods to flexible aircraft, such as in the High Aspect Ratio Wing (HARW) concept [29–31]. It is therefore fundamental that the application of exergy analysis to the field of aeroelasticity be discussed. This requires each node of Collar's triangle to be addressed (Figure 4.1).

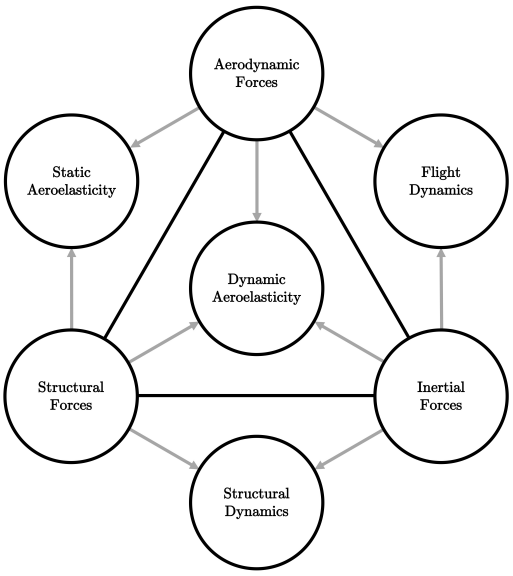

Figure 4.1: Collar's Aeroelastic Triangle [27]

Energy methods are common in the analysis of structures, with the Lagrangian and Hamiltonian derivations for the structural equations of motion [77]; both based on the conservation of energy in the first law of thermodynamics. An evident extension to this, is to incorporate all the laws of thermodynamics into structural dynamics. However, increasing the complexity of an analysis method would need to be justified by showing clear benefit or additional insight.

1 Typically the deformation is calculated such that with an unloaded pre-twist of the wing, the deflected position is that of optimal lift distribution

This chapter examines the concept of structural dynamics from an exergy perspective, with rigid body flight dynamics and aeroelasticity being discussed in chapters 5 and 6 respectively. This chapter includes a discussion on the problems outlined above, by first reviewing the energy derivation for the equation of motion and methods to solve for system state properties. Following this, energy and exergy system equations are derived and discussed with the aid of a worked example. The complexities of incorporating non-linearities into the exergy method are discussed with another worked *toy* example. The chapter concludes by scaling the simple one Degree-of-Freedom (DoF) system method to multi-DoF systems, through the use of finite element exergy analysis using beam element theory.

4.1 LINEAR STRUCTURAL EXERGY ANALYSIS

All aircraft structural models in this thesis are written using the conventional body axis system (Figure 4.2a), with rotations around the axis assumed to follow the right-hand grip rule. Assuming a node with six DoF, shown in Figure 4.2c, the state vector is defined for displacement, $\mathbf{q}$, velocity, $\dot{\mathbf{q}}$ and acceleration, $\ddot{\mathbf{q}}$ by

$$\mathbf{q} = \begin{bmatrix} u & v & w & \phi & \theta & \psi \end{bmatrix}^T$$
$$\dot{\mathbf{q}} = \begin{bmatrix} \dot{u} & \dot{v} & \dot{w} & \dot{\phi} & \dot{\theta} & \dot{\psi} \end{bmatrix}^T$$
$$\ddot{\mathbf{q}} = \begin{bmatrix} \ddot{u} & \ddot{v} & \ddot{w} & \ddot{\phi} & \ddot{\theta} & \ddot{\psi} \end{bmatrix}^T$$

The derivations presented in this chapter are applicable for six DoF systems, but can equally be applied to lower DoF system by excluding relevant terms in the state vector, for example, the toy examples are typically one or two DoF.

Any structural dynamics system DoF can be represented in the form of Figure 4.3, a single DoF mass-spring-damper. The mass can be driven to oscillate by the application of an external force doing Work (W) on the system, defined as

$$W = \int F d\mathbf{q} \tag{4.1}$$

During motion the system potential energy (V) is stored in the massless spring as a function of displacement, whilst the mass in motion represents the kinetic energy (T), a function of the velocity. These energies can be defined as

$$V = \frac{1}{2}[K]\mathbf{q}^2$$
$$T = \frac{1}{2}[M]\dot{\mathbf{q}}^2$$

Once work has been input to the system an ideal lossless system allows the energy to the be continuously transferred between kinetic and potential energy. The difference between the kinetic (T) and potential (V) energies is defined as the Lagrangian (L) where

$$L \equiv T - V \tag{4.2}$$

However, no real system can transfer energies without losses, as such in Lagrangian mechanics losses are accounted for by modelling damping, C, in the system, as shown in Figure 4.3a. An *ideal* damper means the only dissipation of energy from the system is via the *viscous* damper, thus surface contact is considered frictionless, and unlike the mass and spring, the damper cannot store any form of energy. Instead all mechanical energy is ideally transferred to thermal energy. The use of a viscous damper, means the quantity of energy damped is a function of rate/velocity, and not

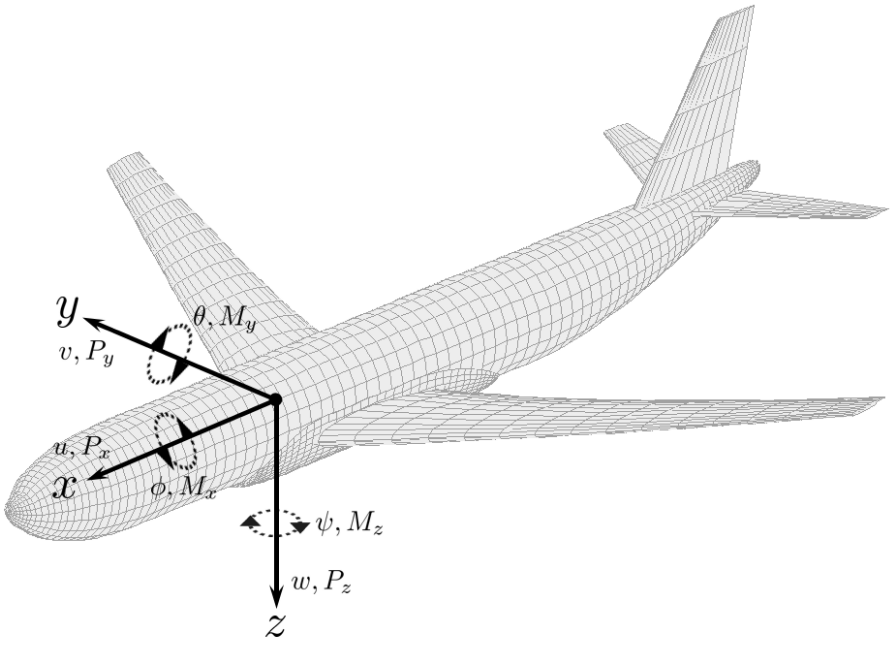

(a) Conventional body axis system

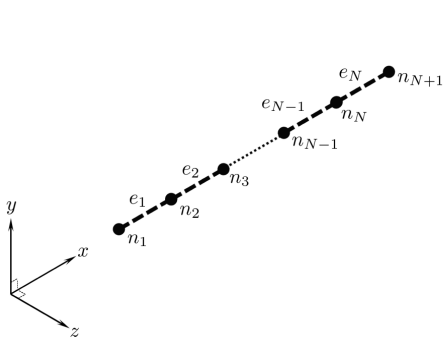

(b) Beam discretization

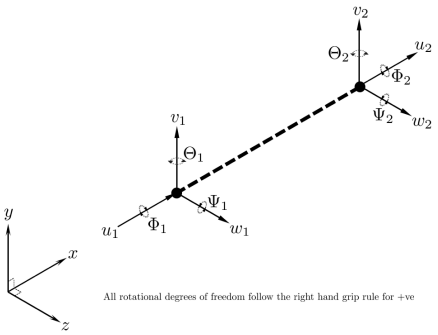

(c) Sign convention for a beam element

Figure 4.2: Multi-DoF structural representation

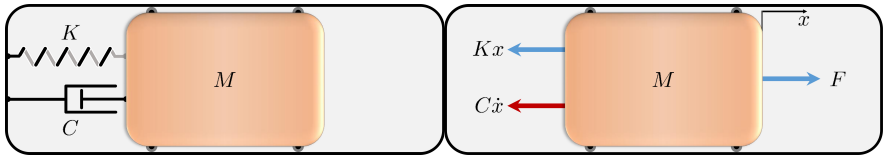

(a) Configuration

(b) System Forces

Figure 4.3: Mass-Spring-Damper Dynamic System arrangement

displacement as defined by structural damping. Thus, structural damping must be converted to comparable viscous damping.

The energy lost from the system due to the damper is modelled using the *Rayleigh dissipation function* (D_r) [77], a function used to handle the effects of velocity-proportional frictional forces. The dissipation function describes the rate of decrease of the mechanical energy of a system with N particles. The dissipation function is defined as half the rate at which energy, $\dot{E}_{\text{lost}}$, is being dissipated by the system

$$D_r = \frac{1}{2}\sum_{i=1}^{N}\left(c_u\dot{u}_i^2 + c_v\dot{v}_i^2 + c_w\dot{w}_i^2 + c_\psi\dot{\psi}_i^2 + c_\theta\dot{\theta}_i^2 + c_\phi\dot{\phi}_i^2\right) = \frac{1}{2}\underbrace{C\dot{\mathbf{q}}^2}_{\dot{E}_{\text{lost}}} \tag{4.3}$$

where c_x, c_y,c_z,c_ψ, c_θ and c_ϕ are the damping terms in the orthogonal axis system defined in Figure 4.2b, however note for a single DoF system we only consider damping in x.

The total dissipated energy describes the loss of useful work from the system, and for a given time interval can be defined as

$$E_{\text{lost}} = \int_{t_1}^{t_2}\dot{E}_{\text{lost}}dt = \int_{t_1}^{t_2}[C]\,\dot{\mathbf{q}}^2 dt \tag{4.4}$$

4.1.1 *Deriving the Structural Equations of Motion*

The motion of the mass body can be defined in terms of the system states, acceleration ($\ddot{\mathbf{q}}$), velocity ($\dot{\mathbf{q}}$) and displacement ($\mathbf{q}$), as such the expected expression is a second-order Ordinary Differential Equation (ODE). The equations of motion can be derived from energy principles using the Euler-Lagrange equation of the second kind[177],

$$\frac{d}{dt}\left(\frac{\partial L}{\partial\dot{\mathbf{q}}}\right) - \frac{\partial L}{\partial\mathbf{q}} + \frac{\partial D_R}{\partial\dot{\mathbf{q}}} = \frac{\partial(\delta W)}{\partial(\delta\mathbf{q})}$$

Substituting in Equations 4.1, 4.2 and 4.3, the four system properties required to identify the system states are force $F(t)$, mass M, stiffness K and damping C

$$[M]\ddot{\mathbf{q}} + [C]\dot{\mathbf{q}} + [K]\mathbf{q} = [F(t)] \tag{4.5}$$

Mass and stiffness properties can be determined from the material and geometric properties of the structure, however accurate estimation of damping is more challenging. Rayleigh damping, is commonly used in non-linear dynamic analysis. During formulation, the damping is assumed to be proportional to the mass and stiffness matrices, using damping coefficients η and λ

$$[C] = \eta[M] + \lambda[K] \tag{4.6}$$

The equations of motion can then be reduced to variables of mass specific force, $f(t)$, eigenvalues, ω_n and damping ratio, ζ

$$\ddot{\mathbf{q}} + 2\zeta\omega_n\dot{\mathbf{q}} + {\omega_n}^2\mathbf{q} = [f(t)] \tag{4.7}$$

$$[f(t)] = \frac{[F(t)]}{[M]} \qquad \omega_n = \sqrt{\frac{[K]}{[M]}} \qquad \zeta = \frac{[C]}{2[M]\omega_n} = \frac{[C]}{2\sqrt{[M][K]}}$$

Similarly, the Rayleigh damping coefficients η and λ are given in terms of ζ and ω_n

$$2\zeta\omega_n = \eta + \omega_n^2\lambda$$

$$\zeta = \frac{\eta}{2\omega_n} + \frac{\omega_n\lambda}{2} \tag{4.8}$$

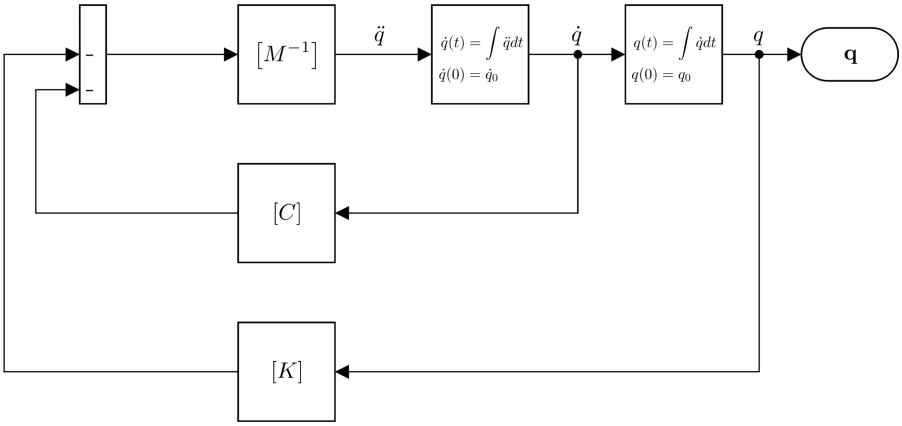

Figure 4.4: Second Order ODE solver in Simulink®

4.1.2 *Solving the Equations of Motion*

The equations of motion are second order differential equations, and as such can be solved in two separate ways using software such as Simulink®

i A direct solver, caculates the system state from the equations of motion in the form

$$\ddot{\mathbf{q}} = [F(t)][M]^{-1} - [C][M]^{-1}\dot{\mathbf{q}} - [K][M]^{-1}\mathbf{q}$$

which in the multi-variable case a stiff solver (for example Matlab `ODE15s`) is used due to the sparse nature of the mass and stiffness matrices. Figure 4.4 provides an example block diagram for the solving of linear equations of motion.

ii An alternative method is the application of a state-space model, defined by the governing equation

$$\dot{\mathbf{x}} = A\mathbf{x} + Bu$$
$$y = C\mathbf{x} + Du$$

In this formulation the 'A' matrix is the system matrix, and the 'B' matrix is the input matrix. The output state vector, $\mathbf{x}$, is a vector of the displacement and velocities of the system, $[\mathbf{q} \quad \dot{\mathbf{q}}]^T$. The output matrix 'C', and feedthrough matrix 'D', are identity ($\mathbb{I}$) and null respectively. Transforming the equations of motion in Equation 4.5 into state space form gives

$$\underbrace{\begin{bmatrix}\ddot{\mathbf{q}}\\ \dot{\mathbf{q}}\end{bmatrix}}_{\dot{\mathbf{x}}} = \underbrace{\begin{bmatrix}-CM^{-1} & -KM^{-1}\\ \mathbb{I} & 0\end{bmatrix}}_{A}\underbrace{\begin{bmatrix}\dot{\mathbf{q}}\\ \mathbf{q}\end{bmatrix}}_{\mathbf{x}} + \underbrace{\begin{bmatrix}M^{-1}\\ 0\end{bmatrix}}_{B}\underbrace{F(t)}_{u}$$

Figure 4.5 provides an example block diagram for the solving of linear equations of motion using the state space method.

Both methods will produce the same state output, and can both be applied to the BEaR framework, which is discussed later in the chapter. The state-space form allows more versatility in applying feedback, feedthrough and reduced output commands, however the direct ODE solving method uses smaller matrices, thus for large DoF systems will be less computationally expensive. So both methods are included, such that the appropriate method can be used for each analysis.

4.1.3 *Energy and Exergy Equations*

By deriving Equation 4.5, parallels can be drawn to the forms of energy given by the terms. The system kinetic energy, T and potential energy, V, are conservative

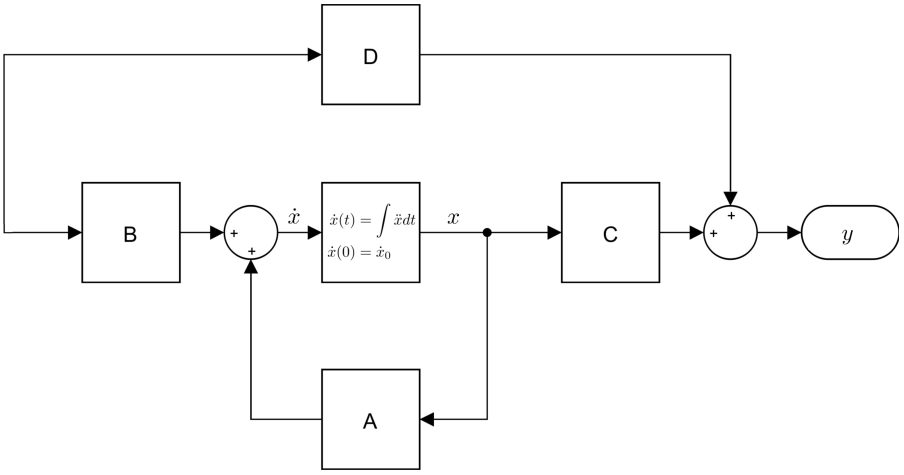

Figure 4.5: State Space ODE solver in Simulink®

meaning the energy is interchanged freely between the two states without losses. For conservative energies, the exergy and energy parameters of the system are equal. The term responsible for dissipation of energy or exergy destruction is the damping term $[C]\dot{\mathbf{q}}$.

Starting with the first law (Equation 2.1) the system energy can be defined as the work done, integrating the force over a generalised distance, as in Equation 4.1

$$\int F d\mathbf{q} = E = \underbrace{\frac{1}{2}M\dot{\mathbf{q}}^2}_{T} + \underbrace{\frac{1}{2}K\mathbf{q}^2}_{V} + \underbrace{\int C\dot{\mathbf{q}}^2 dt}_{E_{\text{lost}}} \tag{4.9}$$

The power can then be seen as the rate of energy transfer

$$\frac{\partial E}{\partial t} = P = \frac{1}{2}M\frac{\partial \dot{\mathbf{q}}^2}{\partial t} + \frac{1}{2}K\frac{\partial \mathbf{q}^2}{\partial t} + C\dot{\mathbf{q}}^2 \tag{4.10}$$

For a purely mechanical mass-spring-damper system the internal and chemical exergies of Equation 2.5 equate to zero, and focus shifts to the conservative exergies of potential and kinetic, such that

$$X_{sys} = \cancel{X_U} + X_T + X_V + \cancel{X_C}$$

These are freely converted to useful work, and as such equal to their energy equivalents. However, exergy has a use when considering stored energy of a system that cannot be transferred to useful work. System exergy is defined as the amount of *useful work* that can be extracted from a system's total energy. Exergy is therefore a proportion of any energy, and as such can take the form of any energy. Coupling the laws of thermodynamics and accounting for the environment (or fixed initial position in this case, $\mathbf{q}_0$, $\dot{\mathbf{q}}_0$, $\ddot{\mathbf{q}}_0$) in which the system resides, we can apply exergy analysis, to inform us of the exergy available in the system at any point of time

$$X_{\text{sys}} = \underbrace{\frac{1}{2}M\left(\dot{\mathbf{q}}_i^2 - \dot{\mathbf{q}}_0^2\right)}_{X_T} + \underbrace{\frac{1}{2}K\left(\mathbf{q}_i^2 - \mathbf{q}_0^2\right)}_{X_V} \tag{4.11}$$

The rate of exergy destruction from the system can be seen using the second law of thermodynamics (Equation 2.2), and calculating the rate of entropy production. Assuming this is an ideal viscous damper the work is a function accounting for the effect of the forces of viscous friction on the motion of the mechanical system, where all *work* is converted into *heat*, such that

$$C\dot{\mathbf{q}}^2 = \dot{Q}$$

$$\dot{S}_{\text{gen}} = \frac{\dot{Q}}{T_\infty} = \frac{C\dot{\mathbf{q}}^2}{T_\infty}$$

given T_∞ as the environment temperature. Given no transfer of energy out of the system via work, reduction in system exergy is through the exergy destruction term which quantifies the entropy generation of the system in terms of Joules lost. Incorporating the Guoy-Stodola theorem (Equation 2.12) the exergy destruction can be defined as

$$\dot{X}_D = C\dot{\mathbf{q}}^2 \equiv \dot{E}_{\text{lost}}$$

Thus the exergy transfer equation (Equation 2.11) can be written for a structural dynamic problem as

$$\frac{dX_{cv}}{dt} = -\underbrace{C\dot{\mathbf{q}}^2}_{\dot{X}_D} \tag{4.12}$$

It was previously mentioned, that one of the additional capabilities of exergy analysis over energy analysis is the ability to distinguish between stored energy and energy which can be transferred via work. This example looks at a common case of stored energy, that for gravitational potential, comparing the energy and exergy approaches.

EXAMPLE 2

A single-DoF mass-spring-damper system has a pre-load due to gravitational acceleration, F_m. The *minimum energy point* of equilibrium is reached with an opposing force from the linear tension spring, F_s. Any additional force applied to the system will increase the system energy above the minimum energy point. As the mass oscillates energy is dissipated from the system via heat through the damper until the energy returns to that of the minimum energy point. The preloaded energy is thus not available, and anything added on top of this would be considered *exergy*. The quantity of exergy can then be dissipated via the damper, or can be removed from the system as work.

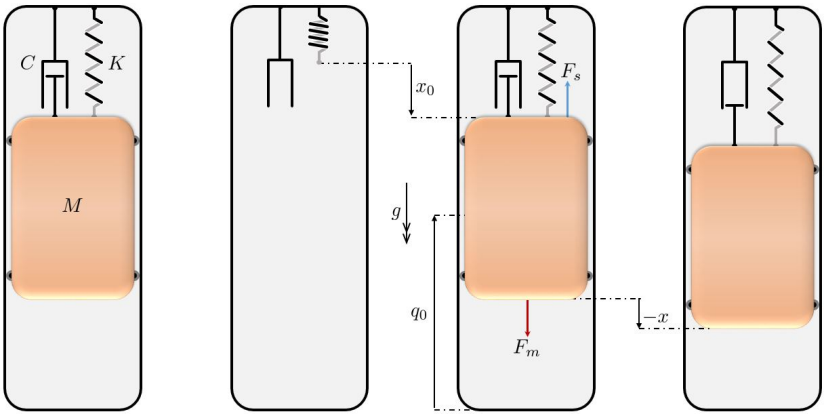

The depicted system has a spring stiffness, $K = 2200\frac{N}{m}$, which acts on a mass, $M = 20kg$. Assuming damping coefficients $\eta = 0.01$ and $\lambda = 0.005$, using Equations 4.7 and 4.8, the natural frequency, $\omega = 1.67Hz$, equivalent to a period of $\tau = 0.60s$.

Using the direct second order ODE solver outlined in Section 4.1.2 the state of the system can be calculated at every time step. To assess this system with both the energy and exergy methods, the gravitational potential energy term, V_G,

needs to be incorporated into Equations 4.9, 4.10, 4.11 and 4.12, so the method solves

$$E = \underbrace{Mg\mathbf{q}}_{V_G} + \frac{1}{2}M\dot{\mathbf{q}}^2 + \frac{1}{2}K\mathbf{q}^2 + \int C\dot{\mathbf{q}}^2 dt$$

$$P = \underbrace{Mg\frac{d\mathbf{q}}{dt}}_{\dot{V}_G} + \frac{1}{2}M\frac{d\dot{\mathbf{q}}^2}{dt} + \frac{1}{2}K\frac{d\mathbf{q}^2}{dt} + C\dot{\mathbf{q}}^2$$

$$X_{\text{sys}} = \underbrace{Mg(\mathbf{q} - \mathbf{q}_0)}_{X_{V_G}} + \frac{1}{2}M\left(\dot{\mathbf{q}}_i^2 - \dot{\mathbf{q}}_0^2\right) + \frac{1}{2}K\left(\mathbf{q}_i^2 - \mathbf{q}_0^2\right)$$

given q_0 as the reference height for the gravitational potential exergy term.

The results from the impulse response analysis are plotted in Figure 4.6, where the following insights can be made:

- The *force plot* shows the gravitational acceleration acting against the mass as a constant force, along with the impulse input into the system.
- The input of energy can be seen in the *energy plot* where the total system energy increases at the point of impulse input. The fact that the total energy is constant after input shows the first law is being met as energy is conserved.
- Before the impulse input the stored energy is evident in the system from the *energy plot* in the form of gravitational potential energy of the mass and also stored strain energy in the spring.
- After the impulse, the transfer between these forms of energy and kinetic energy of mass can be seen to the point when the mass returns to the minimum energy condition.

The lower two graphs of Figure 4.6 are the output from the exergy analysis, which in addition to the above conclusions, stated that:

- The impulse inputs approximately 2.5J of energy, which is the *exergy* of the system.
- As the damper generates entropy the total system exergy can be seen to decrease to the point of minimum energy where there is no system exergy.
- Exergy is transferred between kinetic and potential (GPE and strain).
- The exergy destruction can be seen to be the cumulative sum of the entropy generation, which is a function of the velocity, in that maximum entropy is generated at points of maximum kinetic exergy and no entropy is generated when there is no kinetic exergy and just potential exergy.

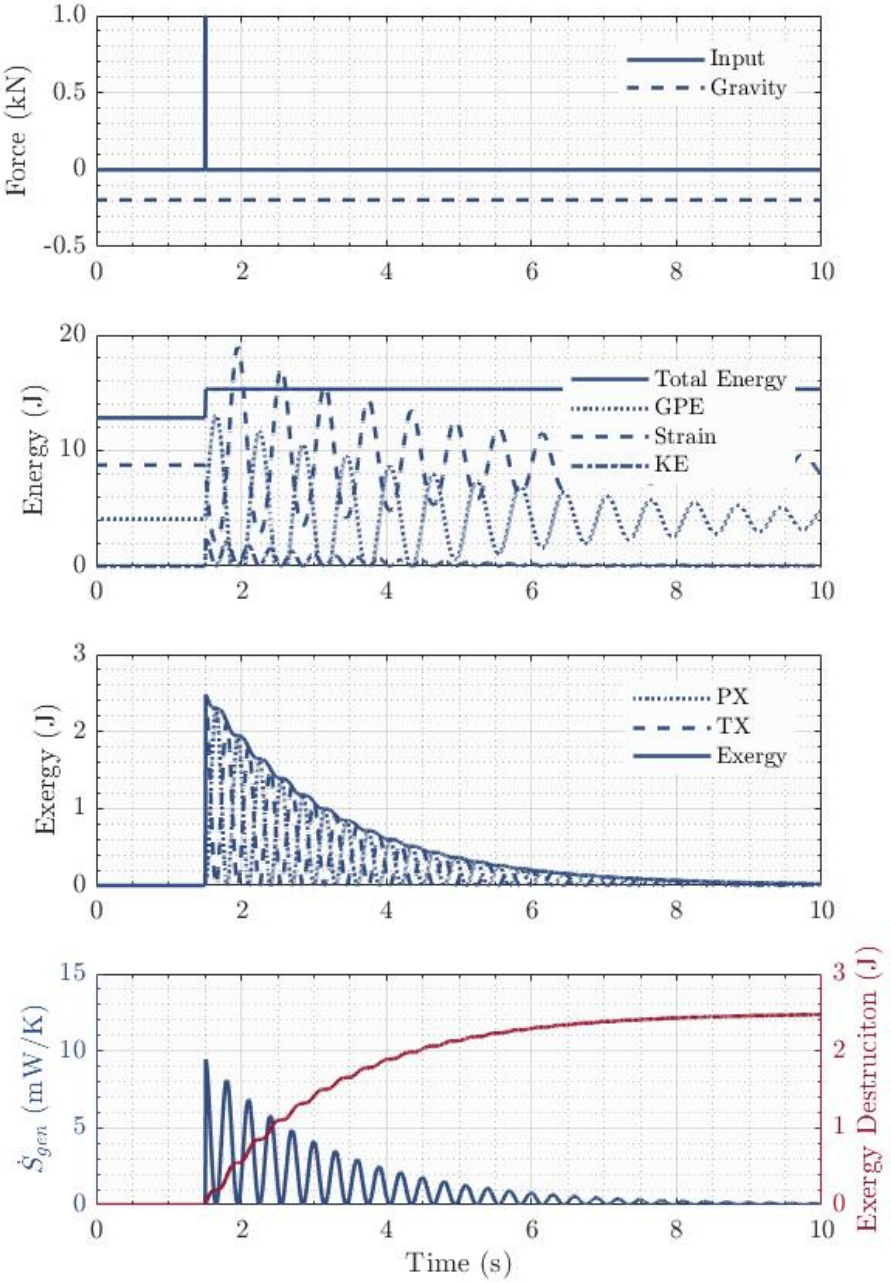

Figure 4.6: Simulation results of single DoF MSD with gravity, where: GPE = Gravitational Potential Energy, KE = Kinetic Energy, PX = Potential Exergy (grouped), TX = Kinetic Exergy, $\dot{S}_{gen}$ = Entropy generation rate

4.2 NON-LINEAR STRUCTURAL EXERGY ANALYSIS

Any deformation of a structure is inherently non-linear [29–31], however for the small deformations of conventional aircraft a linear assumption is usually suitable. However, with the large deformations seen in HARW aircraft, non-linearities may need to be considered. Non-linearities can be both geometric and material, where parameters previously considered constant are treated as a function of the system state, examples being

- Material non-linearities
  - Elastic (Young's) Modulus (E)
  - Shear Modulus (G)
  - Poisson Ratio (ν)
- Geometric non-linearities
  - Second Moment of Area (I_{xx}, I_{yy} and I_{zz})
  - Torsional Constant (J)
  - Cross-sectional area (A)
  - Element length (l)

The above are the fundamental components to the mass, stiffness and damping matrices, and should any of these vary with state a function must be sought to describe the variation and incorporated into the model. Non-linearities can be implemented by modelling a feedback loop within the solver which varies the mass and stiffness matrices with each time step and subsequent state change. A feedback matrix, 'K' is defined in Figure 4.7 and 4.8 to allow for non-linear behaviour in the stiffness and damping of the system, in the direct ODE solver and state space solver respectively.

The difficulty arises in understanding how these variables vary with the system states. A typical example of geometric non-linearities is the centrifugal stiffening seen on turbine blades, where the rotation creates an inertial force which pre-loads the structure, causing it to become stiffer than in the unloaded state. Material non-linearities are not considered here because materials are assumed to operate within their elastic (linear) region. Materials exceeding the elastic region (i.e. the elastic modulus becomes non-linear) the structure would permanently deform.

To account for stiffness non-linearities Equations 4.9, 4.10 and 4.11 need to be re-derived for non-linear stiffness, where the system total stiffness can be sub-divided

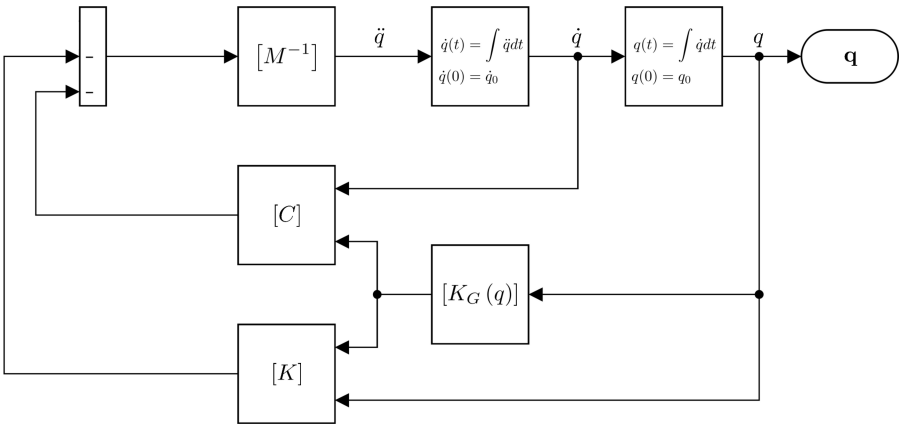

Figure 4.7: Second Order ODE non-linear solver in Simulink®

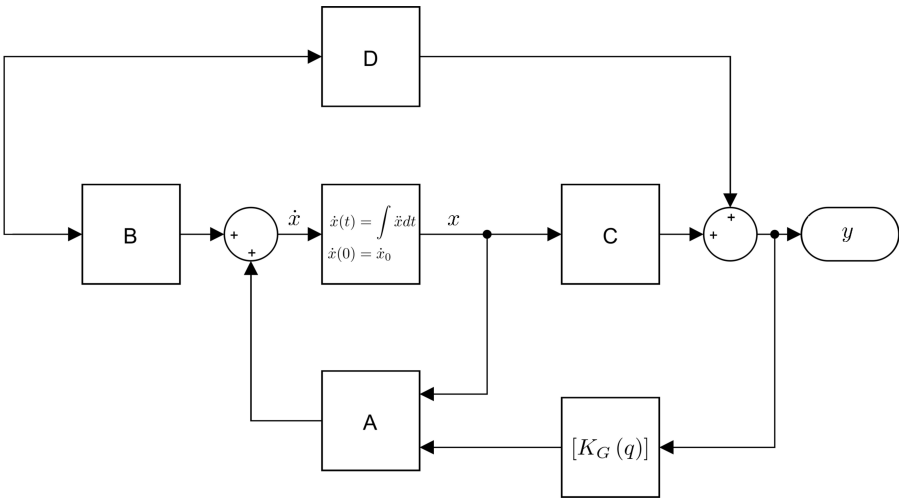

Figure 4.8: State Space ODE non-linear solver in Simulink®

into the elastic linear stiffness, K_E and the geometric non-linear stiffness, K_G, which is assumed to be a function of displacement, giving

$$\begin{aligned} K &= K_E + K_G(\mathbf{q}) \\ F_s &= \int K d\mathbf{q} = K_E\mathbf{q} + \int K_G(\mathbf{q}) d\mathbf{q} \\ V_s &= \int F_s d\mathbf{q} = \underbrace{\frac{1}{2}K_E\mathbf{q}^2}_{\text{Linear}} + \underbrace{\iint K_G(\mathbf{q}) d\mathbf{q}^2}_{\text{Non-Linear}} \end{aligned}$$

Thus, the structural equations of motion are rewritten as

$$F(\mathbf{q}, t) = M\ddot{\mathbf{q}} + C\dot{\mathbf{q}} + K_E\mathbf{q} + \int K_G(\mathbf{q}) d\mathbf{q} \tag{4.13}$$

EXAMPLE 3

A 200kg mass, M, is suspended between two *non-linear* ideal springs, of stiffness

$$K_1 = 10000\delta_1 + 1200 \quad (N/m)$$
$$K_2 = 6500\delta_2 + 1000 \quad (N/m)$$

the Rayleigh damping coefficients are $\eta = 0.01$ and $\lambda = 0.05$. The mass is positioned by the two pre-loaded springs in tension, and the position in 'x' will be subject to the relative spring stiffness (k_1 and k_2) which at the point of rest will have deflected δ_1 and δ_2 respectively, giving a non-zero point of minimum energy. This point is defined as the displacement at which the mass is at rest, and without additional work input to the system, there is no available energy (exergy). In this example the potential energy created by the initial deflection is freely converted into kinetic energy in the mass, with no losses in the mass or spring. Displacing the mass by, $\mathbf{q} < \delta$, will cause the spring forces to oppose one another. With the non-linear springs not only are the system energies unequal, the motion and exergy of the system differ to a linear system.

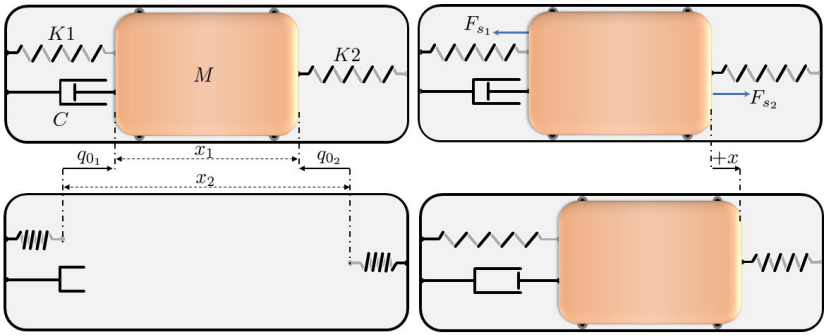

Initially the system parameters are built as a non-linear model, using the direct second order ODE solver in Figure 4.7. As the springs stiffness is linearly proportional to the displacement, the spring force of spring K_1 and K_2 is defined as

$$F_{K_i} = K_{i_E}\mathbf{q} + \frac{1}{2}K_{i_G}\mathbf{q}^2$$

Thus the initial position of minimum energy is solved through a series of simultaneous equations At any point of displacement the energy of the spring is given as

$$V_{K_i} = \frac{1}{2}K_{i_E}\mathbf{q}^2 + \frac{1}{6}K_{i_G}\mathbf{q}^3$$

The output of this analysis with a periodic pulse input is presented in Figure 4.9, where the following insights can be made:

- At $t = 0$, the stored strain energy in the preloaded springs can be seen in the Energy plot. However as this energy cannot be extracted from the system the exergy plot shows there is zero exergy at the start of the analysis. Thus the position of minimum energy (starting point) is considered the reference state (environment), $\mathbf{q}_\infty$.
- The force plot shows the dual impulse input into the system at $t = 1s$ and $t = 6s$. The energy plot shows the conserved energy increasing as each impulse puts energy into the system, in this example circa $0.8J$ per impulse.
- The rate of entropy generation (exergy destruction) is at a maximum at the point of the second impulse, as the initial impulse energy hasn't been fully dissipated, thus the velocity at the instance after the second impulse is highest point, and given exergy destruction is a function of velocity this is where the maximum point is.
- Due to the large initial displacement of the non-linear springs the energy plot shows the potential energy of each spring being significantly higher than the mass kinetic energy, making variations in kinetic energy harder to decipher. The exergy plot makes the transfer between potential and kinetic energy clear, with the decreasing amplitudes as the exergy is destroyed in the damper.
- The non-linearity modelled in the spring is shown in Figure 4.10. The non-linearity has an effect on the stiffness and damping of the system, as the Rayleigh damping used is stiffness and mass proportional.

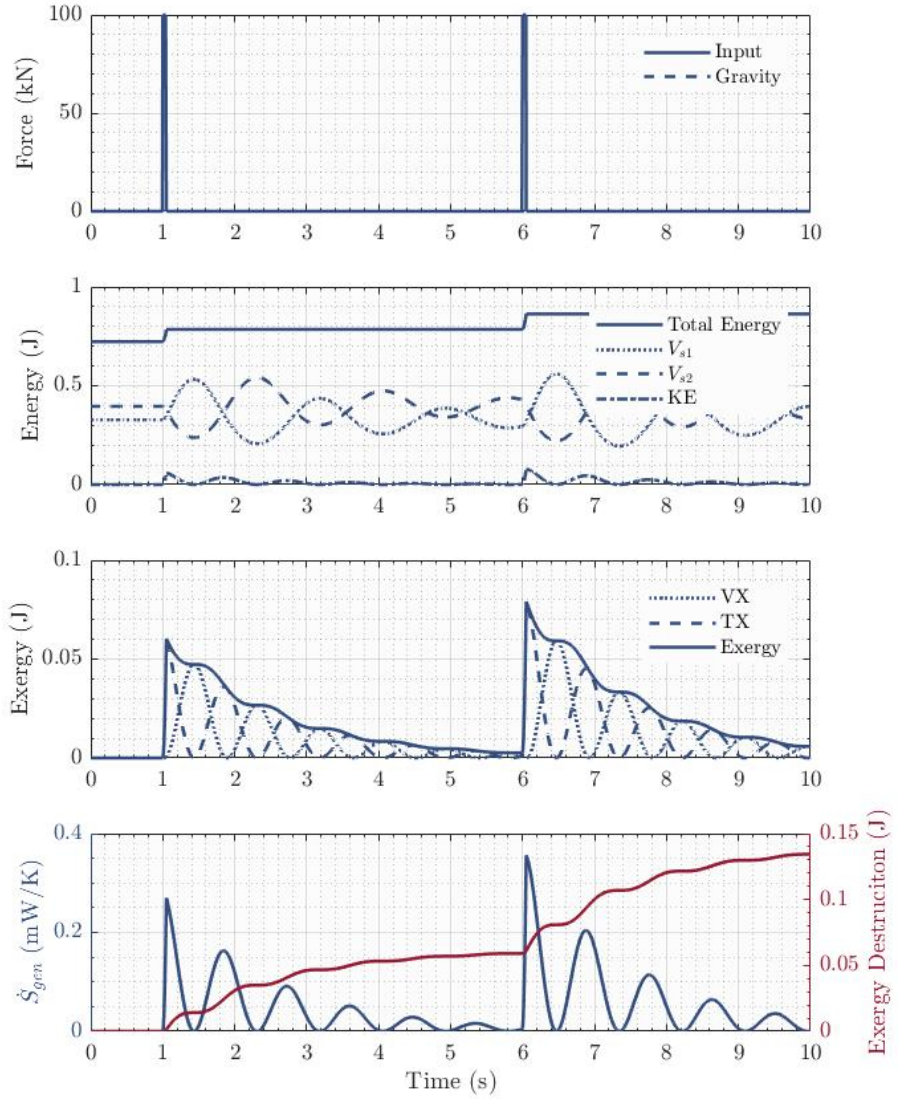

Figure 4.9: Simulation results of single DoF MSD with dual spring

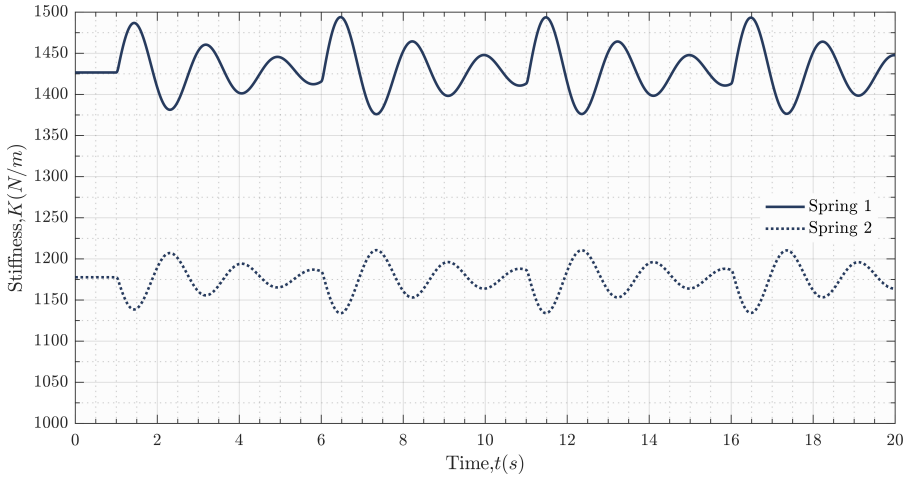

Figure 4.10: Simulation results of spring non-linearity with time

4.3 MULTI-DOF STRUCTURAL EXERGY ANALYSIS

The Cranfield Accelerated Aeroplane Loads Model (CA²LM), based on Andrews' AX-1 framework [10], uses a linear analysis approach to the structural dynamics of the aircraft, by mapping the displacements to the mode shapes, as outlined in the integrated *BEMMODES* code [26]. This approach is suitable for aircraft with small deflections such as the A340, however when high aspect ratio aircraft large deformation modelling is required. The aim of this section is to expand the basics of structural exergy analysis outlined previously for a multi-DoF system. This essentially models the structure as a series of six DoF mass-spring-dampers (see Figure 4.2b) in place of the previous single DoF.

The primary features of an aircraft structure, being the wings, fuselage, horizontal and vertical tailplane, which can all be considered *slender*, in that the cross-sectional dimensions are small compared to the length. As such for low fidelity design and analysis the aircraft structure can be discretised into a Finite Element Model (FEM) of nodes and one-dimensional beams, with characteristic properties[2]. This is shown for the Cranfield AX-1 configuration in Figure 4.11a. The beam representation model has two constituent parts:

1. The lumped mass model places the aircraft mass on the nodes of the reduced model (Figure 4.11b).
2. The structural model connects the nodes via one-dimensional beams, which model the stiffness of the structure (Figure 4.11c).

4.3.1 *The Beam Reduction Model*

For a low fidelity model an approximate solution to the exact beam deflection theory is required, there are three popular theories for this solution:

- Euler-Bernoulli Theory
- Rayleigh Theory
- Timoshenko Theory

The simplest interpretation of these three is that the Euler-Bernoulli formulation only accounts for lateral displacement and bending moment. The Rayleigh method is an improvement of this as it models the rotational inertia of the beam. However the Timoshenko beam representation takes into account the shear deformations and rotational inertia as the beam is displaced, making it the most comprehensive analysis of the three, the others can thus be viewed as simplifications or special cases of the Timoshenko beam analysis. Given the slender nature of the aircraft structure an argument can be made that shear deformations and rotational inertia will have little effect on the dynamics. However as the method is to be applied to HARW aircraft where it is expected large deformations will occur, shear deformations and rotational inertia will have a more prevalent impact. Using the Timoshenko method also allows for the modelling of both thin and thick section beams.

Take the beam outlined in Figure 4.12, the geometry is defined by cross-sectional area (A), and also the second moment of area (I) defined about the bending axis. For the application to aeroelastics the beam material properties can be defined with the Elastic modulus (E) and the poisson ratio (ν).

2 Characteristic properties mean the aircraft structural properties are reduced such that they are modelled as a one-dimensional beam, with cross sectional properties (I,A,J) representative of the full size aircraft

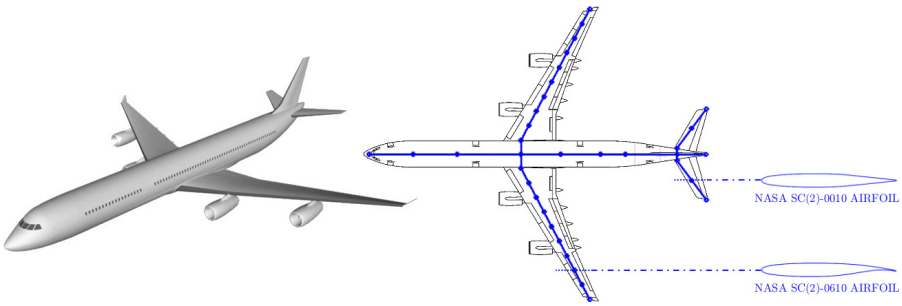

(a) Ax-1 aircraft beam representation

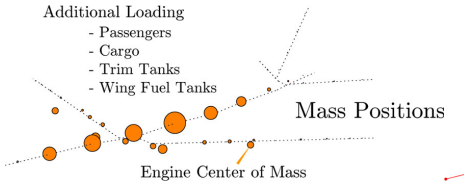

(b) Lumped Masses

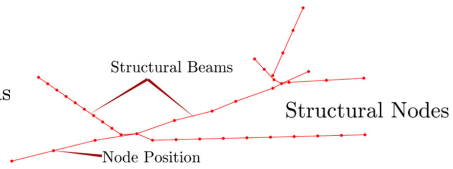

(c) Structural Model

Figure 4.11: Cranfield AX-1 Aircraft Characteristic Properties

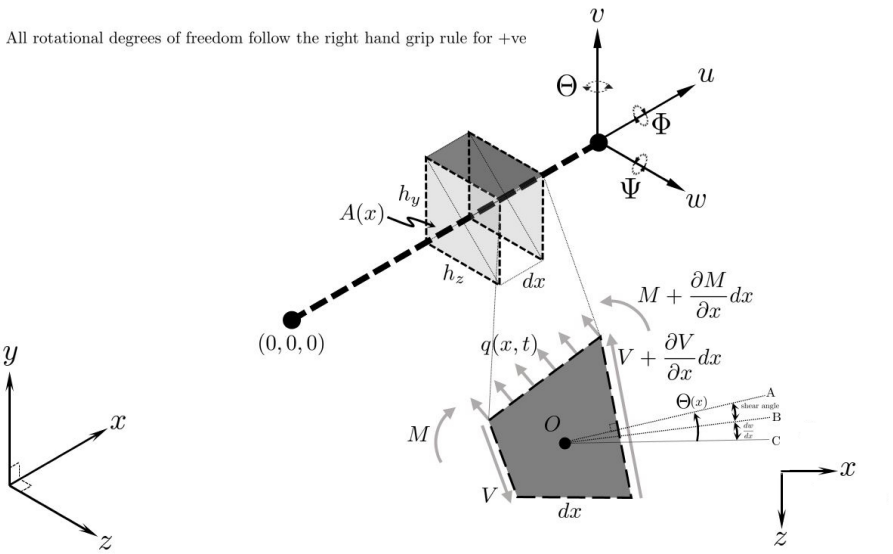

Figure 4.12: Beam geometry for derivation of Timoshenko

As the ratio of area, A, to length, l, becomes smaller, meaning the beam is more compact (non-slender), the effects of shear deformations begin to have a significant impact on the calculated deflection. The Timoshenko theory builds on the Euler-Bernoulli and Rayleigh theories by incorporating both rotary inertia and shear deformations, as outlined in Figure 4.12. From the figure it can be noted that:

- The line OA is a line through the centre of the element dx perpendicular to the face at the right hand side
- The line OB, is the line through the centre tangent to the centreline of the beam
- The line OC is the centre line of the beam whilst at rest
- As the beam bends the length is decreases relative to the beam width, creating a shear angle.
- For the case of a long beam, the lines OB and OA coincide.
- Note that the shear angle given by $\Theta - \frac{dw}{dx}$ (the difference between the total angle due to bending, Θ and the slope of the centerline of the beam, $\frac{dw}{dx}$), represents the effect of shear deformation.

All the information required to derive the Timoshenko six DoF stiffness matrix is provided in Figure 4.12. The bending moment, M, is given in terms of shear deformation as

$$M = EI\frac{d\Theta}{dx}$$

Defining the shear modulus, G (a function of the Young's modulus and poisson ratio) and κ as the shear coefficient that depends on the cross-sectional area shape, the shear force acting on the beam can be defined as

$$V = \kappa AG\left[\Theta - \frac{dw}{dx}\right]$$

A force balance of figure 4.12 yields

$$V - \left[V + \frac{\partial V}{\partial x}dx\right] + q(x,t)dx = \rho A dx\frac{\partial^2 w}{\partial t^2}$$

Finally, if the rotary inertia is included, then the moment balance on dx gives

$$\left[M + \frac{\partial M}{\partial x}dx\right] - M + \left[V + \frac{\partial V}{\partial x}dx\right]dx + q(x,t)\frac{dx^2}{2} = \rho I dx\frac{\partial^2 \Theta}{\partial t^2}$$

Coupling these four equations, derives the governing Timoshenko dynamic equation for the vibration of a beam including the effects of rotary inertia and shear deformation

$$\begin{aligned} EI\frac{\partial^4 w}{\partial x^4} + \rho A\frac{\partial^2 w}{\partial t^2} - \rho I\left(1 + \frac{E}{\kappa G}\right)\frac{\partial^4 w}{\partial x^2 \partial t^2} + \frac{\rho^2 I}{\kappa G}\frac{\partial^4 w}{\partial t^4} \\ = q(x,t) + \frac{\rho I}{\kappa AG}\frac{\partial^2 q}{\partial t^2} - \frac{EI}{\kappa AG}\frac{\partial^2 q}{\partial x^2} \end{aligned} \tag{4.14}$$

Using Equation 4.14 the mass and stiffness matrices for any beam reduced structure can be defined by following the flowchart process outlined in Figure 4.13. The matrices and their derivation are shown in detail in Appendix C, in the form of a mass, stiffness and dampening matrix for a beam element. The mass matrix derived in Appendix C is the *consistent mass matrix* for the structure, to account for non-structural loads (fuel, engines etc.) the generated mass matrix is the sum of the consistent and a non-structural lumped mass matrix (leading diagonal populated only), as shown in Figure 4.13.

Appendix C outlines how the BEAR code models bending and torsional displacements when the structure is subjected to a load. Bending is a function of the elastic modulus, E, and second moment of area, I, whilst the torsional displacements are a function of shear modulus, G, and polar moment of area, J. The formation of these terms in line with the Timoshenko equation gives the 6 DoF Timoshenko stiffness matrix given in Appendix C.

The Beam Reduction (BEAR) Model was written to provide a framework for demonstrating exergy analysis of multi-DoF structures. BEAR uses a bending theory approach using Timoshenko mechanics (outlined previously) for the elastic stiffness of the beam, with the additional geometric non-linearity as defined by Przemieniecki [138]. The model was written as a stand-alone six DoF code capable of modelling any structure that can be simplified into beam elements. BEAR, has been successfully used in other programmes to this thesis, including the Airbus Helicopters BladeSense programme [180] and Airbus Agile Wing Integration (AWI) programme [109].

The framework works as shown in Figure 4.14. An initialisation script (FEED*the*BEAR) takes a common NASTRAN style punch input and generates the structural mass and stiffness matrices, along with a Rayleigh damping matrix, which is a function of the mass and stiffness matrices. Using these matrices along with either the direct-ODE non-linear solver (Figure 4.7) or the state-space non-linear solver (Figure 4.8), BEAR takes an input force vector and outputs the system states displacement (q), velocity ($\dot{q}$) and acceleration ($\ddot{q}$). The force input and state outputs are of the same size ($n \times 1$), where n is equal to the number of nodes the structure has been discretised into, m, multiplied by the number of DoF, so in this case $n = 6m$.

BEAR is built around the data flow shown in Figure 4.13. The primary difference to the derivations earlier in the section is that the equations of motion are matrices as opposed to scaler values, giving the following equations of motion

$$\begin{bmatrix} F_{x_1} \\ F_{y_1} \\ F_{z_1} \\ M_{x_1} \\ M_{y_1} \\ M_{z_1} \\ \vdots \\ F_{x_m} \\ F_{y_m} \\ F_{z_m} \\ M_{x_m} \\ M_{y_m} \\ M_{z_m} \end{bmatrix} = [M_{aa}] \begin{bmatrix} \ddot{u}_1 \\ \ddot{v}_1 \\ \ddot{w}_1 \\ \ddot{\phi}_1 \\ \ddot{\theta}_1 \\ \ddot{\psi}_1 \\ \vdots \\ \ddot{u}_m \\ \ddot{v}_m \\ \ddot{w}_m \\ \ddot{\phi}_m \\ \ddot{\theta}_m \\ \ddot{\psi}_m \end{bmatrix} + [C_{aa}] \begin{bmatrix} \dot{u}_1 \\ \dot{v}_1 \\ \dot{w}_1 \\ \dot{\phi}_1 \\ \dot{\theta}_1 \\ \dot{\psi}_1 \\ \vdots \\ \dot{u}_m \\ \dot{v}_m \\ \dot{w}_m \\ \dot{\phi}_m \\ \dot{\theta}_m \\ \dot{\psi}_m \end{bmatrix} + [K_{aa}] \begin{bmatrix} u_1 \\ v_1 \\ w_1 \\ \phi_1 \\ \theta_1 \\ \psi_1 \\ \vdots \\ u_m \\ v_m \\ w_m \\ \phi_m \\ \theta_m \\ \psi_m \end{bmatrix}$$

where F_{x_i} is a tension load, F_{y_i} and F_{z_i} are shear loads, M_{x_i} is a torsional moment and M_{y_i} and M_{z_i} are bending moments. The matrices M_{aa}, C_{aa} and K_{aa} are all $n \times n$ in size and can be seen in full in Appendix C. In matrix/vector form the equations of motion are given as

$$\mathbf{F}(t) = [M_{aa}]\ddot{\mathbf{q}} + [C_{aa}]\dot{\mathbf{q}} + [K_{aa}]\mathbf{q} \tag{4.15}$$

4.3.2 *Non-Linearity in BEAR*

The BEAR framework implements geometric non-linearity as defined by Przemieniecki [138] for a 3 DoF system, which in this thesis is extended for a 6 DoF beam. Consider the beam element connecting two nodes in Figure 4.15, under an applied

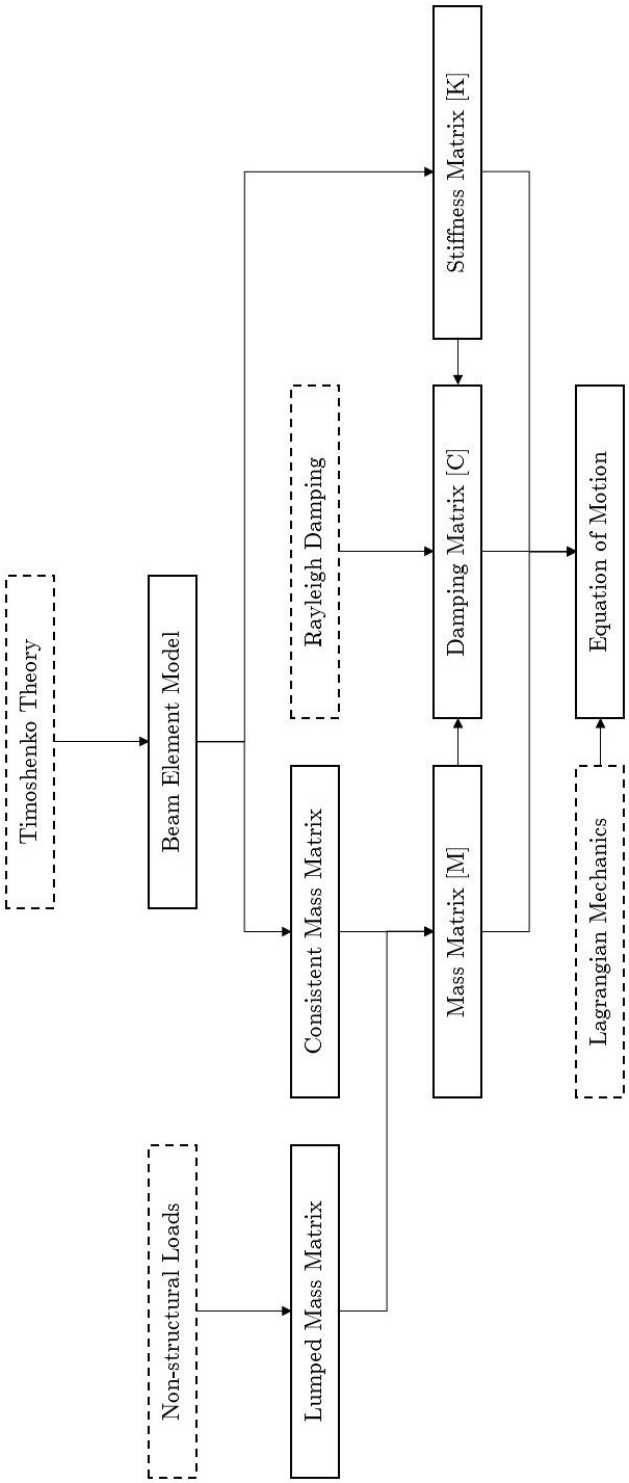

Figure 4.13: Methodology Flowchart for the Theoretical Generation of Beam model

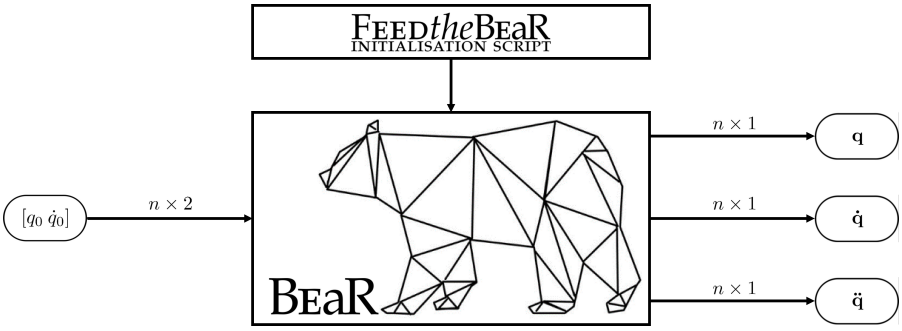

Figure 4.14: Schematic of the BEAR framework

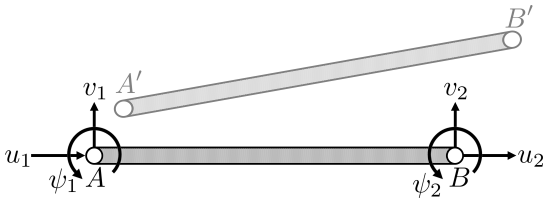

Figure 4.15: Przemieniecki 3DoF non-linear beam schematic

load the beam moves from position AB to $A'B'$, where for a non-linear large deflection $u_2 - u_1 \neq 0$, such the beam has extended. The normal strain in the beam (ignoring smaller shear strains terms) is defined as

$$\epsilon_u = \frac{\partial u_0}{\partial x} - \frac{\partial^2 v}{\partial x^2} y + \frac{1}{2}\left(\frac{\partial v}{\partial x}\right)^2 \tag{4.16}$$

where y is the distance from the neutral axis of the beam and u_0 is the deflection in x axis at $y = 0$. Here the first term in linear, with the remaining terms being the non-linear component of the strain. Assuming the material obeys Hooke's law (thus is linear) the strain energy for the non linear structural element due to deformation is given by Przemieniecki [138] as

$$\begin{aligned} V_i = & \underbrace{\frac{EA}{2}\int_0^l \left(\frac{\partial u_0}{\partial x}\right)^2 dx + \frac{EI}{2}\int_0^l \left(\frac{\partial^2 v}{\partial x^2}\right)^2 dx}_{\text{Linear}} \\ & + \underbrace{\frac{EA}{2}\int_0^l \frac{\partial u_0}{\partial x}\left(\frac{\partial v}{\partial x}\right)^2 dx}_{\text{Nonlinear}} \end{aligned} \tag{4.17}$$

From the non-linear strain energy equation (Equation 4.17), and defining a constant (per time step) force $F = \frac{EA}{l}(u_2 - u_1)$, Przemieniecki's 3DoF derivation can be extended to 6DoF to give

$$K_G = \frac{EA}{l}\left(u_2 - u_1\right)\left[K_{G_M}\right]$$

$$K_{G_M} = \begin{bmatrix}
0 & & & & & & & & & & & \\
0 & \frac{6}{5l} & & & & & & & & & & \\
0 & 0 & \frac{6}{5l} & & & & & & & & & \\
0 & 0 & 0 & \frac{I_x}{Al} & & & & & & & & \\
0 & 0 & -\frac{1}{10} & 0 & \frac{2l}{15} & & & & & & & \\
0 & -\frac{1}{10} & 0 & 0 & 0 & \frac{2l}{15} & & & & & & \\
0 & 0 & 0 & 0 & 0 & 0 & 0 & & & & & \\
0 & -\frac{6}{5l} & 0 & 0 & 0 & -\frac{1}{10} & 0 & \frac{6}{5l} & & & & \\
0 & 0 & -\frac{6}{5l} & 0 & \frac{1}{10} & 0 & 0 & 0 & \frac{6}{5l} & & & \\
0 & 0 & 0 & -\frac{I_x}{Al} & 0 & 0 & 0 & 0 & 0 & \frac{I_x}{Al} & & \\
0 & 0 & \frac{1}{10} & 0 & -\frac{l}{30} & 0 & 0 & 0 & \frac{1}{10} & 0 & \frac{2l}{15} & \\
0 & \frac{1}{10} & 0 & 0 & 0 & -\frac{l}{30} & 0 & -\frac{1}{10} & 0 & 0 & 0 & \frac{2l}{15}
\end{bmatrix}$$

This requires the expanded equation of motion to be solved as

$$\mathbf{F}(q,t) = \mathbf{M}\ddot{\mathbf{q}} + \mathbf{C}(q)\dot{\mathbf{q}} + (\mathbf{K}_E + \mathbf{K}_G(q))\,\mathbf{q} \tag{4.18}$$

where K_E is the linear stiffness matrix and K_G is the non-linear component, which as a function of state vector, q, needs to be recalculated every time step using non-linear solvers such as that of Figure 4.7 and 4.8.

EXAMPLE 4

For the chapters worked examples of the BEAR code an isotropic beam is defined for simplicity using the properties defined in `ISO_beam_build.m` (Appendix C). The beam has a length,l, of $1m$ and a constant cross section ($w \times h$) of $0.1m \times 0.01m$. The material of the beam has a density, ρ, of $2800kg.m^{-3}$, elastic (Young's) modulus, E, of $69GPa$ and Poisson ratio, ν, of 0.3. The Rayleigh damping coefficients, η and λ, are 3×10^{-4} and 2×10^{-4} respectively. The beam is assumed to be a cantilever, with all free nodes having 6 DoF.

4.4 VALIDATION

The model has been validated against commercial codes, in this case MSC NASTRAN was used. The same cantilever model was built using NASTRAN BEAM elements, which allow for the shear deformation as per a Timoshenko beam would. The discretised BEAM elements have a defined density and no external "lumped" (CONM2) masses are applied. The use of density for the mass allows NASTRAN to generate the propriety coupled mass matrix. The discretisation, material and geometry properties are all consistent between the BEAR example and the NASTRAN model.

Figure 4.16 displays the mode shape output from the BEAR framework, and displays the modal frequencies compared to the same model built in NASTRAN (note the first torsional mode at $1744rad$ is shown clearer in Figure 4.17). The numerical comparison between the modal frequencies can be seen in Table 4.1. The error between the BEAR values and that of NASTRAN is probably due to the *coupled* mass

Table 4.1: BeaR modes comparison with NASTRAN

Mode	Modal Frequencies				% Error
	BeaR		NASTRAN		
	$rad.s^{-1}$	Hz	$rad.s^{-1}$	Hz	
1	47.8	7.6	50.4	8.0	5.4
2	315.4	50.2	315.6	50.2	0.1
3	500.2	79.6	500.8	79.7	0.1
4	883.1	140.5	883.0	140.5	0.0
5	962.4	153.2	932.2	148.4	3.2
6	1728.5	275.1	1728.7	275.1	0.0
7	2853.1	454.1	2854.3	454.3	0.0

matrix NASTRAN uses by default, which is a propriety combination of the consistent and lumped mass matrices BeaR can generate. Thus it is concluded that the comparison shows BeaR generates suitable mass and stiffness matrices (linear).

The BeaR model has been successfully integrated into the CA^{2}LM framework. The AX-1 aircraft (Figure 4.11) was modelled as a series of beams, with a comparison made to the previous structural *BEMMODES* code [26] [109] made by evaluating the first 12 modes, an example of which is given in Figure 4.18. From the comparison of BeaR to *BEMMODES* the mode shapes are consistent, and the eigenvectors are in the same order. The minor discrepancy seen in the frequency of each mode shape is probably due to variations in how the stiffness matrix is built (perhaps Rayleigh or Euler as opposed to Timoshenko) or due to variances in the mass matrix, similar as found in the comparison of BeaR to NASTRAN. However, BEMMODES is a *black box* executable, as such the variance can only be speculated. The correlation between BeaR and BEMMODES does however provide further confidence in the output of BeaR .

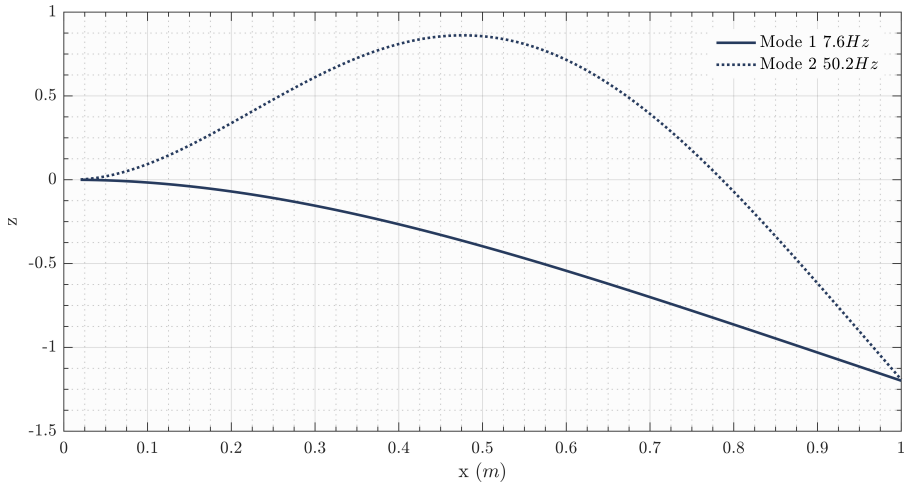

(a) XZ Bending Modes 1 and 2

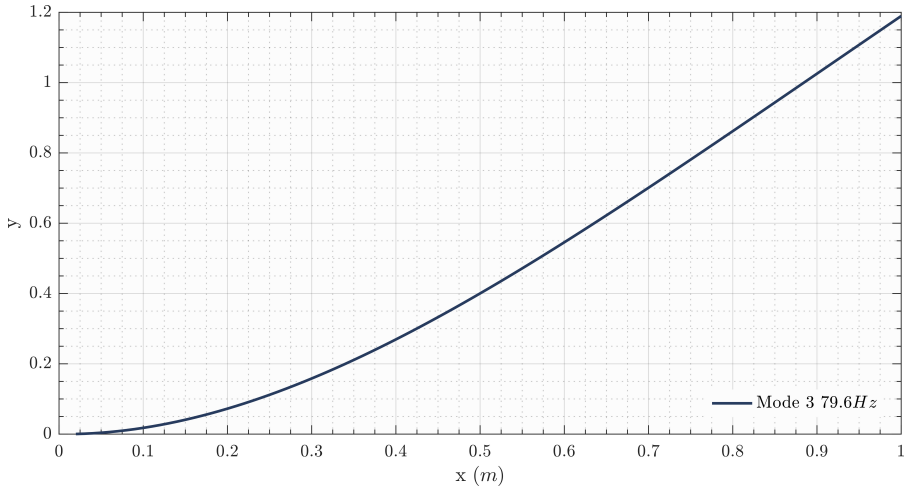

(b) XY Bending Mode 3

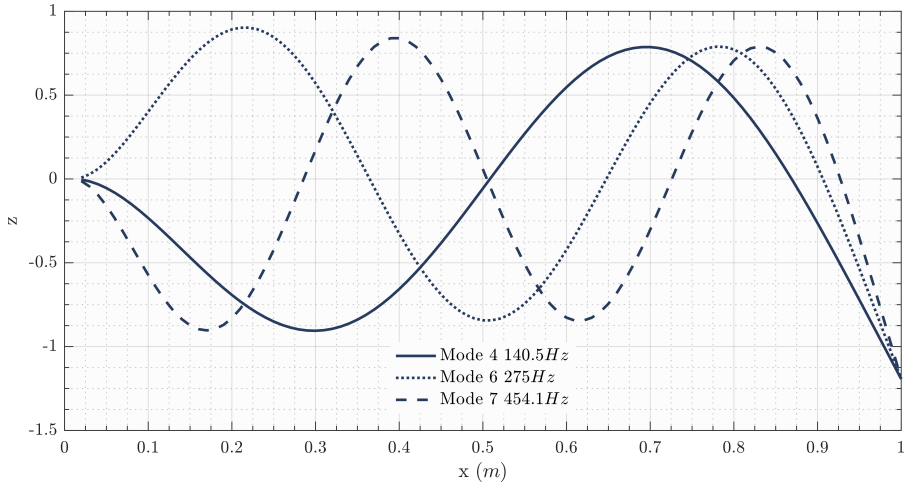

(c) XZ Bending Modes 4,6 and 7

Figure 4.16: Plotted eigenvectors from the BEAR framework

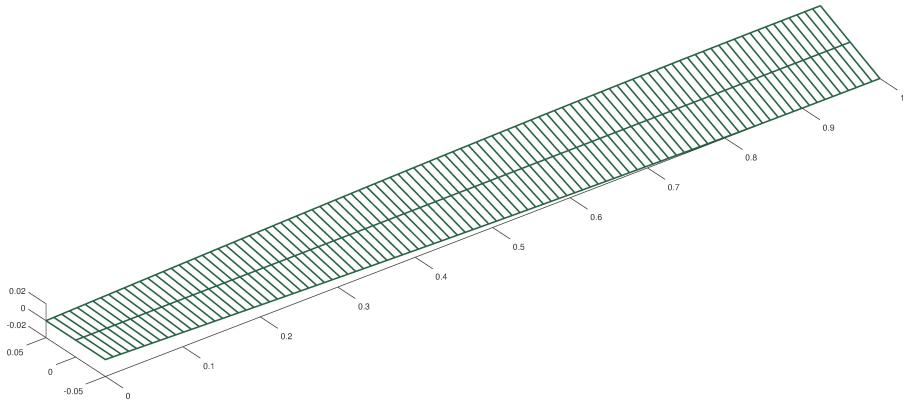

Figure 4.17: XX Torsional Mode 5 (153.2 Hz)

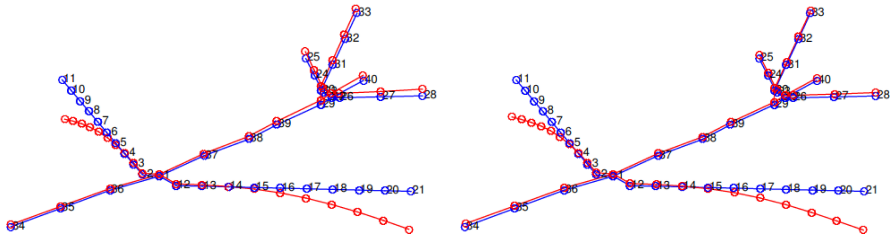

(a) Mode 1 *BEMMODES* 7.80$rad.s^{-1}$ (b) Mode 1 BEAR 7.44$rad.s^{-1}$

Figure 4.18: Comparison of Mode 1 output from BEAR and *BEMMODES*

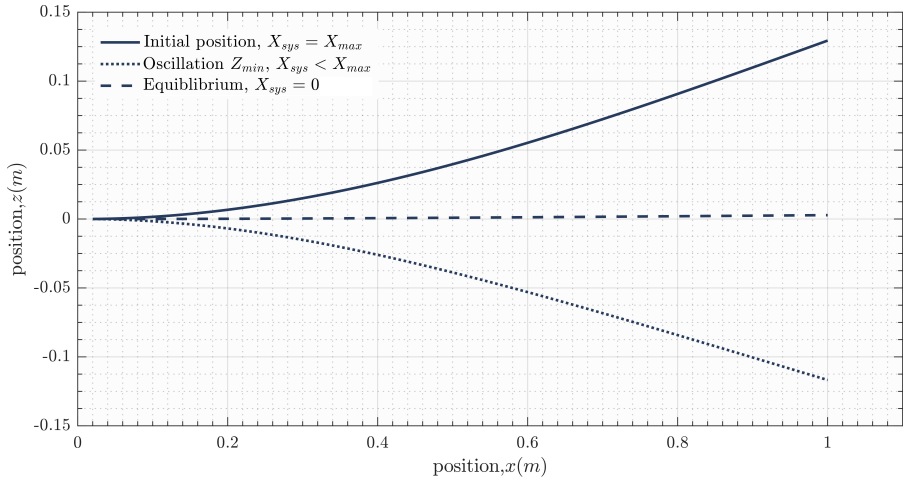

Figure 4.19: BEAR framework example for isotropic beam deflection

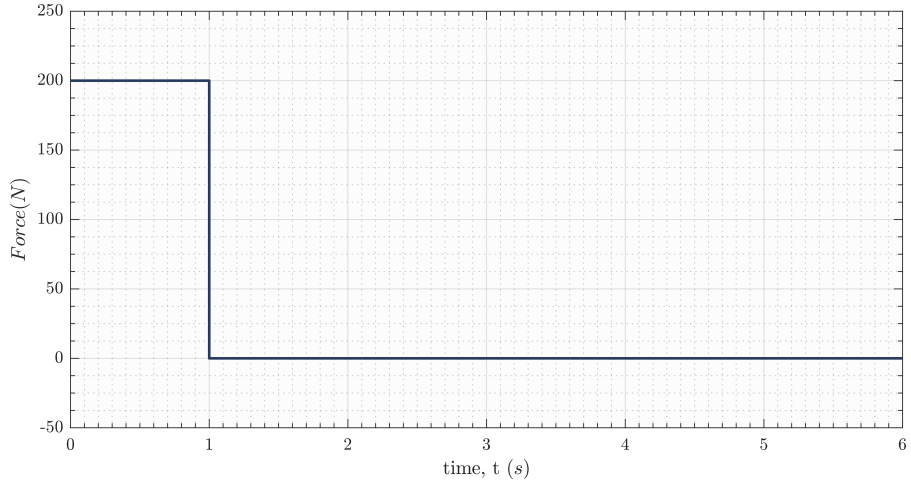

Figure 4.20: BEaR framework example for isotropic beam force input (tip)

EXAMPLE 5

Using the isotropic beam, a dynamic exergy analysis can be shown. Figure 4.19 shows the beam in its initial deflection position, where the beam is deformed with a constant load to a position where it has strain energy and is at the maximum exergy point of the analysis, which is equal to the total energy seen in Figure 4.21a. On releasing the initial load at $t = 1$ (see Figure 4.20) the beam begins to oscillate, transferring the energy between strain and kinetic, as shown in Figure 4.21a.

The reduction in the strain and kinetic energies seen in Figure 4.21a is due to the Rayleigh damping implemented in the model, where energy is dissipated from the beam through entropy generation. The similitude between the rate of entropy generation, $\dot{S}_{\text{gen}}$, and total exergy destroyed, X_D, is shown in Figure 4.21c. As entropy is generated the exergy (available energy) in the beam reduces. Note that the rate of reduction decreases as the velocity of the beam decreases due to Rayleigh damping being a function of velocity. The exergy reduces in Figure 4.21b until the point of mechanical equilibrium shown in Figure 4.19 where no more energy can be extracted from the system as work.

It should be noted, that given the mechanical equilibrium state with the environment is the beam at rest the potential (strain) and kinetic energies are equivalent to the exergy terms in Equation 4.11. The first law is satisfied with this analysis as seen in Figures 4.21a and 4.21b, as the total energy (Equation 4.9) is constant. This method of analysis is useful as it allows the engineer to see where energy is being dissipated at the maximum rate, and how the available energy changes with regard to time, even though the total energy is constant.

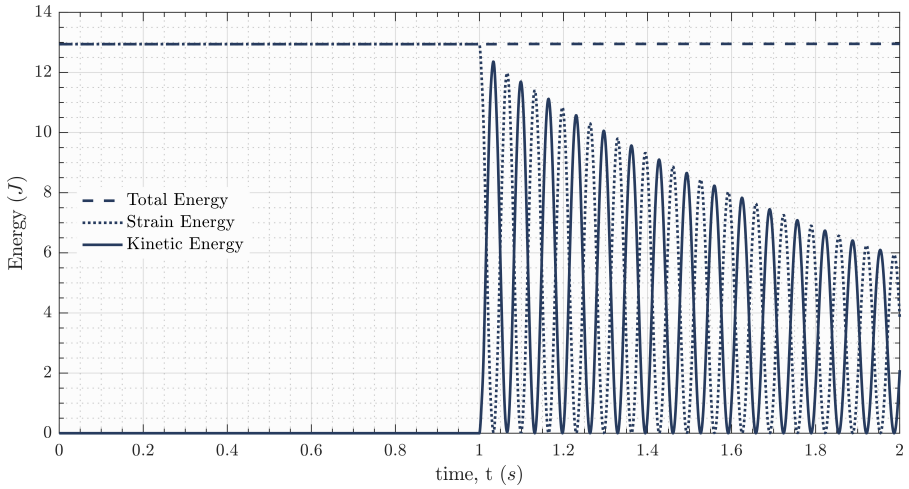

(a) BEAR framework example Energy plot

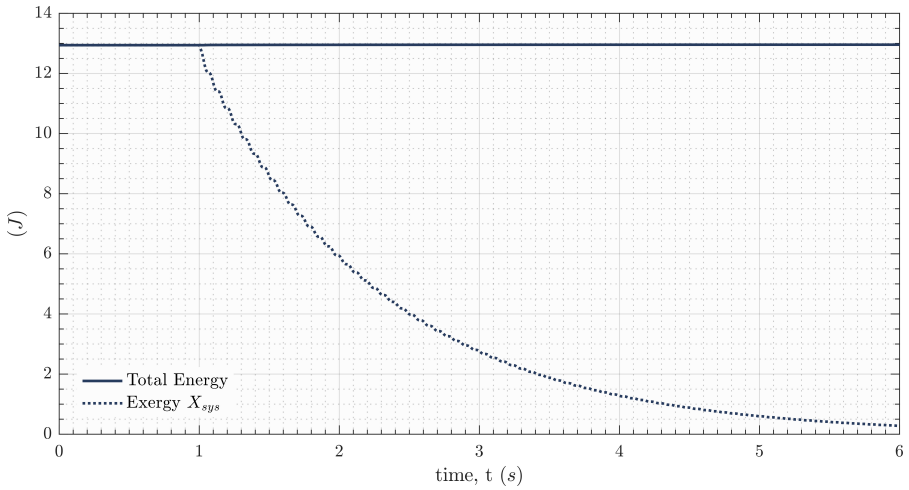

(b) BEAR framework example Exergy plot

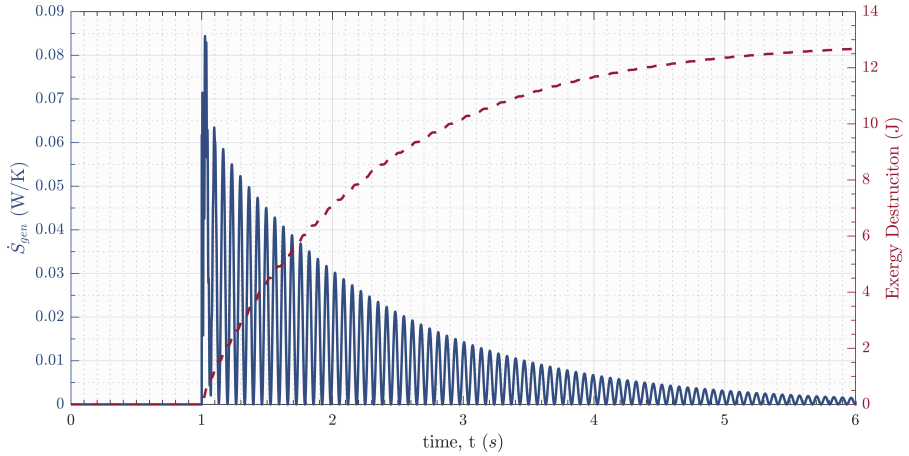

(c) BEAR framework example Exergy Destruction and Entropy plot

Figure 4.21: BEAR framework example for isotropic beam results

4.5 OPTIMAL DAMPING OF DYNAMIC BEHAVIOUR

The typical damping coefficient for a commercial aircraft's wing structure is around $\zeta = 0.03$, known as 3% structural damping. However for highly flexible airframes that will see large deflections from the designed flight deflection under loads such as gust events or turbulence, it may be beneficial to design in viscous dampers to the system to control the response. The aim of this section is therefore to:

> *Identify the optimal damping coefficient for the structure of a HARW aircraft. In this case the term optimal is defined as the damping ratio which returns the structure to the initial position with the fastest dissipation rate after a dynamic event. This will be achieved using an exergy based approach to optimal damping analysis.*

The optimal rate of damping is defined as the highest rate of energy dissipation or exergy destruction from the system to bring it back to the state of minimum energy. This is not equal to the critical damping which is defined as the term where the system returns to the state of minimum energy without overshoot asymptotically.

Consider the systems exergy plotted in Figure 4.22; optimal damping of the system will dissipate the initial system exergy (summation of kinetic and potential terms, see Equation 4.11) in the shortest time possible, thus the exergy dissipation rate, $\dot{X}$, should be maximised; doing this over all time gives the cost

$$\int_0^\infty -\dot{X}(t)\,dt$$

However, evaluating this cost gives

$$\int_0^\infty -\dot{X}(t)\,dt = X(0)$$

which is a constant. Hence it is proposed that the cost is the integral of the exergy dissipation function

$$J = \int_0^\infty X(t)\,dt \tag{4.19}$$

and the aim is to minimise this cost so that the exergy, $X(t)$, dissipates to zero in the shortest time, thus minimising the shaded region in Figure 4.22. This gives the optimisation problem

$$J_{\text{opt}} = \min_{\zeta \in \mathbb{R}_+} J(\zeta) \tag{4.20}$$

The exergy at any point in time can be defined using Equation 4.11 as

$$X(t) = \frac{1}{2} q^T(t) \begin{bmatrix} K & 0 \\ 0 & M \end{bmatrix} q(t) \tag{4.21}$$

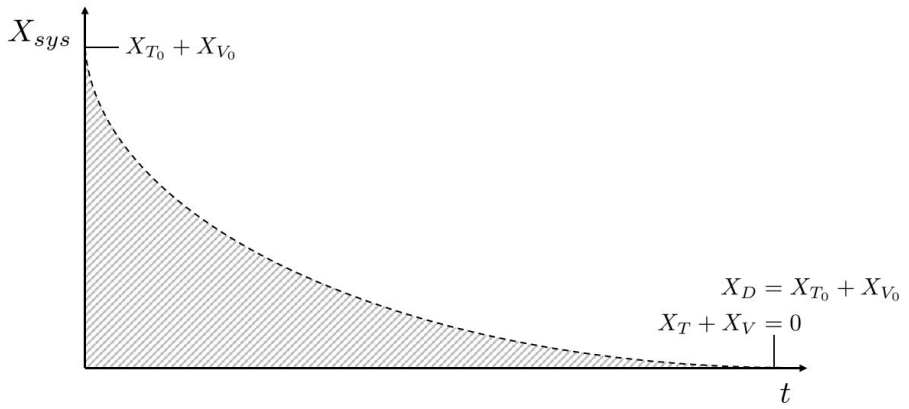

Figure 4.22: Graphical Representation of a an Initial Exergy Content being Dissipated to Zero

where the state vector, q is defined in terms of the displacement, x, velocity, $\dot{x}$ as

$$q(t) = \begin{bmatrix} x \\ \dot{x} \end{bmatrix}$$

Equation 4.21 can be rewritten as

$$X(t) = q^T(t)\, Q\, q(t) \tag{4.22}$$

where Q is the exergy weighting matrix, defined in terms of the mass, M, and stiffness, K, as

$$Q = \begin{bmatrix} \frac{K}{2} & 0 \\ 0 & \frac{M}{2} \end{bmatrix}$$

The state vector can be solved using the equation of motion, formed from Equation 4.18 in terms of natural frequencies, ω_n and damping ratio, ζ, as

$$f(t) = \ddot{x}(t) + 2\zeta\omega_n\dot{x}(t) + {\omega_n}^2 x(t)$$

Assuming no input force, $f(t) = 0$, (analysis is performed with initial conditions only)

$$\ddot{x}(t) = -\omega_n^2 x(t) - 2\zeta\omega_n\dot{x}(t)$$

Arranging in the standard state-space form gives

$$\overbrace{\begin{bmatrix} \dot{x} \\ \ddot{x} \end{bmatrix}}^{\dot{q}} = \overbrace{\begin{bmatrix} 0 & 1 \\ -\omega_n^2 & -2\zeta\omega_n \end{bmatrix}}^{A} \overbrace{\begin{bmatrix} x \\ \dot{x} \end{bmatrix}}^{q}$$

The equation of motion is solved for the state vector in the standard form, where q_0 is the initial condition, by

$$q(t) = e^{At} q_0 \tag{4.23}$$

Substituting Equation 4.23 into Equation 4.22 yields

$$X(t) = q_0^T \underbrace{e^{A^T t}\, Q\, e^{At}}\, q_0 \tag{4.24}$$

Differentiating the under-braced section in Equation 4.24 with respect to time gives

$$\frac{d\left(e^{A^T t}\, Q\, e^{At}\right)}{dt} = A^T e^{A^T t}\, Q\, e^{At} + e^{A^T t}\, Q\, e^{At} A$$

Integrating the function between zero and infinity gives

$$\cancelto{0}{e^{\infty A^T}\, Q\, e^{\infty A}} - \underbrace{e^{0.A^T}}_{I}\, Q\, \underbrace{e^{0.A}}_{I} = A^T \int_0^\infty e^{A^T t}\, Q\, e^{At} dt + \int_0^\infty e^{A^T t}\, Q\, e^{At} dt A \tag{4.25}$$

The first term on the left hand side cancels to zero as the A matrix is stable, as such $e^{\infty A} = 0$. Defining the function P as

$$P = \int_0^\infty e^{A^T t}\, Q\, e^{At} dt$$

and substituting P into Equation 4.25 reduces the equation to a Lyapunov Equation [163] as

$$-Q = A^T P + PA \tag{4.26}$$

For simplicity, the mass and stiffness are normalised, such that matrix Q is the identity matrix, I, and the system state matrix, A, is reduced to contain only the damping ratio, ζ. Expanding Equation 4.26 gives

$$
\begin{aligned}
0 &= A^T P + PA + Q \\
0 &= \begin{bmatrix} 0 & -1 \\ 1 & -2\zeta \end{bmatrix} \begin{bmatrix} P_1 & P_2 \\ P_2 & P_3 \end{bmatrix} + \begin{bmatrix} P_1 & P_2 \\ P_2 & P_3 \end{bmatrix} \begin{bmatrix} 0 & 1 \\ -1 & -2\zeta \end{bmatrix} + \begin{bmatrix} 1 & 0 \\ 0 & 1 \end{bmatrix} \\
0 &= \begin{bmatrix} 1 - 2P_2 & P_1 - 2\zeta P_2 - P_3 \\ P_1 - 2\zeta P_2 - P_3 & 1 + 2P_2 - 4\zeta P_3 \end{bmatrix}
\end{aligned}
$$

Solving equations for matrix P gives

$$
P = \begin{bmatrix} P_1 & P_2 \\ P_2 & P_3 \end{bmatrix} = \begin{bmatrix} \zeta + \frac{1}{2\zeta} & \frac{1}{2} \\ \frac{1}{2} & \frac{1}{2\zeta} \end{bmatrix}
$$

Substituting matrix P into Equation 4.24 and then the optimal damping cost function (Equation 4.19) gives

$$
J = q_0^T \, P \, q_0 \tag{4.27}
$$

This is an algebraic expression for $J(\zeta)$ and the problem given by Equation 4.20, for a given value of q_0, can be solved by finding the turning points, such that

$$
\frac{\partial J}{\partial \zeta} = 0 \tag{4.28}
$$

From the cost function in Equation 4.27, the optimal damping ratio can be ascertained based on the initial exergy ratio of the system. As the derivation is based on conservative exergies only, the following initial conditions are considered:

- Non-zero potential energy and zero kinetic energy (initial displacement)
- Zero potential energy and non-zero kinetic energy (initial velocity)
- Non-zero potential energy and non-zero kinetic energy (initial displacement and velocity)

Note, the environmental/reference state of the system (x_∞ and $\dot{x}_\infty$) are taken as zero for the examples, as such the exergy and energy quantities are equal.

4.5.1 *Initial Displacement*

The initial displacement condition is non zero, so the initial state vector is defined as

$$
q_0 = \begin{bmatrix} 1 \\ 0 \end{bmatrix}
$$

Substituting q_0 and P into Equation 4.27 yields

$$
\begin{aligned}
J(\zeta) &= \begin{bmatrix} 1 & 0 \end{bmatrix} \begin{bmatrix} \zeta + \frac{1}{2\zeta} & \frac{1}{2} \\ \frac{1}{2} & \frac{1}{2\zeta} \end{bmatrix} \begin{bmatrix} 1 \\ 0 \end{bmatrix} \\
&= \zeta + \frac{1}{2\zeta}
\end{aligned}
$$

The solution to the minimisation of the cost function (Equation 4.20) for the initial displacement condition is given using Equation 4.28 as

$$
\begin{aligned}
\frac{\partial J}{\partial \zeta} &= 1 - \frac{1}{2\zeta^2} = 0 \\
\zeta_{\text{opt}} &= \frac{1}{\sqrt{2}}
\end{aligned} \tag{4.29}
$$

The same result can be found by running the BEAR model for a single degree of freedom and an initial displacement with a variable damping coefficient. The results of which are given in Figure 4.23.

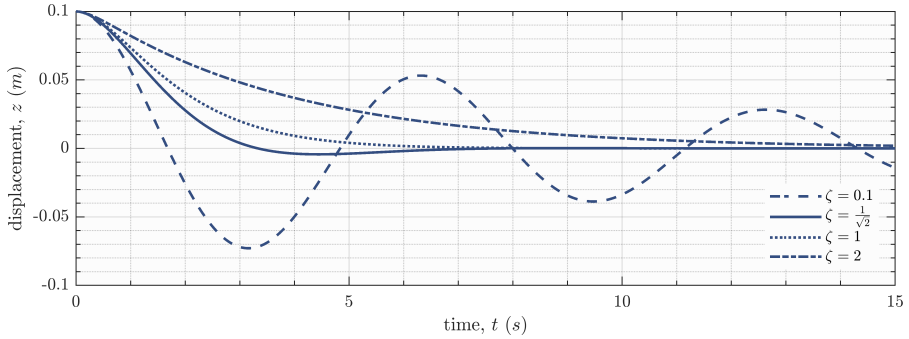

(a)

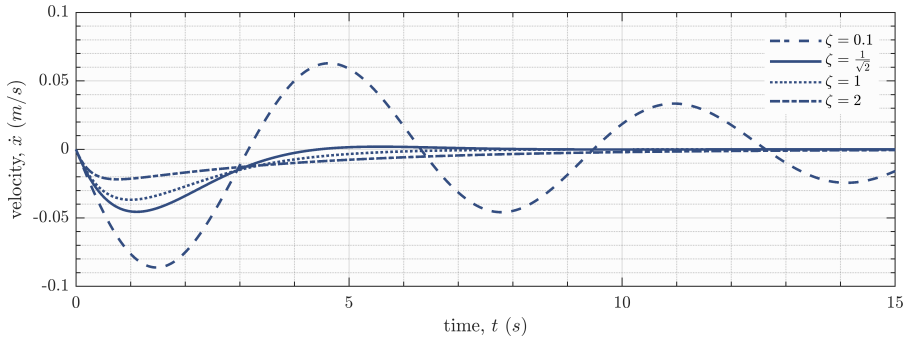

(b)

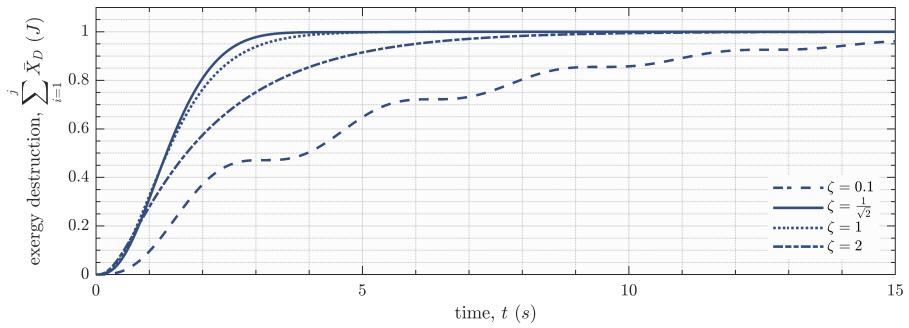

(c)

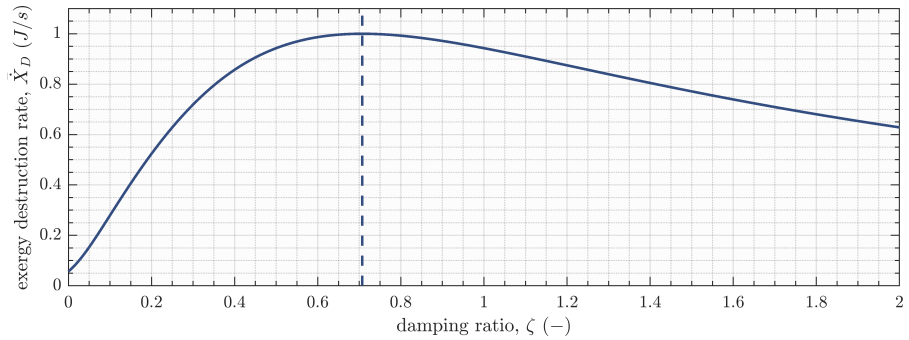

(d)

Figure 4.23: Initial potential exergy optimal damping

4.5.2 *Initial Velocity*

The initial velocity condition is non zero, so the initial state vector is defined as

$$q_0 = \begin{bmatrix} 0 \\ 1 \end{bmatrix}$$

Substituting q_0 and P into Equation 4.27 yields

$$\begin{aligned} J(\zeta) &= \begin{bmatrix} 0 & 1 \end{bmatrix} \begin{bmatrix} \zeta + \frac{1}{2\zeta} & \frac{1}{2} \\ \frac{1}{2} & \frac{1}{2\zeta} \end{bmatrix} \begin{bmatrix} 0 \\ 1 \end{bmatrix} \\ &= \frac{1}{2\zeta} \end{aligned}$$

The solution to the minimisation of the cost function (Equation 4.20) for the initial velocity condition is given using Equation 4.28 as

$$\begin{aligned} &\frac{\partial J}{\partial \zeta} = -\frac{1}{2\zeta^2} = 0 \\ &\zeta_{\text{opt}} = \infty \end{aligned} \tag{4.30}$$

The same result can be found by running the BEAR model for a single degree of freedom and an initial velocity with a variable damping coefficient. The results of which are given in Figure 4.24.

4.5.3 *Initial Displacement and Velocity*

The initial potential and kinetic condition is non zero and equal, so the initial state vector is defined as

$$q_0 = \begin{bmatrix} 1 \\ 1 \end{bmatrix}$$

Substituting q_0 and P into Equation 4.27 yields

$$\begin{aligned} J(\zeta) &= \begin{bmatrix} 1 & 1 \end{bmatrix} \begin{bmatrix} \zeta + \frac{1}{2\zeta} & \frac{1}{2} \\ \frac{1}{2} & \frac{1}{2\zeta} \end{bmatrix} \begin{bmatrix} 1 \\ 1 \end{bmatrix} \\ &= \zeta + \frac{1}{\zeta} + 1 \end{aligned}$$

The solution to the minimisation of the cost function (Equation 4.20) for the initial potential and kinetic condition is given using Equation 4.28 as

$$\begin{aligned} &\frac{\partial J}{\partial \zeta} = 1 - \frac{1}{\zeta^2} = 0 \\ &\zeta_{\text{opt}} = 1 \end{aligned} \tag{4.31}$$

The same result can be found by running the BEAR model for a single degree of freedom and an initial velocity with a variable damping coefficient. The results of which are given in Figure 4.25.

4.5.4 *Energy Ratio*

The previous *initial kinetic and potential* assumed an equal exergy contribution from both forms of exergy. This section identifies the optimal damping coefficient for any given ratio of potential and kinetic exergy. Figure 4.26 shows the sum of the exergies is always one, $X_{T_0} + X_{V_0} = 1$ and the initial condition ratio of the exergies is parameterised as a function of θ such that

$$q_0(\theta) = \begin{bmatrix} \cos(\theta) \\ \sin(\theta) \end{bmatrix}$$

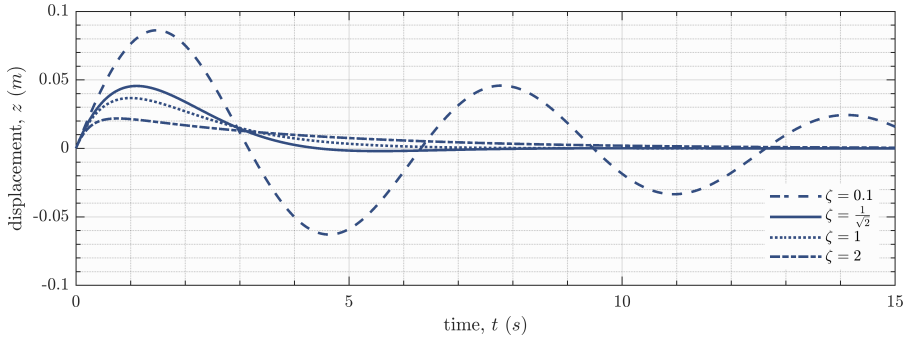

(a)

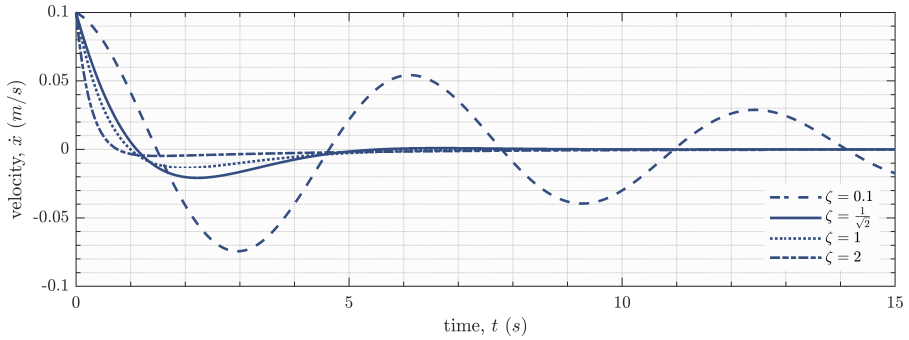

(b)

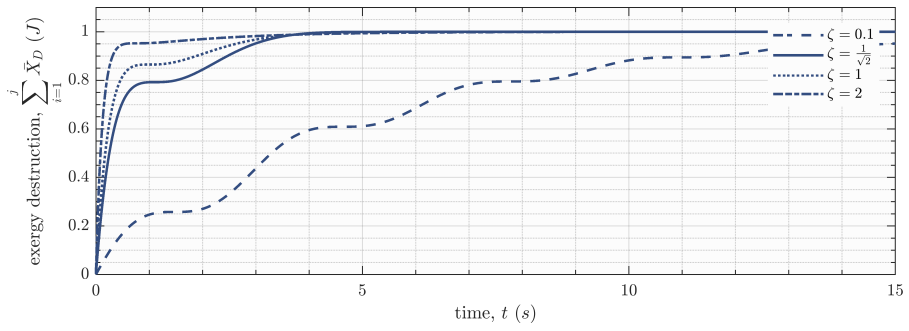

(c)

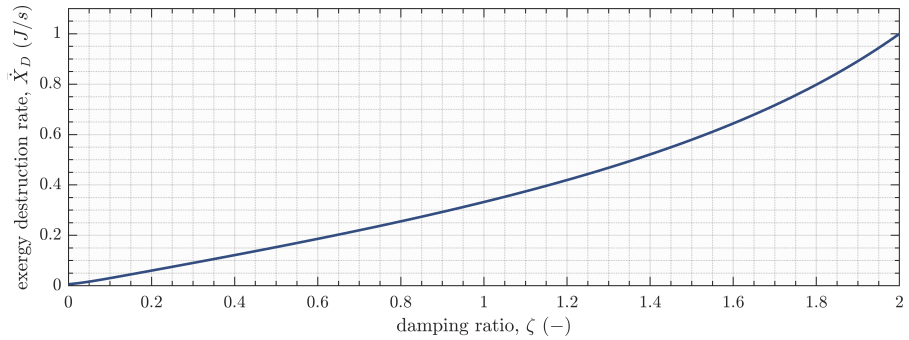

(d)

Figure 4.24: Initial kinetic exergy optimal damping

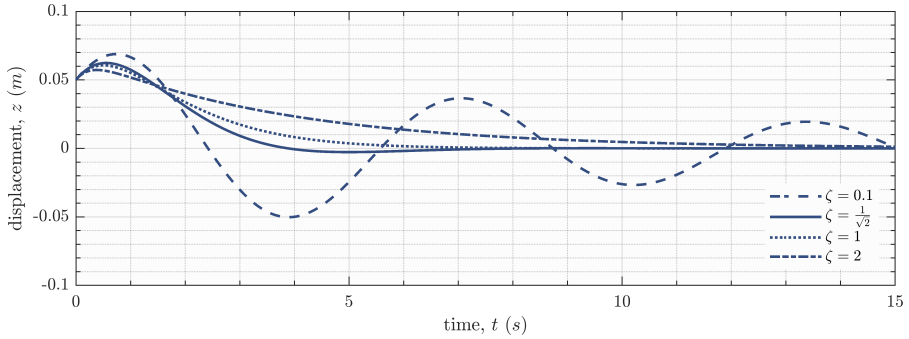

(a)

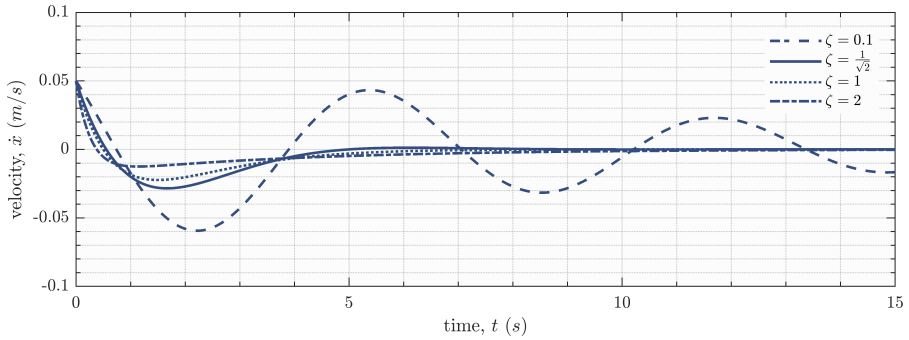

(b)

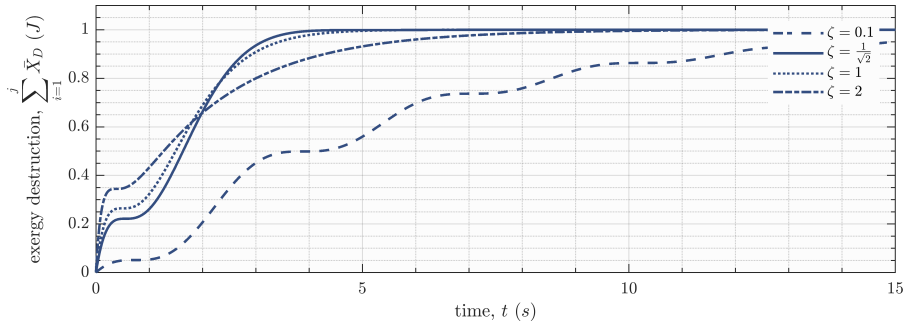

(c)

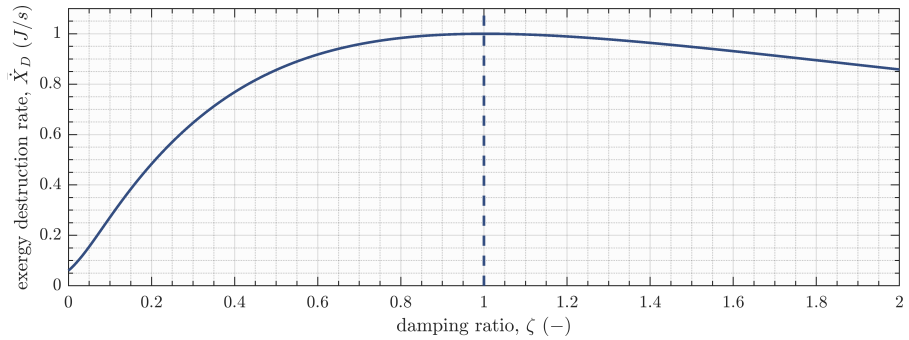

(d)

Figure 4.25: Initial kinetic and potential exergy optimal damping

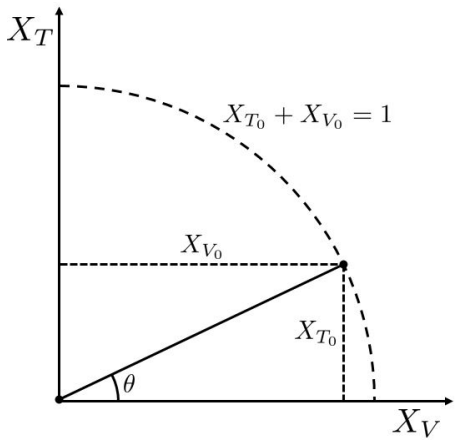

Figure 4.26: Definition of the Exergy Ratio

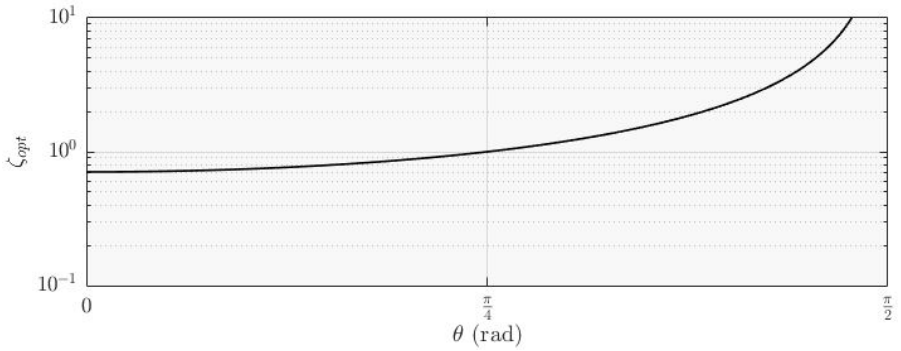

Figure 4.27: Optimal Damping as a function of Energy Ratio

Substituting q_0 and P into Equation 4.27 yields

$$\begin{aligned} J(\zeta) &= \begin{bmatrix} \cos(\theta) & \sin(\theta) \end{bmatrix} \begin{bmatrix} \zeta + \frac{1}{2\zeta} & \frac{1}{2} \\ \frac{1}{2} & \frac{1}{2\zeta} \end{bmatrix} \begin{bmatrix} \cos(\theta) \\ \sin(\theta) \end{bmatrix} \\ &= \frac{\zeta^2 \cos(2\theta) + \zeta^2 + \zeta \sin(2\theta) + 1}{2\zeta} \end{aligned}$$

The solution to the minimisation of the cost function (Equation 4.20) for the initial potential and kinetic condition (as a function of the intial ratio θ) is given using Equation 4.28 as

$$\begin{aligned} \frac{\partial J}{\partial \zeta} &= \frac{1}{2}\left(-\frac{1}{\zeta^2} + \cos(2\theta) + 1\right) = 0 \\ \zeta_{opt} &= \frac{1}{\sqrt{2}\cos\theta} \end{aligned} \tag{4.32}$$

The same result can be found by running the BEaR model for an initial exergy ratio with a variable damping coefficient. The results of which are given in Figure 4.27, which shows the optimal damping coefficient for a given initial exergy ratio. It should be noted that for $\theta = 0$, the optimal damping ratio is $\zeta_{\text{opt}} = \frac{1}{\sqrt{2}}$ as for the initial displacement. Equally for the exergy ratio, $\theta = \frac{\pi}{2}$, the optimal damping ratio tends to $\zeta_{\text{opt}} = \infty$, as per the initial velocity.

Here, exergy principles have been applied to derive and show that the optimal damping ratio varies based on the initial exergy of the system, be it potential, kinetic or ratio of the two.

Critical damping is defined as the point where the system returns to its equilibrium position at the fastest rate given no overshoot of the system, defined at the point

of $\zeta = 1$. However, this does not mean it is the maximum rate of damping or exergy destruction. In fact $\zeta = \frac{1}{\sqrt{2}}$ provides an overshoot of the system from equilibrium, but then returns asymptotically to the point of equilibrium with no undershoot. The variable damping ratio response can be grouped and described as:

- $0 < \zeta < \frac{1}{\sqrt{2}}$
  - output overshoots, then undershoots below the equilibrium value and continues this response with a damped oscillation.
- $\frac{1}{\sqrt{2}} \leq \zeta < 1$
  - overshoot less than 5% and no subsequent undershoot of the final value, that means the system output overshoots and then approaches the final value asymptotically from above.
- $1 \leq \zeta$
  - the system output does not overshoot, but approaches the final value asymptotically from below.

4.6 CHAPTER SUMMARY

This chapter demonstrates how exergy is transferred and destroyed within structural dynamic systems, and derived a series of equations that can be used for exergy analysis of aerospace systems. The concepts were demonstrated on simple single DoF systems before being scaled to more complex six DoF beam geometry. The main output from this chapter is the BEaR framework (see additional information in Appendix C) which provides a versatile structural solver to solver that can

- generate stiffness and mass matrices for any beam geometry (given standard NASTRAN punch input) based in Timoshenko mechanics
- apply Rayleigh damping (mass and stiffness proportional) to generate a viscous damping matrix to represent structural damping
- undertake eigenvalue analysis to calculate the modal response of the system
- use either a direct or state-space solver to solve the second order ODE equations of motion for any defined force input or initial condition
- apply geometric non-linearity to the system based on beam extension which results in stiffening of the beam

The chapter concluded with an investigation into the optimal damping of a structure, using an exergy approach. Here the optimal damping was defined as the highest rate of energy dissipation or exergy destruction from the system to bring it back to the state of minimum energy. The optimal damping coefficient was calculated for a given initial energy input.

This chapter summaries the work done in the thesis on the first node of Collars triangle (Figure 4.1), the structural dynamics. The following two chapters will investigate at the remaining nodes, rigid body dynamics and aeroelasticity.

5

EXERGY ANALYSIS OF RIGID BODY FLIGHT DYNAMICS

Entropy generation or exergy destruction due to aircraft aerodynamics are typically overshadowed by the exergy destruction within the propulsion system [40][1]. This does not however mean that there is no purpose in optimising aircraft aerodynamics, as it may be the case reducing exergy destruction due to drag is more cost effective than reducing the total engine exergy destruction. It is also important when trying to move towards a more integrated aircraft design where the engine and aerodynamics need to be optimised together.

Thermodynamic analysis, with the concepts of heat and work transfer, are already used in the design and analysis of aircraft systems such as propulsion and environmental control. However, applying thermodynamic analysis to an aerodynamic system appears to be in contrast to the classic force balance approach, so does such an application provide any beneficial insight? Consider the insight of Nixon [123] that,

> *"Aeronautics is generally thought to be a mature discipline with little extra benefit to be obtained from further specialized research ... The only way that the science of aerodynamics can be made fertile again is to change the building blocks of knowledge"*
>
> - David Nixon [123]

The stated *building blocks of knowledge* is in reference to the force balance approach (Figure 5.1a), a theoretical concept to explain the basic aerodynamics of how a body flies, based on Newtonian mechanics. A crude view of an airframe, using the traditional force balance approach, it has two primary purposes; (i) to house the payload and (ii) to provide lift. In providing lift the airframe generates a drag, D (with contributions from lift-induced, D_i, parasitic, D_p and wave, D_w). This defines the drag, as the opposing force to thrust, T, and the vertical lift force, L, opposing the aircraft weight, W. When in a trimmed cruise configuration all these forces are in equilibrium.

An alternative viewpoint, based on the laws of thermodynamics, is where the aircraft system in flight is considered to have *stored energy* with contributions from gravitational potential energy

$$V = m\mathbf{g}\mathbf{q}$$

and kinetic energy

$$T = \frac{1}{2}m\dot{\mathbf{q}}^2$$

This is the energy balance approach (Figure 5.1b) where drag is stated as a proxy for the energy dissipation through entropy generation, which results in decreasing system stored energy. In studying the transfer and conversion of energy, exergy analysis can be of benefit in improving the thermodynamic performance of the system by highlighting the mechanisms generating entropy and allowing the designer to pinpoint areas for improvement, or help dump unwanted energy from the system in landing or gust events. Viewing an aircraft as a system that uses energy is

1 The proportion of exergy destroyed due to the propulsion compared with aerodynamic losses (viscous and lift-induced) is discussed in Chapter 9

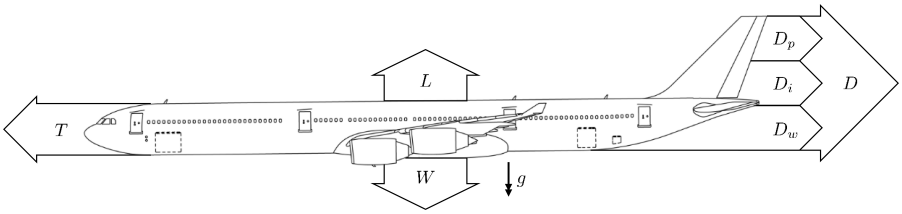

(a) Traditional force balance approach

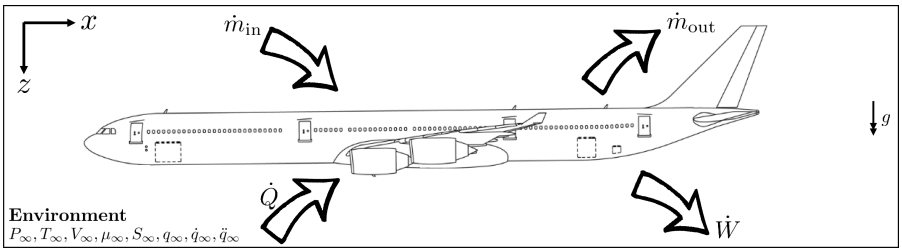

(b) Thermodynamic energy balance approach

Figure 5.1: Methodologies for undertaking aerodynamic design and analysis

not radical, as clear links to the force balance approach can be seen, however using such a methodology may provide additional insight to the traditional force balance approach, which is the premise this chapter looks to investigate.

From this brief discussion there are areas of aerodynamic exergy analysis that need to be investigated, thus this chapter discusses

1. Modelling fluid flow over an aircraft, and identifying how work is transferred to and from the fluid and how entropy is generated.
2. The exergetic efficiency of an aircraft, based on the minimum entropy required to maintain level flight.
3. Optimal lift distributions derived from an entropy method to generate required lift with minimal entropy generation.

5.1 FLUID EXERGY ANALYSIS

As with any system, energy is transferred throughout the airframe, but what needs to be identified is how the aerodynamics uses and converts energy. The rate of work lost (see sign convention in Figure 2.3a) or power lost due to aerodynamic drag, $\dot{W}_D$, can simply be calculated as the drag force multiplied by the velocity

$$\dot{W}_D = Du_\infty \tag{5.1}$$

This section aims to show that the energy dissipated into the fluid as a result of drag contributions has both an entropy (destroyed exergy) and available energy (exergy) content, and that the proportions of each in the fluid can be quantified as the air flows over the aircraft.

It is expected that in line with the second law the total entropy content (system and environment) will always increase, yet as the aircraft is doing work on the fluid, the exergy content can vary as the air passes each section of the aircraft. As the air flow passes the tail of the aircraft the exergy content in the fluid will no longer increase, and instead decrease as the viscous dissipation of the vortices generates entropy and thus destroys the exergy content until the wake exergy is zero and in thermodynamic equilibrium with the environment. This premise will be verified

by using a Computational Fluid Dynamics (CFD) model of the fluid flow over the Cranfield AX-1 aircraft.

5.1.1 *Modelling Drag as Entropy Generation*

Early work in gas dynamics created the framework for deriving the entropy production through drag, notably from Oswatitsch, an assistant to Ludwig Prandtl. Oswatitsch [124] stated that drag was simply a generation of entropy;

> *"The power required to move a body immersed in a fluid with the constant velocity u_∞ is equal to the temperature of the approach flow times the flow of entropy through an area which includes all entropy changes caused by the body"*
>
> - Klaus Oswatitsch [124]

This statement is related to the *Guoy-Stodola Identity* (Equation 2.12), which states that the decrease of useful work of a thermal machine is equal to the entropy change of the system times the surrounding temperature. In the case that no useful work is done, Du_∞ corresponds to the lost energy and the increase of the entropy flow represents the rate of entropy increase of the whole system, such that

$$Du_\infty = T_\infty \iint_{F_i} (s - s_\infty)\, \rho \dot{\mathbf{q}}_n dA = \dot{X}_D \tag{5.2}$$

where s is the entropy per unit of mass, $\dot{\mathbf{q}}_n$ is the velocity vector, the ∞ index is the parameter value in undistributed parallel flow and the integral is taken over a planar area, F_i, at a distance, i, behind the aircraft. Equation 5.2 is known as the *Oswatitsch equality* that assumes all energy lost via drag is entropy generated.

5.1.2 *Modelling the Energy Content of Drag*

Drela [58] presented an analysis focusing on the mechanical power and kinetic energy flow in the induced drag vortices, D_i, utilising the *first law of thermodynamics* (Equation 2.1). He proposed a rate of energy use, where for a wing the *energy loss rate*, defined by the axial kinetic energy, E_a, the transverse (vortex) kinetic energy, E_v, and the pressure-work, E_p, rates are equal to the power due to the induced drag, D_i, in the flow,

$$\dot{E}_a + \dot{E}_v + \dot{E}_p = D_i u_\infty \sim \rho u_\infty \Gamma^2 \tag{5.3}$$

where Γ is the airfoil circulation.

With this approach Drela concluded that

> *"[As] the formulation does not require any separate definitions of thrust and drag, and hence it is especially useful for analysis and optimization of aerodynamic configurations that have tightly integrated propulsion and boundary-layer control systems"*
>
> - Mark Drela [58]

5.1.3 *The Exergy Content of Drag*

A critical difference between the Oswatitsch and Drela wake analyses is that Oswatitsch models the entire aircraft wake as generated entropy, and Drela focuses on the energy content in the vortices. Both these methods seem reasonable, as with Drela's assumption, at any location from the aircraft (x in Figure 5.2) the vortices created by the induced drag will have an available energy content (exergy) in comparison to entropy. This approach is what is required to identify the energy that

can be harvested from the wake vortices through methods such as formation flight, but does not allow aerodynamic optimisation, as only a limited part of the wake is modelled. For example, the entropy generated in the formation of the vortices is not modelled in Drela's method, which is critical for aerodynamic optimisation. Equally, with Oswatitsch's method one can argue that the energy or exergy content of the wake is irrelevant because far behind the aircraft (x_∞ in Figure 5.2) there will be no exergy and entropy will be at a maximum. So when considering an aircraft in isolation (i.e. no formation flight) all drag is entropy generation.

By modelling the exergy content of the drag, an understanding is provided to the available energy in the aircraft wake that could be exploited through formation flight or another energy harvesting method (e.g. turbine). As the wake travels further from the aircraft, exergy analysis would provide understanding on how the initial wake exergy content dissipates as exergy is destroyed, and the fluid returns to thermodynamic equilibrium with the environment, the point of maximum entropy generation.

Modelling the exergy content of the fluid as it flows over the aircraft is also critical for an aircraft designer looking to optimise the aircraft aerodynamic system. Both the Drela and Oswatitsch derivations look to quantify thermodynamic parameters of the fluid state, be it energy or entropy. This derivation aims to combine the methods, by stating that as an aircraft flows through a fluid at free stream velocity, u_∞, energy is transferred to the flow from the aircraft with accompanying entropy generation. So if the exergy content of the flow can be characterised at different planer positions in the flow along the aircraft, areas and processes inefficiencies will be highlighted which can be targeted for performance improvement.

Relating the exergy transfer into a fluid flow has previously been studied by Naterer [118], Drela [58] and Bejan [18], whose work showed the fundamental exergy equations (Equations 2.5 and 2.11) can be rewritten to describe the rate of work transfer to the fluid (Equation 5.1)

$$\dot{E}_f = \dot{X}_U + \dot{X}_M + \dot{X}_D = Du_\infty \tag{5.4}$$

where $\dot{X}_M$ is the mechanical exergy, a term used in line with Drela's [58] use that describes the pressure-work and kinetic exergy of the system. At an position behind the aircraft the exergy content is the summation of the thermal exergy term, X_U, and the mechanical exergy, X_M, giving the fluid exergy as

$$\dot{X}_f = \dot{X}_U + \dot{X}_M \tag{5.5}$$

which define the maximum work that can be extracted from the fluid by a harvesting method (e.g. formation flight). In line with previous discussions in the thesis, all entropy generation from inefficiencies are modelled in the exergy destruction term, X_D.

From the work of Bejan [18] and Arntz [14] each of the exergy terms in Equation 5.4 can be calculated as a summation of contributing components given in Figure 5.2, each of which is summarised in the below sub-sections to be used in post-processing the CFD output to allow discussion. Note that to keep consistency with the thesis notation some terminology and definitions are different to Arntz's work.

5.1.3.1 *Destroyed Exergy*

The destroyed exergy term, $\dot{X}_D$, is the sum of the volume integral of the losses due to viscous effects, a function of viscous dissipation, Φ, and the energy dissipated due to

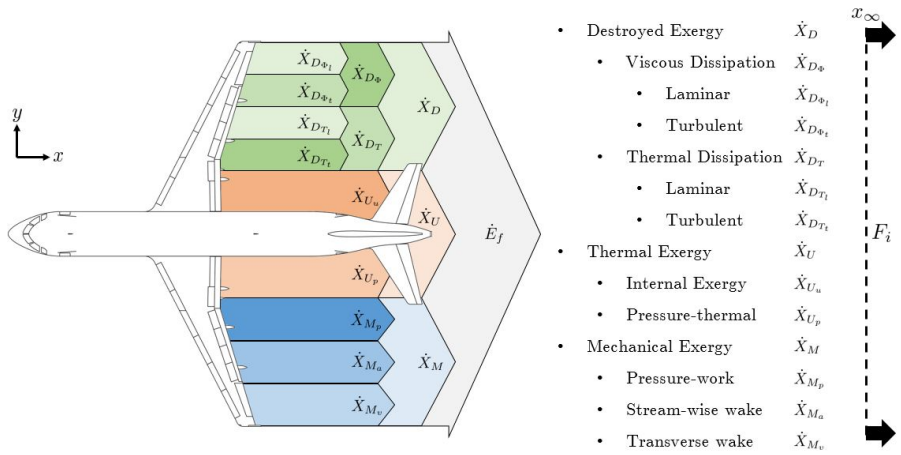

Figure 5.2: Components of exergy in the aircraft wake

thermal mixing due to temperature variations (a function of the thermal conductivity, k) giving

$$\dot{X}_D = \dot{X}_{D_\Phi}(\Phi) + \dot{X}_{D_T}(k) \tag{5.6}$$

The losses due to viscous effects, $\dot{X}_{D_\Phi}$, transforms variations in kinetic energy into thermal energy through molecular friction caused by the viscousity of the fluid. This reduces the mechanical energy in the flow by generating a homogeneous field of velocity and pressure, where the system is brought into mechanical equilibrium with the environment. From Arntz [14] this can be calculated as

$$\dot{X}_{D_\Phi} = \iiint_B \frac{T_\infty}{T} \underbrace{(\mu_l + \mu_t)\,\bar{\varepsilon}}_{\Phi} dV \tag{5.7}$$

where the subscripts l and t refer to laminar and turbulent components of the flow respectively, μ is the fluid dynamic viscosity, and $\bar{\varepsilon}$ is the dissipation function, defined as

$$\bar{\varepsilon} = \left[\left(\frac{\partial u}{\partial x}\right)^2 + \left(\frac{\partial v}{\partial y}\right)^2 + \left(\frac{\partial w}{\partial z}\right)^2 + \frac{1}{2}\left(\frac{\partial v}{\partial x} + \frac{\partial u}{\partial y}\right)^2 + \frac{1}{2}\left(\frac{\partial w}{\partial y} + \frac{\partial v}{\partial z}\right)^2 + \frac{1}{2}\left(\frac{\partial u}{\partial z} + \frac{\partial w}{\partial x}\right)^2 \right]$$

Similarly, the losses due to thermal mixing, $\dot{X}_{D_T}$, reduce the variations in temperature by generating a homogeneous field of temperature, where the system is bought into thermal equilibrium with the environment, giving

$$\dot{X}_{D_T} = \iiint_B \frac{T_\infty}{T^2} \underbrace{c_p \left(\frac{\mu_l}{Pr} + \frac{\mu_t}{Pr_t}\right)}_{k} (\nabla \mathbf{T})^2 \, dV \tag{5.8}$$

where c_p is the specific heat capacity of the fluid, Pr is the Prandtl number of the flow and the temperature gradient, $\nabla \mathbf{T}$ is defined as

$$\nabla \mathbf{T} = \left(\frac{\partial T}{\partial x}, \frac{\partial T}{\partial y}, \frac{\partial T}{\partial z}\right)$$

which describes the direction and temperature rate that changes occur around a defined location.

5.1.3.2 *Thermal Exergy*

The thermal exergy, X_U, consists of the system internal exergy, X_{U_u}, and the thermal exergy generated due to pressure, X_{U_p}. From Arntz [14] the thermal exergy term is lowered by the losses in Equation 5.6, giving the thermal exergy as

$$\dot{X}_U = \dot{X}_{U_u} + \dot{X}_{U_p} - \dot{X}_{D_T} \tag{5.9}$$

where the internal exergy is a function of the viscous dissipation, minus the entropy generation due to the viscous dissipation given in Equation 5.7.

$$\dot{X}_{U_u} = \iiint_B (1 - \frac{T_\infty}{T})\Phi_{\text{eff}} dV \tag{5.10}$$

and the thermal pressure-based exergy is a product of the variation of pressure with respect to the environment free stream and the velocity gradient

$$\dot{X}_{U_p} = \iiint_B (p_\infty - p)\nabla\dot{\mathbf{q}} dV \tag{5.11}$$

where the velocity gradient is defined as

$$\nabla\dot{\mathbf{q}} = \begin{bmatrix} \frac{\partial u}{\partial x} & \frac{\partial u}{\partial y} & \frac{\partial u}{\partial z} \\ \frac{\partial v}{\partial x} & \frac{\partial v}{\partial y} & \frac{\partial v}{\partial z} \\ \frac{\partial w}{\partial x} & \frac{\partial w}{\partial y} & \frac{\partial w}{\partial z} \end{bmatrix}$$

similarly to the temperature gradient this defines variations in velocity between locations in the fluid.

5.1.3.3 *Mechanical Exergy*

The mechanical exergy, X_M, is defined in the same terms by Arntz [14] as of Drela [58] where the energy terms are replaced with exergy terms that account for environmental state. The mechanical exergy is therefore an area integral of the boundary pressure work, X_{M_p}, and the streamwise wake (u) and transverse lift-induced (v, w) kinetic exergies of the fluid, X_{M_a} and X_{M_v} to give the formulation

$$\dot{X}_M = \dot{X}_{M_p} + \dot{X}_{M_a} + \dot{X}_{M_v} \tag{5.12}$$

where boundary pressure work

$$\dot{X}_{M_p} = \iint_f (p - p_\infty)(\dot{\mathbf{q}} - \dot{\mathbf{q}}_\infty) \cdot n \, dA \tag{5.13}$$

streamwise wake kinetic exergy is

$$\dot{X}_{M_a} = \iint_f \frac{1}{2}\rho u^2(\dot{\mathbf{q}} \cdot n) dA \tag{5.14}$$

and transverse lift-induced kinetic exergy is

$$\dot{X}_{M_v} = \iint_f \frac{1}{2}\rho(v^2 + w^2)(\dot{\mathbf{q}} \cdot n) dA \tag{5.15}$$

5.1.4 *Application of Fluid Exergy*

To illustrate the capabilities of exergy analysis for use in aerodynamic design, an example is presented using the Cranfield AX-1 configuration [10] (Appendix B.3 and Figure 5.3). A conventional long-haul aircraft, with swept cranked wings, horizontal

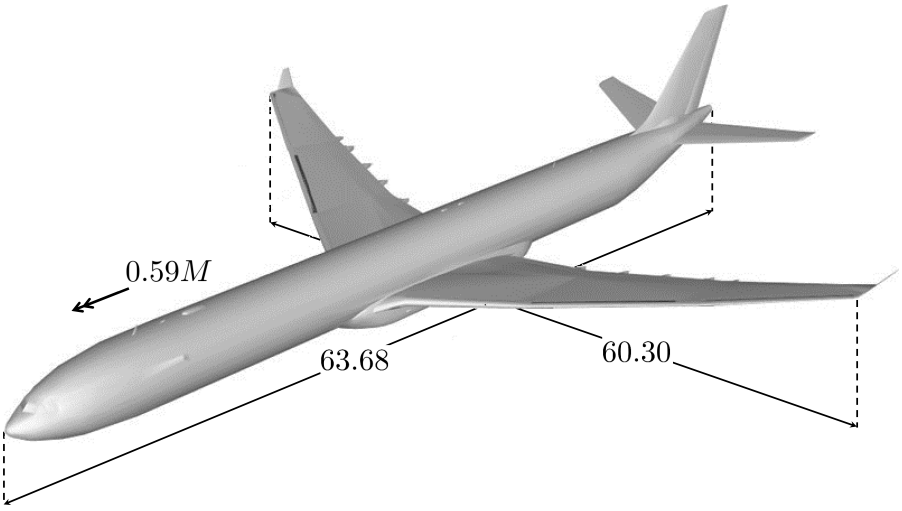

Figure 5.3: Cranfield AX-1 configuration used in CFD analysis

and vertical stabilizers. It is assumed for simplicity to have no engines or nacelles present on the wings.

The example aims to highlight how a design engineer can use near-field CFD analysis to identify regions of high entropy production that design improvement can be focused on. In addition to the discussion on the near-field analysis, far-field analysis is considered in defining the useful work available in the wake of an aircraft and how this dissipates through entropy generation.

5.1.4.1 *Analysis Set-Up*

This section provides a brief overview of the CFD analysis set-up[2], for comprehensive details see Reference [36].

This example considers the AX-1 aircraft in a trimmed condition at an altitude of $15,000ft$ ($4572m$), travelling at $0.59M$ (equivalent to a TAS of $190ms^{-1}$, a low Mach number is used as to avoid transonic behaviour such as wave drag). Only the longitudinal aerodynamics are evaluated, thus the sideslip angle equates to zero, with a fixed angle of attack 0.7° calculated to be the trim condition. This set up provides a plane of symmetry along the aircraft XZ plane (Figure 5.4), allowing the domain to be halved to reduce the computational cost with the symmetry condition. A pressure-far-field condition is applied for the inlet, the outlet and the sides of the domain (excluding the symmetry plane). The aircraft surfaces are considered as stationary walls with no slip shear condition. The aircraft is considered to be structurally rigid, such that aerodynamic loading causes no wing deflection[3].

A Reynolds Averaged Navier Stokes (RANS) finite volume solution is used with the k-epsilon (k-ϵ) turbulence model [160] implemented. The choice of turbulence model was justified from the work of McGuire [111] who undertook an exergy based CFD analysis of the NASA CRM geometry[4] which compared the use of $k-\epsilon$ realizable and the $k-\omega$ SST turbulence models. A $y_+ = 150$ was selected for the prism layers as provided suitable mesh quality. An iterative mesh refinement study pro-

2 The results presented in the example for this thesis, were calculated using the fluid state properties output from a CFD model developed in collaboration with a masters student for their thesis, see Reference [36].

3 Chapter 6 considers the same example but incorporating flexibility with a static aeroelastic analysis.

4 A Cranfield masters thesis the author supported technically, as a precursor to the work done with Cadillon [36]

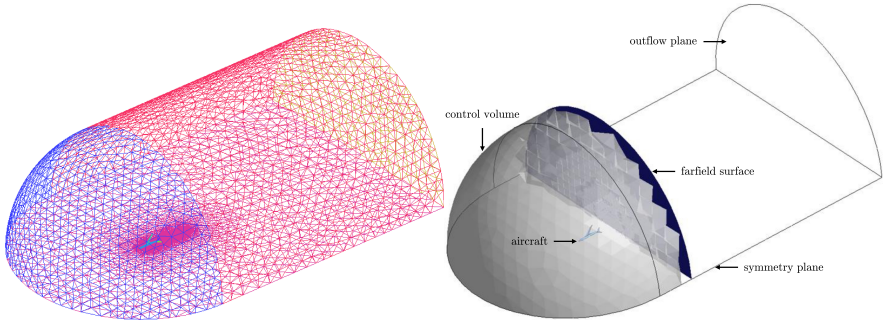

(a) Computational mesh volume

(b) CFD analysis regions

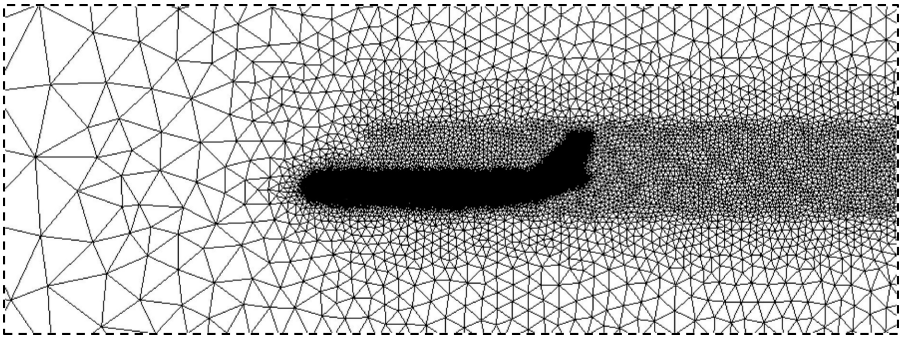

(c) Cross-section of the near-field refined mesh around aircraft

Figure 5.4: Cranfield AX-1 CFD set up

vided a compromise between accuracy and computational cost with a mesh size of 17.6 million cells, including density refinement being considered near the aircraft to increase the accuracy in the wake (Figure 5.4c). The grid convergence study was validated against C_L and C_D values. Additional information on the CFD model can be found in Cadillon [36].

For this thesis the CFD model was used as a method of producing fluid state properties of temperature, pressure and velocity, which can be exported from the CFD analysis, and by using Equations 5.4, 5.6, 5.9 and 5.12 in a post-processing script. This allows the author to undertake a comprehensive aerodynamic exergy analysis for the AX-1 aircraft at the previously defined flight condition, which is considered the contribution to knowledge of this section.

5.1.4.2 *Destroyed Exergy*

The components of the generated destroyed exergy in Equation 5.6 are plotted over the length of the aircraft in Figure 5.5. Both the viscous and thermal terms are calculated with a volume integral, where the positive increment of the destroyed exergy along the aircraft means that these phenomena are irreversible, proving that the second law of thermodynamics is not being violated. In an isosurface plot, Figure 5.8a provides a pictorial representation of the exergy destruction with viscous exergy destruction (orange) and thermal exergy destruction (blue).

As the $k-\epsilon$ turbulence model was used to generate the data, only the turbulent viscous and thermal dissipation will contribute to the destroyed exergy, as there is no laminar component. This can be seen in Figure 5.5 where the laminar components of both viscous, $X_{D_{\Phi_l}}$ and thermal, $X_{D_{T_l}}$ dissipation are negligible. The main contributor to the destroyed exergy is the turbulent viscous term, $X_{D_{\Phi_t}}$, with a small addition from the turbulent thermal exergy destruction, $X_{D_{T_t}}$. Given the low Mach

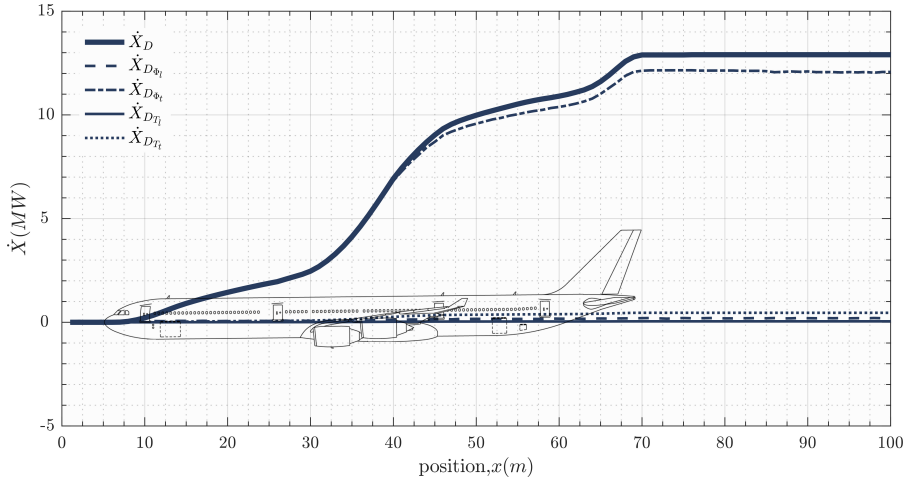

Figure 5.5: CFD destroyed exergy

velocity, the viscous components dominate, as the temperature gradients are low. If the aircraft was travelling at a transonic or supersonic velocity this component would be more significant.

The influence of the three zones (nose, wing and tail) are clearly distinguishable with high accumulations of exergy destruction. The wing is the main source of interest because, from a thermodynamic point of view, it causes the largest increase of destroyed exergy. From a technical standpoint, some design improvements can be made in this region. From an economic perspective, less destroyed exergy will reduce the amount of fuel burnt.

5.1.4.3 *Thermal Exergy*

As seen in Equation 5.9, a volume integral is used to calculate the thermal exergy in a control volume. For the purposes of thermodynamic analysis, the volume is considered a reservoir, as the small relative variation in temperature and pressure is considered to have a negligible effect given the size.

Due to the low Mach number in this analysis, the temperature variation of the effected flow compared to the free stream is minimal, as such the majority of the thermal exergy is the result of pressure-based effects, $\dot{X}_{U_p}$. A net decrease pressure (as the flow accelerates) will result in a positive thermal exergy gain, as seen in Figure 5.6 at the wing location. Conversely a net deceleration of the flow would decrease the thermal exergy, as seen post-wing in Figure 5.6.

The main pressure differential occurs around the wing where the flow accelerates around the aerofoil lowering the pressure and thus increasing the total flow exergy to circa $9MW$ (Figure 5.6), followed by the flow decelerating post-aerofoil where the flow exergy decreases to circa $5.5MW$, still at a lower pressure than freestream. This is as expected from basic aerofoil theory, where the differential between the increased air velocity ($\nabla V > 0$) on the upper and lower surfaces of the aerofoil produces an overall lower pressure. A less pronounced, yet same effect on the thermal exergy can be seen at the horizontal tailplane location.

As seen in the destroyed exergy term, due to the low Mach number the thermal differential is small, as such the thermal exergy term is dominated by the viscous dissipation term of Equation 5.10.

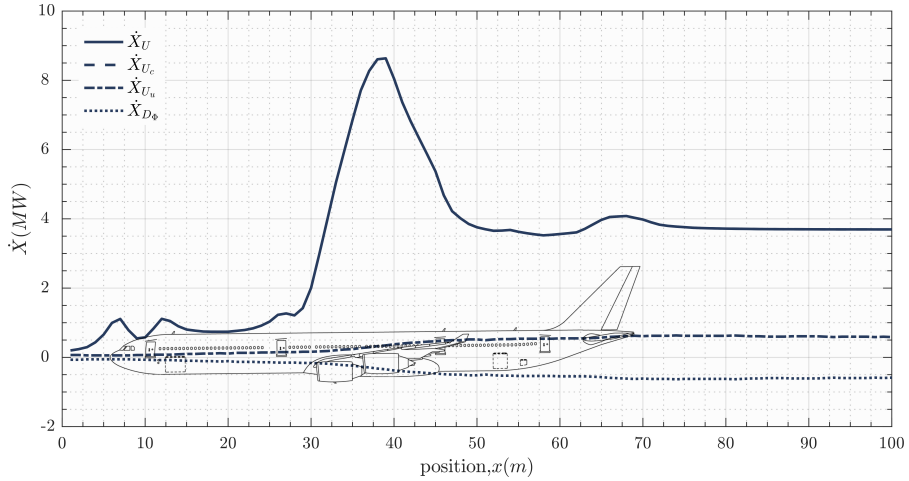

Figure 5.6: Near-Field Air Flow Thermal Exergy

5.1.4.4 *Mechanical Exergy*

In contrast to the volume integral used to calculate the thermal exergy, the mechanical exergy is evaluated with a surface integral normal to the flow direction, as defined in Equation 5.12, defining the exergy change as the velocity and pressure varies from one location to the next.

To understand the mechanical exergy, conceive a molecule in the air moving from $x = 0m$ to $x = 100m$ (Figure 5.7a), and the mechanical exergy (exergy due to pressure work and kinetic) of this molecule being plotted for the aircraft at each stage of the aircraft. Thus unlike the entropy state of the air which would always increase so as to not violate the second law, the mechanical exergy state can increase and decrease as work is transferred into and removed from the effected flow. A negative fluid mechanical exergy state means work can be extracted from the environment.

As the flow penetrates the body at the nose of the aircraft the transverse kinetic exergy, $\dot{X}_{M_v}$, term increases due to the acceleration of the flow causing the increase seen in Figure 5.7a from $x = 6m$ to about $x = 14m$. After which the accelerated air rejoins the free stream leading to the decrease in the transverse term. Due to this acceleration round the obstacle, the pressure term, $\dot{X}_{M_p}$, and a lower magnitude increase in the streamwise kinetic energy is observed. Upwind of the wing leading edge, the same trend (with a lower magnitude) is observed due to the joint, the flow moves around the joint and perturbations are introduced.

At the wing location, $x = 32m$, the mechanical exergy is dominated by the boundary pressure work, $\dot{X}_{M_p}$. This is due to the fluid accelerating around the wing, leading to a relative decrease in pressure to the environment ($p - p_\infty$ term in Equation 5.13). This is a negative exergy as work is extracted from the environment, to cause the *suction* effect in lift. As the air flows over the wing the streamwise kinetic energy, $\dot{X}_{M_u}$ increases in line with the reduction in pressure trend, as the flow acceleration decreases pressure and increasing velocity. Due to the three-dimensional wing transverse velocity is introduced to the flow on the wing increasing the transverse kinetic energy, $\dot{X}_{M_v}$. The transverse kinetic exergy rises in line with the reduction in pressure work as the pressure differentials leave the wing and curl to deposit the lift-induced generation of vortices in the wake.

In the wake of the aircraft the mechanical exergy is dominated by the transverse kinetic energy in the induced vortices. The mechanical exergy term is seen to decrease, this trend means the greater the distance behind the aircraft the less mechanical ex-

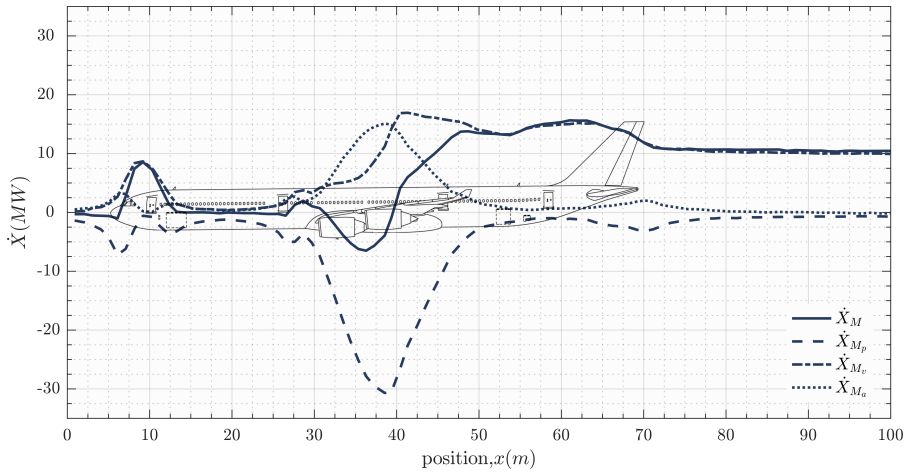

(a) Near-Field Air Flow Mechanical Exergy

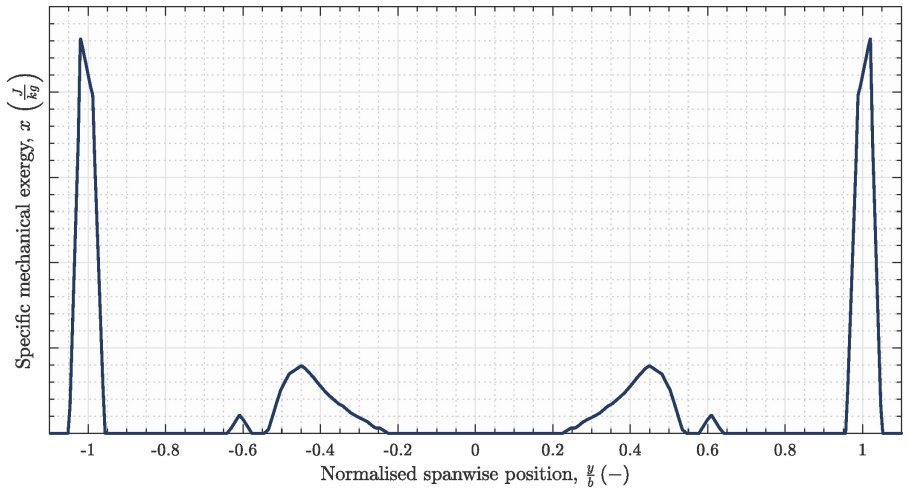

(b) Normalised Transverse Kinetic Energy in Aircraft Wake Vortices (plane located at $x = 51.6m$ from reference point, see $0m$ position in Figure 5.7a)

Figure 5.7: Mechanical Exergy for AX-1 CFD simulation

ergy can be extracted from the air as useful work. This is as expected as the rotational velocity of the vortices is dissipated into thermal energy, through entropy generation (due to viscosity), to the point of zero kinetic exergy, which is in mechanical equilibrium with the environment.

Figure 5.8b provides an isosurface plot of the available energy (exergy) terms in Equation 5.4. In orange is the thermal exergy and in green is the conservative exergy terms. The available work (exergy) in the wake can be seen in the isosurface plot for the mechanical and thermal exergy. A strong vortex is formed at the tip and a secondary vortex, more than 5 times weaker is observed inner wing between $\bar{y} = 0.1$ and $\bar{y} = 0.5$ which corresponds to the first peak in the spanwise lift coefficient variation. Figure 5.7b shows the vortex exergy content on a plane located at $x = 51.6m$ from the reference point. Note that the further the plane is behind the aircraft the lower the exergy content of the energy.

5.1.4.5 *Total Exergy*

Figure 5.8 provides the isosurface plots for the three categories of exergy given in Equation 5.4, and a graphical representation of the fluid energy is given in Figure

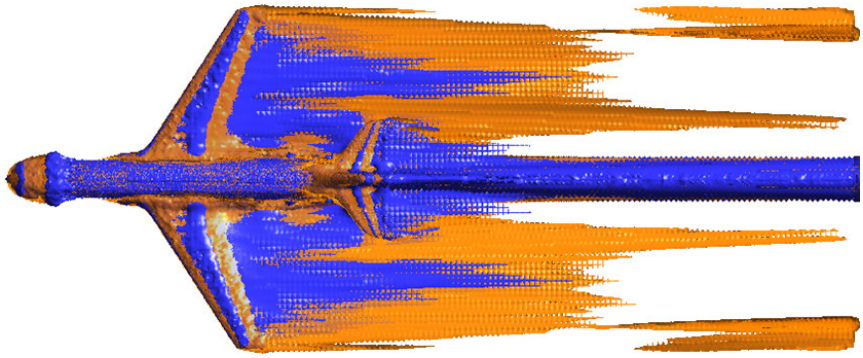

(a) Exergy Destruction, Viscous (orange), Thermal (blue)

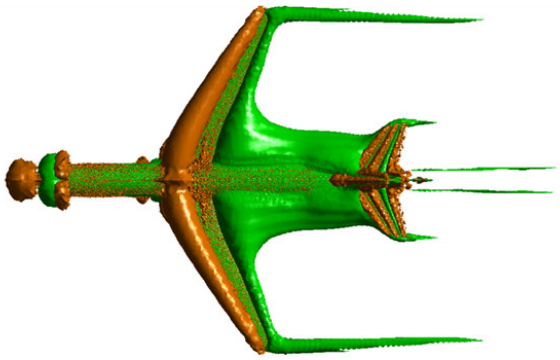

(b) Thermal Exergy (orange), Mechanical Exergy (green)

Figure 5.8: Fluid exergy isosurface plots for AX-1 CFD simulation

5.9. The fluid energy content can vary as work is transferred to and from the fluid by the aircraft system, too the system in terms of aerodynamic inefficiencies and from the fluid in terms of extracting pressure work to provide lift. Critically, to satisfy the laws of thermodynamics, the destroyed exergy term is always increasing (see Figure 5.5), thus the entropy content of the fluid is only being generated, and after energy transfers are complete (thus past the aircraft) the total exergy is constant to conform with the first law.

For an aircraft treated in isolation, all components of the fluid energy will result, at a large distance behind the aircraft, in entropy generation due to viscous dissipation of the vortices (which dominate the exergy content of the fluid post aircraft), and thus count as an inefficiency. It can be argued that an optimised aircraft will transfer no energy to the surrounding fluid, a premise that will be challenged in the proceeding section.

From the analysis it can be deduced that entropy generation is affected mainly by three zones; the nose, the wing and the tail. For aerodynamic optimisation, an engineer needs to focus on reducing the viscous dissipation, $\dot{X}_{D_\Phi}$ and the thermal mixing $\dot{X}_{D_T}$, primarily the former, because as discussed the exergy destruction is primarily due to viscous effects of low speed flight. The viscous dissipation is a function of the square of the velocity gradients so entropy generation can be avoided by reducing strong velocity changes over the aircraft surface. Similarly, the thermal mixing is a function of the square of the temperature gradients so that avoiding strong temperatures variations is important for aircraft flying at transonic and supersonic speeds. It is also important to note whether the flow is laminar or turbulent, as laminar flow can reduce velocity gradients and thus reduce the entropy generation, an improve-

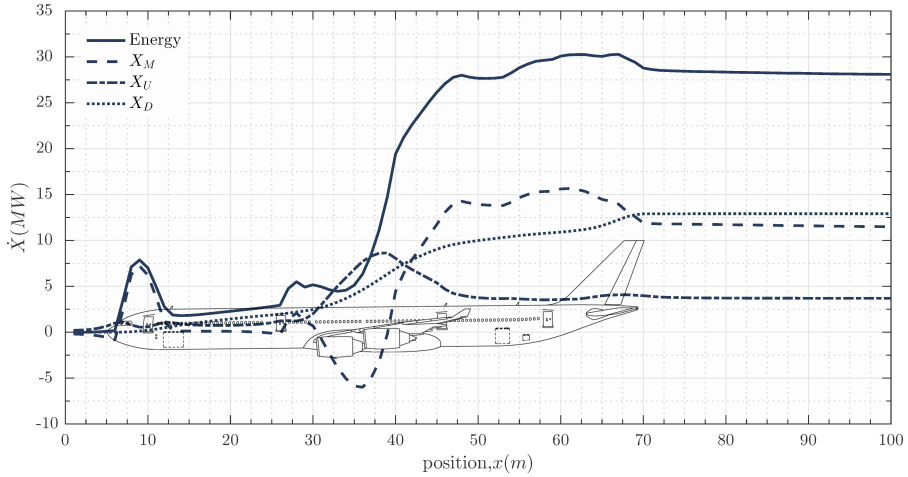

Figure 5.9: CFD total exergy

ment aircraft such as the Airbus BLADE are trying to take advantage of (see Figure 1.4b).

The major outcome from the example is to show with fluid exergy analysis, further information can be derived than the methods of Oswatitsch and Drela, in that by looking at the flow over the aircraft areas that generate entropy can be highlighted and targeted for design improvement, and also features that transfer exergy to the flow, which will result in entropy generation far field from the aircraft, can be focused for design improvement. From an energy harvesting perspective the analysis shows that the aircraft wake deposits energy at a rate of $28MW$, approximately half of this (circa $13MW$) is generated entropy, and thus not extractable as work. For a method such as formation flight that harvests transverse kinetic energy, circa $12MW$ is available energy or exergy, however this is destroyed due to viscous effects further behind the aircraft, so a useful extension to this study would be to perform far-field exergy analysis on the aircraft wake to see how the exergy content varies downstream to the point of mechanical equilibrium with the environment.

To provide confidence in the calculations of energy in the wake, a simple hand calculation can be done using Equation 5.2. The trimmed aircraft mass is given as $215,500kg$ [36], travelling at $190ms^{-1}$. The Cranfield AX-1 has a lift-drag ratio L/D of 17. Using Equation 5.2 the power lost due to aerodynamic drag is given as:

$$\dot{X}_D = Du_\infty = \left(\frac{mg}{L/D}\right) u_\infty = 23.6$$

The hand calculation gives a lower value than the CFD simulation. One of the main contributors to the discrepancy is the lift-to-drag ratio, which in practice will be lower than the optimal value as the aircraft is flying at a lower speed in the simulation than designed (optimal would be around $M0.8$). Thus the calculation shows the CFD simulation is producing results in the correct order of magnitude.

Further downstream of the aircraft, the amount of destroyed exergy increases. For an outflow plane located at an infinite distance from the aircraft, the exergy destroyed term will reach a maximum. In other words, the drag is now considered as a loss (not recoverable energy).

5.2 AERODYNAMIC PERFORMANCE METRICS

This section aims to correct two published aerodynamic performance metrics that are based on exergy, and then combine the corrected metrics to propose a new aero-

dynamic exergetic efficiency. Camberos [38] defined a unified exergy destruction coefficient as a measure for aerodynamic performance as:

$$C_X = \frac{\rho T_0 \dot{S}_{gen}}{\gamma P M^2} \tag{5.16}$$

where γ = heat capacity ratio and P = Pressure. The issue with this exergy coefficient (as discussed with Dr Camberos) is that it is not dimensionless. In the paper *The Exergy of Lift and Aircraft Exergy Flow Diagrams* Paulus [129] states that:

> The purpose of this paper is to present an expression developed for the exergy of lift, applicable not only in level flight but in other modes of flight as well. [129]

The concern with the proposed exergy use do to lift, is that in level flight there is no vertical velocity, as such the exergy use or power ($P = Fv$) must be zero. As such this section aims to re-examine Paulus's concept but develop a similar metric based on the rate of exergy to overcome induced drag.

5.2.1 *Exergy Coefficient*

Taking a similar approach to that of the lift and drag coefficients derivations, the rate of energy use or power in a fluid, $\dot{E}_f$, can be defined in terms of air density, ρ, dynamic viscosity, μ, velocity, u, and characteristic length, l, such that

$$\dot{X} = f(\rho, \mu, u, l)$$

In-line with classical aerodynamic analysis, the parameters of Reynolds number, Re, and dynamic pressure, q can be introduced as

$$Re = \frac{\rho u l}{\mu}$$
$$q = \frac{1}{2}\rho u^2$$

Then through dimensional analysis these variables can only be combined in one way, where the non-dimensional exergy coefficient, C_X, can be introduced as a function of the Reynolds number to give

$$C_E(Re) = \frac{\dot{E}_f}{uqS}$$

Equation 5.4 states that in the wake of an aircraft there is an available energy content (the exergy) and an entropy content (destroyed exergy). Thus, substituting in Equation 5.4 gives:

$$C_E(Re) = \frac{\dot{X}_U + \dot{X}_M + \dot{X}_D}{uqS}$$

Taking the far-field assumption where all the available energy or exergy in the fluid is converted to entropy, and as such the wake becomes a pure energy loss from the system, the exergy destruction coefficient can be defined as:

$$C_{X_D}(Re) = \frac{\dot{X}_D}{uqS}$$

Given the Gouy-Stodola relation in Equation 2.12, the exergy coefficient can be defined in terms of entropy generation

$$C_{X_D}(Re) = \frac{T_\infty \dot{S}_{\text{gen}}}{uqS} \equiv \frac{C_D}{u} \tag{5.17}$$

From the definition of power lost due to aerodynamic drag in Equation 5.1, it can be seen the exergy coefficient is equivalent to the drag coefficient divided by the free stream velocity. As with the drag coefficient, the exergy coefficient is a measure of the efficiency of an aircraft, as the higher the value of C_{X_D} the more energy deposited into the wake. The entropy generation term, S_{gen} will be the combined entropy generation of the viscous, lift-induced and wave drag generated by the aircraft.

This formulation of the exergy coefficient is in contrast with that published by Camberos [38], however after discussions with Dr Camberos, it is agreed the coefficient in Equation 5.17 is the corrected value.

5.2.2 *Rate of Exergy use to Overcome Induced Drag*

The rate of exergy use to overcome induced drag metric aims to determine the rate of work that needs to be put into the system to maintain level flight during cruise. From Equation 5.2 the rate of work done (power) to provide lift, $\dot{W}_L$, on a body to move through a fluid is defined as

$$\dot{W}_L = L\cancelto{0}{w} = 0$$

where L is the lift force on the body and z-component of velocity w. Given steady cruise flight, $w = 0$, which suggests no exergy input is required to maintain level flight and keep the system mass aloft. This is as expected with a zero vertical velocity. However, the generation of lift in an aircraft (which counters weight to maintain level flight) is accompanied by induced drag, and power in required to overcome the induced drag. Thus the rate of exergy input to overcome induced drag is defined as

$$\dot{X}_{D_i} = D_i u_\infty \tag{5.18}$$

In classic aerodynamics the vortex (lift-induced) drag is defined as,

$$D_i = \underbrace{\left(\frac{C_L^2}{\pi e \cancel{A}R}\right)}_{C_{D_i}} qS \tag{5.19}$$

Substituting the lift-induced drag (Equation 5.19) into the rate of exergy input (Equation 5.18) gives

$$\dot{X}_{D_i} = u_\infty \left(\frac{C_L^2}{\pi e \cancel{A}R}\right) qS \tag{5.20}$$

which can be simplified by substituting in the lift coefficient, defined in terms of dynamic pressure as [9]

$$C_L = \frac{L}{qS}$$

giving the rate of exergy input to overcome induced drag as

$$\dot{X}_{D_i} = \frac{L^2 u_\infty}{qS\pi e \cancel{A}R} \tag{5.21}$$

Thus the exergy coefficient to overcome induced drag can be defined using Equation 5.17 as

$$C_{X_{D_i}} = \frac{L^2}{q^2 S^2 \pi e \cancel{A}R} \tag{5.22}$$

Similarly to Equation 5.17, the coefficient provides insight to how efficient the aircraft is in terms of induced drag only.

5.2.3 *Aerodynamic Exergetic Efficiency*

The power required by an aircraft to maintain steady level flight in cruise is given by Equation 5.4, which can be a useful tool for identifying regions of entropy generation that can be targeted for design improvement. However, the fluid energy, E_f, provides no indication as to how close the solution is to the theoretically achievable optimal solution of minimum power required. For *loss accounting* of an entire aircraft system, the airframe generated drag, can be considered a total loss when accounted for in the aircraft efficiency, with the optimum value being zero.

However, consider the physics of ice skating, in order to move forward friction (heat transfer resulting in entropy generation) is required between the blade and ice, without which nothing would happen. The same analogy is true for an aircraft, as an aircraft has to generate lift otherwise the system potential energy decreases due to gravitational acceleration, and as a result of generating lift, lift-induced drag is generated. Thus to maintain a trimmed cruise configuration, defined as

$$\frac{dV}{dt} + \frac{dT}{dt} = 0$$

the aircraft must generate lift, which results in lift-induced drag, and thus generates entropy. It can therefore be stated that,

> *The minimum entropy generated to maintain the systems potential energy is the ideal minimum exergy input to overcome the minimum induced-drag that must be produced as a result of generating lift.*

In the same method to identifying a Carnot efficiency, the ideal aircraft system thus needs to be defined. For the purpose of this thesis, and to meet the statement above, the ideal flying machine is defined as:

> *a two dimensional frictionless lifting surface (zero volume) that provides the lift to support the aircraft mass (contained in an infinitely small volume) using a optimal circulation distribution.*

Like the Carnot efficiency for heat engines [41], what is required is an efficiency parameter that accounts for the minimum energy requirement not being zero, thus a second law efficiency, termed for this thesis the *aerodynamic exergetic efficiency*, η_X, is required. This leads to the definition of the *exergetic efficiency* as the required power to ideally overcome the induced drag resulting from generating lift to maintain position in cruise, $\dot{X}_{D_{i_{\min}}}$, divided by the actual total power input to the system aerodynamics due to additional inefficiencies, which for constant velocity is equal to the energy dissipation rate in the aircraft wake, $\dot{X}_D$. From this, the second law efficiency, can be defined as

$$\eta_X = \frac{\text{desired output}}{\text{required input}} = \frac{X_{D_i} \text{to overcome minimum induced-drag}}{\text{total exergy destruction}} = \frac{C_{X_{D_{i_{\min}}}}}{C_{X_D}} \tag{5.23}$$

Thus, to determine the exergetic efficiency, first the total exergy coefficient, C_{X_D}, and minimum exergy coefficient, $C_{X_{D_{i_{\min}}}}$ must be determined. $C_{X_{D_i}}$ is minimised with the optimal lift distribution for a constrained span, as defined by Prandtl [136] to be an ellipse. The Oswald efficiency factor define by Raymer [143] as

$$e = 4.61\left(1 - 0.045\mathcal{R}^{0.68}\right)\left[\cos\left(\Lambda_{LE}\right)\right]^{0.15} - 3.1$$

defines how close a specific lift distribution is to this optimal case. What this informs is that, even with the implementation of winglets and higher aspect ratio wings to minimise lift-induced drag, it can never be completely eliminated. Therefore, to minimise lift-induced drag, the vortex drag can be viewed as the entropy generation

Table 5.1: Data for analysis for a selection of Airbus commercial aircraft

Aircraft	Cap.	Year	h[1] (m)	M[1] $(-)$	S[1] (m^2)	Æ[1] $(-)$	OWE[1] (kg)	MTOW[1] (kg)	$\frac{L}{D}$ $(-)$
A300-600	345	1972	10,668	0.78	260.0	7.7	88,626	171,700	15.2[2]
A310-300	275	1982	12,530	0.80	219.0	8.8	79,207	164,000	15.3[2]
A320-200	150	1987	11,280	0.78	122.4	9.5	42,100	73,500	16.3[2]
A330-300	375	1992	12,500	0.82	361.6	10.1	124,500	235,000	18.1[2]
A340-300	375	1991	12,500	0.82	363.6	10.1	129,800	276,500	19.1[2]
A350-900	325	2013	12,630	0.85	443.0	9.5	134,700	268,000	21.0[3]
A380-800	544	2005	10,670	0.82	845.0	7.5	270,010	559,995	17.4[3]

[1] IHS Jane's all the world's aircraft : Development and Production [85]

[2] Historical Perspective of Air Transport Productivity and Efficiency [108]

[3] New Models of Innovation for Economic Growth and Sustainability [66]

[4] Airbus A380 Design Scope [139]

required to overcome the minimum induced drag and thus cannot equal zero, whilst the parasitic and wave drag can theoretically be reduced to zero. This is due to the viscosity of air and non-zero surface area of the aircraft. Friction will reduce the kinetic energy of the aircraft, thus energy must also be put in to maintain the kinetic energy of the system. Thus,

$$C_{X_{D_{i_{\min}}}} = \frac{L^2}{q^2 S^2 \pi Æ} \tag{5.24}$$

Then substituting in Equation 5.24 and 5.17 into Equation 5.23 results in

$$\eta_X = \frac{L^2 u}{qS\pi Æ \dot{X}_D} \equiv \frac{C_{D_{i_{e=1}}}}{C_D} \tag{5.25}$$

5.2.3.1 *Applying the Aerodynamic Exergetic Efficiency*

In this section exergy coefficients (Equation 5.17), exergy coefficient for minimum drag (Equation 5.22) and exergetic efficiencies (Equation 5.25) are calculated for various in-service and historical Airbus aircraft. The aircraft parameters used in the analysis are given in Table 5.1 with a graphical representation of the wing planforms in Figure 5.10.

Note this is not official Airbus data, as such the derived values may not be truly representative of the actual aircraft, but will be sufficient to allow discussion on the validity of the exergy performance metrics. Also note that the metrics are calculated with assumed mid mass between OWE and MTOW, and only viscous and induced drag are calculated. Not calculating wave drag will cause unusual discrepancies as it has a high impact on the aircraft's total drag, and modern aircraft typically generate lower wave drag than older models, however in line with the thesis parameters wave drag is not considered.

The exergetic efficiencies $(C_{X_D}, C_{X_{D_{i_{\min}}}}, \eta_X)$ are heavily influenced by the mass of the aircraft used, and to make the values comparable between aircraft's an equivalent mass case for each must be used. For the values given in Table 5.2 the mass is calculated as the aircraft OWE with an additional payload mass, which is a function of the passenger capacity.

The exergetic efficiency value for the various aircraft are given in Table 5.2. The *exergy coefficient*, C_{X_D} term is comparable to the drag coefficient of the aircraft, and as such a similar trend can be seen, where the more modern aircraft typically have a lower C_{X_D} value. The *exergy coefficient for minimum drag*, $C_{X_{D_{i_{\min}}}}$, reflects the rate of

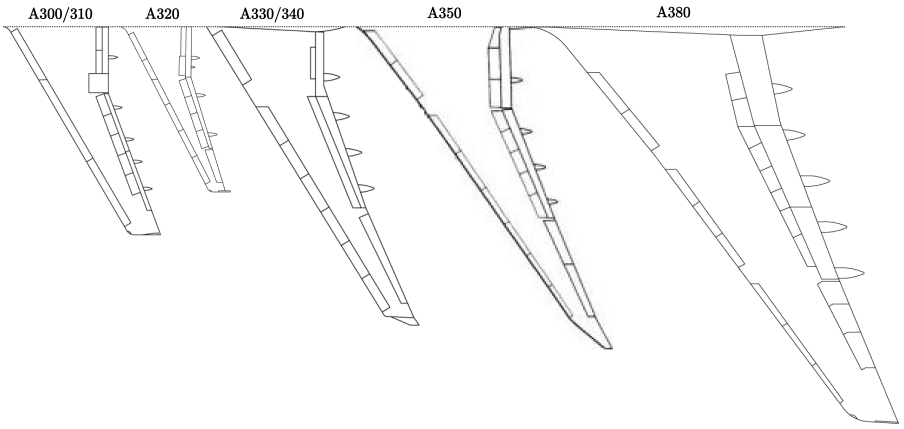

Figure 5.10: Evolution of Airbus wing planforms

Table 5.2: Aircraft exergetic efficiencies

Aircraft	$\mathbf{C_{X_D}}$	$\mathbf{C_{X_{D_{i_{min}}}}}$	η_X
A300-600	0.0428	0.0175	40.8%
A310-300	0.0544	0.0250	46.1%
A320-200	0.0424	0.0160	37.8%
A330-300	0.0389	0.0156	40.2%
A340-300	0.0376	0.0162	43.2%
A350-900	0.0257	0.0098	38.0%
A380-800	0.0241	0.0075	31.0%

exergy input required overcome induced drag generated from lift, as such with the implementation of composite technology and improved wing planform and aerofoil geometry it is also expected and shown that the more modern aircraft have lower exergy requirements than older generation aircraft. The trend in C_{X_D} and $C_{X_{D_{i_{min}}}}$ is unsurprising as typically with each generation of aircraft comes an efficiency improvement, which in this case is shown with the aerodynamic efficiency.

Consider the formulation of the *exergetic efficiency* in Equation 5.23, it is the ratio of the minimum exergy requirement for lift over the total exergy lost due to the aerodynamics. In terms of the force balance approach, the efficiency is comparable to the minimum lift-induced drag to maintain lift over the total drag. So consider, the A350-900 has a lower exergy coefficient and exergy coefficient for minimum drag than the A300-600, however the A350-900 is less exergetically efficient than the A300-600. As the composite structure of the A350-900 has allowed for a comparatively lower OWE, it results in a lower exergy requirement to maintain potential energy, however the same rate of exergy reduction is not seen with the total exergy coefficient, as whilst the minimum lift-induced drag is decreased substantially due to the lower lift requirement, the parasitic drag will be similar to that of the A300-600, as even with improvements in surface finish, the presence of a boundary layer on a tube with swept back wings still generates a significant parasitic drag. So the rate of improvement in $C_{X_{D_{i_{min}}}}$ is faster than C_{X_D}. However, as stated previously, modelling the wave drag would have a significant impact on these results, as the A350 generates lower wave drag than the A300.

The exergetic efficiency, η_X is showing how close the aircraft aerodynamic design is to the theoretically optimal aerodynamic design for that specific mass case and wing characteristics.

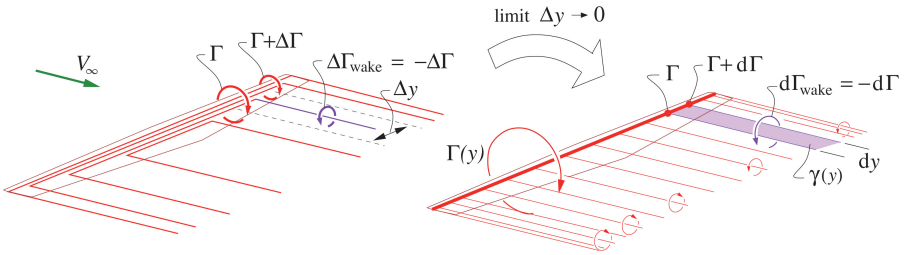

Figure 5.11: Graphical Representation of Prandtl Lifting Line Theory [57]

5.3 OPTIMAL LIFT DISTRIBUTION

Since the development of modern aeronautics, Prandtl's [136] lifting line theorem [91] (Figure 5.11) has shown that for a constrained span aircraft the optimal lift distribution to produce minimum induced drag is an ellipse

$$\Gamma = \Gamma_0 \left[1 - \left(\frac{y}{s}\right)^2\right]^{\frac{1}{2}} \tag{5.26}$$

where Γ_0 as the circulation at the wing root where the circulation Γ can be calculated at any point y along the wingspan s. This derivation defines the span efficiency factor, e, as equal to unity, with all real lift distributions being less. This premise was challenged by Yates [182], Jones [88], Lissaman [103] and Cone [48] through investigations into lift-induced drag reduction devices. Greene[75] collated this work, and derived the spanwise lift distribution that produced the minimum lift-induced drag using an entropy based method.

Critically, previously defined exergy performance metrics, $\dot{E}_f$, η_X and C_X are all a function of the *optimal* lift distribution. Given the similitude between drag and entropy it is evident an exergy based approach could be taken to optimise lift distributions, a thought shared by Monsch [115] who commented

> *"The prediction of entropy generation can be used to estimate the viscous drag of a wing with good fidelity and that entropy generation can be used to correct for the artificial viscosity found in numerical methods to allow for good prediction of induced drag"*
>
> - Scott Monsch [115]

Notable work in the area of exergy based wing optimisation include that of Nixon [120–122], Monsch [114] and Li [100, 101]. Li and Monsch use exergy analysis applied to subsonic wing planform shapes, in an effort to study the impact of exergy utilisation on aircraft. The primary aim was to optimise wing lift distributions for different phases of aircraft flight. Traditional derivations for optimal lift distributions for conventional wing optimisation has been done by Prandtl [137] and Raymer [143], methods which are being extended today to provide more robust or *agile* tools. Alternative minimum induced drag lift distributions were studied by Camberos [169] and Figliola [67] as a part of the US Air Force Research Laboratories aerodynamic assessment into a unified methodology for aerospace systems integration based on entropy and the second law of thermodynamics, using so called *exergy* analysis.

Greene [75] applied Oswatitsch's identity (Equation 5.2) of entropy flow to identify the lift distribution which provides the minimum lift-induced entropy generation. His use of this method has been disputed and thus put the result into question [67] [151]. This section aims to generate novel insights into the comparisons of Greene's entropy based work to that of Prandtl, and provide additional insight through an initial derivation that is an expansion of the work of Greene [75] and Camberos [169], to show Greene's conclusion of a parabolic optimal lift distribution is credible.

The optimal distributions presented are for the minimisation of induced drag only, wave drag has not been considered, as the High Aspect Ratio Wing (HARW) that is developed as a result of this analysis flies at $M0.6$, where wave drag will have minimal impact.

5.3.1 *Constant Lift and Span*

Based on the understanding of Prandtl's lifting line theory derivaton for optimal lift distirbutions and the Kutta–Joukowski theorem

$$L = \rho u_\infty \int_{-s}^{s} \Gamma(y) dy$$

the induced drag force can be defined as an integral over the span, $2s$, of the induced drag function, F_i

$$D_i = \int_{-s}^{s} F_i \left(\Gamma, \frac{d\Gamma}{dy}, y \right) dy$$

The lifting line derivation uses the axes and terminology of Figure 5.11, making the following assumptions

- the *lifting line* is located in an infinitely thin control volume (a plane), normal to the free stream velocity
- the induced velocities are small enough such that the local velocity at the lifting line is equal to the freestream velocity, u_∞
- the flow is steady, incompressible and not subject to temperature gradients (thus constant temperature)
- all entropy is produced by the induced drag at the lifting line

Yates [182] assuming an incompressible flow, derived the entropy flux through the Trefftz plane (*Oswatitsch identity*, Equation 5.2) to the rate of entropy production in the control volume

$$\iint_S u_\infty T \left(s - s_\infty \right) dA = \mu \iiint_V |\vec{\omega}|^2 dV \geq 0 \tag{5.27}$$

where $\vec{\omega}$ is the vorticity vector, defined as

$$\vec{\omega} = \nabla \mathbf{v}$$

From Yates' definition linking entropy production and drag, Greene [75] derives the lift induced drag force, D_i as

$$D_i = \frac{\mu K_1}{u_\infty} \int_{-s}^{s} \left(\frac{d\Gamma}{dy} \right)^2 dy \tag{5.28}$$

Thus, the lift induced drag is proportional to the square of the circulation gradient over the span.

The optimal lift distribution can then be determined using the Euler-Lagrange method, based on a series of defined constraints, which are taken here to be the same Prandtl used in the original derivation. Taking $\Gamma_{P1}(y)$ as the circulation function of the Prandtl derivation and $\Gamma_{G1}(y)$ as this parameter from Greene, the constant lift constraint is defined as

$$\rho u_\infty \int_{-s}^{s} \Gamma_{P1}(y) dy = \rho u_\infty \int_{-s}^{s} \Gamma_{G1}(y) dy \tag{5.29}$$

Table 5.3: Aerodynamic Parameters for variable Lift Distributions

Distribution	Equation	$\bar{L}$	$\bar{s}$	$\bar{M}$	$\bar{X}_D$
Elliptical	$\Gamma = \Gamma_0 \left[1 - \left(\frac{y}{s}\right)^2\right]^{\frac{1}{2}}$	1.00	1.00	1.00	1.00*
Parabolic	$\Gamma = \Gamma_0 \left[1 - \left(\frac{y}{s}\right)^2\right]^{\frac{2}{2}}$	1.00	1.00	0.88	0.91
Horten-Bell	$\Gamma = \Gamma_0 \left[1 - \left(\frac{y}{s}\right)^2\right]^{\frac{3}{2}}$	1.00	1.25	1.00	0.54
Greene (M_E)	$\Gamma = \Gamma_0 \left[1 - \left(\frac{y}{s}\right)^2 - f(M_E)\right]^{\frac{2}{2}}$	1.00	1.23	1.00	0.54
Greene (M_P)	$\Gamma = \Gamma_0 \left[1 - \left(\frac{y}{s}\right)^2 - f(M_P)\right]^{\frac{2}{2}}$	1.00	2.01	0.88	0.54

*exergy destruction is ∞, thus values normalised for 99.5% $\bar{X}_D$

Using the same indices the constant span constraint is defined as

$$2s_{P1} = 2s_{G1}$$

Then applying the following boundary conditions

$$\frac{d\Gamma}{dy} = 0 \quad \text{at} \quad y = 0 \qquad \Gamma = \Gamma_0 \quad \text{at} \quad y = 0 \qquad \Gamma = 0 \quad \text{at} \quad y = s_0$$

Solving Equation 5.28 results in a parabolic distribution rather than Prandtl's classical elliptic form, defined as

$$\Gamma = \bar{\Gamma}_0 \left[1 - \left(\frac{y}{s}\right)^2\right]^{\frac{2}{2}}$$

where $\bar{\Gamma}_0$ defines the root circulation for the parabolic distribution.

From Figure 5.12a it can be noted that the parabolic distribution has an increased circulation (thus lift) at the wing root. Figure 5.12b plots the derivative of the circulation in terms of exergy destruction. The square of the entropy variation with span is shown by Equation 5.28 which is proportional to the lift induced drag. The entropy gradients show that the parabolic distribution has higher gradients along the majority of the wingspan, but significant reductions at the wing tip when compared to the elliptic. The reason for this is the elliptic distribution has an infinite gradient at the tip, which corresponds to an infinite generation of entropy.

Whilst entropy must always be positive, it must also be finite, so with the entropy derivation it shows an elliptic distribution is not a feasible concept because it is physically impossible to create, a key application of the second law of thermodynamics. This means Greene's theory is not stating Prandtl is incorrect with the elliptic distribution, as theoretically it may be optimal, however as it is not feasible, an entropy based method discounts the solution, and results in a distribution with a finite gradient at the tip: the parabola.

A cumulative plot of the exergy destroyed is given in Figure 5.12c to show how the elliptic and parabolic distributions compare. Finally, it should be noted that the parabolic distribution provides a 12% reduction in wing root bending moment when compared to the elliptic, which could lead to a lighter more efficient wing structure.

5.3.2 *Constant Lift and Wing Root Bending Moment*

An overlooked addition to Prandtl's lifting line theory was highlighted by Bowers [28]. When the span constraint is removed, and replaced with a constraint that the revised lift distribution is to provide an equal wing root bending moment, Prandtl

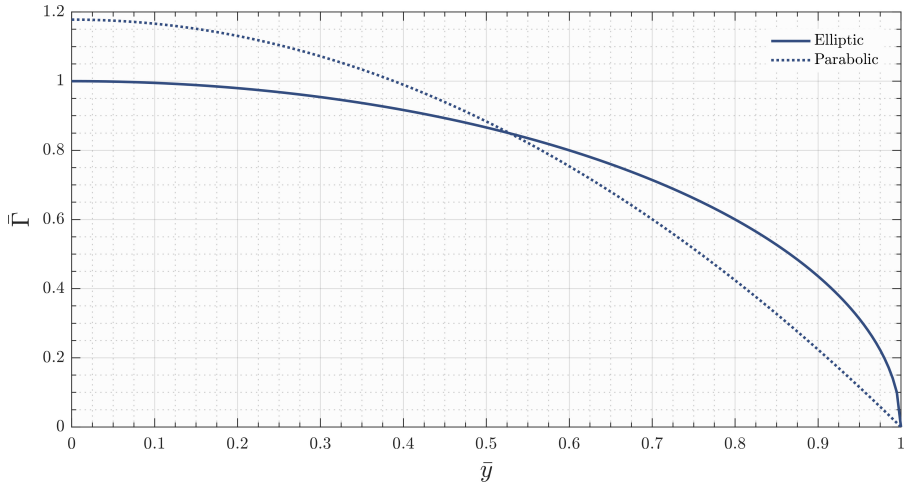

(a) Optimal Lift for a given Lift and Span

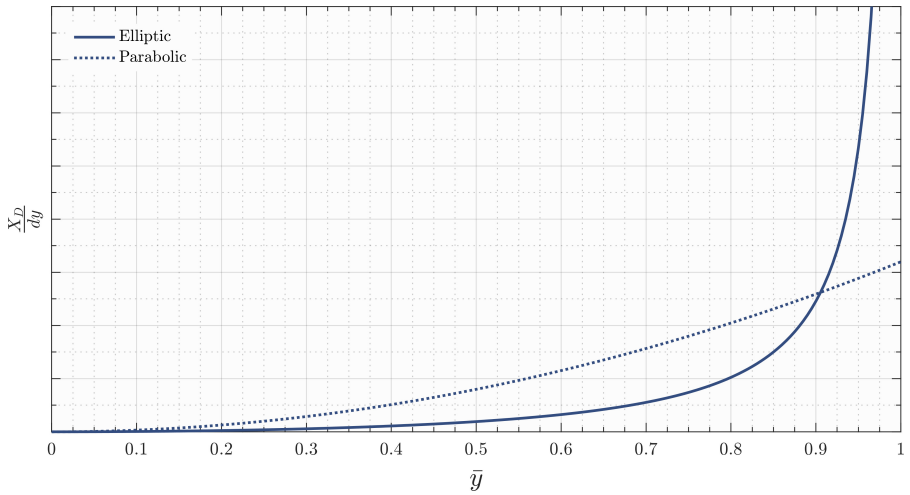

(b) Specific Destroyed Exergy along Wingspan

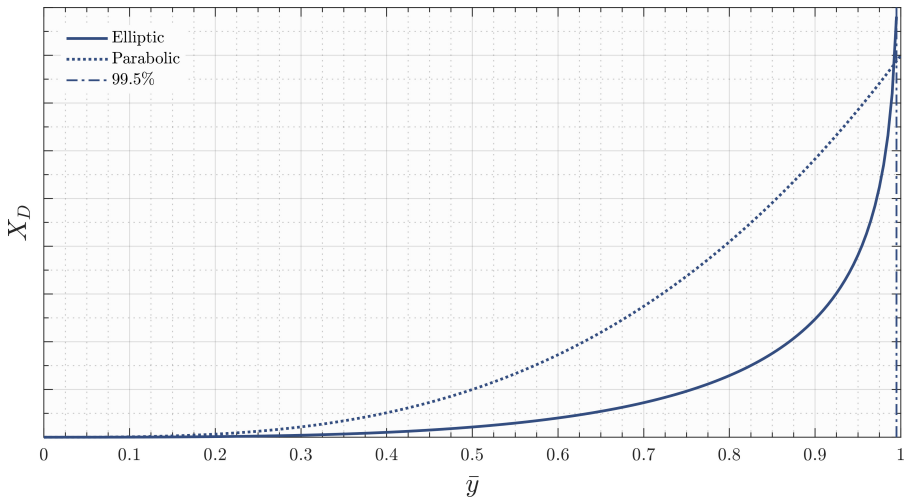

(c) Cumulative Destroyed Exergy along Wingspan

Figure 5.12: Comparison of Prandtl's elliptic lift distribution and Greene's parabola

found the optimal lift distribution was a bell shape, which for this thesis is designated the Horten-Bell, after the designation from Horten,

$$\Gamma = \Gamma_0 \left[1 - \left(\frac{y}{\bar{s}}\right)^2\right]^{\frac{3}{2}} \tag{5.30}$$

Working with Greene's derivation for the same lift constraint but allowing the span to vary for a constant wing roote bending moment to that of the span constrained ellipse

$$\int_{-s}^{s} L_{P1}(y)dy = \int_{-s}^{s} L_{P2}(y)dy = \int_{-s}^{s} L_{G2}(y)dy$$

$$\int_{-s}^{s} L_{G1}(y)dy = \int_{-s}^{s} L_{G3}(y)dy$$

where $L_{P2}(y)$ and $L_{G2}(y)$ are optimal lift distributions for an unconstrained span using Prandtl's and Greene's methods respectively. Using Greene's method the optimal distribution is given as a *modified parabola*, defined as

$$\Gamma = \Gamma_0 \left[1 - \left(\frac{y}{\bar{s}}\right)^2 - K_1 \left\{\left(\frac{y}{s}\right)^2 - \left(\frac{y}{s}\right)^3\right\}\right] \tag{5.31}$$

where

$$\Gamma_0 = \frac{L}{\rho u_\infty s_0}\left[\frac{8\left(\frac{s}{s_0}\right) - 5}{2\left(\frac{s}{s_0}\right)^2}\right] \qquad \text{and} \qquad K_1 = \frac{40\left(\frac{s}{s_0} - 1\right)}{8\left(\frac{s}{s_0}\right) - 5}$$

Here s_0 is the reference span, defined as the span when using Greene's span constrained parabola provides the same wing root bending moment. For clarity, in Figure 5.13a two modified parabolas are plotted, Greene (M_E) where the reference span provides the equivalent bending moment to the elliptical distribution, and Greene (M_P) which matches the reduced bending moment of the original parabolic distribution.

The results of the three distributions are shown in Figure 5.13a which all provide the same reduction in total exergy destruction with a variable span. The Horten-Bell and Greene (M_E) match remarkably well given the different formulations. The Greene modified parabolas as shown in Figure 5.13b can calculate exergy destructions for variable spans, with the trend showing that as span increases the exergy lost due to induced drag decreases. However whilst this suggests higher aspect ratio wing aircraft will prove to be more aerodynamically efficient, it doesn't account for the effect of the additional span, including additional mass and aeroelastic complexities.

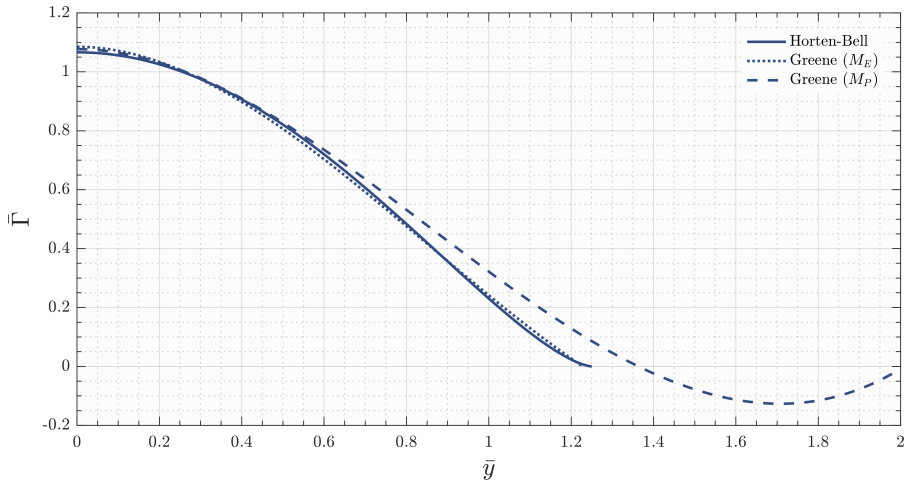

(a) Optimal Lift for a given Lift and Root Bending Moment

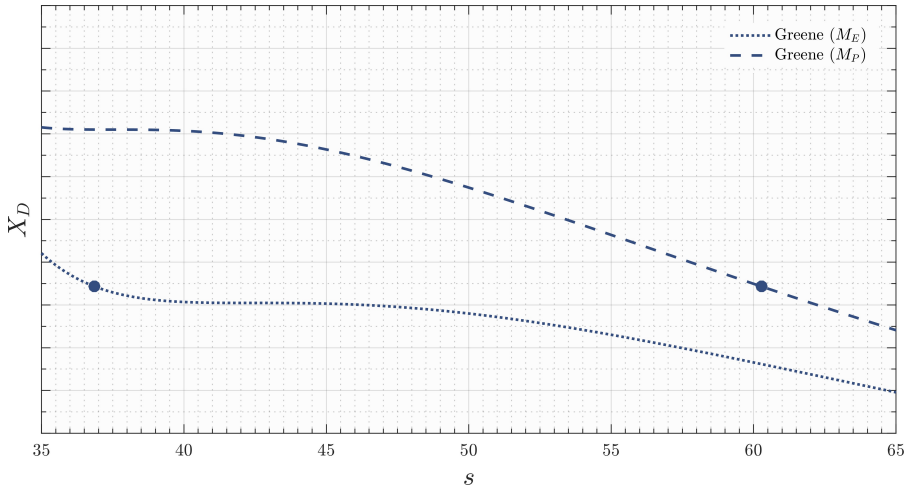

(b) Total Destroyed Exergy for variable Span. Highlighted points represent the span and exergy destruction of the M_E and M_P distributions in Figure 5.13a

Figure 5.13: Comparison of Prandtl's elliptic lift distribution and Greene's parabola unconstrained

5.4 CHAPTER SUMMARY

This chapter considers three aspects of exergy analysis of rigid body flight dynamics, and provides the following new insights:

- The Oswatitsch and Drela formulations for thermodynamic analysis of aircraft wake have been reformulated from an exergy perspective so as to allow the design engineer to model the fluid flow over the aircraft in the near-field. This highlights areas of entropy generation and exergy transfer that can be targeted for design improvement to improve the aerodynamic efficiency. The exergy content of the wake has also been discussed, to show energy harvesting methods such as formation flight, not all the energy is available, thus the exergy content is defined which can be extracted as useful work.
- Exergy analysis has also allowed the definition of three thermodynamics based performance metrics, the exergy coefficient, fluid exergy content and exergetic efficiency.
- Finally using an expansion of Greene's entropy derivation for optimal lift distributions, is shown from an entropy generation perspective, the optimal lift distribution is a function of the circulation gradient squared. This results in a parabolic distribution for a constrained span and a modified parabola for an unconstrained span. The latter is compared to the unconstrained optimal lift distribution of Prandtl, and show two competing methods, provide similar results.

The next chapter aims to couple these concepts with that of Chapter 4, to assess how exergy analysis can be used for fluid-structure interaction modelling through static and dynamic aeroelastic effects.

6

EXERGY ANALYSIS OF AEROELASTIC SYSTEMS

Airframe flexibility effects have always been of concern to aircraft designers. As a consequence, manufacturers have developed extensive loads and aeroelastic analysis processes to minimise airframe weight, and allow the implementation of technologies to achieve environmental targets and satisfy safety requirements set by the regulatory authorities. For the design of traditional aircraft, aeroelastic analysis processes are usually decoupled from the analysis and assessment of rigid body flight dynamics, such as the discussion in Chapter 5. This has been justified by the relatively low span and high stiffness of the traditional airframe. With the advent of modern large transport and high altitude long endurance (HALE) aircraft, where extensive use of advanced materials has led to flexible airframes, the interaction between rigid body flight dynamics and structure dynamics has become a significant design driver, given the overlap of these dynamic phenomena in the frequency domain. This can be seen in the Airbus Concept Plane (Figure 6.1) where during flight the wings and tail are designed to be highly flexible when compared to conventional aircraft.

The wings of current generation aircraft will deform under aerodynamic loading, just to a lesser extent than for future configurations. Current generation aircraft, which see comparatively small deflections, account for this with wing pre-twist, which deforms under cruise loading to provide the desired lift distribution. Thus the aircraft can be considered inelastic (rigid) in the deflected cruise trimmed state for aerodynamic design, in the so called *flight* or *jig shape*. However with a flexible wing under small variations in load such as climb, descent, manoeuvre or environmental loading, the aircraft will see a significant change in the deflection shape, impacting the load distribution and thus aerodynamic efficiency.

This chapter aims to assess the effects of static aeroelastics on the exergy use of the aircraft aerodynamics and the resultant efficiency, by increasing the complexity by analysing a fully dynamic aeroelastic system. Structural dynamics can be modelled using exergy analysis with a defined input load from the aerodynamics, in the designated BeaRDS^{TM} (Beam Reduction and Dynamic Scaling Theoretical Model) fluid-structure interaction framework. The structural component of this model is then validated against static loading and Ground Vibration Tests (GVT) undertaken as apart of the BeaRDS (Beam Reduction and Dynamic Scaling) programme [134].

Figure 6.1: Airbus concept plane in flight showing wing flexibility

6.1 EXERGY ANALYSIS OF STATIC AEROELASTICITY

In an effort to produce lightweight wings, flexibility effects are becoming significant design drivers, and the assumption of a rigid aircraft for aerodynamic design is no longer valid. This section investigates how the flexibility of an aircraft effects the aerodynamic efficiency of the wing, and also how this deflection influences the recoverable energy in the wake of the aircraft for applications such as formation flight.

Consider Collars aeroelastic triangle (Figure 4.1, page 47), the *static aeroelasticity* node can be partitioned into different aeroelastic phenomena, the most common of which are given by the effect on:

- load distribution
- control effectiveness
- divergence
- control system reversal
- static stability

These phenomena are factored into the flight dynamic analysis of an aircraft. However with highly flexible aircraft the effect on load distribution can have an impact on the aerodynamic performance, and are thus suitable for inclusion in the exergy analysis of an aircraft.

The complexity raised by wing flexibility is shown by the two test case aircraft that will be used for this analysis. The baseline configuration is the *inelastic* AX-1 aircraft used in Chapter 5. Here in the aircraft YZ plane (see Figure 6.2a) the aerodynamic force can be equated to the lift, and the wing is twisted as such to give the *optimal* elliptical lift distribution. For comparison the same aircraft configuration is used but in this case the structural stiffness is accounted for in the *flexible* AX-1 aircraft. For this configuration when the wing flexes under aerodynamic loading, as in Figure 6.2b, the aerodynamic force creates two components, the vertical lift and a side force. Whilst a simplistic approach would assume this doesn't affect the aircraft flight dynamics as this side force is countered by an equal and opposite force from the other wing, it does mean theoretically the aircraft will be less aerodynamically efficient as a larger aerodynamic force is needed to create the same lift. In addition to this, the effective wing aspect ratio will reduce due to the span shortening, which will adversely affect the efficiency. Thus this section aims to validate the proposition that;

> *Considering only the aircraft aerodynamic performance; as the structure deforms from the inelastic jig shape the aerodynamic efficiency will reduce in reference to the baseline configuration*

This premise is also valid where an aircraft is designed with wing pre-twist. In the trimmed condition the designed lift distribution is achieved, and in this case the proposition is that the aerodynamic efficiency decreases at any deformation away form this trim condition.

To evaluate the aerodynamic efficiency of flexible aircraft and argue the validity of the above proposition, two analyses with different aircraft and flight conditions are presented below:

- a constant angle of attack analysis, where the inelastic and flexible aircraft are fixed in pitch, and the aerodynamic loads are modelled with a varying free stream velocity.

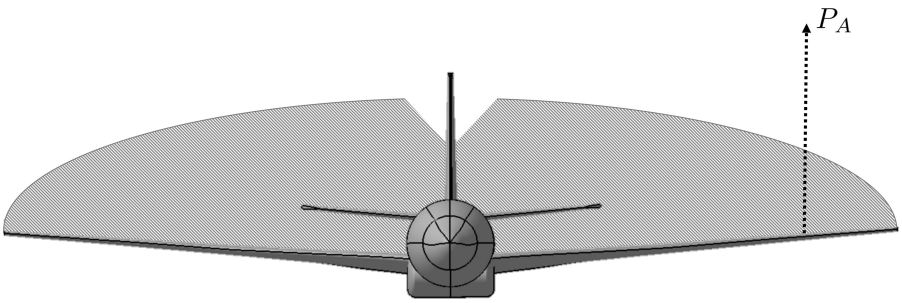

(a) Inelastic AX-1 Aircraft

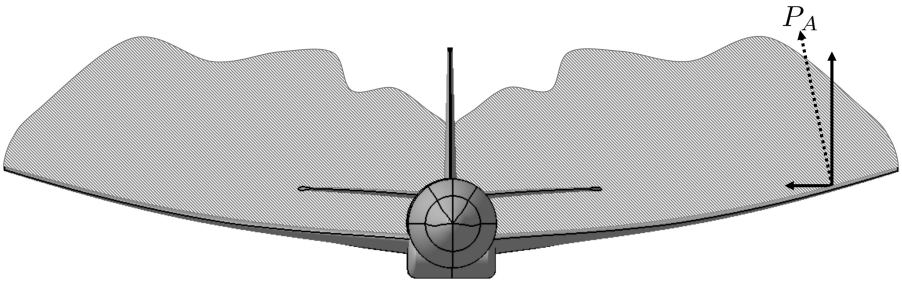

(b) Flexible AX-1 Aircraft

Figure 6.2: Aerodynamic lift distributions of test case aircraft configurations

- a constant lift analysis, where the inelastic and flexible aircraft are trimmed for each flight condition which varies the velocity at a constant altitude.

For both analyses the Cranfield Accelerated Aircraft Loads Model (CA^2LM) [59] framework is used to calculate aerodynamic loads and structural deflections for the flexible case.

6.1.1 *Cranfield Accelerated Aircraft Loads Model (CA^2LM)*

To calculate the structural deflection under a given aerodynamic load, along with the aerodynamic lift and drag parameters for a given flight condition this analysis utilises the CA^2LM framework; a real-time, aero-servo-elastic, six DoF aircraft flight simulation framework, developed by Andrews [10] (Figure 6.3).

CA^2LM is based on the coupling of both a structural and an aerodynamic solver in the time domain. As a Matlab/Simulink framework, it is a versatile research tool which can be used for a range of purposes ranging from aircraft flight dynamic analysis, critical loads investigation or the development of realistic pilot models. An input in the time domain, representing the control surfaces deflection (aileron, elevator, rudder, throttle), allows the aerodynamic forces and moments to be calculated. This allows the framework to trim the aircraft at defined flight conditions, accounting for the structural deflection impact on the aerodynamic forces.

CA^2LM uses the same aircraft structural representation as the BEAR model presented in Chapter 4, where the aircraft is discretised into a low fidelity Finite Element Model (FEM) of single point mass nodes connected with one-dimensional beam elements representing structural stiffness. In contrast to the BEAR input, for this analysis the Cranfield AX-1 configuration (Figure 4.11a) has an additional low fidelity aerodynamic model (Figure 6.4a) used to reduce the aerodynamic profile of the aircraft (supercritical airfoil NASA S(2) 0610, Figure 6.4b) to a single node or station, such that loads can be generated that are applied to the structural nodes.

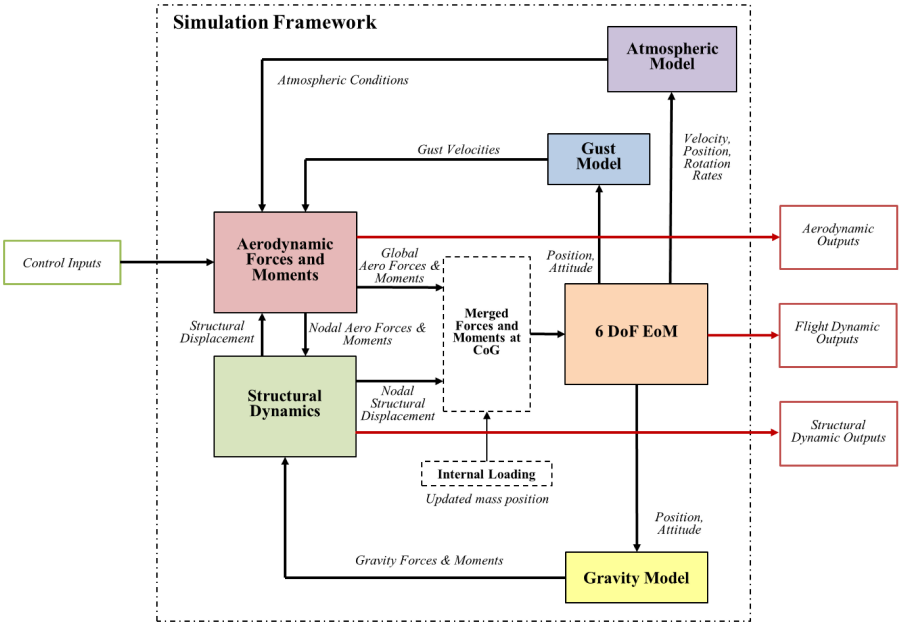

Figure 6.3: Schematic of the CA^{2}LM framework [59]

With distributed aerodynamic stations along the wing, it is possible to obtain local aerodynamic loading. Hence lift distributions can be easily obtained at each step of the simulation. The aerodynamic loading is calculated at each aerodynamic node at each iteration. Stations situated within the lifting surfaces such as wing, tail and fin use Modified Strip Theory (MST) (see Figure6.3) to calculate distributed lift and drag forces. Empirical Scientific Data Units (ESDU) methods are used to capture nacelle and fuselage aerodynamics, as well as the wing-body interaction.

Due to the formulation of this framework there are inherent limitations to the modelling process. The aerodynamic model is only suitable for sub-sonic flight, as such the Mach number must be kept below 0.7. The lift coefficient is read using a look up table, where the data for angle of attack is limited to between $-15\,\text{deg}$ and $+10\,\text{deg}$, does not allow for any stall behaviour (see Figure 6.4b) and limited in Reynolds number.

The calculated drag may have inaccuracies when compared to the real aircraft or the output from a CFD analysis. This is because CA^{2}LM has discretised the lifting surfaces into sections which have a constant aerofoil, for each of these sections the induced drag is calculated. The interaction between these discretised sections (span-wise) is calculated using lifting line theory, which as it is based on empirical coefficients can commonly lead to discrepancies with measured values. Lifting line theory is also limited to modelling induced drag, as such other contributions of drag (e.g. viscous) are estimated using empirical relationships. The reduced order modal structural solver is also limited to only linear deflections, thus it is assumed wing deflection must be kept below 10% of wing semispan (conventional limit of linear models), and also the mode shapes are calculated in the preprocessing of the model, such that there is no update to the shape or frequency during the simulation.

6.1.2 *Constant Angle of Attack*

The constant angle of attack analysis is performed on the AX-1 aircraft with the following conditions:

- flown at fixed altitude of $15000ft$ ($4572m$)

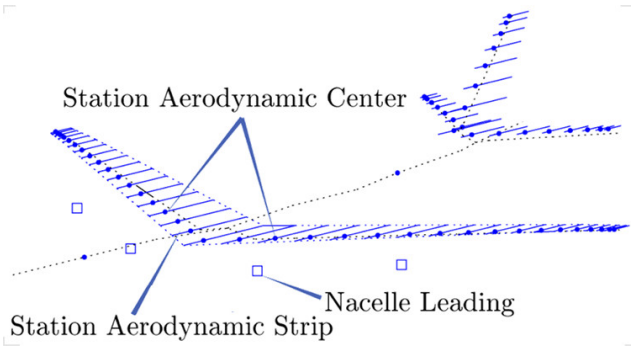

(a) Reduced Order Aerodynamics Model for Cranfield AX-1 Aircraft

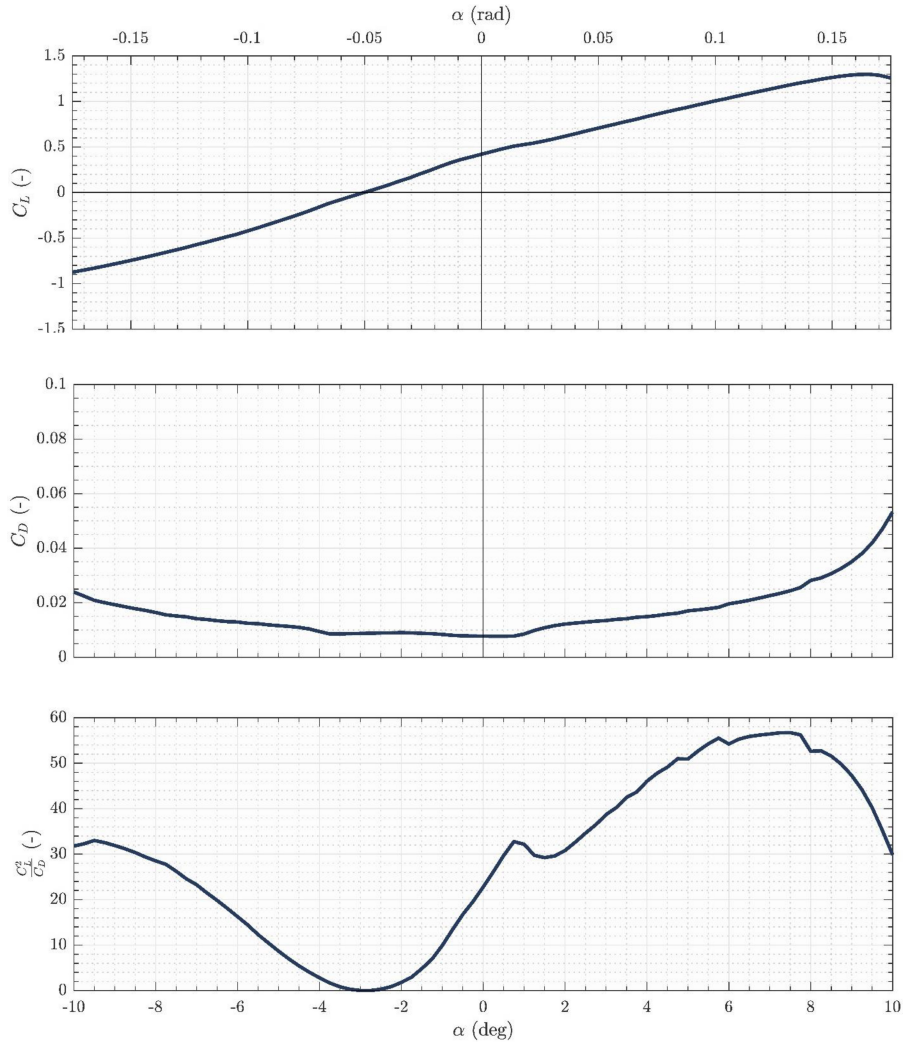

(b) Airfoil NASA S(2) 0610

Figure 6.4: CA^{2}LM Aerodynamics Representation

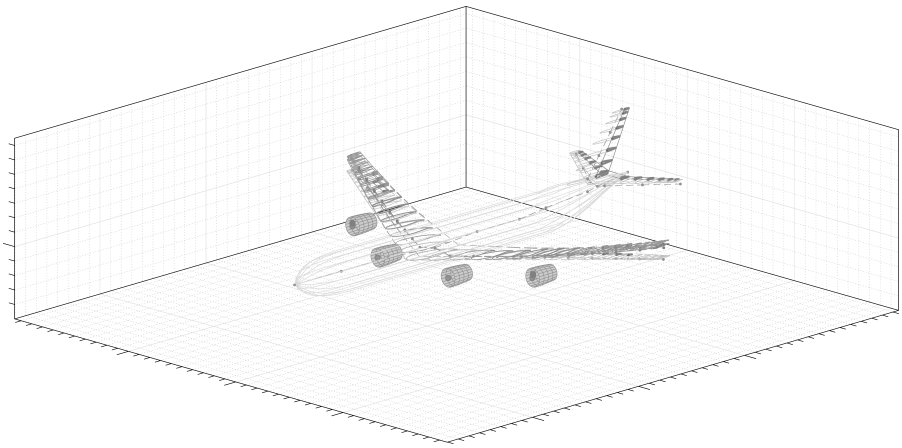

Figure 6.5: Visualisation of the inelastic and flexible aircraft under variable velocities

- free stream velocity varied from $160ms^{-1}$ to $240ms^{-1}$
- fixed in the pitch DoF at an AoA of $0.7°$, untrimmed

This means as the free stream velocity, u_∞, increases, the lift generated will increase, resulting in a higher deflection of the wing for the flexible aircraft and if the analysis premise is true this will result in a lower aerodynamic efficiency. The analysis is run with the structural and aerodynamic state of the aircraft given as the output after the dynamic response of the flexible aircraft has damped out, thus the values can be assumed constant. The results of the analysis are presented graphically in Figure 6.6.

Using the aerodynamic and structural state output, the rate of exergy input to overcome lift-induced drag ($\dot{X}_{D_i}$) can be determined using Equation 5.21 (repeated below for convenience)

$$\dot{X}_{D_i} = \frac{L^2 u_\infty}{qS\pi e\text{Æ}}$$

for the inelastic aircraft and for the flexible aircraft, accounting for the structural deformation. The $\dot{X}_{D_i}$ variance with u_∞ is plotted in Figure 6.6a. It should be noted the exergy input into the system is the same for the flexible and rigid aircraft at each velocity, so the rate of exergy use to overcome lift-induced drag shows essentially how efficiently lift is being generated by the aerodynamics, as by its definition the exergy is overcoming the irreversibilities associated with lift generation.

Given the constant AoA, the lift coefficient will be constant, and substituting this into the rate of exergy input to overcome lift-induced drag ($\dot{X}_{D_i}$) gives

$$\dot{X}_{D_i} = u_\infty \left(\frac{C_L^2}{\pi e\text{Æ}} \right) qS = f\left(u_\infty^3\right)$$

which shows the rate of exergy use for generating lift is proportional to the free stream velocity cubed as shown in Figure 6.6a. From Figure 6.6a it can be noted that with increasing velocity (thus increasing exergy input) a higher proportion is converted used to overcome induced drag for the inelastic aircraft than for the flexible case. This is due to the increasing deformation of the flexible aircraft. As such, less of the aerodynamic load vector is defined as lift as the side force increases as shown in Figure 6.2. Critically, as the aerodynamic load increases, the deformation of the flexible case increases, this results in a greater reduction in efficiency compared to the inelastic case. This indicates that a greater side force and lower vertical lift component are being generated.

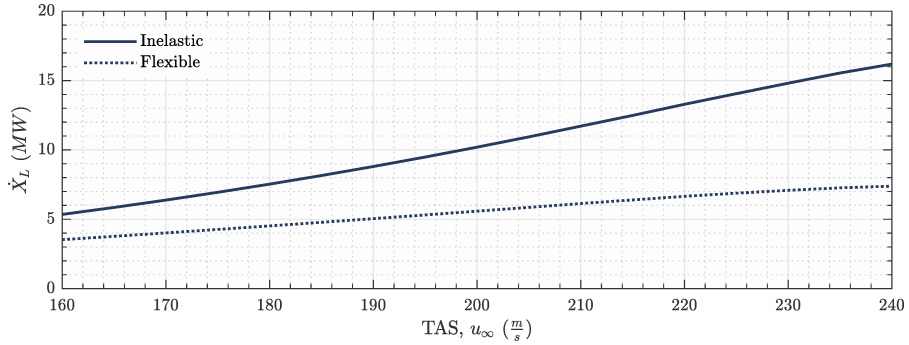

(a) Exergy due to Lift

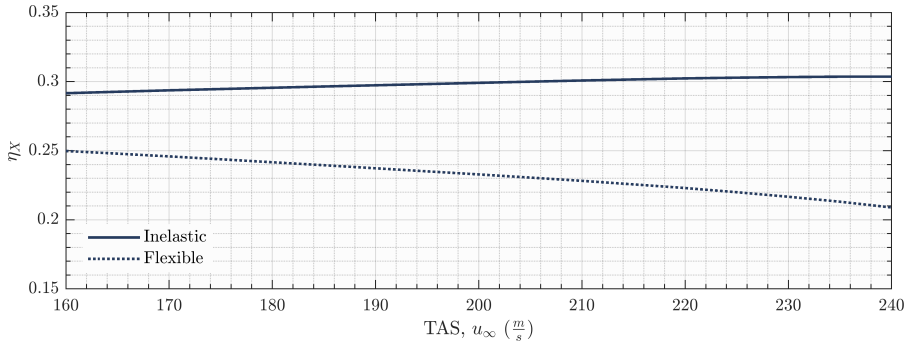

(b) Exergetic Coefficient variance with airspeed

Figure 6.6: Exergy post-processing of CA^{2}LM framework given a constant angle of attack

The overall aircraft aerodynamic exergetic efficiency can be calculated using the aerodynamic and structural state output and Equation 5.23 (repeated below for convenience)

$$\eta_X = \frac{L^2 u_\infty}{qS\pi \mathcal{AR}\left(\cancel{\dot{X}_U} + \cancel{\dot{X}_c} + \dot{X}_D\right)}$$

where the assumption is that all exergy in the wake is destroyed (far-field assumption) thus the internal and conservative exergy terms are zero. This simplification allows the derived exergy terms to be discussed in terms of conventional lift and drag coefficients. The variation of η_X with velocity can be seen in Figure 6.6b. Recalling that the exergetic efficiency is the exergy destruction coefficient for lift divided by the total exergy destruction coefficient, and that the CA^{2}LM framework does not calculate three dimensional effects on vortex drag, using the convention of lift and drag coefficients it can be derived

$$\eta_X = \frac{C_L^2}{C_D \pi \mathcal{AR}} = f\left(C_L^2, C_D\right)$$

Thus given the constant AoA the lift and drag coefficients are constant. This is shown in Figure 6.6b as the exergetic efficiency of the inelastic aircraft does not vary with velocity and thus is constant. It is noted in Figure 6.6b there is a slight increase in the exergertic efficiency for the inelastic aircraft, which can be explained by the non-linear relation for additional drag from the nacelle and fuselage which is calculated using ESDU empirical formulae. The critical output to note from Figure 6.6b is the reducing exergetic efficiency of the flexible aircraft, which confirms the premise that as the wing deformation increases with increasing velocity and lift, making the aircraft less aerodynamically efficient.

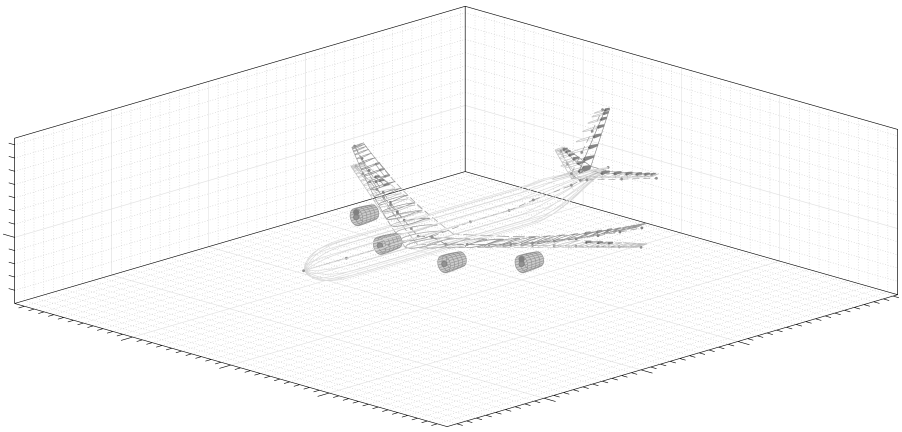

Figure 6.7: Visualisation of the inelastic and flexible aircraft under variable velocities

6.1.3 *Constant Lift*

The constant lift analysis is performed on the AX-1 aircraft with the following conditions:

- flown at fixed altitude of $15000ft$ ($4572m$)
- free stream velocity varied from $160ms^{-1}$ to $240ms^{-1}$
- the aircraft is trimmed for each flight condition (constant lift)

The constant lift analysis means the flexible aircraft will have a constant structural deformation. As such this analysis looks to identify how the aircraft total exergy destruction varies at different trim conditions, most notably with a variable AoA.

The energy generation rate in the wake can be calculated using Equation 5.4 (repeated below for clarity)

$$\dot{E}_f = \cancel{\dot{X}_U} + \cancel{\dot{X}_c} + \dot{X}_D$$

using the structural and aerodynamic state output from CA^{2}LM. As before, implementing the far-field assumption means all wake energy can be assumed to be entropy production and thus exergy destruction.

Over the range of test velocities, the AoA for the inelastic aircraft varies from $\approx 2^\circ \rightarrow -2.5^\circ$ and the flexible aircraft from $\approx 3.5^\circ \rightarrow -1^\circ$. As the velocity increases the aircraft trimmed angle of attack reduces as shown in Figure 6.8a. It is noticeable that as the flexible aircraft needs to produce a higher aerodynamic force for the same lift as the inelastic, that the flexible angle of attack is higher. Yet, given the aircraft is trimmed, and the total lift is constant, the overall difference between flexible and inelastic remains constant as the velocity increases.

From expanding the energy generation rate in the wake equation (Equation 5.4)

$$\dot{X}_D = \frac{1}{2}\left(C_{D_0} + C_{D_i}\right)\rho u_\infty^3 S = f\left(C_{D_0}, C_{D_i}, u_\infty\right)$$

the trend seen in Figure 6.8b can be explained by considering Figure 6.4 where given the higher AoA at any given velocity, the flexible aircraft will generate a higher induced drag (C_{D_i}). The parasitic drag variance between the two configurations will have less of an impact at the airspeeds considered, yet given the higher angle of attack, the exposed area of the aircraft will be higher. The reason the inelastic aircraft has a near constant $\dot{X}_D$, is due to the variation of C_{D_α} and C_L with AoA shown in Figure 6.4, the latter affecting the induced-drag coefficient.

The exergy coefficient is plotted for the inelastic and flexible aircraft at different velocities in Figure 6.8c, using Equation 5.17

$$C_{X_D} = \frac{\cancel{\dot{X}_U} + \cancel{\dot{X}_c} + \dot{X}_D}{uqS}$$

The reducing exergy coefficient is a function of the velocity and AoA, thus the trend mirrors that of Figure 6.8a.

As the rate exergy destruction per kilometre is calculated in Figure 6.8d a similar trend can be seen between the inelastic and flexible aircraft, where the flexible is worse performing. It is this graph that allows the optimal velocity to be defined for a given aircraft, as there is a minimal point in the exergy destruction per kilometer.

6.1.4 *Fluid Exergy Analysis for Static Aeroelasticity*

This section uses the same CFD analysis developed for Section 5.1, however the test case AX-1 configuration from the original analysis is taken as the inelastic configuration, and the flexible configuration considers the structural deflection subjected to the wing at trimmed cruise condition. This allows an understanding to be developed of how the static aeroelastic response of the aircraft effects the exergy use over the aircraft (near-field) and in the wake for applications such as formation flight. All parameters of the CFD model set-up are the same as in Section 5.1.4 from [36], with the exception of the plane geometry which is that of the flexible Cranfield AX-1 configuration.

CA^{2}LM is used to identify the trim conditions (angle of attack and structural deformation) of the AX-1 aircraft at the same flight condition (altitude and velocity) for the inelastic aircraft configuration in Section 5.1:

- flown at fixed altitude of $15000ft$ ($4572m$)
- free stream velocity $190ms^{-1}$, equivalent to $0.59M$

For the purposes of the inelastic aircraft, the framework structural model can be disengaged, and for the flexible aircraft the trimmed structural deflection can be assumed *frozen* in flight shape. Given the previously discussed lower aerodynamic efficiency of the flexible aircraft, the trimmed angle of attack will be higher than that for the rigid aircraft. The derived trimmed angle of attack output from CA^{2}LM:

- inelastic aircraft trim AoA 0.697° equivalent to 0.012 rad
- flexible aircraft trim AoA 1.678° equivalent to 0.029 rad

As with Chapter 5.1, the fluid state output from the CFD analysis can be used to calculate the fluid; destroyed, thermal and mechanical exergies using Equations 5.6, 5.9 and 5.12 respectively. Equation 5.4 shows that the sum of these and also gives the total exergy content in the fluid.

The exergy content and destroyed exergy of the fluid is shown in Figure 6.9. Validating the conclusion from the previous analysis, the CFD exergy study shows that due to added inefficiencies at the wing and horizontal tailplane the deformed flexible aircraft requires a higher rate of exergy input into the system to fly in the same trim condition as the inelastic aircraft, meaning the flexibility of the wing makes the aircraft less aerodynamically efficient, by a margin of circa $1MW$. The values for the total exergy content of the fluid are higher in Figure 6.9 than the total exergy destroyed predicted in Figure 6.8 (note these two values are comparable as the previous analysis assumes that at an infinite distance behind the aircraft all fluid exergy is destroyed). This variance is due to the CFD modelling the aircraft drag more accurately as it accounts for the 3D and viscous effects which CA^{2}LM framework cannot.

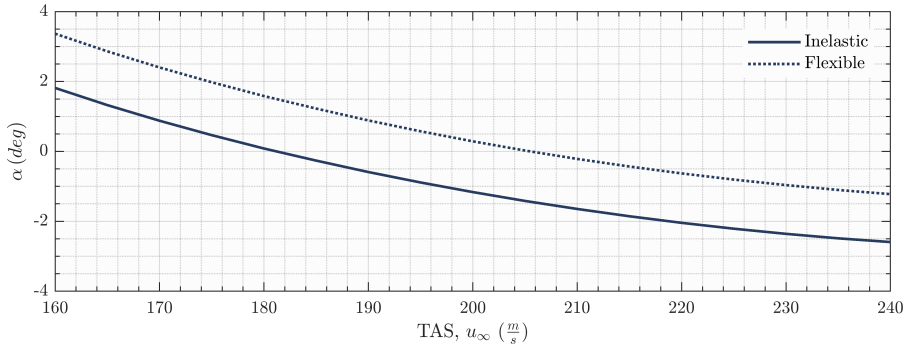

(a)

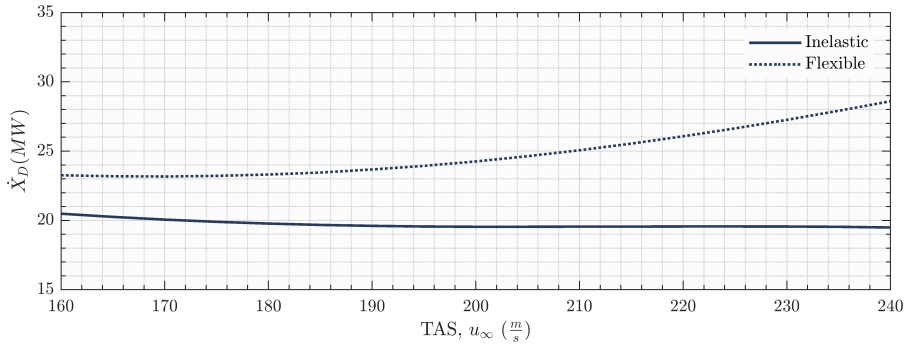

(b)

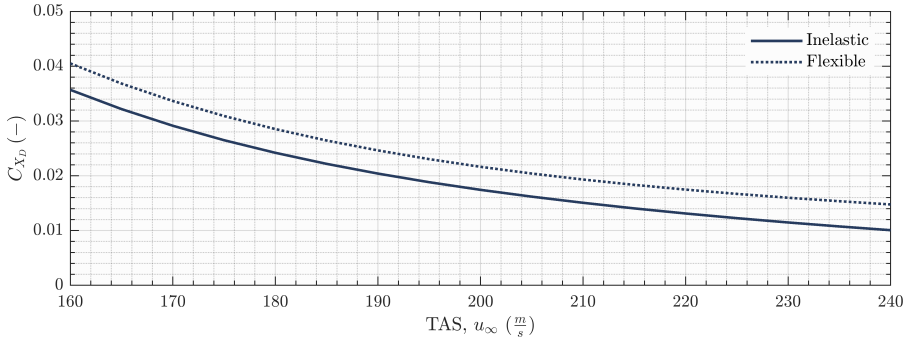

(c)

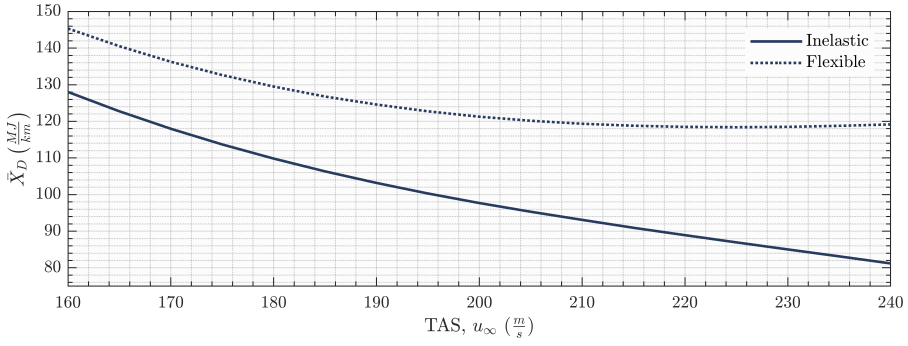

(d)

Figure 6.8: Exergy post-processing of CA^{2}LM framework given a constant lift

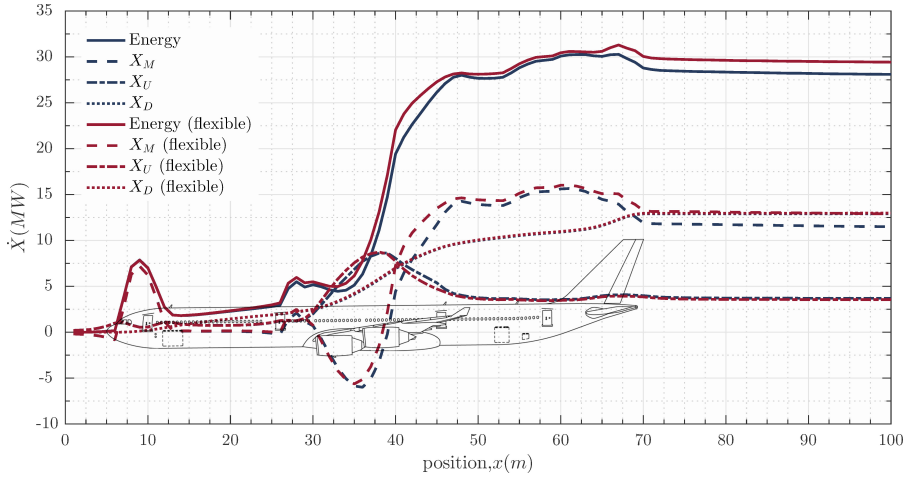

Figure 6.9: CFD total exergy comparison between inelastic and flexible aircraft

Further analysis as to the variation between an inelastic and flexible aircraft can be found by looking at the individual fluid exergy contents as before.

- *Destroyed Exergy*
  - The deformation, which changes the features of the flow in the wake, has little impact on the magnitude of destroyed exergy, considering that numerical errors can appear due to different meshes. It is therefore concluded that the destroyed exergy, (thus entropy content) of the inelastic and flexible aircraft wake are equal.
- *Thermal Exergy*
  - Whilst the thermal exergy at a plane behind the aircraft appears near equal for the inelastic and flexible aircraft, there are clear variations in the conversion of thermal exergy around the aircraft wing of the two configurations.
  - The pressure-based effects are the dominant factor in the variation of the thermal exergy along the aircraft. Therefore, it is expected that the main difference between the inelastic and flexible configuration will concern the term $\dot{X}_{U_p}$ (Equation 5.9).
  - A similar variation is found in the boundary pressure work deposition rate $\dot{X}_{M_p}$ in the mechanical exergy (5.12). The difference with the freestream pressure is reduced on the wing (less twist, especially at the tip). In other words, the flow acceleration and then the deceleration of the deformed aircraft is less pronounced which is in accordance with a lower lift.
- *Mechanical Exergy*
  - The curvature of the wing straightens the flow, increasing the streamwise component of the velocity and decreasing the transverse component.
  - There is also a reduction in mechanical exergy for the flexible case at the horizontal tailplane. This is due to the difference in downwash created by the deformed wing.
  - Wing deflection results in a reduction in the aspect ratio of the wing. In line with Equation 5.19 this would result in an increase in the induced drag, which reflects what is seen by the increased energy deposition into the fluid, shown in Figure 6.9.

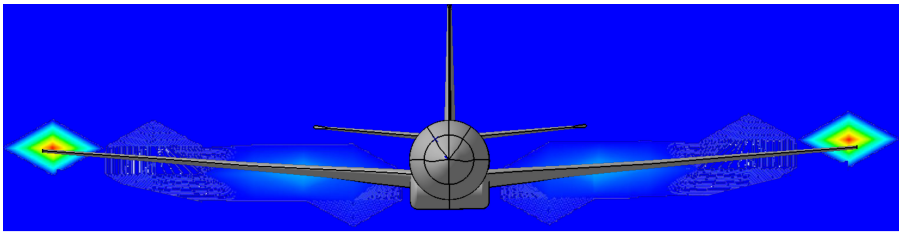

(a) Vortex mechanical exergy plot - inelastic

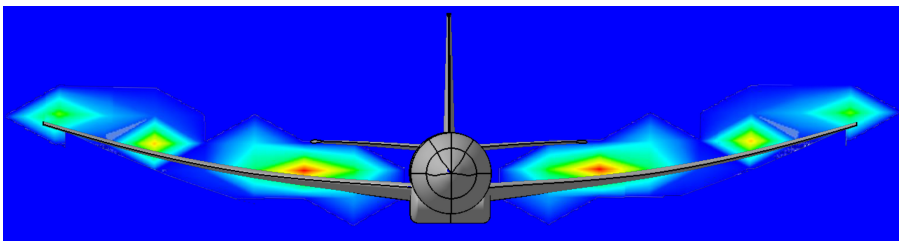

(b) Vortex mechanical exergy plot - flexible

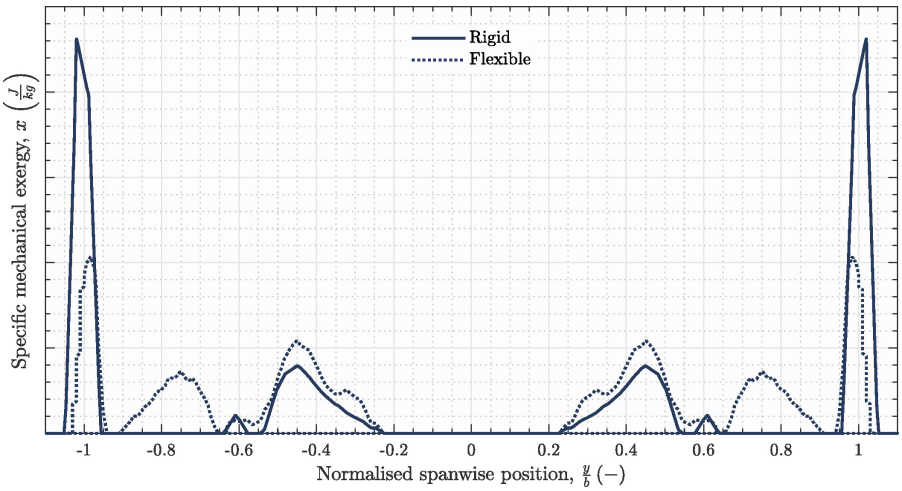

(c) Rotational Kinetic Exergy in the Wake

Figure 6.10: Results from Application of Fluid Exergy to a Deformed Structure (all figures plane located at $x = 51.6m$ from reference point, see $0m$ position in Figure 6.9)

- The wing deflection modifies the spanwise lift distribution which has consequences on the vortices shed from the wing. The local lift coefficients are reduced for the flexible aircraft. The complex vortex structure shedding from the flexible aircraft forms a more dispersed distribution of the exergy destruction. A more complex distribution, with three vortex systems instead of two, is noticed with the structural deformation (Figure 6.10a and Figure 6.10b).
- The distribution of the mechanical exergy is unimportant as downstream the vortices roll into larger vortices which are used in formation flight. Further work looking at the far field analysis should show this. Critically the analysis shows the proportion of energy in the aircraft wake that can be extracted as useful work. This is the mechanical exergy content of the wake energy. Further work would be to see how the exergy dissipates into X_D downstream and how this can be used to identify positioning for formation flight. One needs to consider maximum exergy content versus concentration of exergy in the vortices.

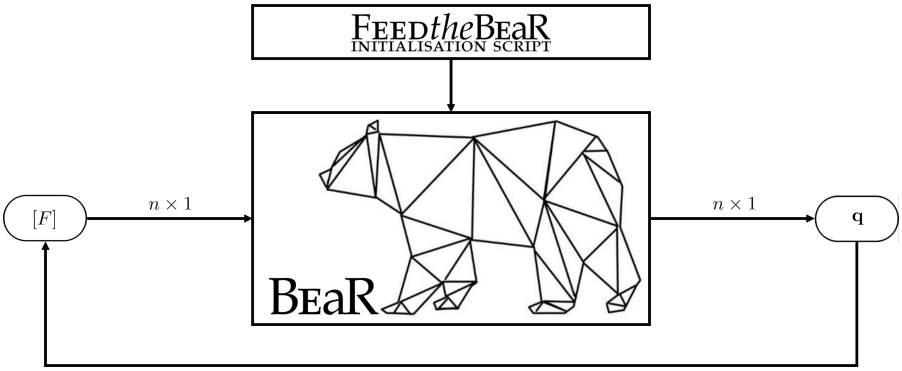

(a) BEAR structural framework with an aerodynamic load input

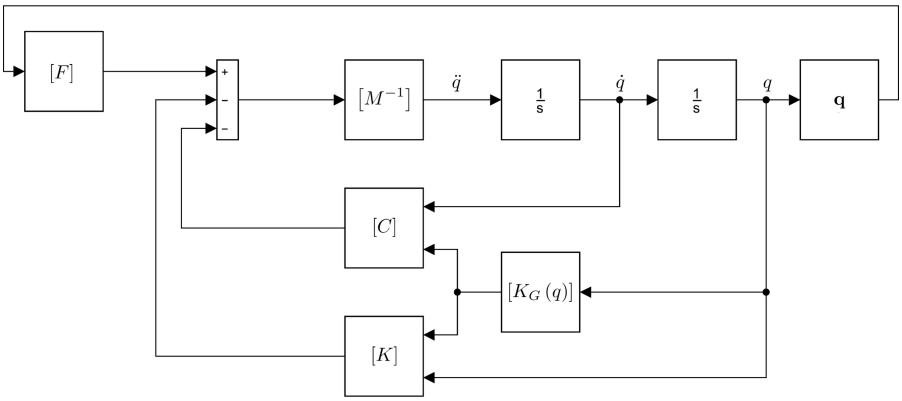

(b) Expanded Direct ODE Solver using aerodynamic load input

Figure 6.11: BEAR code for 2D dynamic aeroelasticty analysis

6.2 EXERGY ANALYSIS OF DYNAMIC AEROELASTICITY

Similarly to the static aeroelasticity node, Bisplinghoff [27] partitions the *dynamic aeroelastic* node of Collars triangle into the phenomena of:

- flutter
- buffeting
- dynamic response
- effect to dynamic stability

Even with a more flexible aircraft, avoiding flutter and buffeting are critical for the safety of the aircraft. However the structure can be expected to have a significant dynamic response under control loads or environmental disturbances. With this coupling of the structural dynamics and aerodynamics of the aircraft, a comprehensive analysis of an aircraft in flight would need to consider these phenomena together under a single metric, an ideal application for exergy analysis as previously discussed.

This section aims to show how the BEAR framework introduced in Chapter 4 can be extended beyond analysis of initial condition dynamic response, to a forcing function ($[F]$) dynamic response, where the forcing function is generated from an aerodynamics model. The changes to the BEAR framework can be seen in Figures 6.11a and 6.11b to allow a force input into the non-linear structural model, which is governed by the feedback of the output structural state, $[q]$.

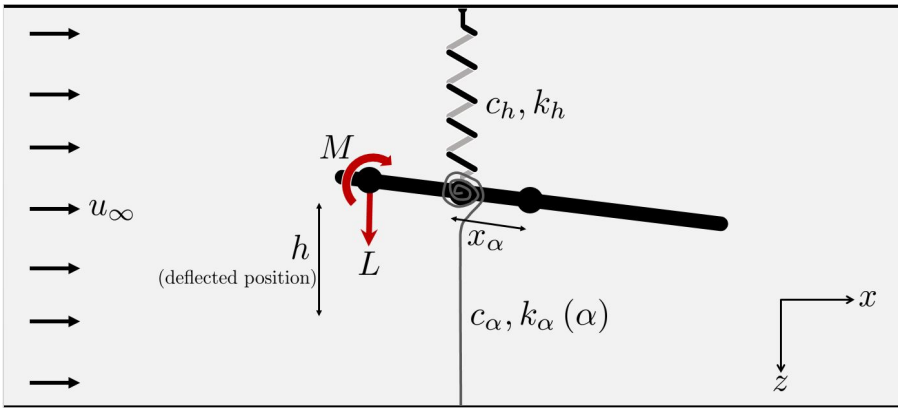

Figure 6.12: Classic 2D aeroelastic wing section set up

6.2.1 *A classic aeroelastic wing section with structural nonlinearity model*

As in Chapter 4 the forced non-linear structural response will initially be demonstrated on a two DoF toy example, the classic aeroelastic wing section with structural nonlinearlity (Figure 6.12). This is a simplified and corrected version of that presented by Baranyi [16]. This style of model is commonly used for the theoretical, as well as the experimental analysis of two-dimensional aeroelastic behaviour, which Baranyi showed exhibited various non-linear phenomena such as limit-cycle oscillation, flutter and chaotic vibrations.

The airfoil is modelled as a flat plate, that has only two degrees of freedom, that of plunge, $h(m)$, and pitch $\alpha(rad)$. The equations of motion for a 2 DoF system are defined as

$$\begin{bmatrix} m & mx_\alpha c \\ mx_\alpha b & I_\alpha \end{bmatrix} \begin{bmatrix} \ddot{h} \\ \ddot{\alpha} \end{bmatrix} + \begin{bmatrix} c_h & 0 \\ 0 & c_\alpha \end{bmatrix} \begin{bmatrix} \dot{h} \\ \dot{\alpha} \end{bmatrix} + \begin{bmatrix} k_h & 0 \\ 0 & k_\alpha(\alpha) \end{bmatrix} \begin{bmatrix} h \\ \alpha \end{bmatrix} = \begin{bmatrix} -L \\ M \end{bmatrix}$$

the structural non-linearity is incorporated as a non-linear torsional spring of stiffness $k_\alpha(\alpha)$ which is calculated at each time step based on the system state as

$$k_\alpha(\alpha) = 2.82\left(1 - 22.1\alpha + 1315.5\alpha^2 - 8580\alpha^3 + 17289.7\alpha^4\right)$$

The forcing function is defined as a quasi-steady aerodynamic force and moment which is dependent on the system state (as shown with the feedback in Figure 6.11)

$$\begin{bmatrix} -L \\ M \end{bmatrix} = \begin{bmatrix} -\rho u^2 c c_{l_\alpha} \left(\alpha + \frac{\dot{h}}{u} + \left(\frac{1}{2} - a\right) c\left(\frac{\dot{\alpha}}{u}\right)\right) \\ \rho u^2 c^2 c_{m_\alpha} \left(\alpha + \frac{\dot{h}}{u} + \left(\frac{1}{2} - a\right) c\left(\frac{\dot{\alpha}}{u}\right)\right) \end{bmatrix}$$

The simple model is checked against the parameter set up of Baranyi [16] and the results. These results are not suitable to be used for an example of exergy analysis, as the chaotic nature of the pitch oscillations would *cloud* any meaningful output. As such the model is run with the parameters given in Table 6.1, with the driving velocity given in Figure 6.13a. With the initial condition $[h_0, \alpha_0] = [0, 0.185]$, a constant free stream velocity, $u = 4ms^{-1}$ and the model geometry given in Table 6.1, the calculated aerodynamic force and moment that drive the model dynamics are shown in Figure 6.13b. Due to the increase in torsional damping (c_α) the pitch state is reduced rapidly during the $3s$ simulation, shown in Figure 6.13c. The longitudinal displacement (plunge) has a lower damping coefficient thus the induced oscillations are seen to damp at a lesser rate in Figure 6.13d.

The added complexity of the aeroelastic analysis in comparison to the initial condition structural response of Chapter 4, is that there is a constant energy input into

Table 6.1: Parameters for 2D aeroelastic analysis

a	-	-0.4
c	m	0.135
c_α	Ns	0.2
c_h	$\frac{Ns}{m}$	1
c_{l_α}	-	2π
c_{m_α}	-	$(0.5+a)\,c_{l_\alpha}$
h_0	m	0.0
I_α	kgm^2	0.065
k_h	$\frac{N}{m}$	2000
m	kg	5
x_α	-	$-0.35-a$
ρ	$\frac{kg}{m^3}$	1.225
α_0	rad	0.175

the system from the air flow. In a closed system aircraft, this is accounted for by the exergy input from the combustion of fuel in the engine, which is converted into kinetic energy of the aircraft via thrust. In the closed aircraft case, the energy in the system would be constant, as the source of input to the aerodynamics (the fuel) is stored in the aircraft. However for the simple analysis of a 2D aerofoil, the air flow models a constant work input into the system from an external source. The following can be concluded from the 2D aerofoil analysis:

- The rate of work input into the system is dependent on the aerodynamic profile rotational state (α). As the pitch angle decreases (Figure 6.13c) the rate of energy input into the system reduces to the point where the aerofoil is rotationally stable and converting none of the air velocity into lift. This is shown in Figure 6.14d where the entropy generation rate decreases to zero, thus there is no cumulative gain on the total destroyed exergy.
- The potential exergy, X_V, is a function of the stiffness

$$\begin{aligned} X_{V_{k_h}} &= [h]^T [k_h] [h] \\ X_{V_{k_\alpha}} &= [\alpha]^T [k_\alpha(t)] [\alpha] \\ X_{V_{k_\alpha}} &= \iint k_\alpha(\alpha)\, d\alpha^2 \\ &= 1.41\alpha^2 - 10.387\alpha^3 + 309.142\alpha^4 - 1209.78\alpha^5 + 1625.23\alpha^6 \\ X_V &= X_{V_{k_h}} + X_{V_{k_\alpha}} \end{aligned}$$

  The potential exergy stored in the torsional spring dominates the total potential exergy (Figure 6.14c) due to the low displacement in the plunge axis (Figure 6.13d).
- The potential exergy stored in the torsional spring is a function of the nonlinear torsional stiffness, Figure 6.14a.
- As with a simple mass-spring-damper, the potential exergy is freely converted to kinetic energy of the system (thus equal to energy). Figure 6.14b shows the system kinetic exergy, X_T, in comparison to the total exergy of the system, X_{sys}.
- As the pitch rotational displacement tends to zero after $1.2s$ the aerofoil stabilises. The exergy content of the system (Figure 6.14b) is at zero, given the negligible impact the linear stiffness exergy term has.

This analysis shows that an aerodynamically driven aeroelastic system can be modelled using exergy analysis, and whilst this is shown on a 2 DoF system it scales up

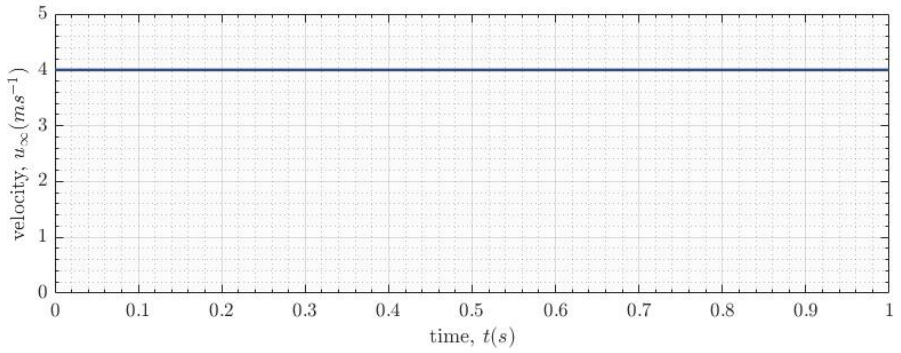

(a)

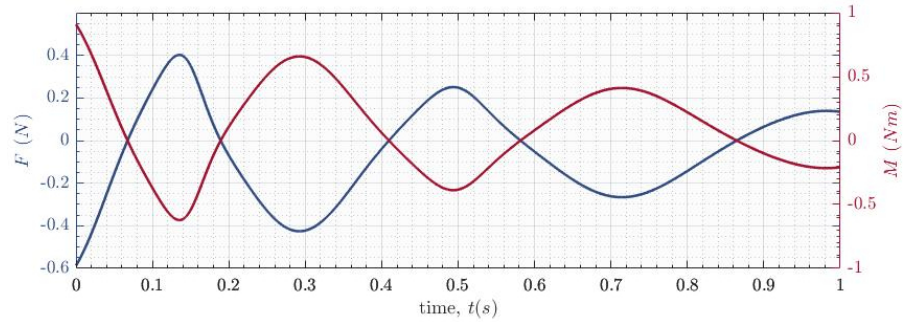

(b)

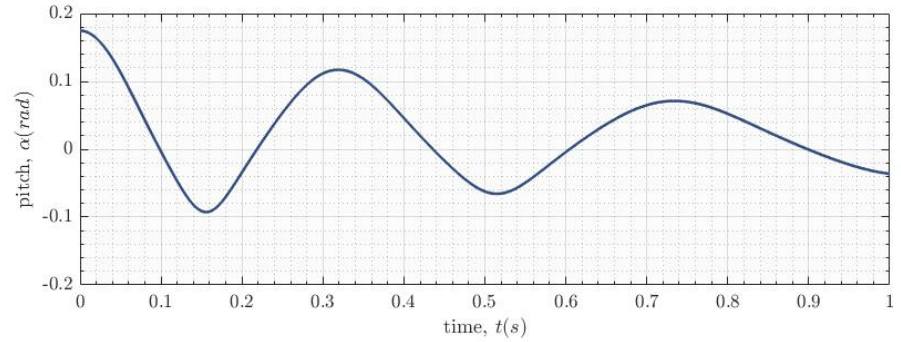

(c)

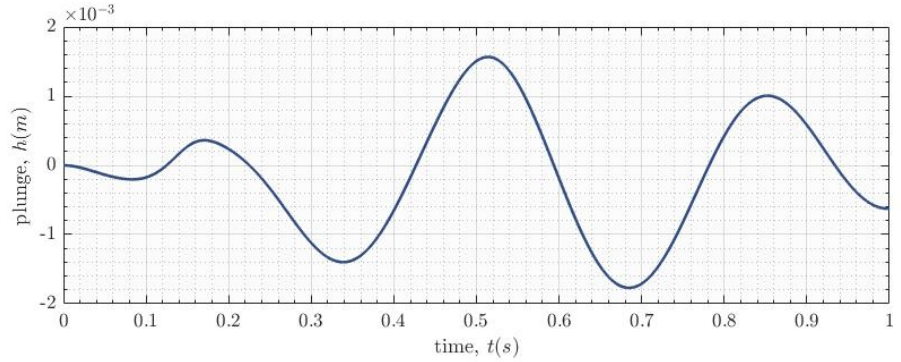

(d)

Figure 6.13: System State output for classic aeroelastic wing section

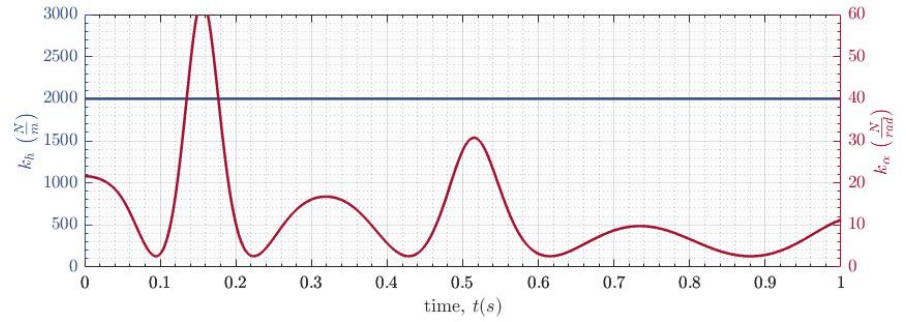

(a)

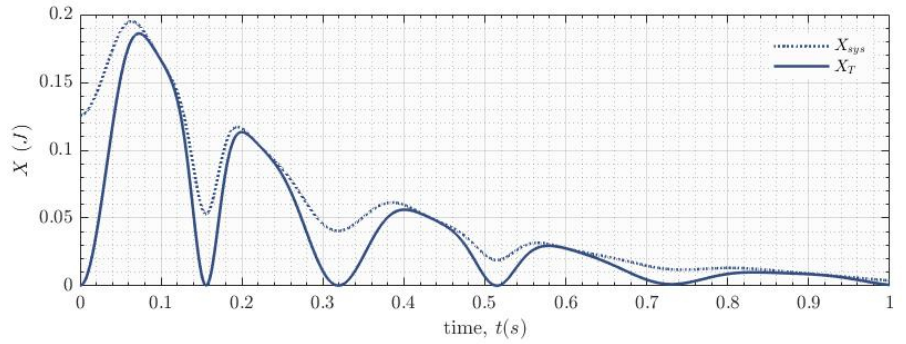

(b)

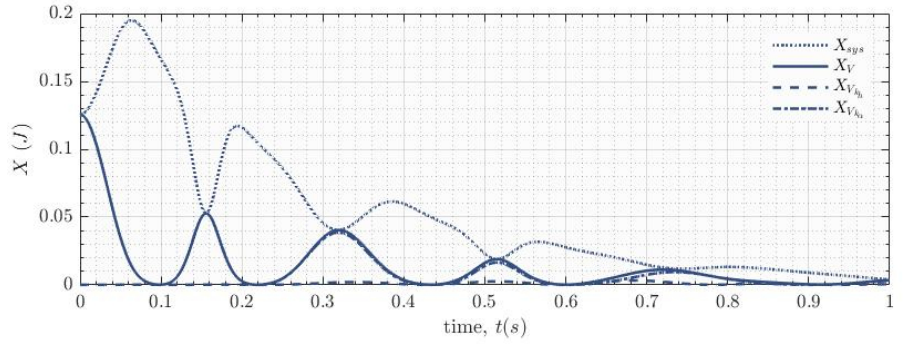

(c)

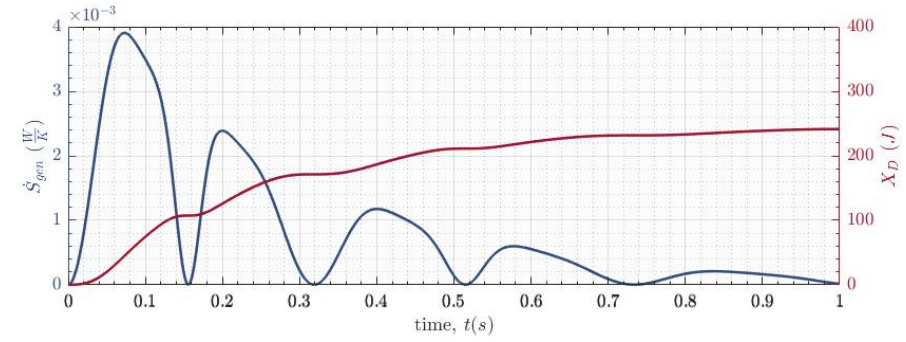

(d)

Figure 6.14: Exergy Analysis output for classic aeroelastic wing section

to multi-DoF systems with the same methodology. This is the focus of the next section, where a multi-DoF dynamically aeroelastic framework is developed for HARW aircraft analysis.

6.2.2 *Beam Reduction and Dynamic Scaling Theoretical Model (BEARDS^{TM})*

Modelling frameworks of varying complexity have been developed both in industry and academia. Industrial frameworks are highly complex and aimed at supporting certification activities. These often couple computational fluid dynamics (CFD) with structural mechanics (CSM), and result in processes that provide the desired insight, but require extensive computing power.

Academia has shown the capability to link aeroelasticity with flight control and develop novel approaches to aeroservoelastic analysis of highly flexible configurations. Research into aeroelastic analysis of highly flexible airframes has generated numerous papers, including those from Palacios [125], Cesnik [87, 92] and Hodges [46, 127], with industrial applications of highly flexible wings in concepts including NASA/Boeing Subsonic Ultra Green Aircraft Research (SUGAR) aircraft and the *Airbus concpet plane*. Although the approach adopted by Palacios et al. is computationally cheaper than those used in industry, real time simulation is still not possible. Structural flexibility effects were modelled through the implementation of a nonlinear structural dynamics formulation. Aerodynamic contributions were captured by means of a unsteady vortex lattice method code.

The aim of real time simulation drove the development of the CA^{2}LM framework [10], where the flight dynamics and transient aerodynamic analysis under different flight conditions can be modelled coupling MST aerodynamics and reduced order modal linear structural dynamics. Yet modelling aircraft aerodynamic-structural coupling to understand how the energy is used is sparsely published. Furthermore, a modal solver whilst computationally efficient and accurate for linear analysis, is not suitable for energy analysis, as the stiffness, mass and damping matrices need to be analysed individually as well as a full state vector, not the reduced modal state vector.

An understanding of the capabilities and limitations of the above frameworks has lead to the development of the Beam Reduction and Dynamic Scaling Theoretical Model (BEARDS^{TM}) which forms part of the wider BEARDS [1] research programme at Cranfield University. An overview of the main characteristics of the BEARDS^{TM} framework (Figure 6.15) are given as:

- The framework is primarily built for cantilevered wing analysis (thus no rigid body DoF exist). However the rigid body equations of motion can be engaged as shown in Figure 6.15 to allow the simulation to move in the test space to simulate flight, for example if a dynamic rig were to be used. For the remainder of the thesis it is assumed the switch is open. As such rigid body motion is constrained.

1 The aims and objectives of the Beam Reduction and Dynamic Scaling (BEARDS) programme is discussed in further detail in Chapter 8

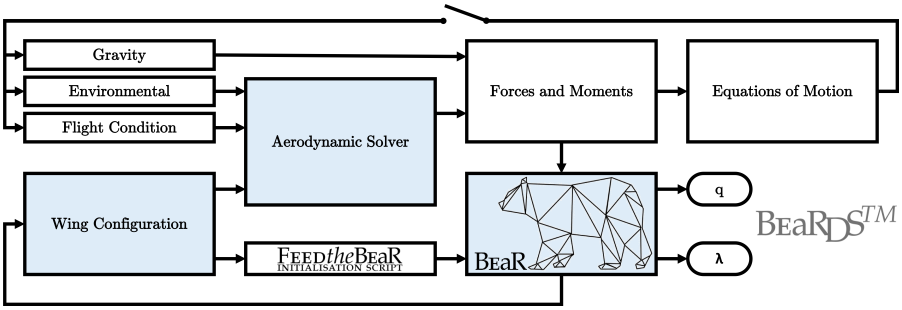

Figure 6.15: BEARDS^{TM} framework

- The wing configuration is defined as per a standard NASTRAN punch file for the structure. The aerodynamics are defined as 2D aerofoils on each of the structural nodes with a defined chord length.
- Various aerodynamic solvers can be implemented; weak coupling Prandtl-Glauret modelling, Modified Strip Theory (MST) (default) and Unsteady Vortex Lattice Method (UVLM) (in development at time of writing thesis).
- The aerodynamics model takes the state of the wing (twist and displacement) along with the flight condition and environmental loading to calculate the forces and moments on the structure at each time step.
- The BEAR code works as a direct solver (solves all degrees of freedom) at each time step (discussed in Chapter 4).
- The structural state vector is output from the simulation and also feeback to update the wing configuration and subsequently the aerodynamic loading.

The exergy analysis is done as a post-processing tool of the state vector output using the structural mass and stiffness matrices along with the flight condition. With this dataset the structural dynamic exergy use (Chapter 4), aerodynamic exergy (rigid body flight dynamics, Chapter 5) and the exergy input into the system (Chapter 6) can be simulated and studied.

6.2.3 *Cranfield A-13*

BEARDS^{TM} is to be used to analyse the *aeroelastic response of scaled technologies* in Chapter 8. Yet in order to have confidence in the output, the remainder of this chapter focuses on validating the static and dynamic response output from BEARDS^{TM} when subjected to aerodynamic forces.

The geometry and model manufactured to validate the model is derived from the Cranfield A-13 aircraft, Figure 6.16a, with parameters given in Table 6.2. For simplicity, the wing is designed without control surfaces and has a conventional aspect ratio, such that the deflections can be assumed to be linear, for assessing the linearised modelling approach. The aerodynamic planform (Figure 6.16c) is taken as a static scale from the full size aircraft, at a ratio of 20:1. The Cranfield A-13 has no formal structural design, as such a generic spar is designed (Figure 6.16c) which is manufactured from aluminium, and designed to be highly flexible under aerodynamic loading (displace in excess of 20% of the semi-span), see [70] for further details. Given the theoretical geometry matches the manufactured geometry this is a suitable test piece to validate BEARDS^{TM}.

Note that the design of the A-13 wing model assumes all the stiffness of the model is in the spar. The zero stiffness cover is built via a Polyjet printing method where materials of varying Shore hardness can be printed in a single part. Thus as shown in Figure 6.16b, the wing planform is manufactured as a series of rigid pods connected via flexible low hardness material, to give the skin a pseudo-zero stiffness property, see Pontillo [134] for further information.

6.2.4 *BEARDS^{TM} Static Response*

The A-13 static test is focused on measuring the static response of the wing under a defined angle of attack and steady flow conditions. The BEAR preprocessor was used

Table 6.2: Cranfield A-13 Aircraft Parameters

Parameter	Symbol	Units	A-13
Passenger Capacity	cap	–	200
Take-Off Weight	TOW_{nom}	kg	87,663
Cruise Speed	u_∞	$\frac{m}{s}$	175
Wing Span	b	m	38.3
Aspect Ratio	Æ	–	12
Wing Area	S	m^2	122.35
Root Chord	c_r	m	6.554
Tip Chord	c_t	m	1.132
Mean Aerodynamic Chord	MAC	m	3.887
Leading Edge Sweep	Λ_{LE}	deg	5.00
0.25C Sweep	$\Lambda_{0.25}$	deg	2.48

(a) Cranfield A-13 Aircraft Overview

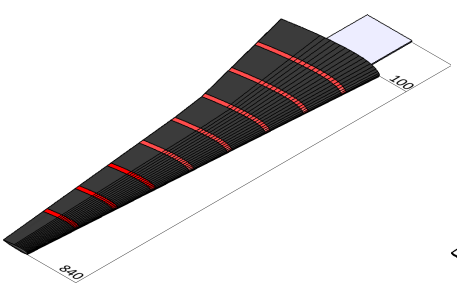

(b) Skin geoemtry of XB-1

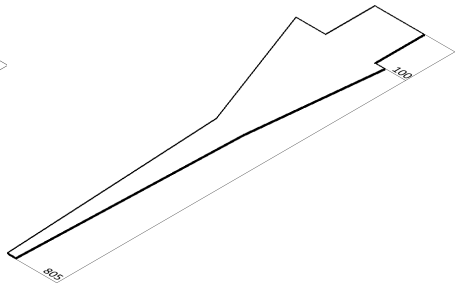

(c) Spar geoemtry of XB1

Figure 6.16: BEARDS XB-1 aerodynamic planform and spar geometry

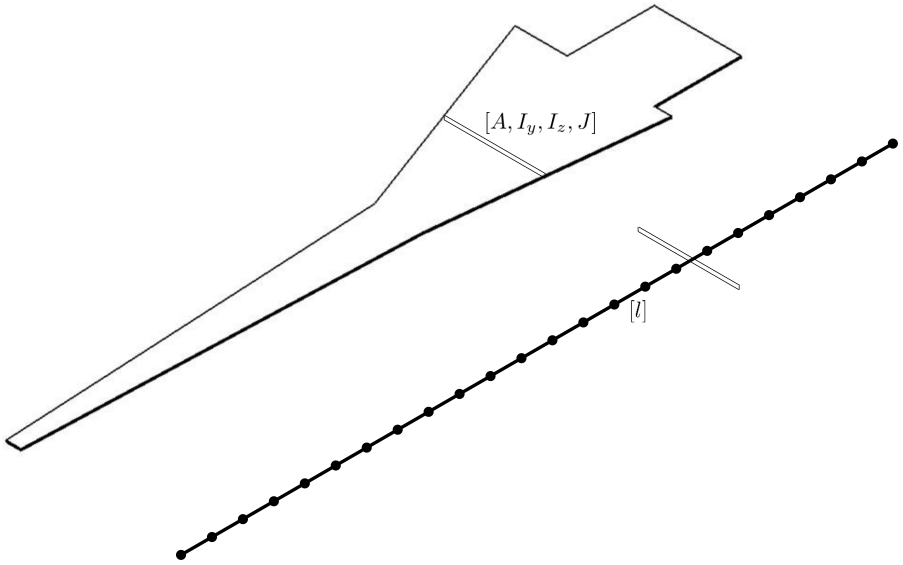

Figure 6.17: FEA model of XB1

to create the mass matrix and Timoshenko style stiffness matrix, defining the shear coefficients as:

$$\phi_y = \frac{12EI_z}{GA_e l_e^2} = 24\,(1+\nu)\,\frac{A}{A_e}\left(\frac{r_z}{l_e}\right)^2$$
$$\phi_z = \frac{12EI_y}{GA_e l_e^2} = 24\,(1+\nu)\,\frac{A}{A_e}\left(\frac{r_y}{l_e}\right)^2$$

and discretising the spar into 52 six DoF nodes (312×312 matrix for mass and stiffness, 312×1 state vector). Each element connecting the nodes is defined with a constant cross section as shown in Figure 6.17, where the section defines the geometric properties, A, I_y, I_z and J along with the length of the beam, l. Note that as the spar geometry of the XB1 wing is responsible for all the stiffness, as the spar is

manufactured from aluminium, the material properties used are those of aluminium. With the geometric and material properties the stiffness matrix can be generated as

$$[K_{e,1}] = \begin{bmatrix} \frac{EA}{l} & 0 & 0 & 0 & 0 & 0 \\ 0 & \frac{12EI_z}{l^3(1+\Phi_y)} & 0 & 0 & 0 & \frac{6EI_z}{l^2(1+\Phi_y)} \\ 0 & 0 & \frac{12EI_y}{l^3(1+\Phi_z)} & 0 & \frac{-6EI_y}{l^2(1+\Phi_z)} & 0 \\ 0 & 0 & 0 & \frac{GJ}{l} & 0 & 0 \\ 0 & 0 & \frac{-6EI_y}{l^2(1+\Phi_z)} & 0 & \frac{(4+\Phi_z)EI_y}{l(1+\Phi_z)} & 0 \\ 0 & \frac{6EI_z}{l^2(1+\Phi_y)} & 0 & 0 & 0 & \frac{(4+\Phi_y)EI_z}{l(1+\Phi_y)} \end{bmatrix}$$

$$[K_{e,2}] = \begin{bmatrix} \frac{EA}{l} & 0 & 0 & 0 & 0 & 0 \\ 0 & \frac{12EI_z}{l^3(1+\Phi_y)} & 0 & 0 & 0 & \frac{-6EI_z}{l^2(1+\Phi_y)} \\ 0 & 0 & \frac{12EI_y}{l^3(1+\Phi_z)} & 0 & \frac{6EI_y}{l^2(1+\Phi_z)} & 0 \\ 0 & 0 & 0 & \frac{GJ}{l} & 0 & 0 \\ 0 & 0 & \frac{6EI_y}{l^2(1+\Phi_z)} & 0 & \frac{(4+\Phi_z)EI_y}{l(1+\Phi_z)} & 0 \\ 0 & \frac{-6EI_z}{l^2(1+\Phi_y)} & 0 & 0 & 0 & \frac{(4+\Phi_y)EI_z}{l(1+\Phi_y)} \end{bmatrix}$$

$$[K_{e,3}] = \begin{bmatrix} -\frac{EA}{l} & 0 & 0 & 0 & 0 & 0 \\ 0 & -\frac{12EI_z}{l^3(1+\Phi_y)} & 0 & 0 & 0 & \frac{-6EI_z}{l^2(1+\Phi_y)} \\ 0 & 0 & -\frac{12EI_y}{l^3(1+\Phi_z)} & 0 & \frac{6EI_y}{l^2(1+\Phi_z)} & 0 \\ 0 & 0 & 0 & -\frac{GJ}{l} & 0 & 0 \\ 0 & 0 & \frac{-6EI_y}{l^2(1+\Phi_z)} & 0 & \frac{(2-\Phi_z)EI_y}{l(1+\Phi_z)} & 0 \\ 0 & \frac{6EI_z}{l^2(1+\Phi_y)} & 0 & 0 & 0 & \frac{(2-\Phi_y)EI_z}{l(1+\Phi_y)} \end{bmatrix}$$

$$[K_E] = \begin{bmatrix} [K_{1,1}] & [K_{1,3}] & 0 & \cdots & 0 & 0 \\ [K_{1,3}]^T & [K_{1,2}] + [K_{2,1}] & [K_{2,3}] & \cdots & 0 & 0 \\ 0 & [K_{2,3}]^T & [K_{2,2}] + [K_{3,1}] & \ddots & \vdots & \vdots \\ \vdots & \vdots & \ddots & \ddots & [K_{n-1,3}] & 0 \\ 0 & 0 & \cdots & [K_{n-1,3}]^T & [K_{n-1,2}] + [K_{n,1}] & [K_{n,3}] \\ 0 & 0 & \cdots & 0 & [K_{n,3}]^T & [K_{n,2}] \end{bmatrix}$$

Additional information on how these matrices are built can be found in Appendix C, which outlines the preprocessing routine of the BEAR code.

To validate the BEARDS^{TM} prediction a wind tunnel model of the A-13 was manufactured and tested in the Cranfield Weybridge wind tunnel. The paper by Pontillo [134] outlines the manufacture and test which forms apart of the BEARDS programme, but for this thesis, the output is used to validate the BEARDS^{TM} framework, that was developed for this thesis. In order to track wing deflections, the model was equipped with an acquisition system of four Inertial Measurement Units (IMUs) distributed along the wingspan. The IMUs are able to monitor angular velocities and accelerations. The placement of the sensors is shown in Figure 6.20a. In addition, a High Speed Video Camera was used to track the displacement of the wingtip using two markers.

EXAMPLE 6

The test case simulated by BEARDS^{TM} and validated in the Weybridge wing tunnel was with a 1 : 22 scale XB-1 wing at a constant angle of attack of 6° at a constant freestream velocity of $27ms^{-1}$ ($Re \approx 500,000$)

The loading condition used to predict the static deflection is defined using the MST solver of BEARDS^{TM}. This aerodynamic loading was validated using the Athena

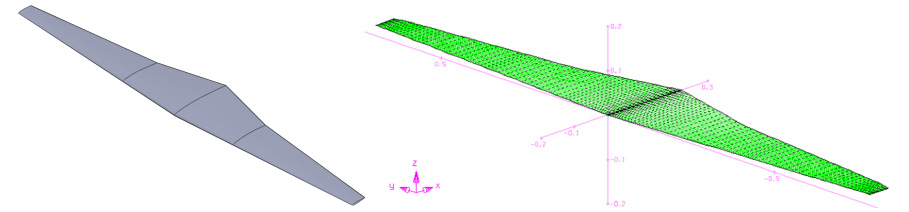

(a) CAD geoemtry of XB-1

(b) AVL mesh set-up for XB-1

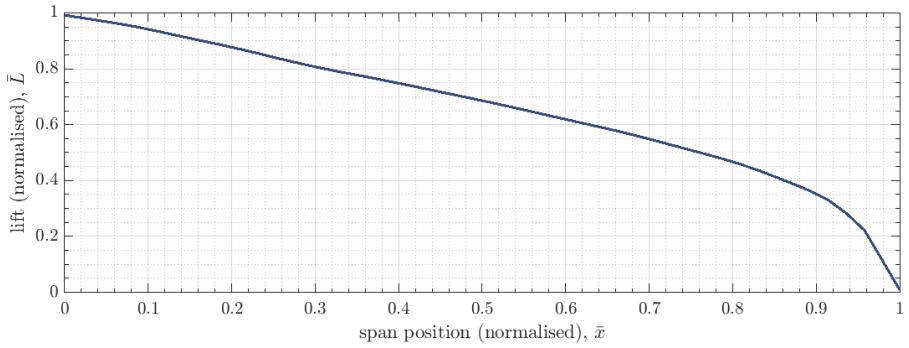

(c) AVL predicted lift distribution

Figure 6.18: AVL lift distribution (A-13 planform untwisted NACA 23012)

Vortex Lattice (AVL) code (Figure 6.18) that is based in work of Lamar [94], and Lan [113]. The state vector output from BeaRDS^{TM} for the static load case is given in Figure 6.19 and used to determine the theoretical static deflection of the wing, which gives a maximum tip deflection of 210mm or 28% of the semi-span from the gravitationally loaded condition of the wing.

Images acquired by the camera are then used in a sensors fusion algorithm, such as the Kalman filter, to estimate the displacement of the wing. Figure 6.22 shows four frames taken from the high speed camera recording during wind tunnel tests run in the Weybridge wind tunnel facility in Cranfield University. As expected, the model is highly flexible and bends at the elastic pods. The displacement output from the wind tunnel test is shown for the tip displacement in Figure 6.21, where each of the frame locations of Figure 6.22 are highlighted.

The following conclusions can be drawn from the static test:

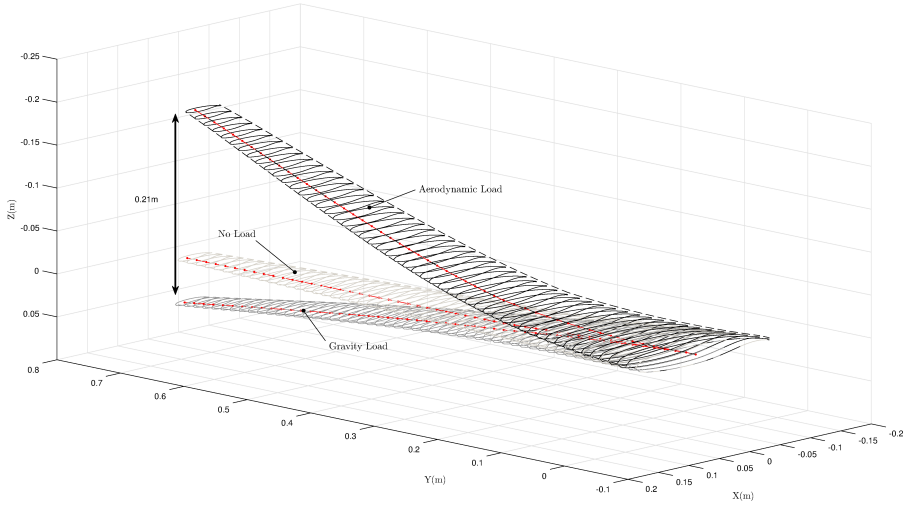

Figure 6.19: BeaRDS XB-1 static deflection prediction using BeaRDS^{TM} solver

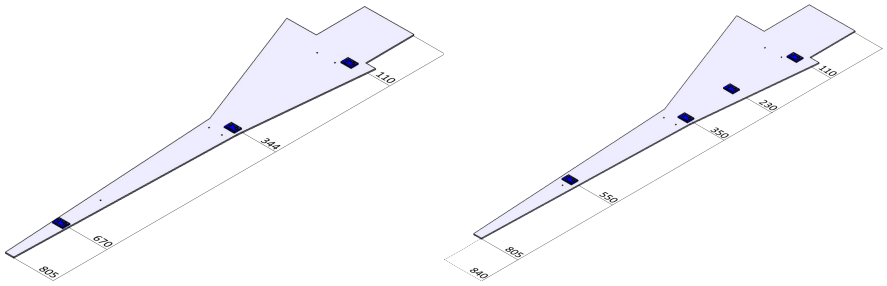

(a) IMU position (b) IMU position

Figure 6.20: IMU position

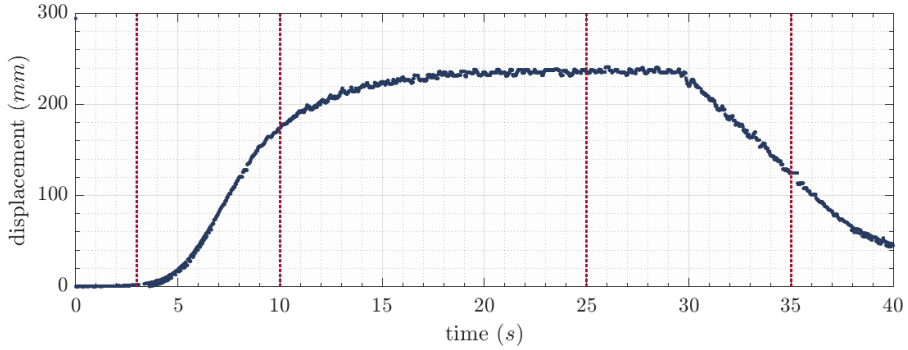

Figure 6.21: BEARDS XB-1 modal response of shaker test

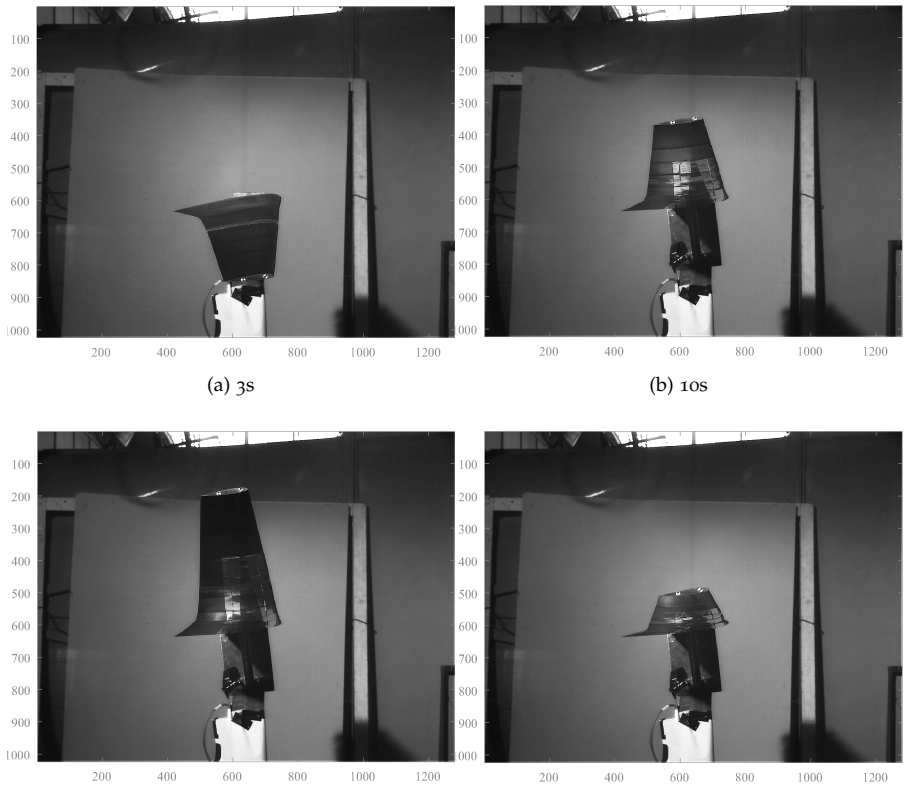

(a) 3s (b) 10s

(c) 25s (d) 35s

Figure 6.22: High speed camera frames at designated times during static test

- The static response is well predicted by the BeaRDS^{TM} solver for the given flight condition
- The slight underestimate from BeaRDS^{TM} is likely down to manufacturing tolerance on the spar thickness, and areas of material that had to be removed to ease assembly. The prediction of the deformation due to gravitational loading (Figure 6.19) only accounts for the load due to the spar mass, as prior to manufacture it was assumed this would dominate the mass term. The aerodynamic skin was delivered and was heavier than expected. For future work the skin has to be included in the gravity loading of the initial position.
- The stiffness matrix used for the static response was constant, thus a linear analysis. If the wind tunnel model was subject to non-linear structural behaviour it is expected the wing would get stiffer. Given no evidence for non-linearity has been seen, it is apparent a slender structure such as a wing can deform up to 28% of its semi-span and still be accurately modelled with a linear solver.
- The aerodynamic cover used to represent the planform area and aerodynamic shape does not add to the stiffness of the model. Thus modelling just spar stiffness for predictions seems adequate.
- This static test validates the aerodynamics model and stiffness matrix used in the BeaRDS^{TM} solver.

6.2.5 *BeaRDS^{TM} Dynamic Response*

Due to the high impact of the aerodynamic skin mass on the static deflection (initial condition), and the fact the mass distribution of the skin is unknown. To validate the BeaRDS^{TM} dynamics this section will consider the dynamic response of just the spar. As outlined in Appendix C, the mass matrix is modelled as a simple lumped mass matrix, defined as

$$[M_e] = \rho A l_e \begin{bmatrix} \frac{1}{2} & 0 & 0 & 0 & 0 & 0 \\ 0 & \frac{1}{2} & 0 & 0 & 0 & 0 \\ 0 & 0 & \frac{1}{2} & 0 & 0 & 0 \\ 0 & 0 & 0 & 0 & 0 & 0 \\ 0 & 0 & 0 & 0 & 0 & 0 \\ 0 & 0 & 0 & 0 & 0 & 0 \end{bmatrix}$$

$$[M] = \begin{bmatrix} [M_1] & 0 & 0 & \cdots & 0 & 0 \\ 0 & [M_1]+[M_2] & 0 & \cdots & 0 & 0 \\ 0 & 0 & [M_2]+[M_3] & \ddots & \vdots & \vdots \\ \vdots & \vdots & \ddots & \ddots & 0 & 0 \\ 0 & 0 & \cdots & 0 & [M_{n-1}]+[M_n] & 0 \\ 0 & 0 & \cdots & 0 & 0 & [M_n] \end{bmatrix}$$

Coupling the mass and stiffness matrix an eigenvalue analysis can be undertaken to evaluate the modal response of the system. Matching the predicted modal frequencies and shapes from the theoretical model to that of an experiment provides confidence in the dynamics of the BeaRDS^{TM} framework. The dynamic analysis uses the Matlab inbuilt QZ factorization for generalized eigenvalues of the mass and stiffness matrices. The eigenvalues and eigenvector output is given in Table 6.3 and graphically in Figure 6.23.

Validation of the BeaRDS^{TM} solver for the dynamic response is required, as such a modal response Ground Vibration Test (GVT) has been conducted using a frequency sweep on a shaker. The test set up and data analysis is detailed in Pontillo [134].

Table 6.3: BEARDS^{TM} Eigenvalue Analysis of A-13 spar

Mode no.	Eigenvalue $\times 10^6$	Frequency rad	Frequency Hz	Mode
1	0.0014	37.7	6.0	1st Bending YZ
2	0.0203	142.6	22.7	2nd Bending YZ
3	0.1328	364.4	58.0	3rd Bending YZ
4	0.2087	456.8	72.7	4th Bending YZ
5	0.9073	952.5	151.6	5th Bending YZ
6	1.4207	1191.9	189.7	6th Bending YZ

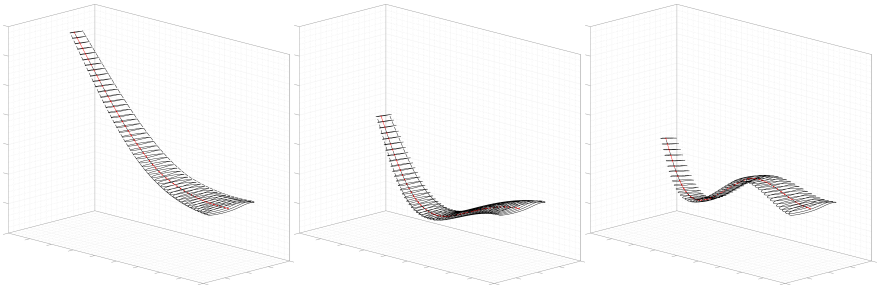

(a) Mode 1 (6.0Hz) (b) Mode 2 (22.7Hz) (c) Mode 3 (58.0Hz)

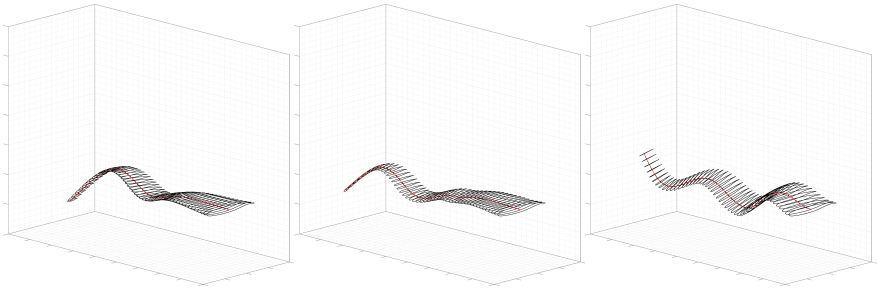

(d) Mode 4 (72.7Hz) (e) Mode 5 (151.6Hz) (f) Mode 6 (189.7Hz)

Figure 6.23: BEARDS XB-1 dynamic response prediction using BEARDS^{TM} solver

Table 6.4: Eigenvalue Analysis of A-13 spar, BeaRDS^{TM} and GVT comparison

Mode no.	Frequency (Hz)		Error	Mode
	BeaRDS^{TM}	GVT	%	
1	6.0	5.4	11.0	1st Bending YZ
2	22.7	22.3	1.7	2nd Bending YZ
3	58.0	55.3	4.9	3rd Bending YZ

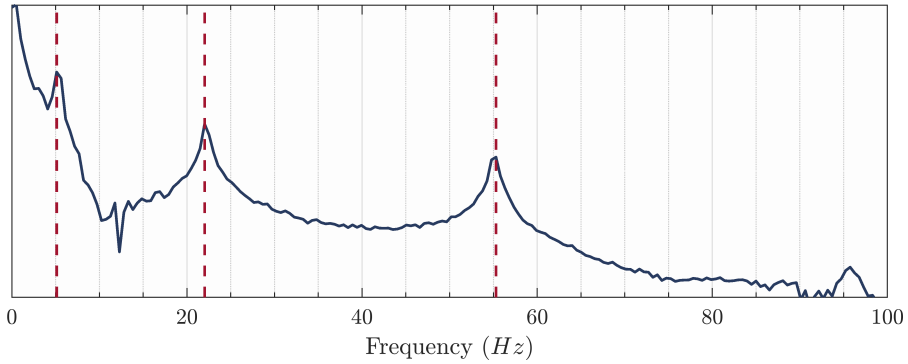

Figure 6.24: BeaRDS XB-1 modal response of shaker test

The Fast Fourier Transform (FFT) results from shaker testing are presented in Figure 6.24, the frequency identified is used to validate the predicted modes. The first three modes identified from the shaker test are 5.4Hz, 22.3Hz and 55.3Hz. The predicted structural modes of the A-13 scaled spar from the GVT are compared to the predicted values in Table 6.4.

The following conclusions can be taken from the dynamic validation exercise:

- The predicted modes match to the GVT results is considered acceptable for validation of the model dynamics.
- The 11.0% error in the first modal frequency is likely due to variations in the test set up compared to the assumed constraints in the theoretical model, and some experimental error in the test results can be expected.
- The match between mode frequencies suggests the stiffness and mass matrices used in the BeaRDS^{TM} framework are correct. Which supports the conclusion from the static test that the larger displacement measured in the wind tunnel test is due to the additional mass of the skin providing a higher deformation as the initial condition.

6.3 CHAPTER SUMMARY

This chapter has studied the capability to perform exergy analysis as a part of aeroelastic analysis, where the aerodynamic loading and structural dynamic response are coupled. Building on the work from Chapter 5, it was shown that any deformation in the wing from the trimmed cruise position (considered optimal) has a negative impact on the exergetic aerodynamic efficiency of the aircraft. Looking at this in more detail with a CFD analysis comparison of an inelastic aircraft, against a frozen deformed elastic aircraft, showed the primary reason for the lower efficiency was an increase in the mechanical exergy in the fluid driven by the need for a higher aerodynamic force to generate the same lift. This results in higher induced drag and vorticity.

The capability to perform exergy analysis on a dynamic aeroelastic system was demonstrated on a simple 2D aeroelastic wing section, for which the method was extended and coupled with the BEAR framework from Chapter 4 to develop the aeroelastic BEARDS^{TM} framework. The chapter concluded by validating the BEARDS^{TM} framework, which allows its use later in the thesis for aeroelastic response of scaled technologies, which is to be shown in Chapter 8.

The chapter also concludes the thesis part, where the knowledge and capability of exergy analysis has been extended beyond what is available in literature in all major nodes of Collar's triangle. This proves that exergy analysis is a capable and useful tool for the analysis of multi-discipline systems that typically make up aeroelastic analysis.

Part III

APPLICATION OF EXERGY ANALYSIS TO AEROSPACE SYSTEMS

"Just like a computer, we must remember things in the order in which entropy increases. This makes the second law of thermodynamics almost trivial. Disorder increases with time because we measure time in the direction in which disorder increases. You can't have a safer bet than that!"

Stephen Hawking
A Brief History of Time: From the Big Bang to Black Holes
1988

7

HIGH ASPECT RATIO WINGS

Pressure to build ever more fuel-efficient aircraft has come in answer to the *climate targets* that have been laid out in *Flightpath 2050* by the European Commission [63] in support of the Air Transport Action Group (ATAG) [2] targets. Moreover, with rising fuel prices airlines are looking to maintain if not increase profits by minimising fuel usage. However the International Energy Agency [84] has highlighted a trend that conventional aircraft configurations are near *optimised*, demonstrated by the plateauing improvements in *energy intensity*[1]. Therefore, for aviation to remain sustainable both environmentally and economically, manufacturers are researching revolutionary technologies and configurations.

One such revolutionary configuration is that of High Aspect Ratio Wing (HARW) aircraft. Consider the de Havilland Comet to the similar geometric and mass sized Airbus A320 in Figure 7.1. Evolutionary improvements to conventional configurations have led to aircraft now being 70% more fuel efficient per seat kilometre, than the early de Havilland Comet. One reason for this is the aspect ratio of the more modern A320 is significantly larger, as increased aspect ratio improves aerodynamic efficiency (lift-to-drag ratio), due to a reduced induced drag,

$$C_{D_i} = \frac{C_L^2}{\pi e \mathcal{AR}} \tag{7.1}$$

providing a more energy efficient aircraft. This trend is apparent in Figure 7.2, that with the evolution in commercial aircraft there has been a general increase in wing aspect ratio with each design iteration, with some exceptions such as that of the Airbus A380. Similar improvements to HARW aerodynamic efficiency can be found

1 *Energy Intensity* is a measure of aircraft fuel economy, stating the amount of energy required to move one passenger one kilometre

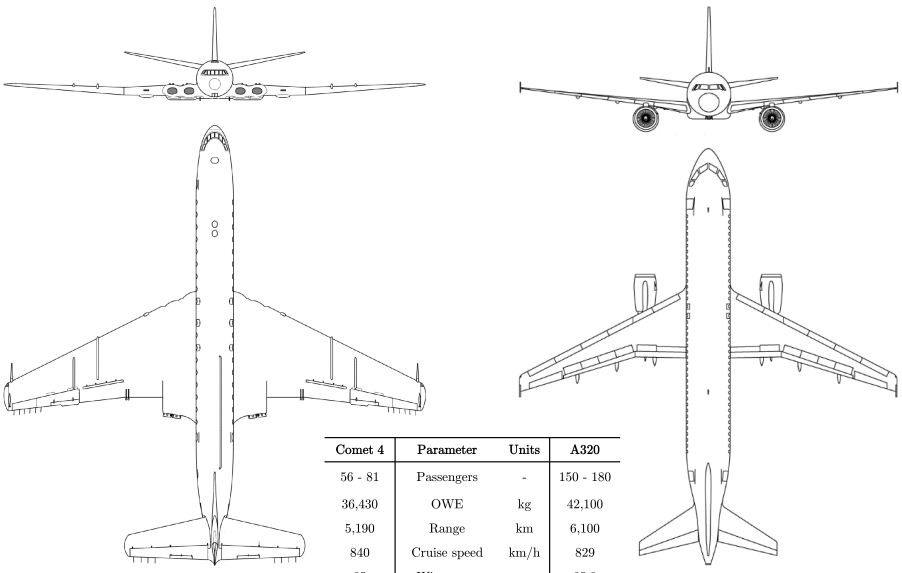

Comet 4	Parameter	Units	A320
56 - 81	Passengers	-	150 - 180
36,430	OWE	kg	42,100
5,190	Range	km	6,100
840	Cruise speed	km/h	829
35	Wing span	m	35.8
197	Wing area	m^2	122.4
6.24	Aspect Ratio	-	9.5

Figure 7.1: Evolution of Commercial Aircraft Wing Planform

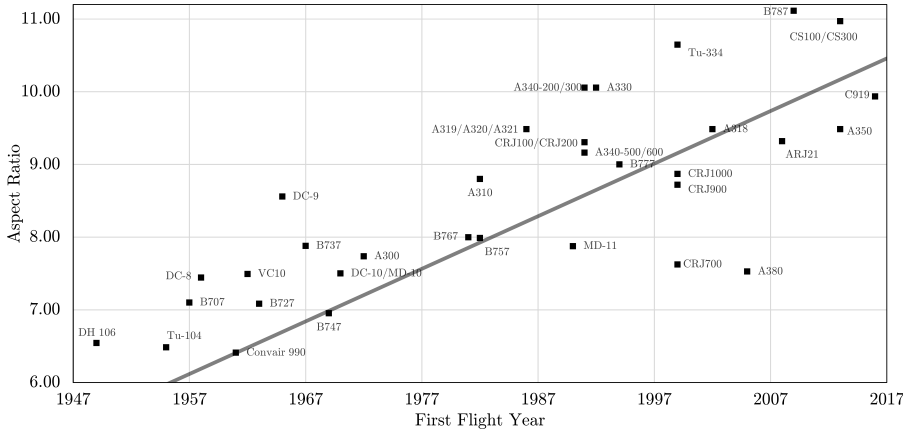

Figure 7.2: Commercial Aircraft Aspect Ratio Trend

(a) Boeing 777X Aircraft

(b) NASA/Boeing Subsonic Ultra Green Aircraft Research (SUGAR)

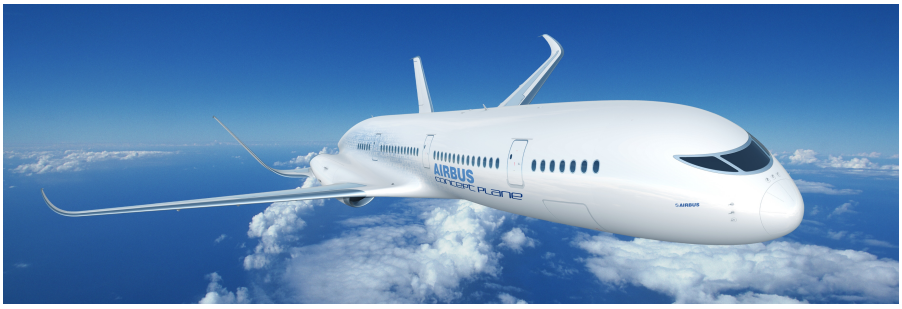

(c) Airbus Concept Plane

Figure 7.3: High Aspect Ratio Wing Aircraft

with the incorporation of span extension technologies. Where the wing span of aircraft is typically limited by the gate constraints of airports. The addition of winglets has provided the semblance of a larger wing span (hence aspect ratio) without changing the aircraft maximum span. This reduces induced drag but does not provide the additional lifting surface a true wing extension would imply.

This proven improvement in design by increasing the aspect ratio of the wings is leading to the development of higher aspect ratio aircraft, such as the current generation Boeing 777X, Figure 7.3a, which incorporates morphing wing and span extension technologies. In the near future conventional fuselages may be seen with strut braced HARW, one such concept is the NASA/Boeing Subsonic Ultra Green Aircraft Research (SUGAR) Volt [30], Figure 7.3b. Revolutionary concepts that move away from the conventional configuration for commercial aircraft are also being proposed utilising the benefits of HARW, such as the Airbus concept plane, Figure 7.3c.

High Aspect Ratio Wing (HARW) aircraft configurations reduce the induced drag on an aircraft during cruise, and as such improve the range and energy efficiency of an aircraft. In a gust event with elongated lightweight wings there is an increase in flexibility, and an imposed higher wing root bending moment, leading to designs either having to increase the weight of the aircraft at the root, potentially negating the benefit of reduced drag, or implementing unconventional aircraft design features, such as gust load alleviation devices, such as struts or braces.

This chapter will use exergy analysis derived methods from Chapter 5 to size a conceptual HARW aircraft, that aims for an in service date similar to the Boeing SUGAR. As such XB-2 will use the fuselage, Vertical Tail Plane (VTP) and Horizontal Tail Plane (HTP) of a conventional short haul aircraft, with a novel low configuration HARW with no strut or brace.

7.1 DEVELOPING THE EXPERIMENTAL BEARD 2 AIRCRAFT

The eXperimental Beard 2 (XB2) aircraft looks to develop a conceptual HARW version of the Airbus A320. In order to facilitate this the following requirements are put in place:

- The aircraft is to have the same OWE and MTOW as an Airbus A320
- The fuselage, HTP and VTP are to be taken from the Airbus A320
- The reference area of the XB2 wing will be equal to the Airbus A320
- The wing root bending moment (WRBM) for the trimmed cruise condition is to be equal to that of an Airbus A320, assuming an optimal elliptic distribution for the baseline aircraft (Figure 7.4a).
- The XB2 wing will have a variable chord constant aerofoil profile of the NACA 23014 (Figures 7.4b and 7.4c).
- A compromise to the efficiency improvement is that HARW aircraft typically fly at lower cruise speeds. The XB2 is thus assumed to cruise at Mach 0.6 as derived from the SUGAR aircraft [30]

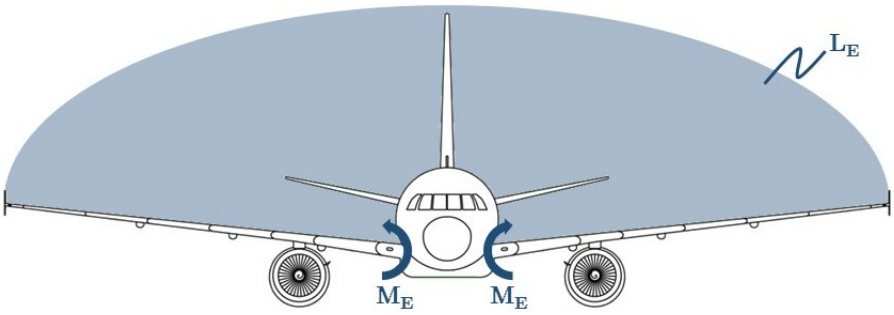

(a) Elliptic distribution on an Airbus A320

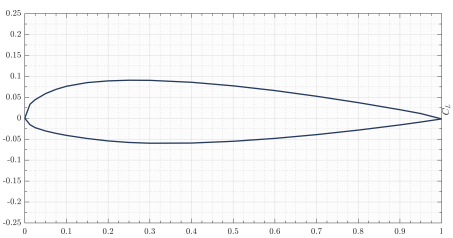

(b) NACA 23015 Aerofoil

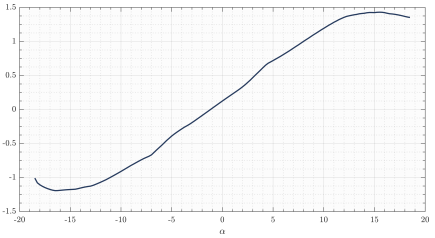

(c) C_{l_α} plot for NACA 23015

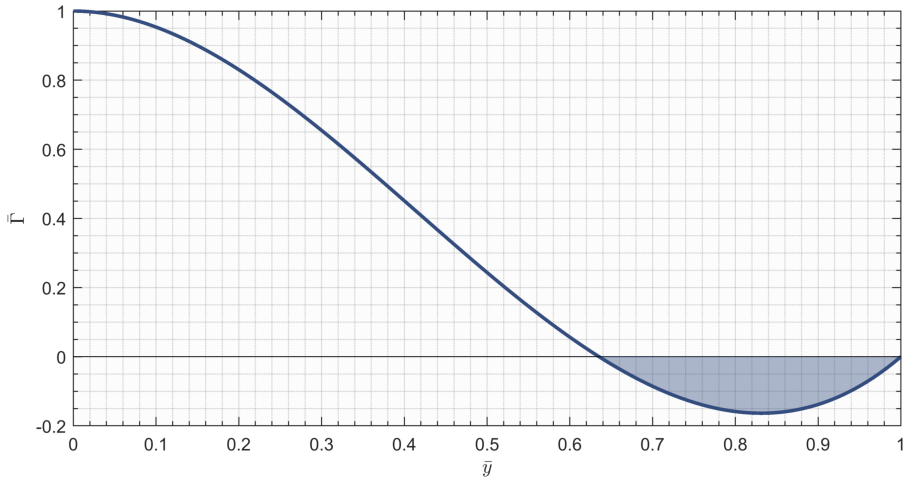

(d) Negative Circulation on Modified Parabola Distribution

Figure 7.4: Minimisation Conditions for XB-2 wing

The typical properties of an Airbus A320 are given in Table 7.2, which provides the baseline parameters for the unconstrained span exergeticically efficient circulation distribution given by Equation 5.31 (repeated below for clarity)

$$\Gamma = \frac{L}{\rho u_\infty s_0}\left[\frac{8\left(\frac{s}{s_0}\right)-5}{2\left(\frac{s}{s_0}\right)^2}\right]\left[1-\left(\frac{y}{\bar{s}}\right)^2-\frac{40\left(\frac{s}{s_0}-1\right)}{8\left(\frac{s}{s_0}\right)-5}\left\{\left(\frac{y}{s}\right)^2-\left(\frac{y}{s}\right)^3\right\}\right]$$

$$\frac{d\Gamma}{dy} = \frac{Ly}{\rho u_\infty s_0}\left[\frac{8\left(\frac{s}{s_0}\right)-5}{2\left(\frac{s}{s_0}\right)^2}\right]\left[\left(\frac{40\left(\frac{s}{s_0}-1\right)}{8\left(\frac{s}{s_0}\right)-5}\right)\left(\frac{3y-2s}{s^3}\right)-\frac{2}{\bar{s}^2}\right]$$

From Equation 5.28 the cost function for exergy destruction due to induced drag, to be minimised is a function of the circulation gradient

$$J(s) = K\mu\int_0^s\left(\frac{d\Gamma}{dy}\right)^2 dy$$

Given the requirements for the XB2 aircraft, minimising $[J(s)]_{\min}$ is subject to constraints on constant lift

$$\underbrace{\rho u_\infty\int_0^{s_0}\Gamma(y)dy}_{L_{A320}} = \underbrace{\rho u_\infty\int_0^{s}\Gamma(y)dy}_{L_{\mathrm{XB_2}}}$$

and constant WRBM

$$\underbrace{\rho u_\infty\iint_0^{s_0}\Gamma(y)dy^2}_{M_{A320}} = \underbrace{\rho u_\infty\iint_0^{s}\Gamma(y)dy^2}_{M_{\mathrm{XB_2}}}$$

such that s_0 is the baseline semi-span of an A320 with an elliptical distribution, and that

$$s_0 \neq s$$

finally to avoid negative lift distributions such as the *Greene (M_P)* in Figure 5.13a the circulation is constrained to always be positive

$$\Gamma \geq 0$$

a distribution that would conflict with this constraint is shown in Figure 7.4c.

Using a simple inbuilt Matlab minimisation routine, the cost function (exergy destruction) is minimised using the Greene unconstrained span parabola circulation distribution, at

- an optimal span of $48m$
- an Aspect Ratio of 18.8

The optimised circulation distribution (normalised to the root circulation of the baseline elliptic distribution) can be seen in Figure 7.5a against the A320 assumed elliptic distribution. The exergy optimised distribution has been constrained to provide the same lift and WRBM of the baseline A320, as seen in Figure 7.5b. In order to give the lift distribution seen in Figure 7.5b a twist distribution is defined as plotted against the spanwise chord lengths, in Figure 7.5c. To produce the same lift as the A320 the planform area $S_{A320} = S_{XB2}$ must be equal, and assuming the wing taper ratio of

Table 7.1: Control surface coordinates for the XB2 wing

Control Surface	Coordinates (X,Y)			
Aileron	(2.40, 18.00)	(1.80, 18.00)	(1.44, 22.70)	(2.04, 22.70)
Spoiler 1	(2.54, 6.00)	(2.09, 6.00)	(1.97, 8.06)	(2.42, 8.06)
Spoiler 2	(2.18, 13.00)	(1.73, 13.00)	(1.62, 15.06)	(2.07, 15.06)

the SUGAR [30] of $\lambda = 0.35$. For simplicity the wing is assumed to have zero sweep on the quarter chord line $\Lambda_{\frac{c}{4}} = 0$ with a dihedral angle of 0. Thus

$$c_r = \frac{2\left(\frac{0.5S}{s}\right)}{1+\lambda} = 3.78m$$
$$c_t = \lambda c_r = 1.32m$$
$$MAC = \frac{2c_r}{3}\left(\frac{1+\lambda+\lambda^2}{1+\lambda}\right) = 2.75m$$

This provides a leading edge sweep $\Lambda_{LE} = 1.47^o$ and trailing edge sweep $\Lambda_{TE} = -4.39^o$. For the purposes of the BeaRDS programme the wing is to have one outboard aileron and two spoilers. Due to the similarity in span, the spoiler and aileron can be read across from the work on the SUGAR [30] to be used as a initial locations for control surface sizing that will be refined as apart of the BeaRDS programme. Figure 7.5d gives an overview of the planform geometry and control surface locations (see Appendix B for further details on the XB-2 aircraft).

The wing is designed to be flexible, such that the structure deflects $< 20\%$ for the twisted lift distribution, such that the deformations can be assumed linear. Thus, defining isotropic wing material properties in line with generic composite wing design properties, the elastic modulus, E, shear modulus, G, and the poisson ratio, v can be defined as

$$E = 5e10$$
$$G = 1.92e10$$
$$v = 0.3$$

The structure geometry, Area, A, Second moment of area, I_{xx},I_{zz} and the second polar moment of area, J_y are assumed to vary linearly along the span, with the coefficients being defined as to provide the required deflections. The structural axis is assumed to follow the quarter chord line of the aerofoil. The wing is assumed to have a total mass of $5000kg$, that follows the same linear trend as the geometry.

A comparison of the properties of the Airbus A320 and the XB2 HARW concept can be seen in Table 7.2, and a simple drawing of the XB2 aircraft can be seen in Figure 7.7.

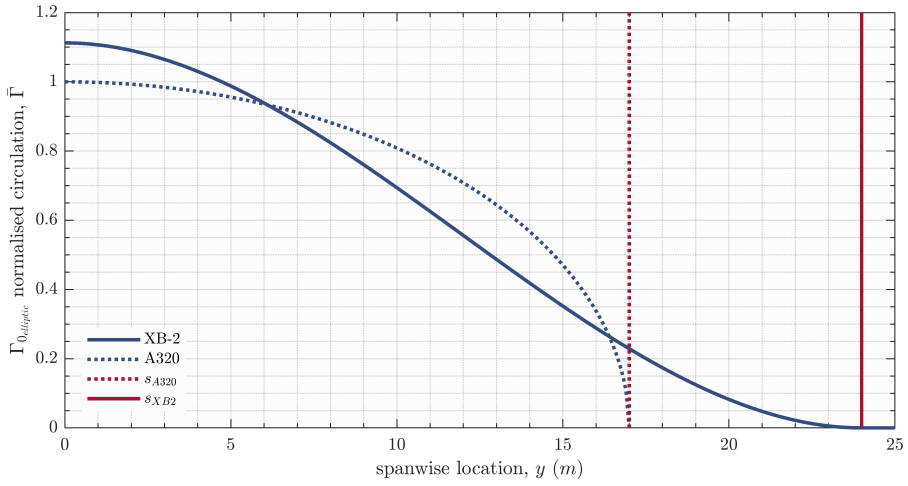

(a) XB2 optimised circulation distribution

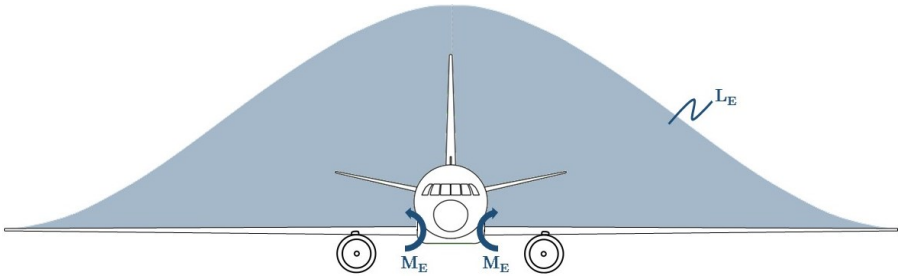

(b) Modified parabolic distribution on XB2 provdes the same lift and WRBM as A320

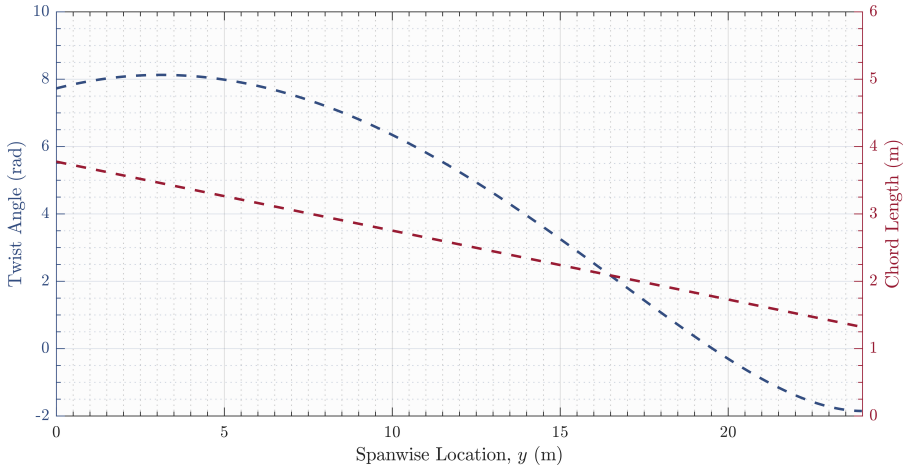

(c) XB2 wing twist distribution and chord lengths

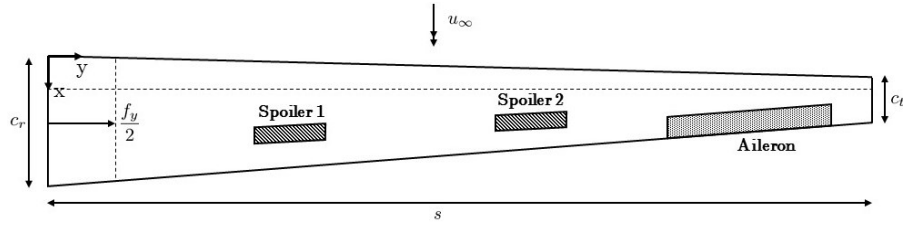

(d) XB-2 wing planform

Figure 7.5: eXperimental Beard 2 (XB2) Development

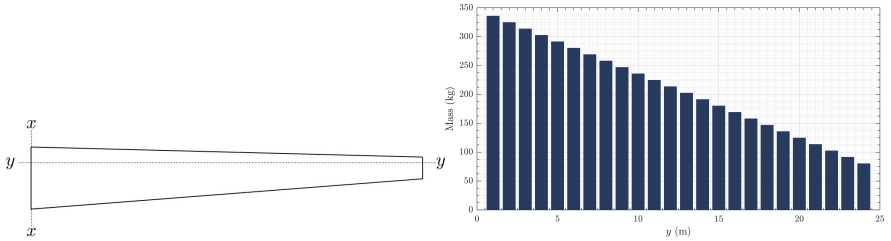

(a) XB2 wing structural axis

(b) Mass distribution on wing

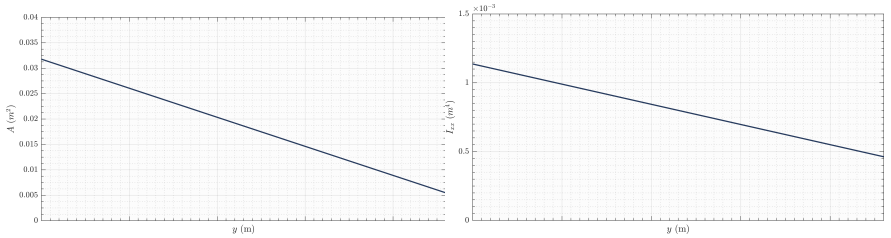

(c) Area

(d) Second Moment of Area

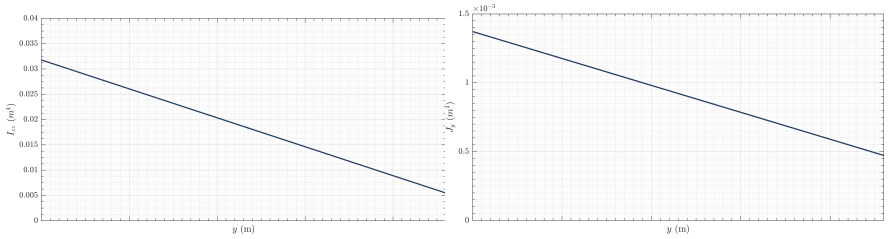

(e) Second Moment of Area

(f) Polar Second Moment of Area

Figure 7.6: Structural variables

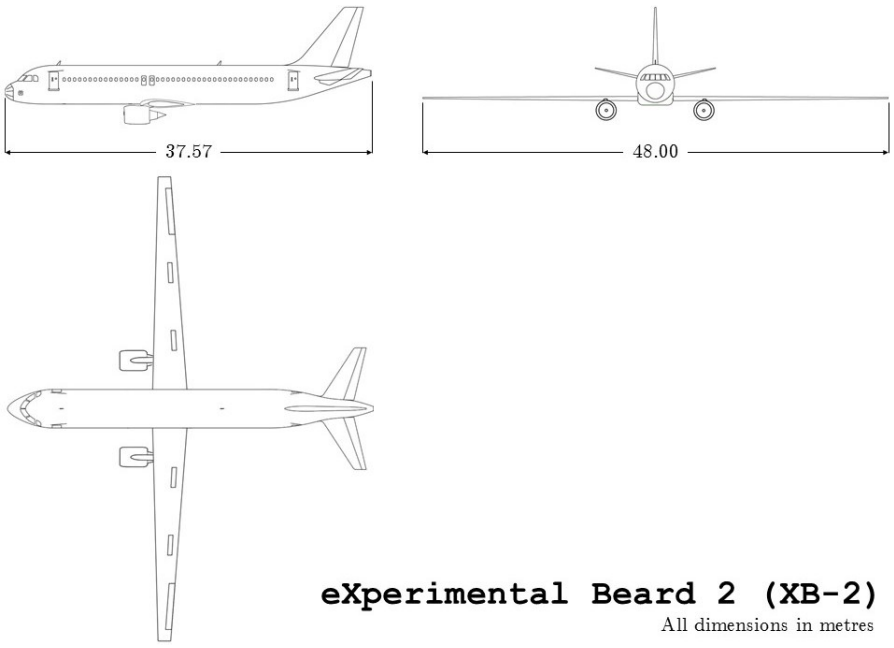

Figure 7.7: eXperimental Beard 2 (XB2) drawing

Table 7.2: Airbus A320 Aircraft Parameters

	Parameter	Symbol	Units	A320	XB2
Performance	Operating Weight Empty	OWE	kg	42,100	42,100
	Maximum Take-Off Weight	$MTOW$	kg	73,500	73,500
	Maximum Payload Weight	W_{pay}	kg	20,400	20,400
	Cruise Altitude	h	m	11,280	11,280
	Cruise Velocity	u_∞	M	0.78	0.6
	Range (typical)	R	km	4,800	>4,800
	Powerplant (x2)			CFM56	gFan+2
	Thrust (x2)	T	kN	111.2	102.3
	Specific Fuel Consumption	SFC	$g/kN/s$	16.88	13.27
	Fuel Consumption (cruise)	$\dot{M}_f$	kg/h	2100	
Body	Length	f_l	m	37.57	37.57
	Fuselage height	f_z	m	4.14	4.14
	Fuselage width	f_y	m	3.95	3.95
Aerofoil	Aerofoil			BAC 449	NACA
	Thickness ratio	$\frac{t}{c}$	–	0.113	0.150
	Lift at zero AoA	C_{l_0}	–	0.208	0.125
	Zero lift AoA	α_0	rad	0.031	-0.022
Planform	Span	b	m	34.09	48.00
	Aspect Ratio	Æ	–	9.5	18.8
	Reference area	S_{ref}	m^2	122.4	122.4
	Sweep (LE)	Λ_{LE}	rad	0.471	0.026
	Sweep ($\frac{c}{4}$)	$\Lambda_{\frac{c}{4}}$	rad	0.436	0.000
	Root Chord	c_b	m	6.10	3.78
	Streamwise c_b position	x_b	m	12.55	-
	Tip Chord	c_t	m	1.62	1.32
	Streamwise c_t position	l_t	m	20.35	
	Taper Ratio	λ	–	0.240	0.350
	MAC	$\bar{c}$	m	4.29	2.75

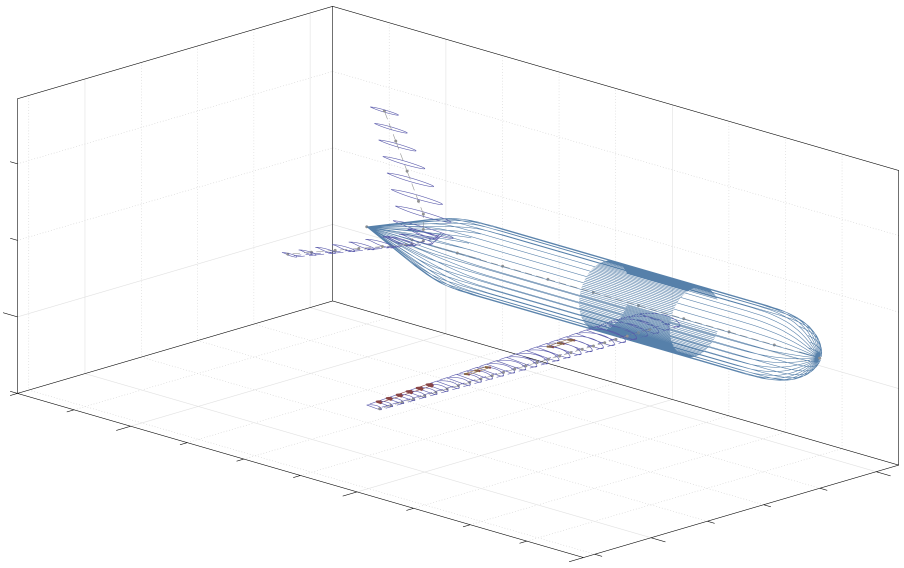

Figure 7.8: eXperimental Beard 2 (XB2) aircraft - Matlab model

7.2 ANALYSIS OF THE AIRCRAFT

Using the BEAR code from chapter 4 the mass and stiffness matrices for the XB2 wing can be generated and seen in the Appendix B. The stiffness matrix is developed using the same linear Timoshenko matrix as the A-13 wing in Chapter 6, however in place of the lumped mass matrix, a consistent mass matrix based on the work of Przemieniecki [138] is used, generated using the matrices in Equation 7.2.

$$[M_{e,1}] = \rho A l_e \begin{bmatrix} \frac{1}{3} & 0 & 0 & 0 & 0 & 0 \\ 0 & \frac{13}{35} + \frac{6I_z}{5Al^2} & 0 & 0 & 0 & \frac{11l}{210} + \frac{I_z}{10Al} \\ 0 & 0 & \frac{13}{35} + \frac{6I_y}{5Al^2} & 0 & -\frac{11l}{210} - \frac{I_y}{10Al} & 0 \\ 0 & 0 & 0 & \frac{J_x}{3A} & 0 & 0 \\ 0 & 0 & -\frac{11l}{210} - \frac{I_y}{10Al} & 0 & \frac{l^2}{105} + \frac{2I_y}{15A} & 0 \\ 0 & \frac{11l}{210} + \frac{I_z}{10Al} & 0 & 0 & 0 & \frac{l^2}{105} + \frac{2I_z}{15A} \end{bmatrix}$$

$$[M_{e,2}] = \rho A l_e \begin{bmatrix} \frac{1}{3} & 0 & 0 & 0 & 0 & 0 \\ 0 & \frac{13}{35} + \frac{6I_z}{5Al^2} & 0 & 0 & 0 & -\frac{11l}{210} - \frac{I_z}{10Al} \\ 0 & 0 & \frac{13}{35} + \frac{6I_y}{5Al^2} & 0 & \frac{11l}{210} + \frac{I_y}{10Al} & 0 \\ 0 & 0 & 0 & \frac{J_x}{3A} & 0 & 0 \\ 0 & 0 & \frac{11l}{210} + \frac{I_y}{10Al} & 0 & \frac{l^2}{105} + \frac{2I_y}{15A} & 0 \\ 0 & -\frac{11l}{210} - \frac{I_z}{10Al} & 0 & 0 & 0 & \frac{l^2}{105} + \frac{2I_z}{15A} \end{bmatrix}$$

$$[M_{e,3}] = \rho A l_e \begin{bmatrix} \frac{1}{6} & 0 & 0 & 0 & 0 & 0 \\ 0 & \frac{9}{70} - \frac{6I_z}{5Al^2} & 0 & 0 & 0 & \frac{13l}{420} - \frac{I_z}{10Al} \\ 0 & 0 & \frac{9}{70} - \frac{6I_y}{5Al^2} & 0 & -\frac{13l}{420} + \frac{I_y}{10Al} & 0 \\ 0 & 0 & 0 & \frac{J_x}{6A} & 0 & 0 \\ 0 & 0 & \frac{13l}{420} - \frac{I_y}{10Al} & 0 & -\frac{l^2}{140} - \frac{I_y}{30A} & 0 \\ 0 & -\frac{13l}{420} + \frac{I_z}{10Al} & 0 & 0 & 0 & -\frac{l^2}{140} - \frac{I_z}{30A} \end{bmatrix}$$

$$[M_E] = \begin{bmatrix} [M_{1,1}] & [M_{1,3}] & 0 & \cdots & 0 & 0 \\ [M_{1,3}]^T & [M_{1,2}] + [M_{2,1}] & [M_{2,3}] & \cdots & 0 & 0 \\ 0 & [M_{2,3}]^T & [M_{2,2}] + [M_{3,1}] & \ddots & \vdots & \vdots \\ \vdots & \vdots & \ddots & \ddots & [M_{n-1,3}] & 0 \\ 0 & 0 & \cdots & [M_{n-1,3}]^T & [M_{n-1,2}] + [M_{n,1}] & [M_{n,3}] \\ 0 & 0 & \cdots & 0 & [M_{n,3}]^T & [M_{n,2}] \end{bmatrix} \tag{7.2}$$

The consistent mass matrix is used in place of the lumped mass matrix, as the latter is highly sparse and contains singularities. This can cause errors when inverting, and the process is required to solve the equations of motion. Note that the consistent mass matrix is also quite sparse (but less so than the lumped matrix), thus singular value decomposition is used for the inversion of the matrices. With the mass and stiffness matrices defined, aerodynamic loads can be generated and the static and dynamic response of the XB-2 wing can be assessed.

Using the circulation distribution calculated in Figure 7.5a, the lift distribution for the exergertic optimised distribution can be applied to the aircraft, with the resultant deflection shown in Figure 7.9a, which corresponds to a 12.5% deflection of the semi span. To show the benefits of the exergertic optimised distribution, AVL is used to define a lift distribution with the same total lift, but without the twist distribution of the wing from Figure 7.5c. Figure 7.9b shows the deformed wing shape under this untwisted load. Note that with a higher WRBM, due to more lift outbound of the root, the deflection is significantly higher than the exergertic optimised distribution,

Table 7.3: Eigenvalue Analysis of XB-2 aircraft

Mode no.	Eigenvalue	Frequency		Mode
		rad	Hz	
1	18.9	4.4	0.69	1st Bending YZ
2	472.5	21.7	3.46	2nd Bending YZ
3	482.9	21.8	3.50	1st Bending XY
4	1483.9	38.5	6.13	3rd Bending YZ
5	3222.7	56.8	9.03	4th Bending YZ
6	8083.4	89.9	14.31	Coupled

with a deflection of 27% of the semi-span. Figure 7.10 shows what the XB-2 aircraft would look like flying with an untwisted wing.

Coupling the mass and stiffness matrix, an eigenvalue analysis can be undertaken to evaluate the modal response of the system. The dynamic analysis uses the Matlab inbuilt QZ factorization for generalized eigenvalues of the mass and stiffness matrices. The eigenvalues and eigenvector output is given in Table 7.3 and shown graphically in Figure 7.11.

The mode frequencies for the XB-2 aircraft are lower than conventional aircraft, but this is due to the highly flexible nature of the HARW. Confidence can be sought in the results from validating the model is NASTRAN, which provides the same modes, and also the values are similar to those of other HARW aircraft, such as the Boeing SUGAR [30].

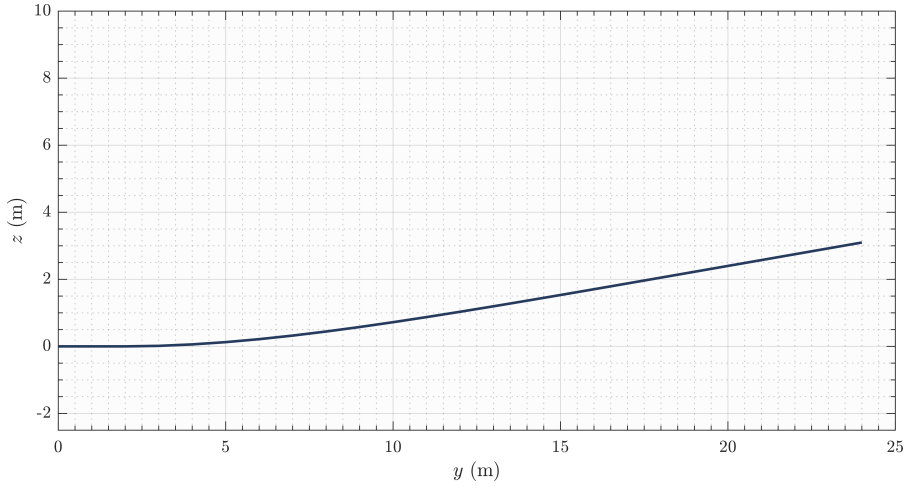

(a) Deformation of wing under twisted distribution

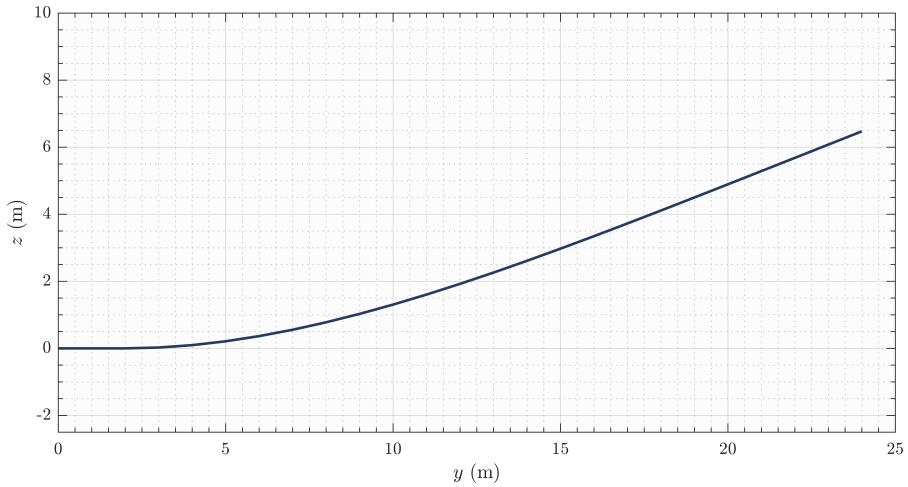

(b) Deformation of wing under untwisted distribution

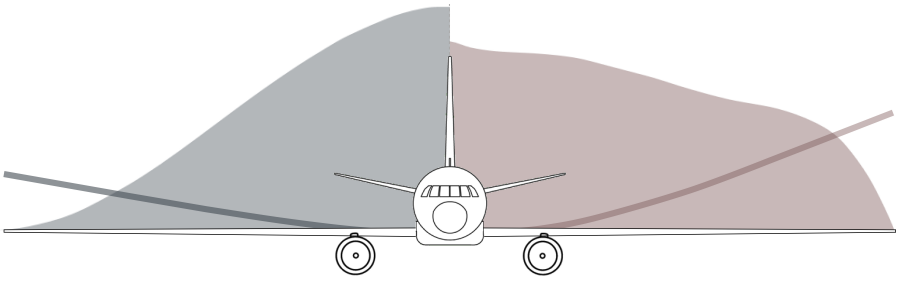

(c) Deformation of the wing shown with lift distributions

Figure 7.9: Static response of the XB-2 wing

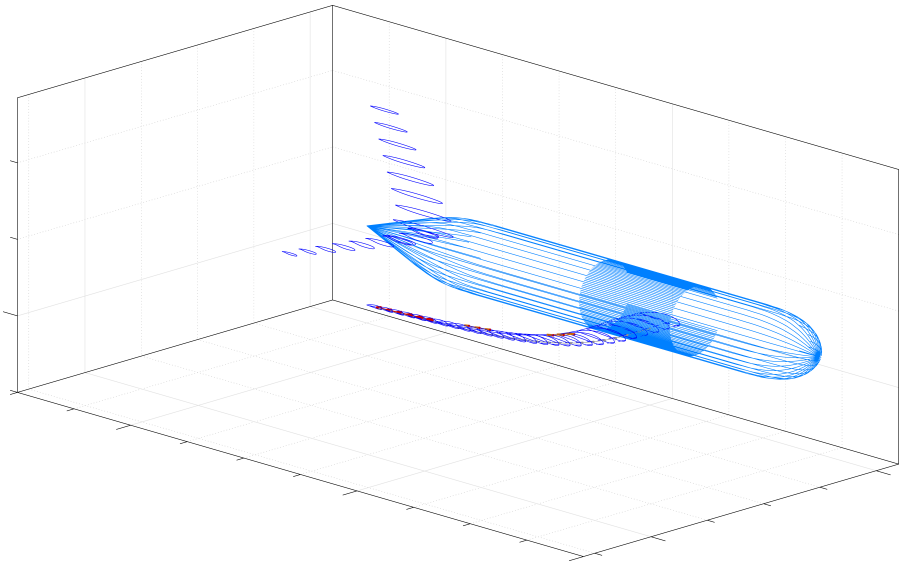

Figure 7.10: eXperimental Beard 2 (XB2) aircraft - Matlab model - deformed

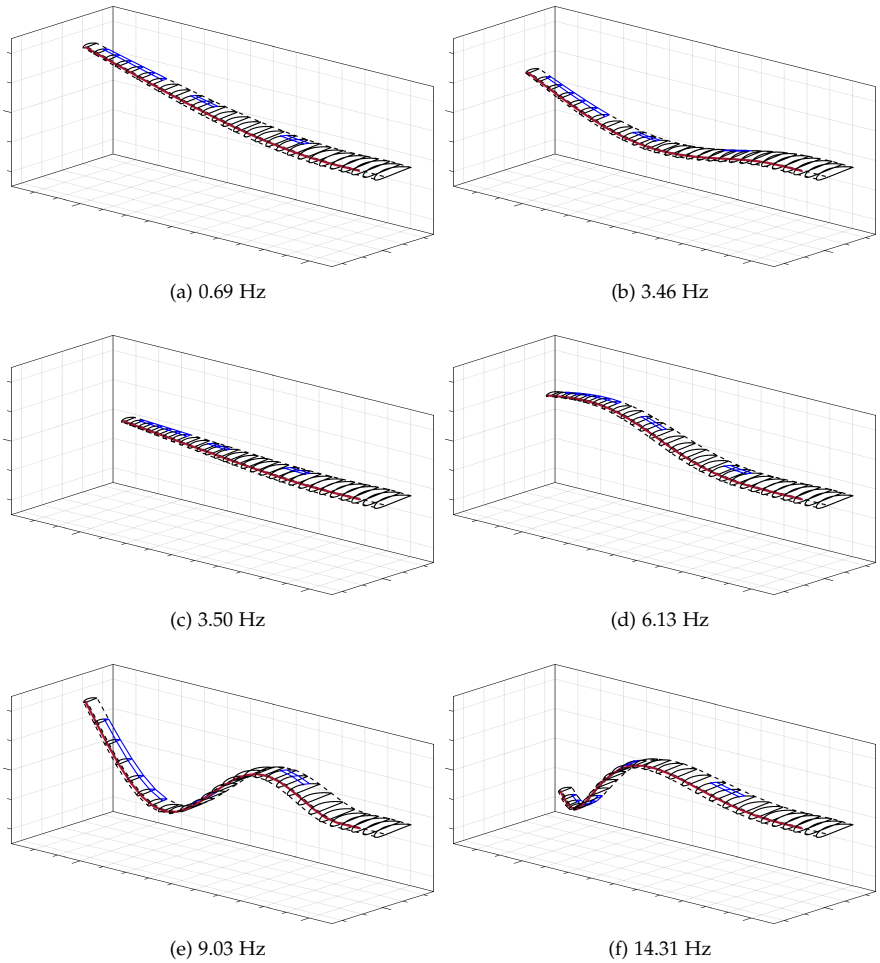

(a) 0.69 Hz

(b) 3.46 Hz

(c) 3.50 Hz

(d) 6.13 Hz

(e) 9.03 Hz

(f) 14.31 Hz

Figure 7.11: Cranfield XB-2 Mode Shapes

7.3 CHAPTER SUMMARY

This chapter has used the exergy destruction minimisation method outlined in Chapter 5 to generate a geometry for a HARW wing aircraft that uses the conventional fuselage, VTP and HTP of the Airbus A320. A structural definition is proposed for the wing geometry which draws influence from other HARW aircraft, notably the Boeing SUGAR and Bristol Ultra Green. The generation of this geometry shows exergy is not only a useful metric to analysis the performance of aircraft, but can also be used in the design and generation of geometry. This aircraft, the Cranfield XB-2, will be used in Chapter 9 looking at thermodynamic modelling of morphing wing aircraft and in Chapter 8 focusing on the aeroelastic response of scaled technologies.

8

AEROELASTIC RESPONSE OF SCALED TECHNOLOGIES

This chapter's content is in response to one of the fundamental research questions, as to whether

> *"exergy analysis is consistent with a scaled model when applied to a high fidelity real world problem?"*

This question came about as in the commercial aerospace industry improvements to system efficiency can be shown on a scaled model, such as a folding wingtip, however when the technology is scaled up to a full size aircraft the previously seen benefit is no longer apparent. Thus, this chapter applies the same exergy analysis to a full scale aircraft and a scaled aircraft to see if tracking exergy can highlight the difficulties in scaling technology.

Before the exergy analysis can show any disparity with the scaled and unscaled technology, it is required that the full size and scaled geometries are similar in static and dynamic behaviour. The importance of this principle of similitude was stated by Lord Rayleigh [142] stating he has

> *"often been impressed by the scanty attention paid even by original workers in physics to the great principle of similitude."*

The idea of similitude has been used extensively within the aerospace industry for validation of mathematical modelling tools and de-risking of novel concepts. Traditionally this idea, with the help of dimensional analysis, is most heavily applied within the aerodynamics domain to design experiments with geometrically scaled models such that the collected data is scalable. Wind tunnel tests are designed to ensure a degree of Reynolds number similarity and in other areas, test engineers strive to match other dimensionless parameters. Aircraft designs of the past ensured sufficient separation in these technical domains that allowed aerodynamicists to focus on geometric similarity, flight dynamicists to focus on mass and inertial similitude and structural engineers to focus on the scaling of bending and torsional stiffnesses. However, when HARW concepts are scaled the similitude of the scaled and full size aircraft needs to take a multi-disciplinary approach, to include areas such as aeroelasticity [145] and flight mechanics [89]. The principle of similitude is important in the field of aerodynamics and in this thesis, because scaled models must be analogous not only in shape to the full size concept, but also in the dynamic interactions. Only under these conditions can the concept or technology be de-risked and explored.

This work forms a part of the Cranfield University Beam Reduction and Dynamic Scaling (BEARDS) programme, where an aircraft wing is dynamically scaled and analysed with the output being validated via a wind tunnel test. Similar projects have been conducted on the NASA/Boeing Subsonic Ultra Green Aircraft Research (SUGAR) aircraft and the University of Washington Variable Camber Continuous Trailing Edge Flap (VCCTEF) on the NASA Generic Transport Model (GTM), see Figure 8.1. For these two cases the energy or exergy transfer in the system was not modelled, as such this additional analysis aims to provide contribution to knowledge in the field of dynamic scaling and testing of aircraft.

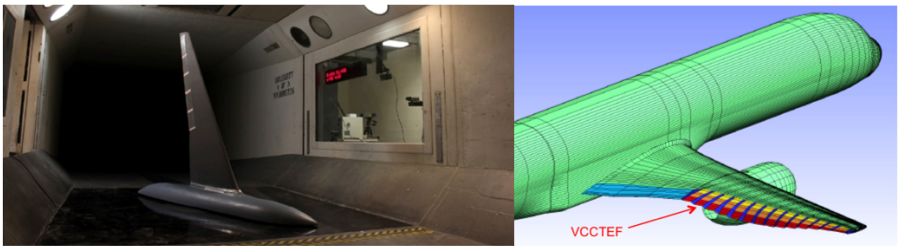

(a) University of Washington Variable Camber Continuous Trailing Edge Flap

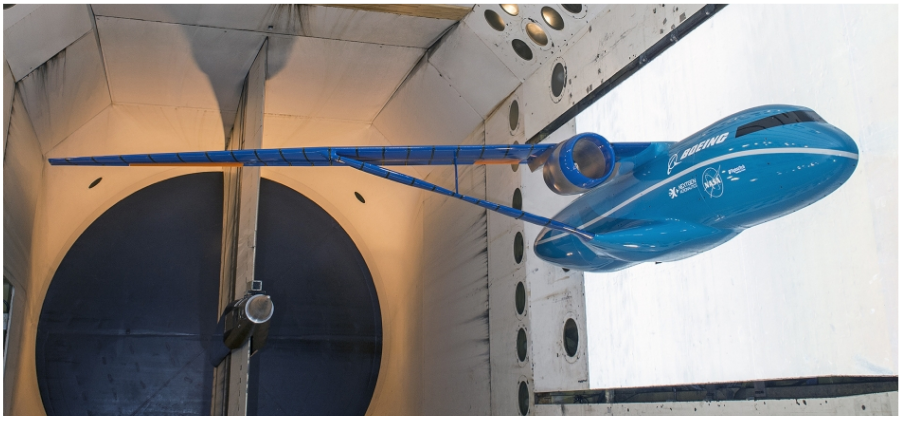

(b) NASA/Boeing Subsonic Ultra Green Aircraft Research (SUGAR)

Figure 8.1: Examples of other dynamically scaled wind tunnel test programmes

8.1 THE CRANFIELD BEARDS PROGRAMME

The Cranfield BeaRDS programme provides a framework that scales a conceptual full size HARW aircraft to a cantilevered wing model of suitable dimensions for Cranfield's 8'x6' wind tunnel, such that the dynamic response of the model is equivalent to the full size aircraft. Data acquisition from wind tunnel testing can then be used to validate fluid-structure interaction frameworks that model the aeroelastic response to the flight dynamics of the aircraft. The idea is to create a methodology that adopts scaling laws to allow experimental testing of wings that exhibit large deformations and flexible behaviour. Fully actuated Load Alleviation Functions (LAF) [119] may be tested, lowering structural loads by implementing both control surfaces [165] and folding wingtip control [42].

The work flow for the BeaRDS programme is shown in Figure 8.2, which splits the programme into the following critical activities: model order reduction; aeroelastic dynamic scaling; fluid-structure interaction modelling; spar and mass minimisation; modular design and manufacture; instrumentation methodology and testing; system identification; and model validation. Below, each of the activities are discussed in further detail.

1. **Model Order Reduction** for BeaRDS is the process of representing an aircraft's structural and aerodynamic properties via one-dimensional beam elements and nodes for the structural model of the aircraft and corresponding aerodynamic profile definitions at each of the nodes. Open source tools such as Neo-CASS (Next generation Conceptual Aero Structural Sizing) [43] can be used to generate such a model, however for BeaRDS a bespoke method is utilised. This method is outlined in Chapter 7, which defines the generation of a HARW aircraft geometry, designated eXperimental Beard 2 (XB-2), and utilises the

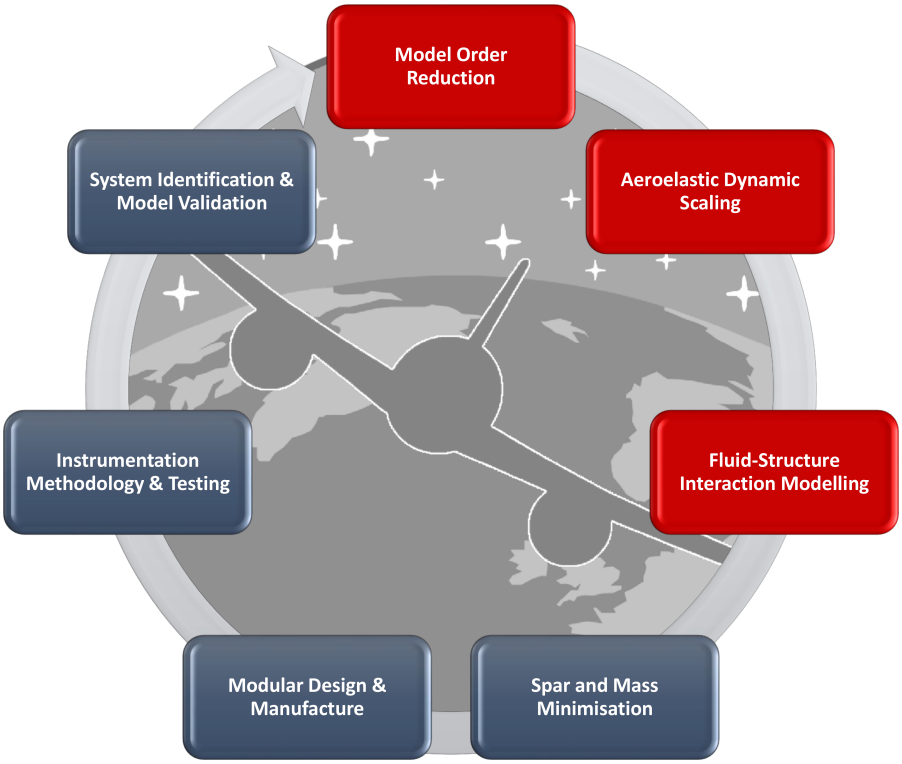

Figure 8.2: BEARDS Work Flow

BEAR code outlined in Chapter 4 to simulate the aircraft as a beam-element geometry.

2. **Aeroelastic Dynamic Scaling** is needed to ensure motion similitude of the full-scale and sub-scaled model [45]. The scaling law is derived based on geometrically nonlinear dynamic aeroelastic equation of motion [146], given in modal coordinates as:

$$\underbrace{[M]\ddot{\boldsymbol{\eta}} + [C]\dot{\boldsymbol{\eta}} + [K]\boldsymbol{\eta}}_{\text{structure}} = \underbrace{[A_k]\boldsymbol{\eta} + [A_c]\dot{\boldsymbol{\eta}} + [A_m]\ddot{\boldsymbol{\eta}}}_{\text{aerodynamics}} + \underbrace{[M]\boldsymbol{a}_g}_{\text{gravity}}$$

As a result, several non-dimensional parameters are required to be consistent between aircraft and model. The scaling process (discussed in more detail in Section 8.3) uses a methodology developed by Ricciardi [144–146] which develops a scaled representation with similitude to the real aircraft n terms of the Froude number, normalized eigenvectors and inertia and mass ratio. Thus the Reynolds number is not scaled. To artificially create Reynolds number similitude between the scaled and full size aircraft *trip wires* can be applied to the wing surface or wire meshes can be incorporated ahead of the model in the wind tunnel.

3. **Fluid-Structure Interaction Modelling** is predicted using BEARDS^{TM} outlined in Chapter 6, which couples structural and aerodynamic codes to ascertain the aeroelastic response. The structural dynamics are modelled using Timoshenko [176] beam bending theory, defined as:

$$EI\frac{\partial^4 w}{\partial y^4} + \rho A\frac{\partial^2 w}{\partial t^2} - \rho I\left(1 + \frac{E}{\kappa G}\right)\frac{\partial^4 w}{\partial y^2 \partial t^2} + \frac{\rho^2 I}{\kappa G}\frac{\partial^4 w}{\partial t^4} = q(y,t) + \frac{\rho I}{\kappa AG}\frac{\partial^2 q(y,t)}{\partial t^2} - \frac{EI}{\kappa AG}\frac{\partial^2 q}{\partial y^2}$$

The resultant ODEs are solved directly in the form of mass and stiffness matrices, using a *finite element* approach, including a non-linear pre-stressed stiffness

term as defined by Przemieniecki [138]. The model solves every nodal degree of freedom, but for computational efficiency there is an alternative Reduced Order Model (ROM) approach using modal states. The aerodynamic modelling is taken from the method used in CA^{2}LM that uses a Modified Strip Theory (MST) method, which includes an unsteady aerodynamic model in state space form based, on work by Theodorsen and Garrick [173, 174] and steady aerodynamic loads generated using modified strip theory for the wing as developed by Weissinger [181].

4. **Spar and Mass Minimisation** is applied in order to reproduce the mass and stiffness distribution of a scaled model. In the BEARDS programme the entire stiffness is modelled on the spar, considering the ideal skin to have zero stiffness. The skin does however have an important role in the mass distribution matching process as the weight of skin is estimated to be half the overall model weight.
5. **Modular Design & Manufacture** of the wing will allow different build definitions of the same wing, by dividing the model in three sections. For example, using a common interface a wing could have a configuration with a fixed wingtip (as per a conventional aircraft) or with an actively driven folding wingtip device. The aim is to produce a low cost manufacturing methodology to allow experimentation of more wings at a low budget.
6. **Instrumentation Methodology & Testing** allows for the state of the wing to be measured during experimentation using a low cost aquisition system. The instrumentation allows the measurement of transverse and rotational displacements, velocities and accelerations. The wing is tested in Cranfield University's Cranfield's 8'x6' low speed wind tunnel. Steady state response is obtained through defined angle of attack and flight speed. A dynamic response can be measured from a control input into the aileron, spoiler or wing tip and alternatively through disturbing the flow, for example via a gust vane.
7. **System Identification & Model Validation** is undertaken on the sub-scale model to validate existing FSI framework where the wing modal properties and aerodynamic coefficients are to be identified. The structural properties, as well as the aerodynamic coefficients, will be quantified using system identification methods. The aeroelastic system will be identified based on measured input and output. The results will then be used to validate and/or update the BEARDS^{TM} framework.

Further details on the BEARDS programme can be found in the paper by Pontillo and Hayes [134], but for the purposes of this thesis only the first three activities are discussed (model order reduction, aeroelastic dynamic scaling and fluid-structure interaction modelling) as this is the limit to the primary contribution of the author, and also provides the necessary information to answer the research question.

8.2 DYNAMIC AEROELASTIC RESPONSE ANALYSIS

In order to produce efficient designs, the effect on the aircraft structure and dynamics in a gust event must be accurately modelled and understood. However, the flight dynamics and structural dynamics are not directly comparable, thus a common currency is required to allow effective comparison. Here it is proposed this is exergy. For the purposes of this thesis and the BEARDS programme, the dynamic event is modelled as an input to the aircraft structure as work. An understanding of what happens to this energy is then undertaken by modelling the rate of energy dissi-

pation through aerodynamic and structural processes, for the full size and scaled aircraft.

A dynamic event response is chosen as it is a transient event (time), where the wing state (displacement, velocity and acceleration) varies, and the change in system forces, power and energy can all be calculated at every time step. Given that the simulated analysis of the full size aircraft is assumed to be at cruise altitude and the wind tunnel model at sea level, there are variances between analyses. These include the air density, temperature and pressure, all previously shown to be critical for exergy analysis. Thus the dynamic event response provides a wide variety of parameters to compare between the full size and scaled analysis, which will enable the research question to be answered.

Aeroelastic effects and flight loads are critical areas of technical focus that require extensive use of simulations. A common form of dynamic excitation is that of gust and turbulence loads, which directly affect the structural design and consequently the weight of an aircraft. Load factors in realistic gust scenarios have to be evaluated for safety and integrity purposes. Furthermore, assessing the response of an aircraft to gusts and turbulence is a major problem when designing and sizing novel wings or control surfaces.

An example gust analysis comes from Dussart using the CA^{2}LM framework in Figure 8.3, where the 1-cosine gust event with respect to the aircraft is shown in Figure 8.3a and the resultant structural deflections are given in Figures 8.3b and 8.3c. During cruise with no external loading events (e.g. gusts) the aircraft will be subjected to a constant lift force, which will deform the structure as shown in Figure 8.3b. Energy as a metric does not provide a clear understanding of the gust encounter, as there is stored strain energy in the aircraft during cruise before any such gust, thus the exergy metric is used. As exergy is defined as the useful work that a system can output, its use allows a clear distinction between gust work input into the system and how it is destroyed. As the aircraft is subjected to gust loading, the structure further deforms as shown in Figure 8.3b. The exergy X_{sys} is difference between the potential energy at the pre-gust and post-gust, defined as:

$$X_{sys} = \frac{1}{2}\{x_g\}^T [K] \{x_g\} - \frac{1}{2}\{x_c\}^T [K] \{x_c\}$$

As this is a dynamic system, at any time during of the gust encounter the system potential and kinetic exergy can be ascertained. As the exergy is destroyed through damping, the system returns to the point of minimum energy (zero oscillation). This transient event can be modelled using the system exergy given as

$$X_{sys} = \frac{1}{2}\{x_i\}^T [K] \{x_i\} + \frac{1}{2}\{\dot{x}_i\}^T [M] \{\dot{x}_i\} - \frac{1}{2}\{x_c\}^T [K] \{x_c\}$$

and with the exergy destruction given as:

$$X_D = \int \{\dot{x}\}^T [C] \{\dot{x}\}\, dt$$

The oscillation of each wing node is given in the three dimensional plot of figure 8.3c.

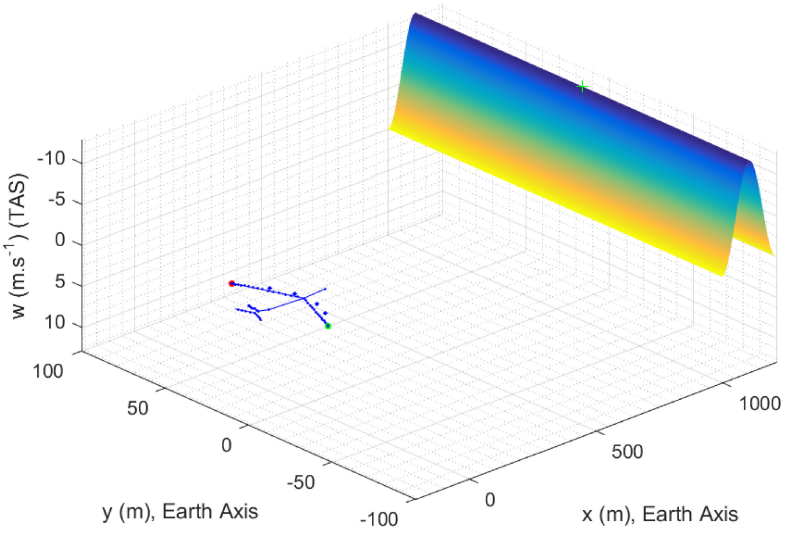

(a) CA^{2}LM aricraft approach to Gust input

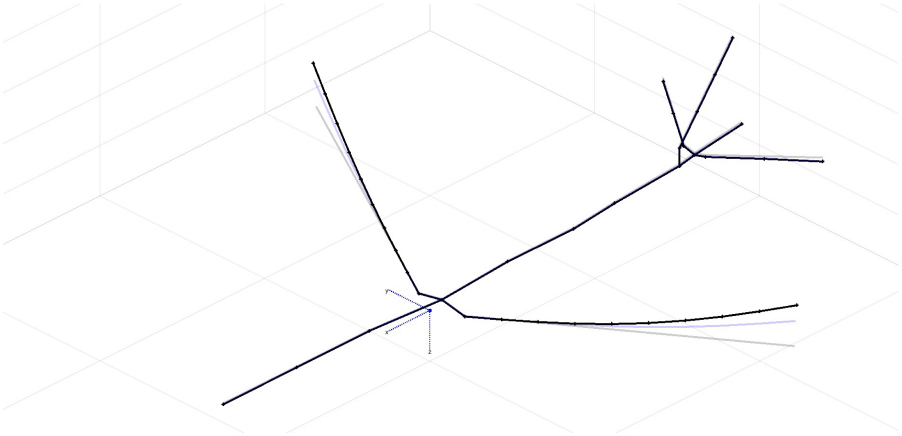

(b) Deflection of Aibus A340-300 under cruise loading and gust input

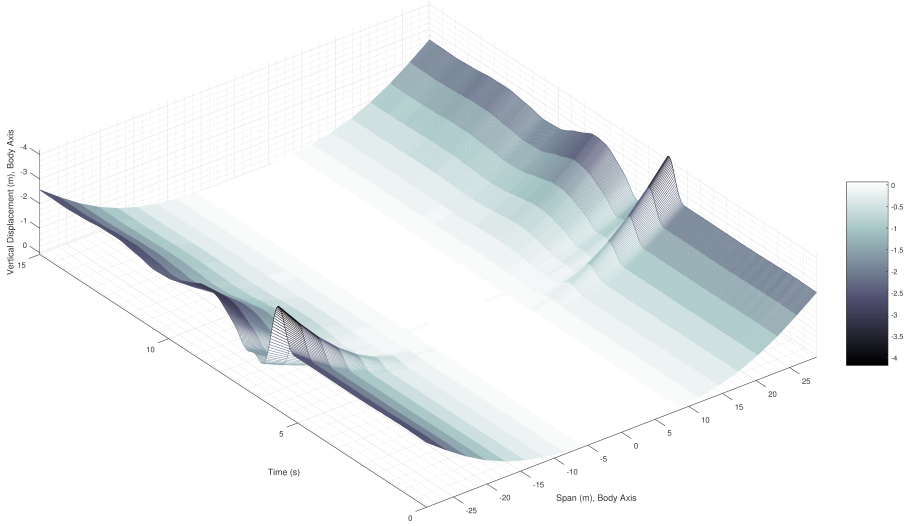

(c) Vertical Displacements of Aircraft Wings under gust loading

Figure 8.3: Example gust response on the Cranfield AX-1 (figure thanks to G Dussart)

8.3 XB-2 DYNAMIC SCALING

To provide similarity in dynamic behaviour it is necessary to develop dimensionless scaling laws for mass distribution, inertia, density factor, Froude (Fr) and Reynolds (Re) number. However, it is not possible to simultaneously match all of these parameters using the same model and same test conditions. As such, BEaRDS uses a scaling methodology outlined by Ricciardi [144–146] where the scaled geometry has similitude with the real aircraft in terms of the Froude number

$$Fr = \frac{u}{\sqrt{gl}}$$

inertia and mass ratio, as well as the normalized eigenvectors.

Ricciardi's method uses Buckingham π theorem [34] to non-dimensionalise the model and test parameters. Buckingham π theorem is an application of the Rayleigh method [142] of dimensional analysis, where a defined set of original defined scaled variables can be used to non-dimensionalise all other parameters in the model. The defined variables (selected to keep constant Froude number between model and aircraft) are derived from the flight condition for the XB-2 aircraft, 35,000 ft (10668 m) at 190 m/s (Mach 0.64)

- the wind tunnel is assumed to be at sea level, so the density scaling is defined as 1 : 0.31.
- the maximum test speed of Cranfield's 8'x6' wind tunnel is 50 m/s, so a velocity scaling of 1 : 4 is selected, giving a test velocity of 47.5 m/s.
- due to test space limitations, a geometric scaling factor of 1 : 16 is used.

These scaling parameters are summarised in Table 8.1, where using the Buckingham π theorem, combining the scaling of displacement and velocity, the time scaling is given as 1 : 4, which means the frequency response of the scaled model should be four times lower than the full size. Similarly the force can be scaled as a combination of all three defined variables, to give a force scaling of 1 : 1268.

The scaling process itself is not required for this thesis, as such this section has provided an overview only of the scaling method. The detailed scaling of the XB-2 mass and stiffness matrices is presented by Yusuf in [134], where the matrices are non-dimensionalised prior to scaling using the methodology outlined above. The output scaled matrices are however important for this thesis, as stated at the beginning of the chapter. If an exergy comparison is to be made, first of all it must be shown that the scaled model and full size have similarity in static and dynamic response.

To validate the scaled matrices a similar analysis is done as was performed for the XB-2 aircraft in Chapter 7, for the static and dynamic response. The static response is presented in Figure 8.4 where a simplified scaled lift distribution (Figures 8.4a and 8.4c) is applied to the full size and scaled models. The static response in Figures 8.4b

Table 8.1: Buckingham π scaling parameters

Parameter	Symbol	SI	π	Scaling Factor	
				model	aircraft
Displacement	x	m	-	1	16
Velocity	$\dot{x}$	ms^{-1}	-	1	4
Density	ρ	kgm^{-3}	-	1	0.31
Time	t	s	$x\dot{x}^{-1}$	1	4
Force	F	$kgms^{-2}$	$x^2\dot{x}^2\rho$	1	1268

Table 8.2: Comparison of Eigenvalue Analysis for XB-2

Mode no.	Aircraft		Scaled		Mode
	eigen-value	Hz	eigen-value	Hz	
1	18.9	0.69	303.2	2.77	1st Bending YZ
2	472.5	3.46	7559.3	13.84	2nd Bending YZ
3	482.9	3.50	7726.8	13.99	1st Bending XY
4	1483.9	6.13	23742.7	24.52	3rd Bending YZ
5	3222.7	9.03	51562.7	36.14	4th Bending YZ
6	8083.4	14.31	129334.5	57.24	Coupled

and 8.4d shows similitude between the scaled and full size stiffness matrix parameters as the deflection is 16 times smaller for the scaled wing. The dynamic response is validated by undertaking an eigenvalue analysis and compared to that of the full size XB-2 aircraft from Chapter 7. In this case, the normalised mode shapes (eigenvectors) are the same as Figure 7.11, which is expected due to the normalisation. A comparison of the frequencies is shown in Table 8.2 where it can be seen the scaled frequencies are 4 times that of the full size, which is expected due to the derived time scaling factor. From this analysis it can be concluded that using the Ricciardi method of scaling provides similitude between the scaled and full size aircraft for a dynamic response.

Validation that the eigenvalues calculated are correct to the scaled model does not form a part of this thesis, as to validate the frequencies the scaled model needs to be manufactured, and then the modal frequencies identified through a Ground Vibration Test (GVT). However, as the modes have been calculated using the BEaR code, confidence can be found in the result, as the structural code was validated in Chapter 6.

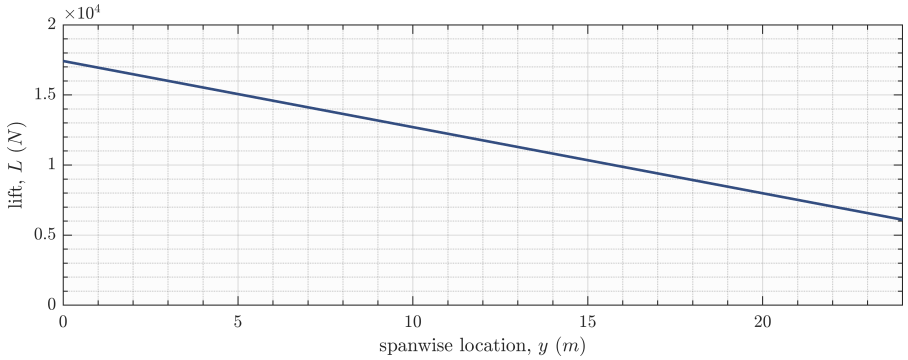

(a) Static response test lift distirbution - aircraft

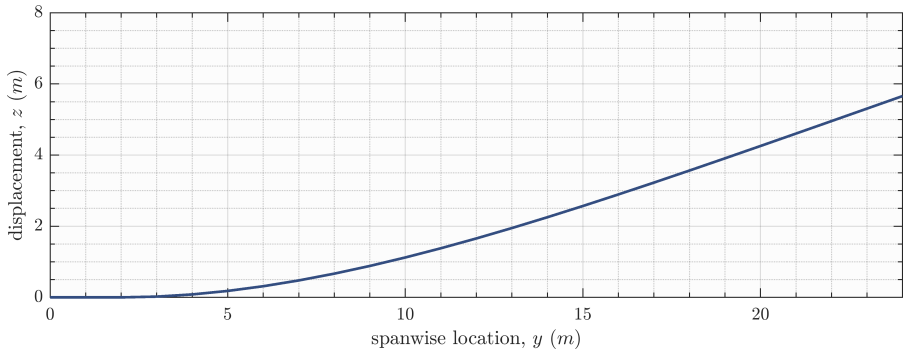

(b) Static response - YZ displacement - aircraft

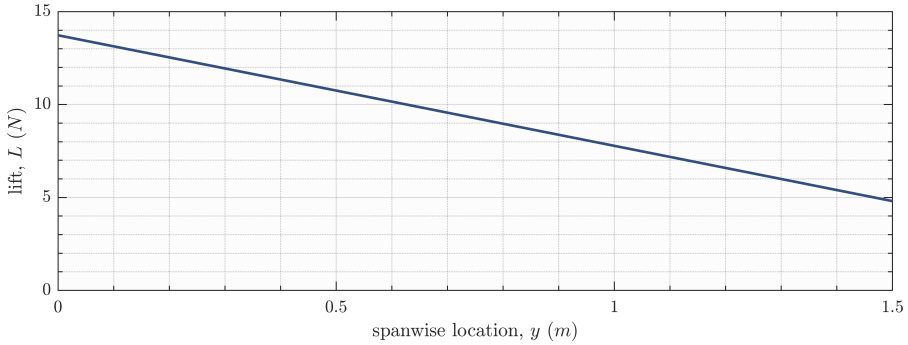

(c) Static response test lift distirbution - scaled

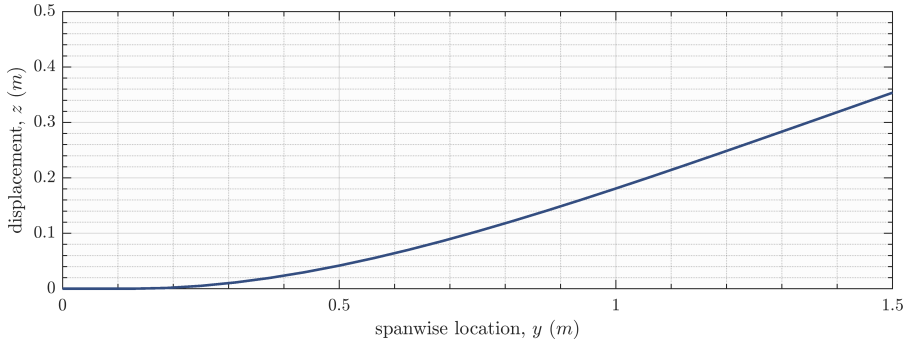

(d) Static response - YZ displacement - scaled

Figure 8.4: Static response comparison for XB-2 aircraft and scaled

8.4 DYNAMIC EXCITATION ANALYSIS

To determine whether exergy analysis can provide additional insight into the process of scaling technology and highlight the difficulties, this section utilises the BEARDS^{TM} framework and a cantilevered XB-2 aircraft wing, undergoing a dynamic excitation.

To dissipate the energy put into the system by the excitation, BEARDS^{TM} models the structural damping of the aircraft as an equivalent viscous damping, using the Rayleigh damping function in Equation 4.6. For the purposes of the example, the damping is given purely as a function of the stiffness matrix (to improve solving time as mass matrix is sparse), such that $[\eta, \lambda] = [0, 0.052]$.

The applied load distribution is ramped to the *trimmed* condition, and approximately half way through the analysis the dynamic excitation is applied. This load case can be seen for both the full size and scaled model in Figures 8.5a and 8.7a respectively. The transient response of both analyses are shown in Figures 8.5, 8.6, 8.7 and 8.8, from which the following can be concluded:

- the trim location (equivalent to the static response) is given in Figures 8.5b and 8.7b, for full scaled and scaled respectively. This location is the point of minimum energy or zero exergy during flight and forms the reference state position for exergy analysis. As with this previous static response analysis, the full size and scaled response varies by a factor of 16.
- The wing response to the load case can be seen in Figure 8.5c and 8.7c, where the initial ramp of the loadcase leads to a similar ramp in the wing deflection, where at the peak a damped oscillation can be seen to the point of zero exergy.
- Once subjected to the dynamic excitation (at 50s and 12.5s for aircraft and scaled respectively) the wing produces an oscillating dynamic response. For the wing tip this can be seen more clearly in Figures 8.6a and 8.8a. Critically the peak displacement of the scaled wing is a sixteenth of the full scale displacement, and the oscillation frequency and time to complete return to zero exergy is four times faster than the full scale aircraft.
- The unloaded, zero exergy and peak displacement of the wings can be seen in Figures 8.6b and 8.8b.
- It can therefore be concluded that the calculated scaling parameters in Table 8.1 are valid and provide similitude between the scaled and full size aircraft. Thus any technology or concept tested on the scaled model, will scale with the defined parameters to a full size aircraft and produce the same dynamic response.

The results of the above dynamic analysis derive the same conclusions as seen in the work undertaken by Ricciardi [144–146]. There has been no published work on how the energy, exergy and power terms scale between scaled geometries and full size equivalents, which appears to be a simple extension to Ricciardi's work and may provide an answer to the chapters critical research question.

The exergy methodology that has been outlined throughout this thesis is therefore applied to the dynamic response state output from the previous scaled and full size XB-2 wings, with the results plotted in Figures 8.9, 8.10 and 8.11. From this exergy post-processing of the data the following can be concluded:

- The similitude in the time parameter is shown again to be valid, with the scaled response being a quarter of the full scale.

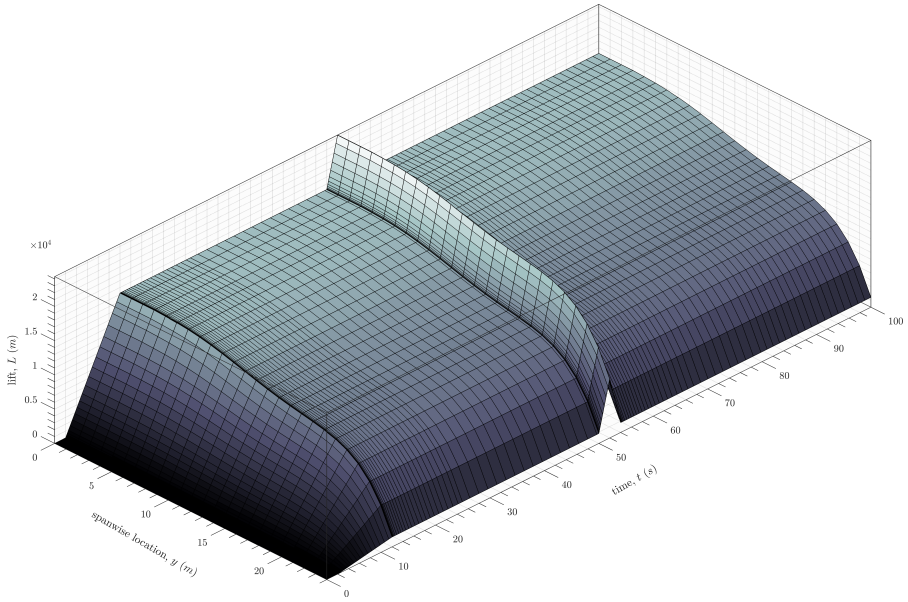

(a) Dynamic loading - full size aircraft

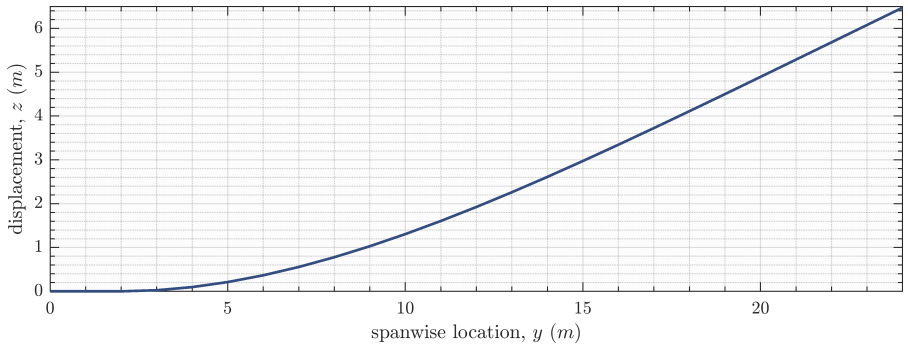

(b) Full size aircraft static response

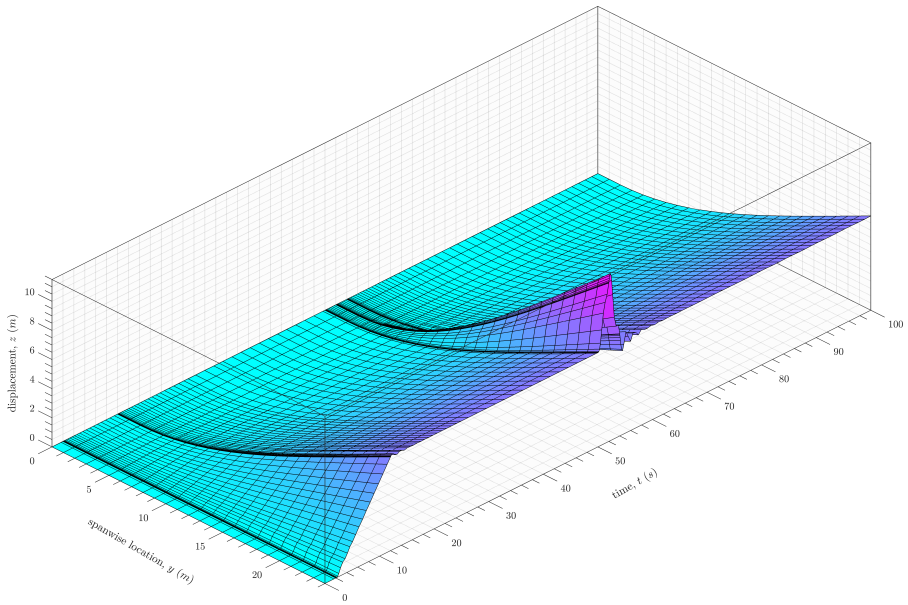

(c) Dynamic wing deflection - full size aircraft

Figure 8.5: Dynamic wing deflection full size

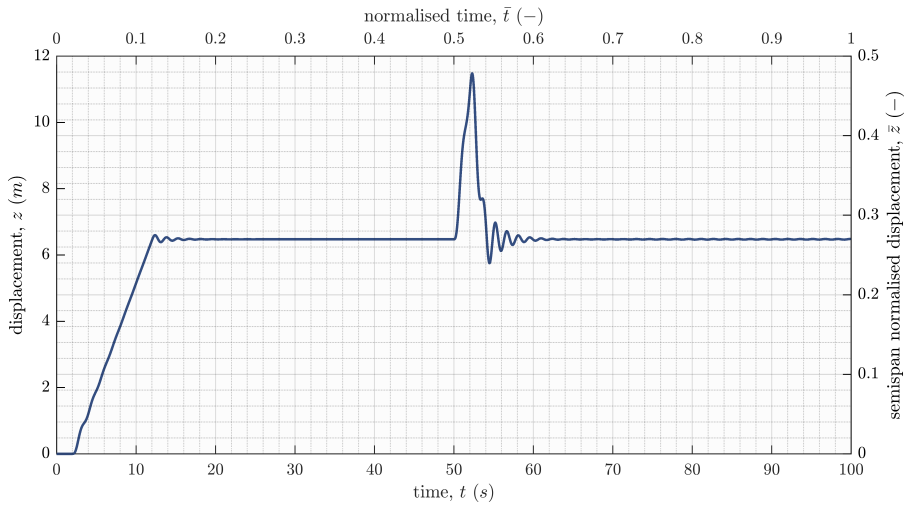

(a) Full size displacement

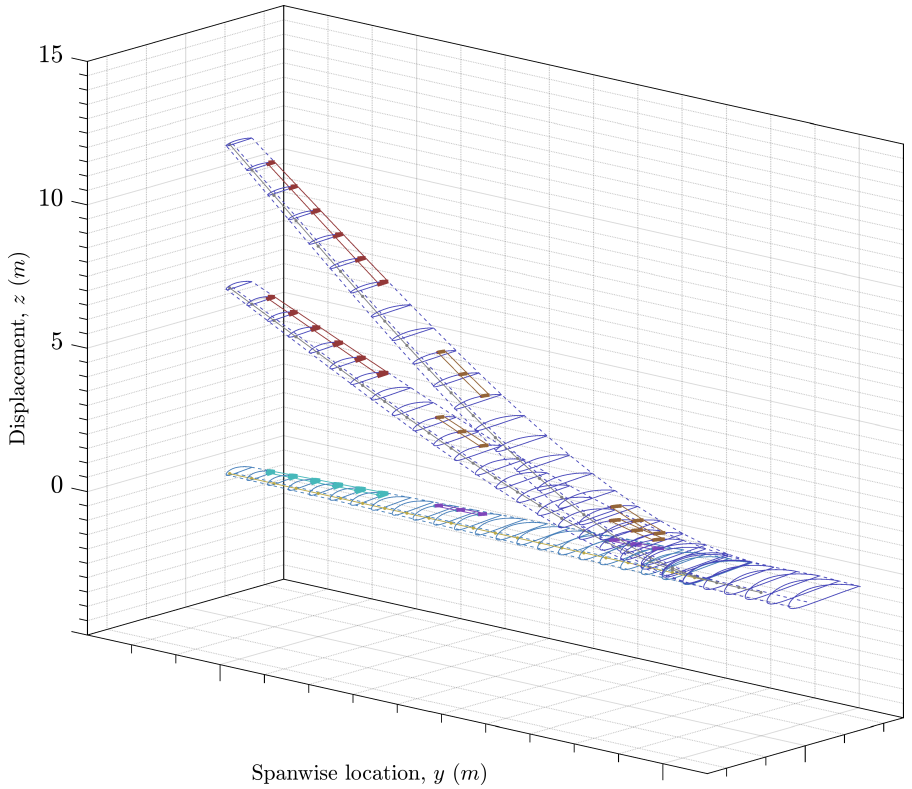

(b) Deflection of XB-2 wing under trim and peak response

Figure 8.6: Full size dynamic response to excitation

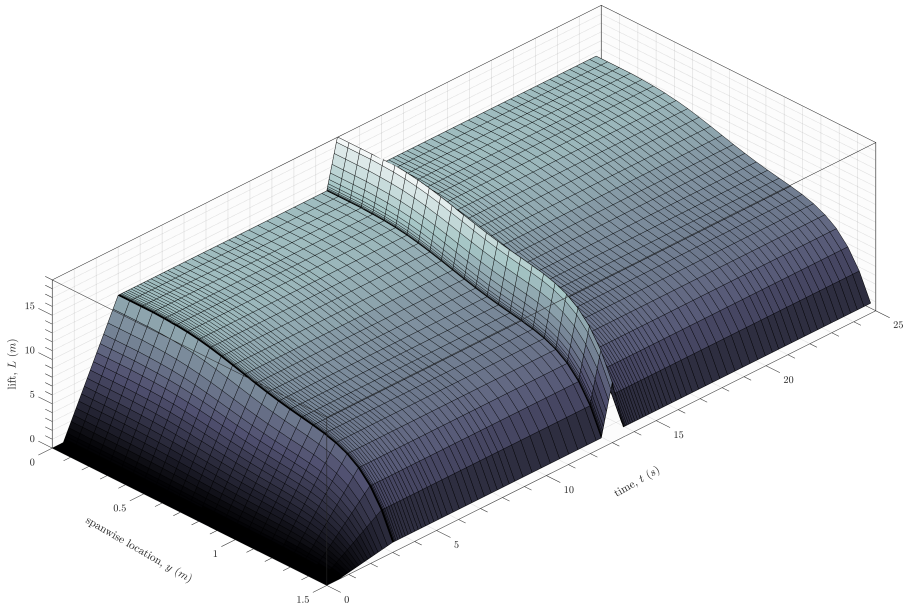

(a) Dynamic loading - scaled aircraft

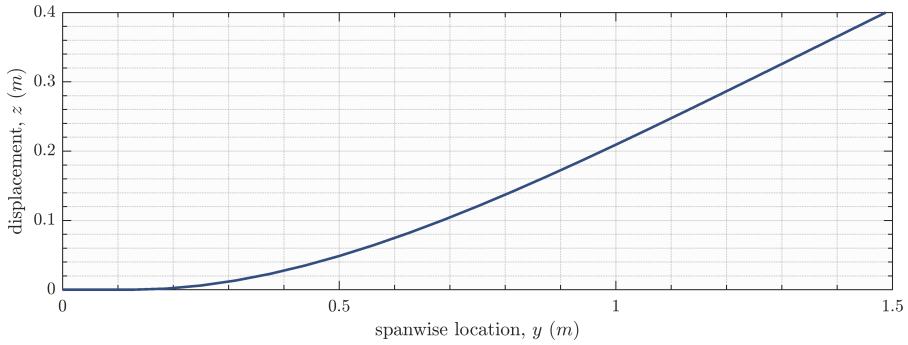

(b) Scaled aircraft static response

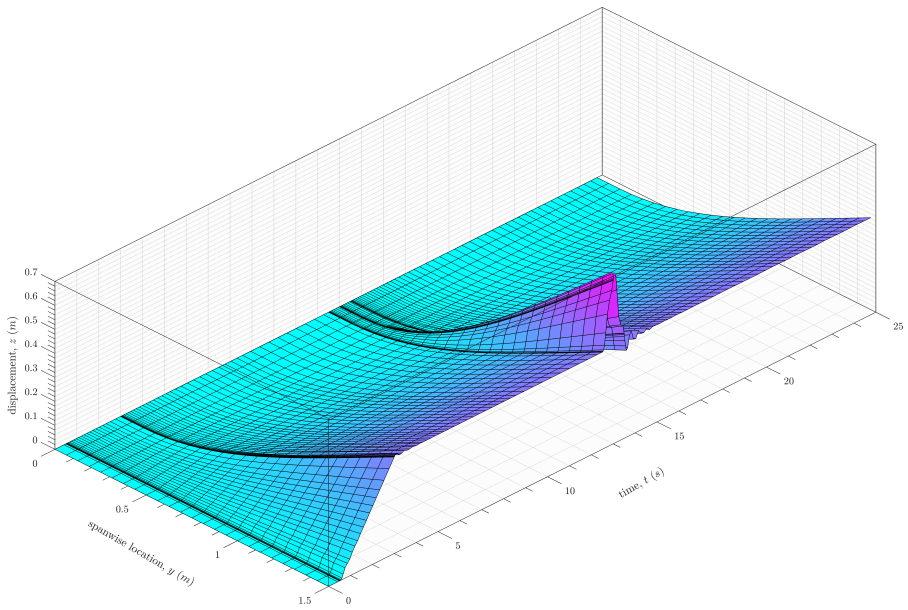

(c) Dynamic wing deflection - scaled aircraft

Figure 8.7: Dynamic wing deflection scaled

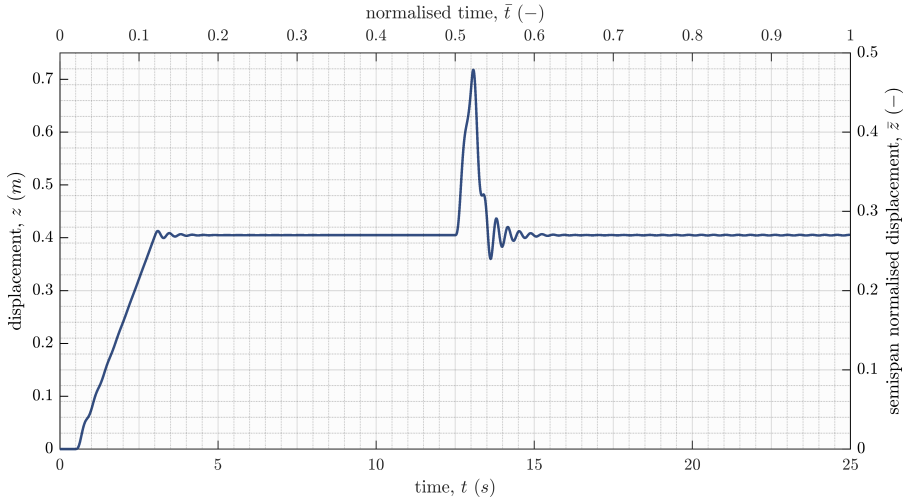

(a) scaled displacement

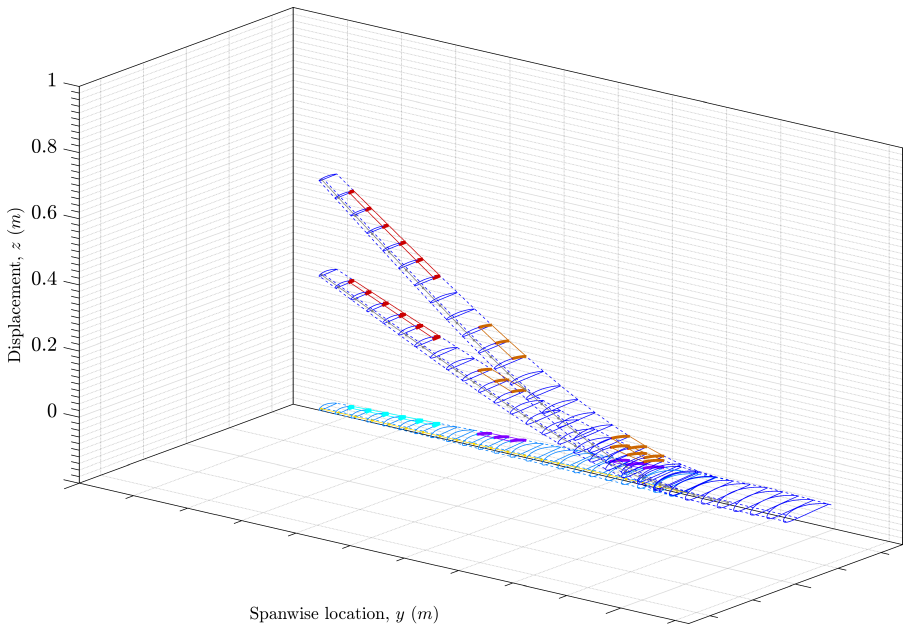

(b) Deflection of XB-2 scaled wing under trim and peak response

Figure 8.8: Scaled size dynamic response to excitation

Table 8.3: Buckingham π scaling parameters

Parameter	Symbol	SI	π	Scaling Factor	
				model	aircraft
Displacement	x	m	-	1	16
Velocity	$\dot{x}$	ms^{-1}	-	1	4.0
Density	ρ	kgm^{-3}	-	1	0.31
Time	t	s	$x\dot{x}^{-1}$	1	4.0
Force	F	$kgms^{-2}$	$x^2\dot{x}^2\rho$	1	1.3×10^3
Energy	E	kgm^2s^{-2}	$x^3\dot{x}^2\rho$	1	2.0×10^4
Exergy	X	kgm^2s^{-2}	$x^3\dot{x}^2\rho$	1	2.0×10^4
Power	P	kgm^2s^{-3}	$x^2\dot{x}^3\rho$	1	5.1×10^3

- The work input into the system via the dynamic event can be seen in Figures 8.9c and 8.10c, which forms the exergy input of the system. Here the exergy is dissipated via structural and aerodynamic damping to the point of zero exergy. The elastic potential exergy here is shown in contrast to the elastic potential energy in the system shown, in Figures 8.9b and 8.10b. This shows the clear distinction between energy and exergy terms.
- Due to the nature of the structure and dynamic event the system exergy is dominated by the elastic potential term, as the kinetic exergy (equivalent to energy in this test) is orders of magnitude smaller than the elastic potential, due to the comparatively high damping.
- The entropy generation in Figure 8.11b is shown to be a function of the velocity in Figure 8.11a and not the displacement, which shows the structural damping has been converted into an equivalent viscous damping.
- An interesting observation is the order of magnitude difference between the scaled and full size exergy terms, and the power terms in the exergy destruction shown in Figures 8.11b and 8.11d. Whilst the scaling factor appears to be significantly higher than that for the other scaled parameters discussed so far (time, force, velocity etc.), using the Buckingham π method does show this to be the case. Table 8.3 presents a repeat of the scaling factors in Table 8.1, but includes those calculated for the energy, exergy and power parameters.
- The reason these values are so significant is that, as discussed throughout the thesis, all systems essentially just convert energy from one form to another to achieve a desired work output. This is also true for folding wing tips, morphing control surfaces and any other novel technology aerospace companies want to test on scaled models. So, if a folding wing tip is shown to work on a scaled model, this should also work on a full scale aircraft. The dynamic response will be the same, and the associated forces will be 1.3×10^3 times higher than measured in the wind tunnel. The power to drive the system will be 5.1×10^3 times higher, and the total energy input is 2.0×10^4 times higher.

By undertaking an exergy post processing of an aeroelastic analysis of both the full scale and scaled aircraft wings, it was shown why it is difficult to scale up technologies that are shown to work on dynamically scaled models. For a model one sixteenth the geometry of the full scale aircraft, if a technology is shown to work on the scaled model (e.g. folding wing tip), when scaled up to the full size the work input to operate the technology is significantly times higher.

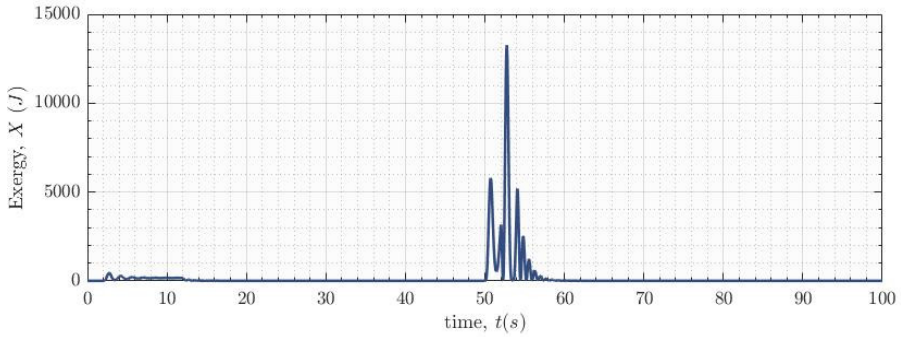

(a) Kinetic Exergy - aircraft

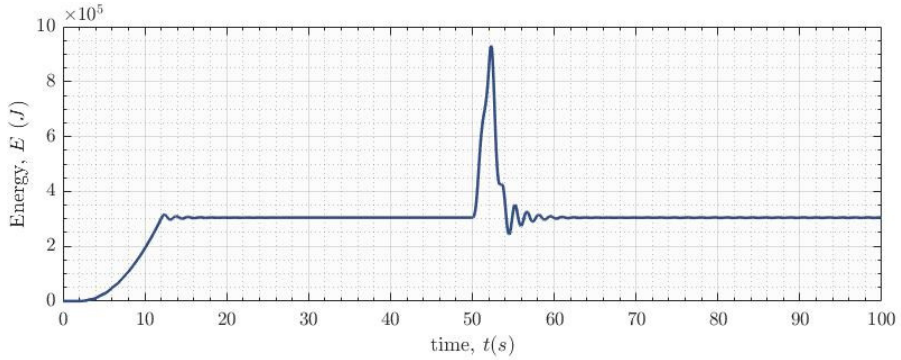

(b) Potential Energy - aircraft

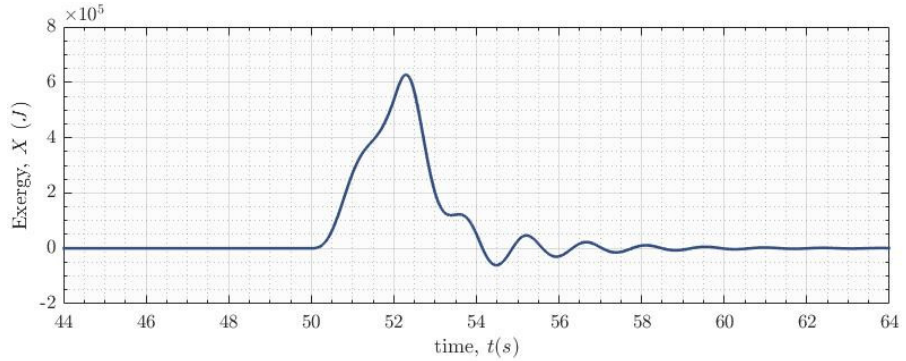

(c) Potential Exergy - aircraft

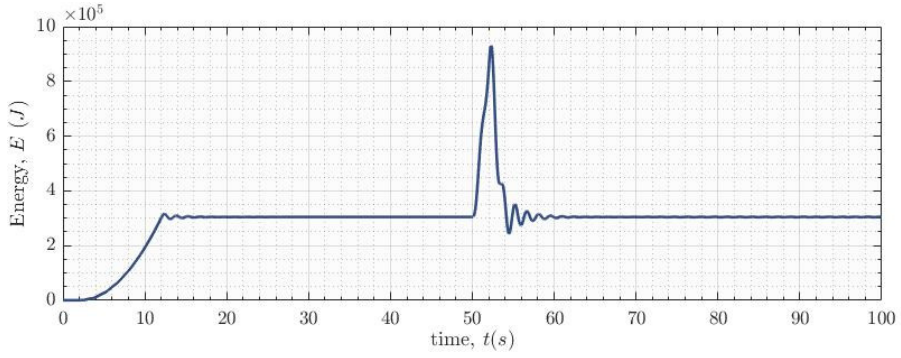

(d) Total System Energy - aircraft

Figure 8.9: Full size exergy analysis

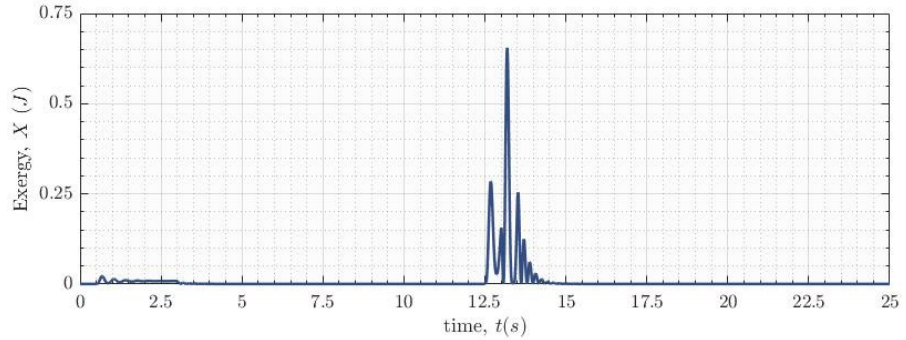

(a) Kinetic Exergy - scaled

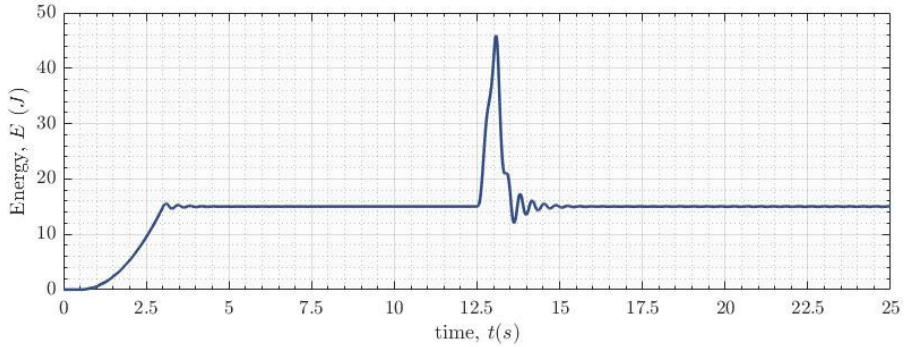

(b) Potential Energy - scaled

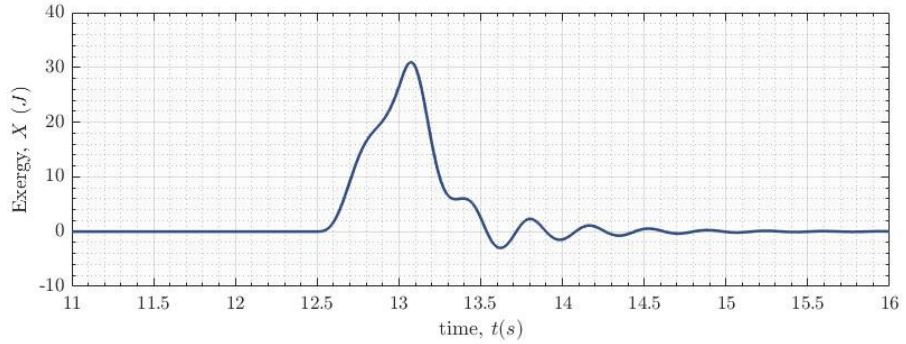

(c) Potential Exergy - scaled

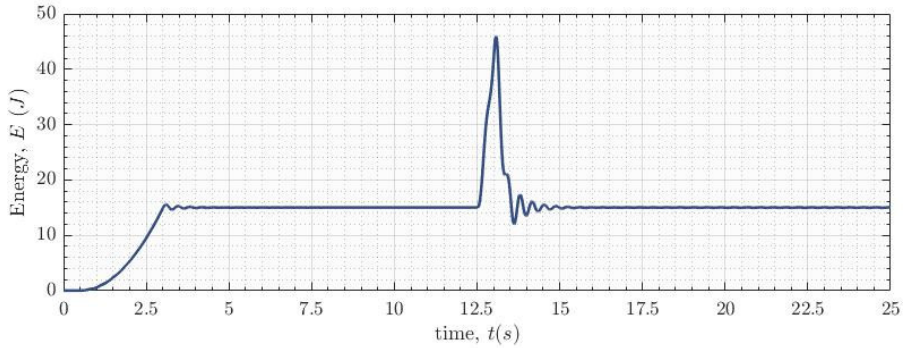

(d) Total System Energy - scaled

Figure 8.10: Scaled model exergy analysis

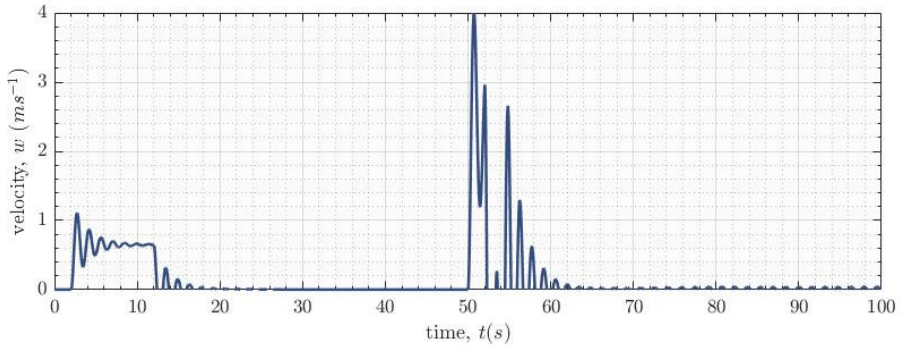

(a) Full size velocity

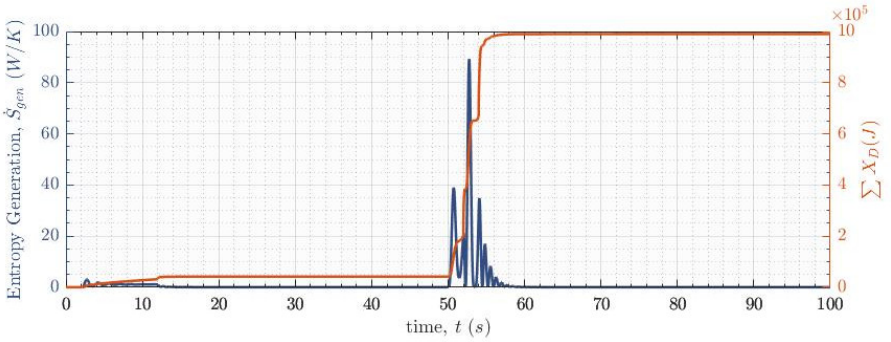

(b) Full size entropy generation and cumulative exergy destruction

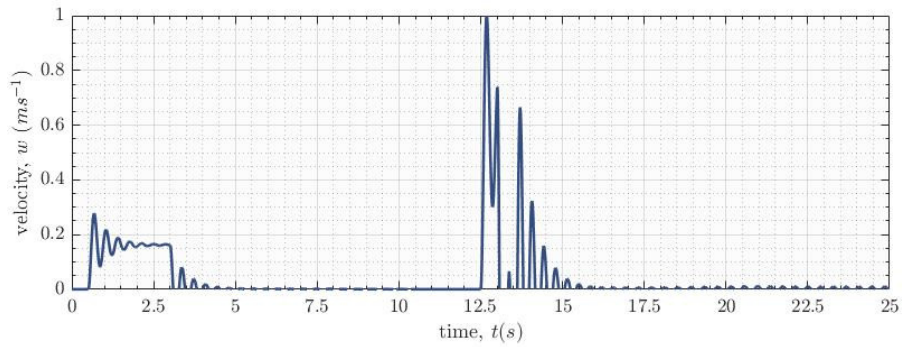

(c) Sclaed velocity

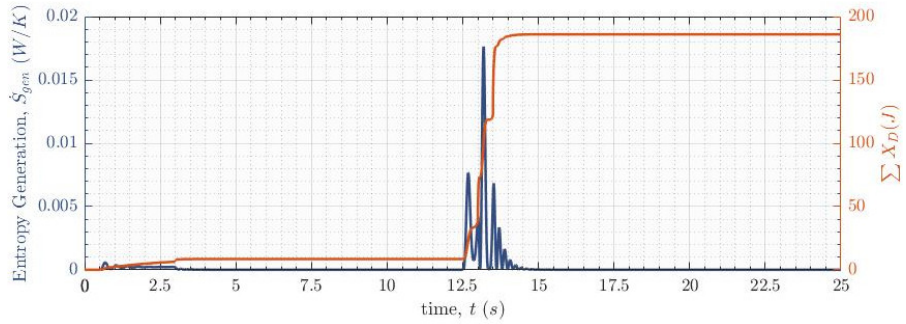

(d) Scaled entropy generation and cumulative exergy destruction

Figure 8.11: Velocity and exegry destruction comparison of full size and scaled

8.5 CHAPTER SUMMARY

This chapter has aimed to show why the benefits of scaling technology from a scaled model to a similar full-size aircraft can be unclear. An overview of Ricciardi's method using the Buckingham π theorem has shown how the scaled XB-2 cantilevered wing has similitude with the full scale aircraft designed in Chapter 7, this was shown with a scalable static and dynamic response. The exergy analysis on the dynamic event showed 2.0×10^4 times as much energy is needed for a similar process at full scale if shown to work on a scaled model, and this conclusion was validated using the Buckingham π theorem. For example, if a folding wingtip reduces the drag by 10N on a scaled model, it can be expected to reduce the drag by 1.3×10^3N on the real aircraft. However, if the folding wingtip requires 5W to drive the actuator, for the same full size aircraft it would require 2.0×10^4W. Thus a study needs to be done looking at the power output relative to the weight of the actuator, as these two parameters would need to follow the same scaling parameters, otherwise the system will not perform as shown on the scaled model.

Ricciardi's scaling method only scales the Froude number, as such testing of the scaled model will not match the Mach or Reynolds number. Both lift and drag are Mach and Reynolds number dependent, as such it is important to *trip* the flow in a wind tunnel to artificially match the Reynolds number for accurate drag calculation. The effect due to the Mach variance will be less pronounced as the real aircraft is designed to fly at $0.6M$, so only subsonic flow exists. Further work will need to be done in the BEARDS project to assess the impact of Mach and Reynolds, as it may also be the case a higher Angle of Attack is applied in the wind tunnel test to generate a similar lift.

9

A THERMODYNAMIC MODEL FOR MORPHING WING AIRCRAFT

The design and development process for future aircraft aims to address the environmental and efficiency challenges needed to facilitate the engineering of concepts that are far more integrated and require a multidisciplinary approach. From a systems engineer's perspective, their role at top level system design is to make trade-offs between competing disciplines and sources of loss, to arrive at a vehicle design with the least possible *cost*[1]. Thus the systems engineer has a need for a loss accounting method that enables systematic analysis of loss where system wide consequences of design trade-off can be evaluated. This premise led Roth [157] to develop *generalized models for vehicle thermodynamic loss management*, where differential loss models can be built for all aircraft sub-systems, and the sources of work can be modelled against the vehicle losses under a unifying metric.

In order to implement an analysis method based on *generalized models for vehicle thermodynamic loss management*, a unifying metric of measure must be defined. In order to allow the analysis of any sub-system or process a universal metric must be used. Within the bounds of known physics three universal metrics exist; energy, entropy and exergy. Many analysis methods in practice implicitly use energy and the first law of thermodynamics as an optimisation metric. This is typically done by charging aircraft systems for their use of resources, such as vehicle weight as an associated cost in terms of fuel weight. This is the approach implicit in the Breguet Range Equation where the propulsive, aerodynamic and structural efficiency are all looked to be improved and judged against the common range metric. Explicit energy tracking is essentially the same as fuel tracking as fuel is the source of energy. Exergy analysis is a time dependent analysis that can be undertaken over the whole mission profile. It can be used for wing optimisation and to even higher level aircraft system analysis where the exergy source is mapped throughout the flight mission to highlight areas of exergy destruction.

In previous chapters the benefits of exergy analysis over the alternatives of energy and entropy based analyses have been discussed. In line with the thesis methodology, this chapter will use the exergy metric to develop a thermodynamic loss management model approach, to assess the performance of aircraft systems. The chapter will initially outline the development of a thermodynamic loss management model, and then use this model to compare the performance of the Airbus A320 against the Cranfield BEARDS XB-2 aircraft developed in Chapter 7. A further application will be shown by modelling the performance improvement provided by wing extensions to the Cranfield AX-1 aircraft, and discussing the applicability of exergy analysis to morphing wing aircraft. To conclude the proposed exergy based thermodynamic performance model is validated against the widely accepted Breguet Range Equation method for performance assessment.

1 for commercial airlines cost is typically in-flight fuel burn

9.1 THERMODYNAMIC PERFORMANCE MODELLING

The steps for the proposed thermodynamic loss management model that will use exergy as the metric is presented in Figure 9.1, based on the model style of Roth [157]. It can be argued that undertaking any exergy analysis inherently follows this process, but the model aims to formalise a process for modelling any aircraft, sub-system or process using exergy. The model provides a representation of exergetic loss as a function of vehicle environmental operating condition, and follows a distinctive five step process:

- **Universal metric selection** is based on identifying a universal metric that can be used to quantify loss or transfer between systems and processes.
- **Sources, stores and losses** are identified in terms of the selected metric. This involves decomposing the system into a series of sub-systems and functions, typically using a method such as a loss relevance tree. It is at this stage the fidelity level of the model is identified, for example, whether an engine is modelled as a top level single system or as a collection of its constituent parts that are all assessed individually.
- **Thermodynamic modelling** is required for each identified function in the loss relevance tree, as whilst exergy provides a common metric to compare dissimilar disciplines, the generation of exergy based data comes from different sources. Examples of required thermodynamic models would be a propulsion model, aerodynamic loss model, environmental control system model, work storage model and models for any aircraft sub-system in the analysis.
- **Through mission analysis** identifies the flight envelope of the system. With this time history of aircraft state (altitude, velocity, etc.) the above thermodynamic models can be run with the corresponding environmental conditions for the given flight condition.
- **Assign system losses** over the complete flight envelope is done by integrating the above analysis. This allows sub-systems generating comparatively high losses to be identified and at what stage of flight. This process provides *total vehicle loss chargeability*. By assessing the assigned system losses for different concepts the impact of the top level design can be ascertained.

In this section these stages to the thermodynamic loss management model will be discussed in more detail, with examples provided where required.

9.1.1 *Universal Metric Selection*

The three universal metrics defined in physics are energy, entropy and exergy, which are all modelled using thermodynamic methods. For consistency within the thesis, exergy is used as the universal metric in this chapter, the benefits of which have been previously discussed in the previous chapters.

There are three fundamental equations used for thermodynamic performance modelling with an exergy metric. As detailed in Chapter 2 the exergy content of an aircraft, system or process can be sub-divided into four forms, the thermal exergy (X_U), the kinetic exergy (X_T), the potential exergy (X_V) and the chemical exergy (X_{Ch}).

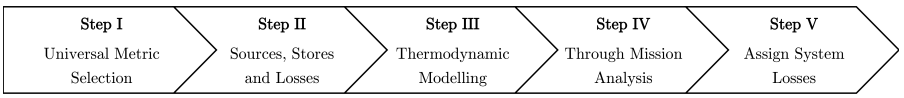

Figure 9.1: Stages of generating a Thermodynamic Performance Model

The combination of these forms of exergy provides the first fundamental equations used for the thermodynamic loss model, being the system exergy given in Equation 2.5. Here, the thermal exergy is the classic thermodynamic *free energy*, based on the internal energy, U, pressure, P, volume, $\mathcal{V}$, temperature, T and entropy, S. The conservative exergies, potential and kinetic, are those that are typically fully convertible to other forms of energy in an idealised system. The chemical exergy is primary source of exegry that is available in the fuel. The Guoy-Stodola identity represents the *principle of decreasing exergy*, and the second fundamental equation, which states that the generation of entropy is proportional to the destruction of exergy, defined Equation 2.12. Finally the third fundamental equation allows the modelling of the transfer of exergy between two systems through any process, and associated losses in this transfer is modelled using the open exergy transfer equation given in Equation 2.11.

9.1.2 *Sources, Stores and Losses*

The exergy use of the aircraft can be mapped from the initial source (the fuel) through to combustion, energy conversion throughout aircraft and the ultimate destruction of exergy as aerodynamic drag and other heat generating processes. The typical sources, stores and losses for an aircraft are shown graphically in Figure 9.2. It is assumed most of the presented sources, stores and losses in Figure 9.2 are understood, however for clarity the following are defined:

- **Environment**. The exergy sourced from the environment can be in many forms, gust and turbulent events input energy into the system causing structural deformation in the aircraft (strain energy), which theoretically could be harvested. Other sources include formation flight, where the velocities in the vortices created by forward aircraft are utilised.
- **Kinetic Energy**. The kinetic energy (or exergy as equivalent) of the aircraft is that stored by the mass of the overall system during flight as it is travelling at a defined velocity. For conventional commercial aircraft this stored energy is dissipated from the aircraft on landing approach by the deployment of flaps and spoilers.
- **Potential Energy**. Specifically the gravitational potential energy the system mass has from flying at an altitude above sea level (where the environmental definition for exergy analysis assumes zero potential energy). Dissipated as with the kinetic energy on landing approach.

The initial exergy reserves are calculated by the exergy of the jet fuel and/or batteries on board the aircraft. The exergy of these sources are then mapped through each conversion process with the exergy destruction highlighted at each stage, to the point of complete exergy destruction. During any stage of flight an exergy flow diagram or loss relevance tree can be formed. An example is given in Figure 9.3, which shows the exergy rate of different aircraft systems and how it is transferred between each system. Note that to simplify the analysis for this chapter (as the purpose is to show the benefit of exergy analysis) only the systems and transfers highlighted in blue on Figure 9.3 are considered.

9.1.3 *Thermodynamic Modelling*

This subsection outlines the thermodynamic models that have been developed for the two example analyses which conclude the chapter. In-line with Figure 9.3 the following thermodynamic models are needed to model all sub-systems and processes:

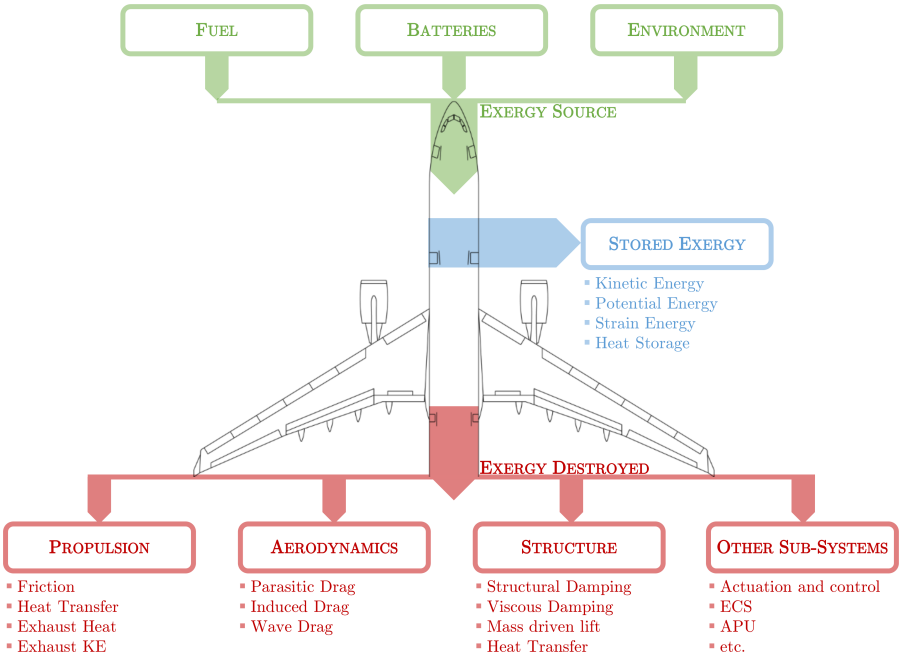

Figure 9.2: Systems of Exergy Sources, Destruction and Storage

- Source Exergy
- Propulsion System
- Aerodynamics
- Stored System Exergy

9.1.3.1 *Source Exergy*

The chemical exergy is more complex than other forms of exergy, as at the environmental state the chemicals themselves may be stable (thus no work potential), however when reacted together they can release exergy. Thus Camberos [40] states that the chemical exergy of a pure chemical compound is:

> *equal to the maximum amount of work obtainable when a compound is brought from the environmental state to the dead state, characterised by the same environmental conditions of temperature and pressure, but also by the concentration of reference substances in a standard environment*

Chemical exergy arises when there is a disequilibrium between the resource and environment leading to a chemical potential. This could be a potential created by a concentration gradient of species freely available in the environment, such as oxygen, carbon dioxide and methane, or from a non-environmental species. In all sources of chemical exergy, work can be extracted as the resource and environment are bought into chemical equilibrium. In addition to the exergy losses through heat generation (entropy production) found in reactions such as combustion, irreversibility is generated as environmental species are released to the environment at their environmental dead state chemical potential.

In practice calculating chemical exergies for various fuels or other species not in equilibrium is not required, as the values are published in multiple texts. Table 9.1 presents some common components along with the molecular mass, $\hat{m}$, enthalpy of formation, h_f^o [110], molar-specific entropy, s^o [110], and the chemical exergy, X_c [171].

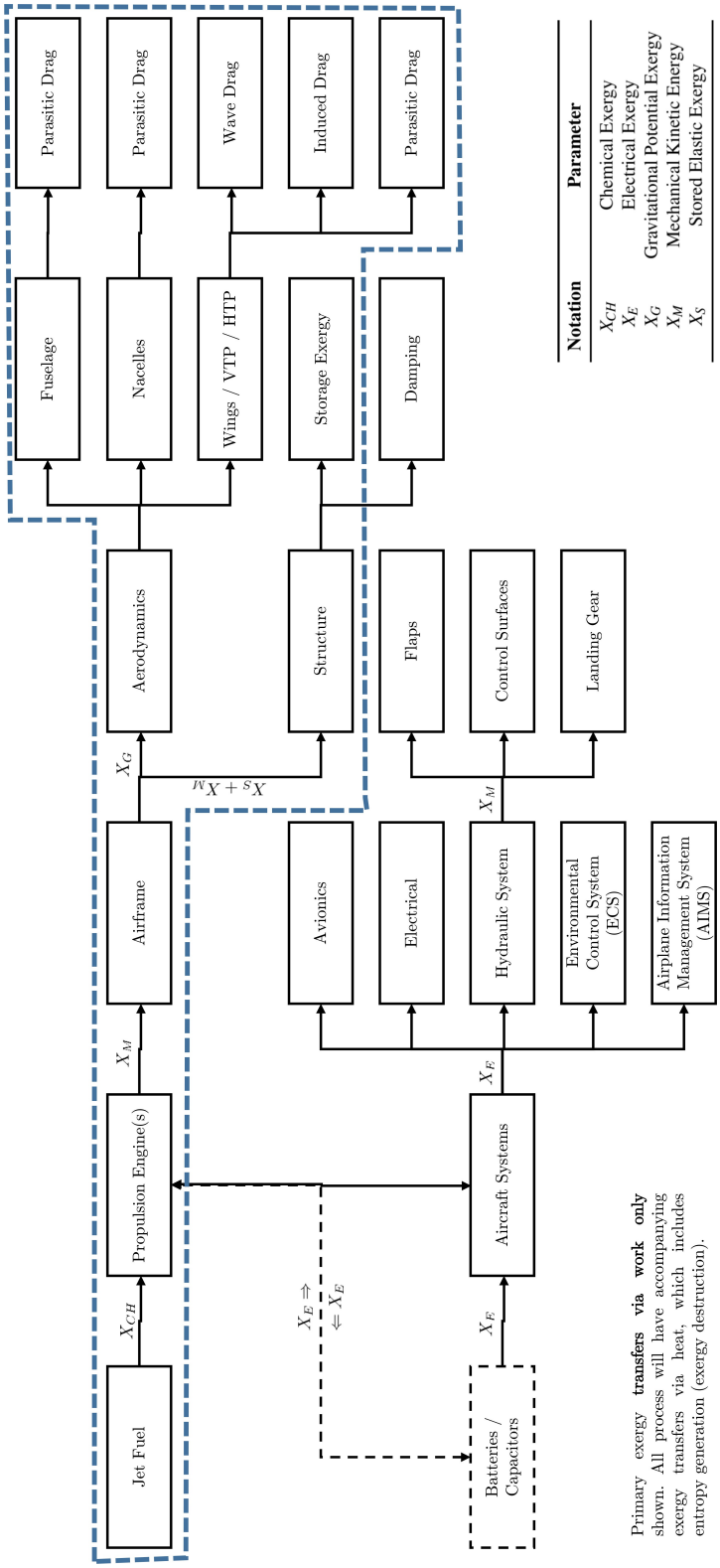

Figure 9.3: Generic Exergy Flow Diagram for Commercial Aircraft

Table 9.1: Standard Chemical Exergy values for common compounds

Substance	Symbol	$\hat{m}$ g/mol	x_k %	h_f^o kJ/mol	s^o J/mol-K	X_c kJ/mol
Oxygen	O_2	32.00	20.3	0	205.1	3.97
Carbon Dioxide	CO_2	44.01	0.037	−393.5	213.8	19.87
Water	H_2O	18.02	3.00	−241.8	188.8	0.9
Methane	CH_4	16.04	0.00	−74.6	186.3	831
Propane	C_3H_8	44.10	0.00	−104.7	270.3	2154
Jet A	$C_{12}H_{23}$	167.31	0.00	−303.4	448.1	7670

Recall from Chapter 2 that Camberos [40] formulates a mass derived chemical exergy (equal to the mole derived function of Simpson [164]) given in Equation 2.6, where the exergy is a function of the chemical potential (μ_{i_j}), in the environment at $j = 0$ and in the fuel at $j = 1$, and the stoichiometric mass ratio (y_i).

$$X_c = \sum_i^n y_i \left(\mu_{i_1} - \mu_{i_0}\right) \tag{2.6}$$
$$\mu_i = \underbrace{\left(h_f^o - T_0 s_k^o\right)}_{\mu_i^o} + RT_0 \ln x_k$$

Definition of the chemical potential (μ_i) is consistent between authors as presented from Szargut [171], as a function of the matter input (in mass or moles) of enthalpy with some losses from entropy production in this process. Note, (μ^o) is the chemical potential at the environmental dead state where $T = T_0$ and $P = P_0$, where x_k is the environmental composition percentage.

EXAMPLE 7

With the definition of chemical exergy content as given in Equation 2.6, the rate of exergy released from the combustion of jet fuel can be calculated. The issue with the values given in Table 9.1 is that they are for a constant environment, defined as $T_0 = 298K$ and $P_0 = 100kPa$. Given an aircraft's mission profile varies in altitude, the reference temperature and pressure for the exergy analysis will vary, thus the chemical exergy available will vary. This example thus aims to see how the exergy released from the combustion of jet fuel varies with altitude.

For the purposes of the thesis all aircraft will be assumed to use standard commercial aviation fuel, Jet A ($C_{12}H_{23}$), the combustion of which is given as:

$$C_{12}H_{23} + 17.75O_2 \rightarrow 12CO_2 + 11.5H_2O$$

The combustion formula provides the stoichiometric ratio given in Equation 2.6, such that $y = [1\ 17.75\ 12\ 11.5]$.

An example calculation is presented assuming environment of $T_0 = 298K$ and $P_0 = 100kPa$, and a standard composition of air for x_k, the chemical potential (μ) in Equation 2.6 for the reactants and products in the combustion of Jet A are calculated using values in Table 9.1 as:

$$\mu_{F_{C_{12}H_{23}}} = -0.437 \times 10^6 \quad \text{J/mol}$$
$$\mu_{0_{O_2}} = -0.065 \times 10^6 \quad \text{J/mol}$$
$$\mu_{0_{CO_2}} = -0.477 \times 10^6 \quad \text{J/mol}$$
$$\mu_{0_{H_2O}} = -0.286 \times 10^6 \quad \text{J/mol}$$

Note that where the substance is not present in the environment $\mu_i = \mu_i^o$.

From Equation 2.6 the chemical exergy is calculated as:

$$X_c = \mu_{C_{12}H_{23},TM} + 17.75\mu_{O_2,0} - 12\mu_{CO_2,0} - 11.5\mu_{H_2O,0}$$
$$X_c = 7.42 \times 10^6 \quad \text{J/mol}$$

Using the molecular mass for Jet A from Table 9.1 the exergy content is defined as:

$$X_c(\text{J/kg}) = \frac{X_{Ch}(\text{J/mol})}{\hat{m}_{C_{12}H_{23}}} = 44.34 \times 10^6 \quad \text{J/kg} \tag{9.1}$$

The chemical exergy in Jet A released during combustion therefore aligns to the value given in Table 9.1.

This analysis can be expanded to account for a variable environmental definition. Here it is assumed the enthalpy of formation and standard molar entropy are constant with pressure variation, and the composition of air is constant within the altitude variation defined. The chemical exergy is to be calculated for altitudes of $0 - 15000m$, where the pressure and temperature variation is defined as:

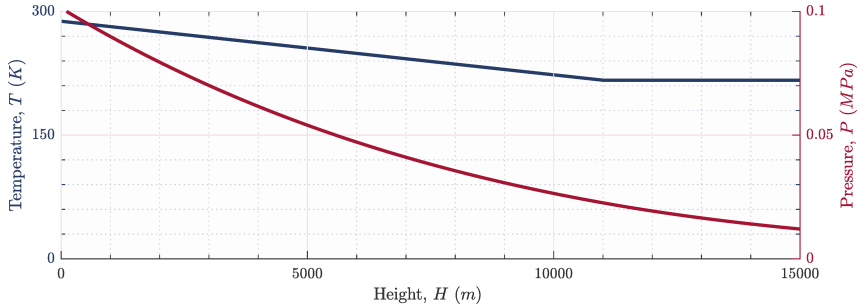

with this environmental variation the chemical exergy of the fuel changes with altitude (variable temperature) as:

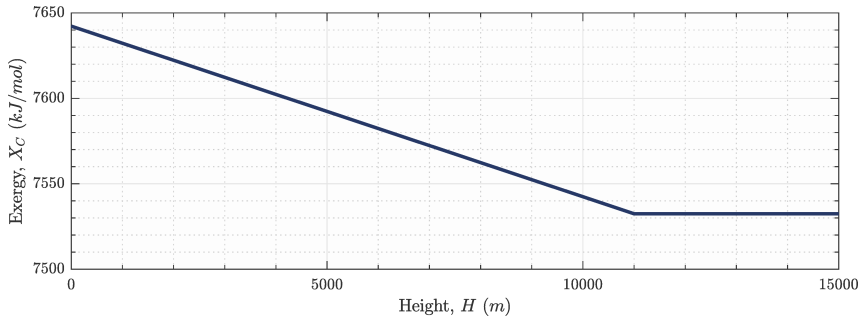

This relationship suggests a decrease in propulsion efficiency with increasing altitude, where in cruise the exergy available is 98% that available at sea level. A trend that is comparable to that seen with in use turbofan engine efficiencies.

9.1.3.2 *Propulsion System*

Chapter 3 showed that modelling of aircraft propulsion systems is an area where exergy analysis has been widely published, with the models having degrees of fidelity. Therefore it would not provide any additional contribution to knowledge to redo a turbofan detailed analysis. For the interested reader references for the optimisation of propulsion systems include Dincer [52], Clarke [47], Marley [107] and Ehyaei [61] in turbojet engines, and Doty [56], Roth [156] [155] [158] and Riggins [147][150][148] in turbofan engines for commercial aircraft. Instead, the thermodynamic loss model

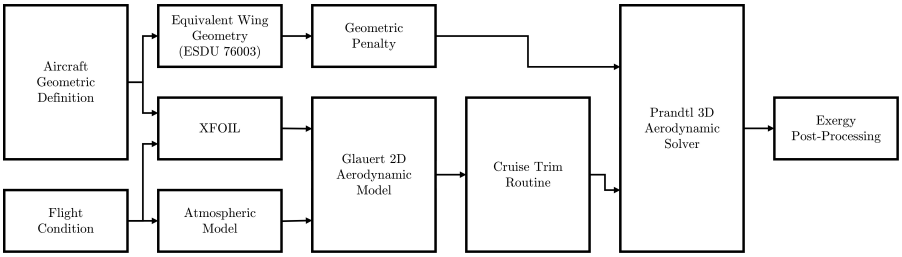

Figure 9.4: Simulink model of Aerodynamics of Glauert Theory

will use a top level propulsion system exergetic efficiency metric to model the losses associated with the engine. The exergetic propulsion efficiency is defined as:

$$\eta_{p_X} = \frac{\text{thrust power (useful work)}}{\text{Ideal available work}} = \frac{\dot{X}_{\text{actual}}}{\dot{X}_{\text{ideal}}}$$

The *ideal available work* would assume zero losses from the engine, thus the available work would be equal to the chemical exergy calculated in the previous section for a given mass flow. Here the chemical exergy is ideally converted to work, defined as:

$$\dot{X}_{\text{ideal}} = \dot{m} X_{Ch}$$

The *useful work* that is output from the real engine is the product of the thrust and velocity, defined as:

$$\dot{X}_{\text{actual}} = T u_\infty$$

Thus the exergetic propulsion system efficiency is:

$$\eta_{p_X} = \frac{T u_\infty}{\dot{m} X_{Ch}}$$

Introducing the thrust specific fuel consumption, $TSFC = \dot{m} f^{-1}$, gives

$$\eta_{p_X} = \frac{u_\infty}{TSFC \times X_{Ch}} \tag{9.2}$$

9.1.3.3 *Aerodynamics*

For the advantage of computational efficiency the aerodynamic model is a low fidelity Simulink based model utilising Glauert theory [73] for the two dimensional aerofoil and extended to a three dimensional wing to determine lift and drag using Prandtl's [137] empirical relationships. The proposed aerodynamics model is graphically shown in Figure 9.4. As the exergy calculation is a post-processing of aerodynamic data, it is in fact irrelevant as to the method the data is generated, and the Simulink model presented could be used on any aerodynamics analysis tool.

As the purpose of this model is to show the method of applying exergy analysis to aerodynamic data, the aerodynamic model presented is quite simplistic, modelling only the profile and lift-induced drag terms. For a more accurate result, where aircraft are flying at transonic speeds, wave drag estimates must be made, and the associated exergy destruction formulated. However this is outside the scope of the thesis and included as further work in Section 10.4.

Each block of the aerodynamics model in Figure 9.4 is discussed in more detail below.

- **Aircraft Geometric Definition**. The aircraft geometry used for simulation is given for each aircraft in Appendix B, which details aircraft; performance, body

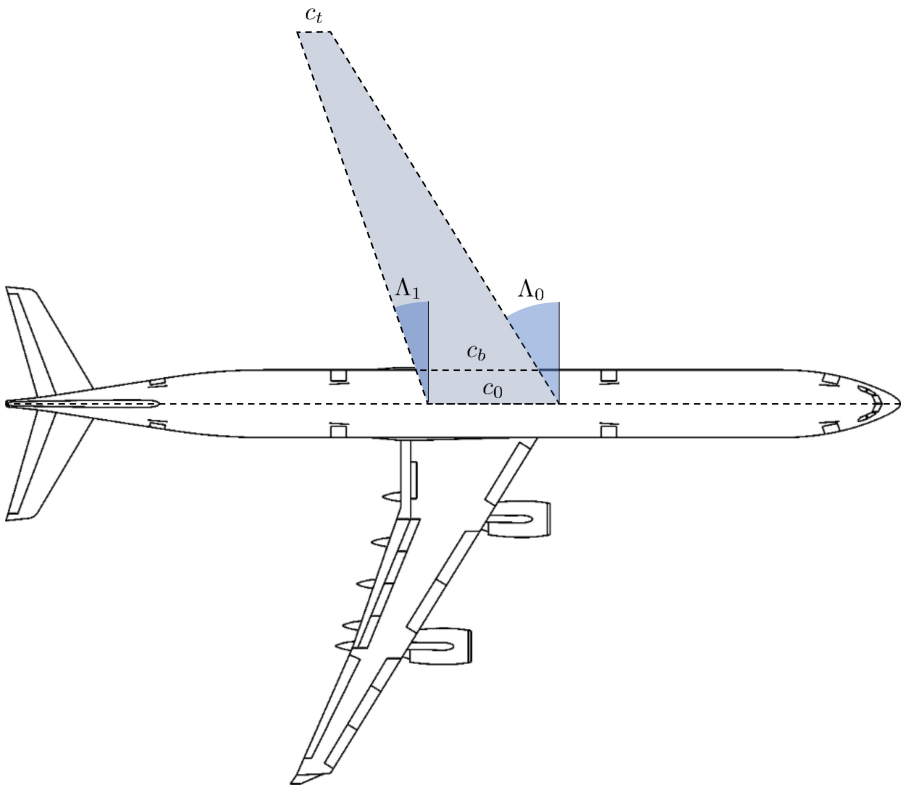

Figure 9.5: Equivalent wing definition using ESDU 76003

(fuselage), aerofoil and wing planform. For values not provided in the data sets, empirical geometric relationships from Raymer [143] and Sadraey [159] are used.

The geometry of the aircraft has a critical role in the performance of the system, and is the only input to the form functions (F_F) of the fuselage and wing, which are in the parasitic drag function (note, nacelles are not modelled in this framework).

$$F_{F_{fuselage}} = \left(1 + \frac{60}{\left(\frac{l}{d}\right)^3} + \frac{\left(\frac{l}{d}\right)}{400}\right)$$

$$F_{F_{wing}} = \left[1 + \frac{0.6}{\left(\frac{x}{c}\right)_m}\left(\frac{t}{c}\right) + 100\left(\frac{t}{c}\right)^4\right]\left[1.34M^{0.18}\left(\cos\Lambda_t\right)^{0.28}\right]$$

- **Equivalent Wing Geometry**. The majority of current generation aircraft do not have constant taper ratio wings, and as such are designated as being cranked. As such the analysis is done using the *equivalent wing* method as outlined in ESDU 76003. This creates a geometry for an equivalent trapezoidal wing which is required because the calculations performed in the Prandtl-Glauert analysis are only valid for swept trapezoid wings. An example of this for the Cranfield AX-1 aircraft is shown in Figure 9.5, and for other aircraft the data can be found in Appendix B with the aircraft geometric definition.
- **Geometric Penalty**. Block allows a mass penalty to be applied to the aircraft dependent on its geometric characteristics. Further details provided in Section 9.2 where it is implemented.
- **Flight Condition**. Defines the aircraft velocity (u_∞) and altitude (h) at any given time of the flight envelope.

- **Atmospheric Model**. Calculates the environment parameters according to the International Standard Atmosphere value for ambient temperature (T_∞), pressure (P_∞), density (ρ_∞), and speed of sound (a_∞) at the defined flight condition altitude.
- **XFOIL**. Drela's [57] XFOIL is used to characterise the aircraft's aerofoil, outputting the parameters for a given Reynolds number and Mach number:
  - Zero Lift Drag, C_{D_0}
  - Zero Lift Angle of Attack, α_0
  - Stall Maximum Angle of Attack, α_{max}
  - Lift at Maximum Angle of Attack, $C_{L_{max}}$
  - Minimum Drag, $C_{D_{min}}$
  - Lift at Minimum Drag, $C_{L_{min}}$

  It should be noted that there are limitations to the use of XFOIL, including that it works for two dimensional aerofoils only, and it is only effective at low Reynolds numbers and incompressible flows.
- **Glauert 2D Aerodynamic Model**. Glauert's [73] *The Elements of Aerofoil and Airscrew Theory* defined the angle of attack lift performance of a sub-sonic aerofoil, as defined by Sadraey [159] as

$$C_{l_\alpha} = 1.8\pi\left(1 + 0.8\frac{t_{max}}{\bar{C}}\right) \approx 2\pi$$

- **Trim Routine**. The trim routine trims the aircraft to the defined flight condition. The model only allows a variation in the aircraft's angle of attack to change the lift to allow cruise, climb or descent. Note that the trim routine does account for the 3D effects in lift reduction calculated in the Prandtl block.
- **Prandtl 3D Aerodynamic Solver**. Empirical relationships for the three dimensional wing and fuselage are used to determine the aerodynamic parameters of lift and drag. The parameters are calculated based on Prandtl [136] and Glauert [73] theory as defined in both Raymer [143] and Sadraey [159]. The lift is defined as:

$$L = \frac{1}{2}\rho u_\infty^2 S C_L$$

Given

$$C_L = C_{L_\alpha}(\alpha - \alpha_0)$$

$$C_{L_\alpha} = \frac{2\pi \mathcal{AR}}{2 + \sqrt{\frac{\mathcal{AR}^2(1-M^2)}{k}\left(1 + \frac{\tan^2\Lambda_t}{(1-M^2)}\right) + 4}}\left(\frac{S_e}{S}\right)\left(1.07\left(1 + \frac{d}{b}\right)^2\right)$$

$$k = \left(\frac{C_{l_\alpha}}{\frac{2\pi}{\left(\sqrt{1-M^2}\right)}}\right)^2$$

Note that drag due to shock waves and additional parasitic drag from nacelles and engines is not considered in this analysis. The Drag force is derived as:

$$D = \frac{1}{2}\rho u_\infty^2 S C_D$$

Table 9.2: Proportion of stored exergy in aircraft during cruise

Stored Exergy	Unit	Cruise	Contribution
Gravitational Potential Exergy	MJ	6279.2	85.3%
Kinetic Exergy	MJ	1083.0	14.7%
Potential Strain Exergy	MJ	0.31	0.00%
Total	MJ	7362.2	100%

The drag coefficient, C_D, is the sum of the parasitic (zero lift) drag, C_{D_0}, and the lift-induced drag, C_{D_i}, which is dependent on the lift coefficient, defined as:

$$
\begin{aligned}
C_D &= C_{D_0} + C_{D_i} \\
C_{D_0} &= \frac{\Sigma \left(C_f F_F Q S_w \right)_c}{S} + \cancel{C_{D_{misc}}} + \cancel{C_{D_{L\&P}}} \\
C_f &= \frac{0.455}{\left(\log_{10} Re \right)^{2.58} \left(1 + 0.144 M^2 \right)^{0.65}} \\
C_{D_i} &= \frac{\left(C_L - C_{L_0} \right)^2}{\pi e A} \\
e &= 4.61 \left(1 - 0.045 \mathcal{A}^{0.68} \right) \left[\cos \left(\Lambda_{LE} \right) \right]^{0.15} - 3.1
\end{aligned}
$$

9.1.3.4 *Stored System Exergy*

The aircraft has three stores of exergy when it is in flight; gravitational potential exergy, kinetic exergy and strain potential exergy. Whilst conventional aircraft dissipate this exergy as additional drag when coming to land, future aircraft configurations may look to harness this exergy and output it as work during the landing stage. To establish the balance of stored strain energy between the three stores, it is assumed the BEaRDS XB-2 aircraft is cruising at 35000ft (10668m) and 190m/s (as the example in Chapter 8). The XB-2 aircraft will assume to have a mass of 60000 kg at this snap shot of the stored exergy in time.

It can be concluded that the strain exergy calculated in Chapter 8 for the XB-2 aircraft is negligible in terms of stored exergy quantity when compared to the gravitational potential exergy and kinetic exergy. The proportions of stored exergy are shown graphically in Figure 9.6.

9.1.4 *Through Mission Analysis*

The exergy post-processing of this thermodynamic loss model is done on a transient analysis, as such exergy can be used as a versatile time domain solver accounting for the changes in environment during flight. Figure 9.7 shows a generic flight envelope for a long haul commercial aircraft, split into three critical phases; climb, cruise and descent.

Commercial aircraft flight envelopes are dominated by the cruise phase of flight and as such it is typical to perform comparative studies at just these conditions. Reviewing the work of Dincer [52] in Chapter 3 (Figure 3.10) showed when undertaking exergy analysis on a commercial aircraft the cumulative exergy loses over the entire flight were effectively the same for the variable reference state, as was found using a constant reference state at the cruise altitude. Error is introduced when a constant environment such as sea level is used throughout the flight envelope. As such to

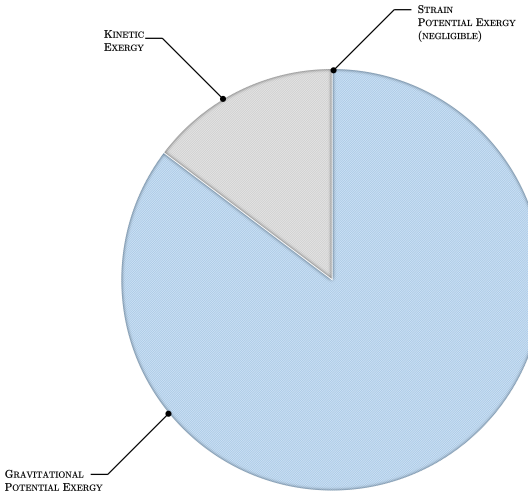

Figure 9.6: Proportion of stored exergy in aircraft during cruise

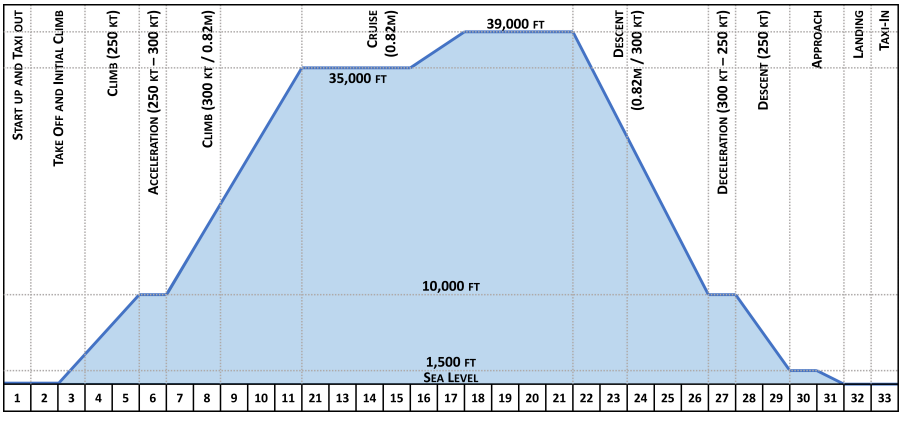

Figure 9.7: Generic flight envelope for a long haul commercial aircraft

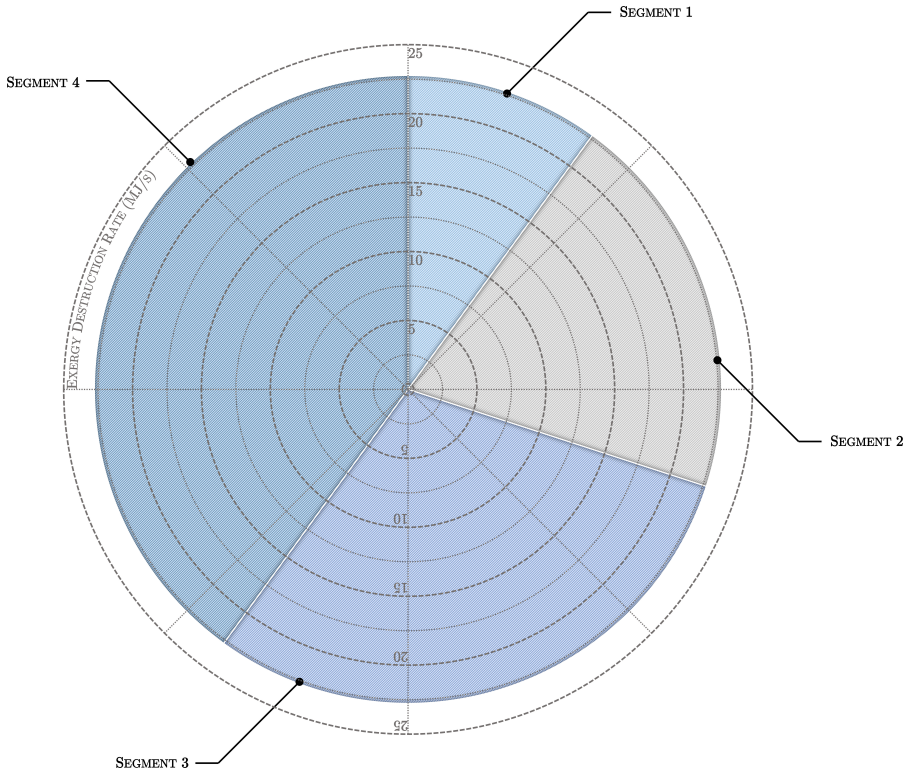

Figure 9.8: Example Exergetic Proportional Pie (EPP) diagram

simplify the analysis, this model will use a constant reference state at cruise altitude for the entire flight envelope in Figure 9.7.

9.1.5 *Assign System Losses*

Once the thermodynamic losses calculated by the modelling are integrated through the flight envelope, losses can be attributed to the specific sub-systems or processes. Chapter 3 defined the various methods in literature for visualising these assigned losses and comparing the results. Options include visualisation of exergy and exergy transfer through Sankey, Grassmann, Bond and Exergy Flow diagrams.

The problem with current exergy visualisation methods is they are focused primarily on the flow of exergy through the system and not on comparing the sub-system losses. As such this thesis advocates the use of a diagram designated as an Exergetic Proportional Pie (EPP) diagram, an example of which is given in Figure 9.8. The EPP diagram is essentially a scaled pie chart, where the comparative proportion of the loses is given by the pie segments, and the radius of the pie chart defines the total exergy transfer / destruction rate.

EXAMPLE 8

To show the capability of the thermodynamic loss model, this example will compare the thermodynamic performance of the BEARDS XB-2 aircraft against that of the Airbus A320. The aircraft geometry used for the thermodynamic modelling is given in Appendix B. Both aircraft are assumed to be cruising at 10668 m, at 231m/s for the A320 and 208m/s for the XB-2 aircraft. As described in Chapter 7 the fuselage, HTP and VTP is common between the A320 and XB-2. The only difference is the HARW on the XB-2 aircraft, and for this analysis two future engine options will be assessed. The future engine options are taken from the Boeing SUGAR programme [30], one being a next generation turbofan and the other an unducted fan (UDF) concept developed by General Electric. Both options are shown on the SUGAR aircraft below.

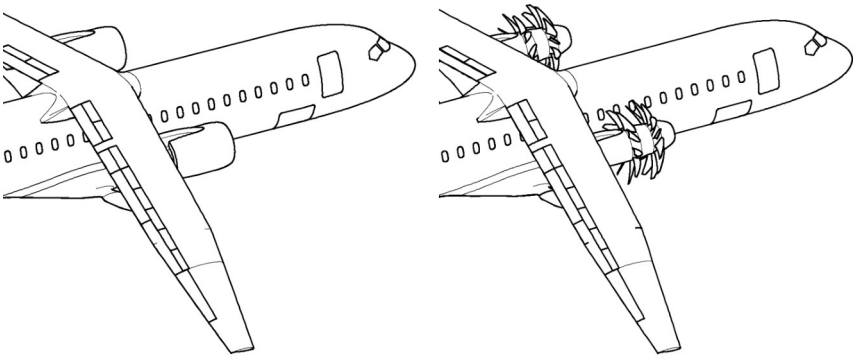

(a) Next Generation Turbofan (b) General Electric Unducted Fan Concept

Equation 9.2 can be used to calculate the exergetic efficiency of the A320 CFM-56, next generation turbofan (gFan+) and General Electrics UDF concept.

Parameter	Unit	CFM-56	gFan+ [30]	GE UDF [30]
TSFC	$kg/N/s$	1.42×10^{-5}	1.29×10^{-5}	1.18×10^{-5}
u_∞	m/s	231	208	208
η_{p_X}	%	36.7	36.4	39.8

The aerodynamics thermodynamics model can then be run with the flight conditions and geometry, assuming both aircraft are trimmed at cruise. The resultant exergy destruction due to aircraft form and lift are given in the table below.

Exergy (MJ/s)	A320	XB-2 (gFan+)	XB-2 (GE UDF)
Propulsion	12.05	12.15	11.11
Form	4.48	3.27	3.27
Lift	3.84	1.94	1.94
Total	20.36	17.36	16.32

The above results are plotted in EPP diagrams in Figure 9.9. The following can be concluded from this analysis:

- The exergy destroyed due to the engines transfer of chemical to conservative exergy is larger than the cumulative aerodynamic losses. Therefore if this is economical there is more improvement to be made on the engines than the aerodynamics.
- The exergy destruction due to aircraft form (function of parasitic drag) is less for the XB-2 than the A320 due to the lower flight speed.
- There is a significant reduction in the total destroyed exergy of the XB-2 against the A320, showing it is exergetically more efficient.

- The improvement in the aerodynamics is greater than that of the engines, as in the EPP diagrams (Figure 9.9) for the XB-2 configurations, the propulsion losses account for a greater proportion of the total losses.

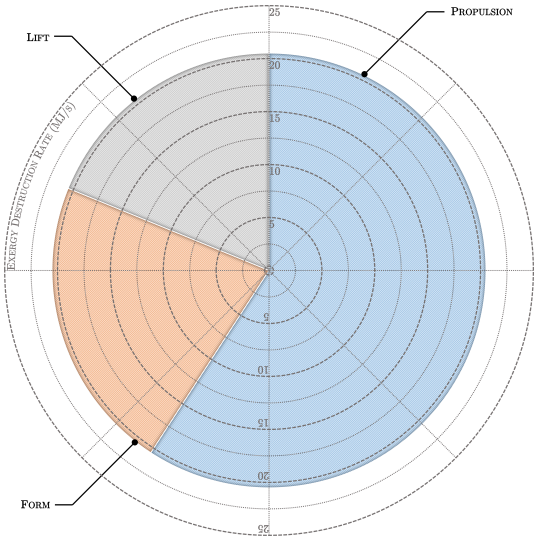

(a) Airbus A320

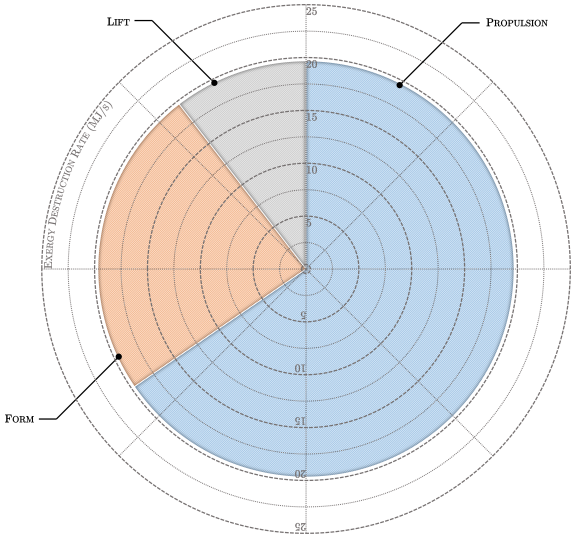

(b) BeaRDS XB-2 (gFan+)

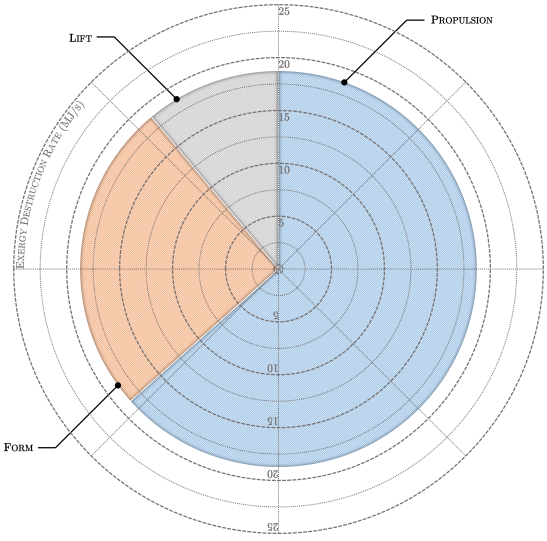

(c) BeaRDS XB-2 (GE UDF)

Figure 9.9: Exergy Analysis comparison between A320 and XB-2

9.2 MORPHING WING PERFORMANCE ASSESSMENT

Morphing the aerodynamic profile of a wing is not a novel concept. Birds *morph* their wings, by changing span, twist and tip gaps, during flight dependent on the required flight condition (see Figure 9.10a-9.10d). Military aircraft concepts have also considered the use of morphing wing. For example the General Dynamics F-111 Aardvark (Figure 9.10e-9.10h), can morph the sweep angle of the wing dependent on altitude, flight speed, manoeuvrability and fuel economy. It is also common to see aircraft carrier stowed aircraft to have ground morphing wings to allow for denser packaging in the carrier hanger.

This study investigates the benefit of incorporating span extension wing tips onto future aircraft configurations as a method of providing improved aerodynamic efficiency, whilst allowing the extension to fold on the ground to meet airport gate size constraints. This is a method already developed by Boeing for the 777X aircraft (Figure 9.10i) where the extended wing span during flight provides efficiency improvements, and the ground based wing fold allows the aircraft to service the same airports as the original Boeing 777. This is also a concept that Boeing have applied to the concept SUGAR aircraft (Figure 9.10j) where the ground based folding wing allows the aircraft to service gates used by the Boeing 737 and Airbus A320 aircraft.

In addition to the gate constraints, HARW aircraft also face challenges when it comes to in-flight loading. As the wings are larger in span and more slender, the wing internal loads are increased during gust incidents and aerodynamic loading in cruise. This results in the requirement of a stiffer wing box or as seen on the SUGAR concept, the addition of a truss which adds weight and drag to the aircraft. This means that careful accounting of the benefits and drawbacks of the improvement in lift-to-drag ratio is needed to ensure the benefits of HARW configurations are achieved.

To date ground folding wing span technology has not seen wide proliferation on commercial aircraft. One reason for this is that changing the aerodynamic profile of a wing requires some form of actuation system, which must be powered and adds weight to the aircraft. Thus, any performance benefit morphing provides must outweigh the penalty due to additional weight and power requirements, in addition to the previously discussed additional weight and drag from structural changes.

Traditional methods of quantifying the performance benefit of a wing extension, such as the Breguet Range Equation, take a force balance approach to the aerodynamics, using the aerodynamic efficiency ratio of lift-to-drag. The premise of this study is to present an energy transfer (thermodynamic) analysis approach to the aerodynamics of an aircraft, in contrast to the well established force balance, in an effort to provide a more holistic method of performance modelling for folding wings. The method uses the concept of exergy, and how it flows through the aircraft system. This method does not look to discredit the use of a force balance approach, instead proposes an alternative energy method to allow multi-disciplinary design of a complete aircraft system. This allows the comparison between the aerodynamics, propulsion, stored exergy and other sub systems under one unifying metric.

This study will therefore present an exergy based performance assessment of ground morphing wing extension technology using the thermodynamic loss management modelling approach presented in this chapter. The results from this analysis will then be validated against the traditional Breguet Range Equation approach, to provide confidence in the modelling method.

(a) (b) (c) (d)

(e) (f) (g) (h)

(i) Boeing 777X Aircraft - Grounded configuration

(j) NASA/Boeing Subsonic Ultra Green Aircraft Research - Grounded configuration

Figure 9.10: Examples of morphing wing aircraft

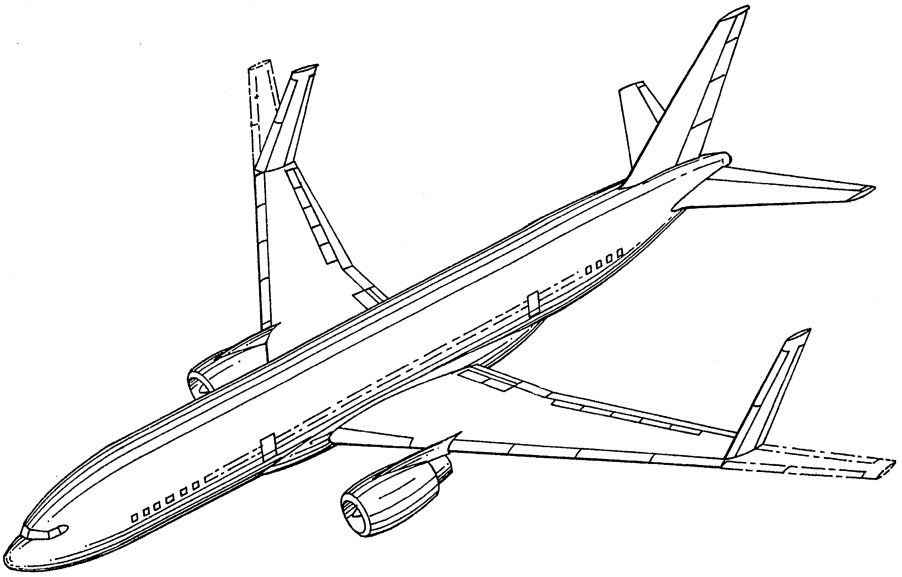

Figure 9.11: Generic concept for commercial aircraft with folded wingtips

9.2.1 *Analysis Motivation*

This premise of modelling a commercial aircraft with folded wingtips (Figure 9.11) is inspired by two separate bodies of work. That of Von Spakovsky[179] (previously discussed in Chapter 3) who used exergy analysis as a comparative measure to justify morphing wing technology for future military aircraft, and Cooper[49], who as part of the Claret programme used the Breguet approach to analyse the effectiveness of various morphing wing tip devices.

The initial study into the Advanced Air-air Fighter (AAF) by Von Spakovsky [179] simplified the AAF into two sub-systems, the propulsion and airframe. The aim of the study, based on the DARPA morphing aircraft structures programme, was to perform optimisation studies on the AAF airframe at different flight phases where the wing sweep, length, root chord length and tip chord length were the parameters to be optimised. An empirical exergy analysis was undertaken on these different configurations by Butt [35] with fuel consumption as the comparable output. A standard fixed wing fighter jet was also included for comparison. The model does not include actual morphing technologies, just the geometries they would create. Therefore to account for the additional components Butt [35] applies fuel and wing weight penalties as shown in Figure 3.8. The conclusion to this work was that if the morphing technology had a weight and fuel usage that lay in the shaded region of Figure 3.7 the morphing wing provided a benefit in terms of total fuel consumption, as derived from an exergy perspective.

Both methods showed the addition of morphing technology was beneficial to overall aircraft performance under certain conditions. However, it is not clear which method proves to be the most useful analysis tool during the design process. The analysis and discussion presented in this study aims to provide further clarity in this area.

9.2.2 *Span Extension using Equivalent Wing Geometry*

The test case used in this study looks to improve the energy efficiency of a long haul aircraft by providing span extension to a baseline configuration. The geometry used

Table 9.3: Wing parameters for baseline and wing extended aircraft variants

Parameter	Unit	Cranfield AX-1	HARW AX-1
Wing span	m	58.0	66.0
Wing area	m^2	363.1	363.1
Æ	–	9.3	12.0

in both analysis methods is the Cranfield AX-1 aircraft [10], a generic long-haul commercial aircraft. As previously discussed, the Prandtl-Glauert aerodynamics model requires simplified trapezoidal wings. As such the analysis calculates the equivalent wing geometry of the Cranfield AX-1 using ESDU 76003, and then changes the equivalent geometry to provide span extension. The baseline aircraft will be compared against a modified AX-1 with an increased wing span of up to 12 metres (6 metres on each semi-span). The extended wing span, b, will increase the aspect ratio, A, for a constant wing reference area, S as,

$$A = \frac{b^2}{S}$$

The reader is referred to Figure 9.12 for an example of the proposed wing extension from a 58 metres span to 66 metres. Given the International Civil Aviation Organization (ICAO) aerodrome reference codes[83] the 66 metre wingspan exceeds the *category E* gate constraint, thus to keep the aircraft category E compliant the wing tips would need to fold when the aircraft is on the ground. The associated wing parameters for the baseline and span extended aircraft in Figure 9.12 are shown in Table 9.3.

9.2.3 *Conventional Aerodynamic Efficiency Validation*

Given the simplification of the aircraft geometry to an equivalent wing and the use of Prandtl's [137] empirical relationships with defined assumptions, it is important to verify the output from the model before post-processing with the exergy solver. Given the main output as the aerodynamic lift and drag forces, along with the equivalent geometry, Figure 9.13 shows that with an increasing aspect ratio the lift-to-drag ratio also increases. The trend is verified against published results in Raymer [143, Figure 3.6], and what can be expected from the lift induced drag formula

$$C_{D_i} = \frac{C_L^2}{\pi e \text{Æ}}$$

where an increasing aspect ratio will lower the induced drag, thus reducing the overall drag and ultimately improving aerodynamic efficiency. So the trend produced by the thermodynamic loss model appears to be valid.

9.2.4 *Geometric Weight Penalty*

In the early stages of concept design, it is expected that all features of an aircraft concept will not be defined. For example, in this case study, the achievable aspect ratio may be known, but the additional structural supports (struts and trusses), increase in wing root structure and actuator mass and location, may not be known. To account for these unknowns, and to generate a mass requirement all additional structure must comply to, the thermodynamic loss model applies a weight penalty to the aircraft. The weight penalty will be added to the extended aircraft to account for the additional structure required and the actuator weight and power required to fold the wing when on the ground.

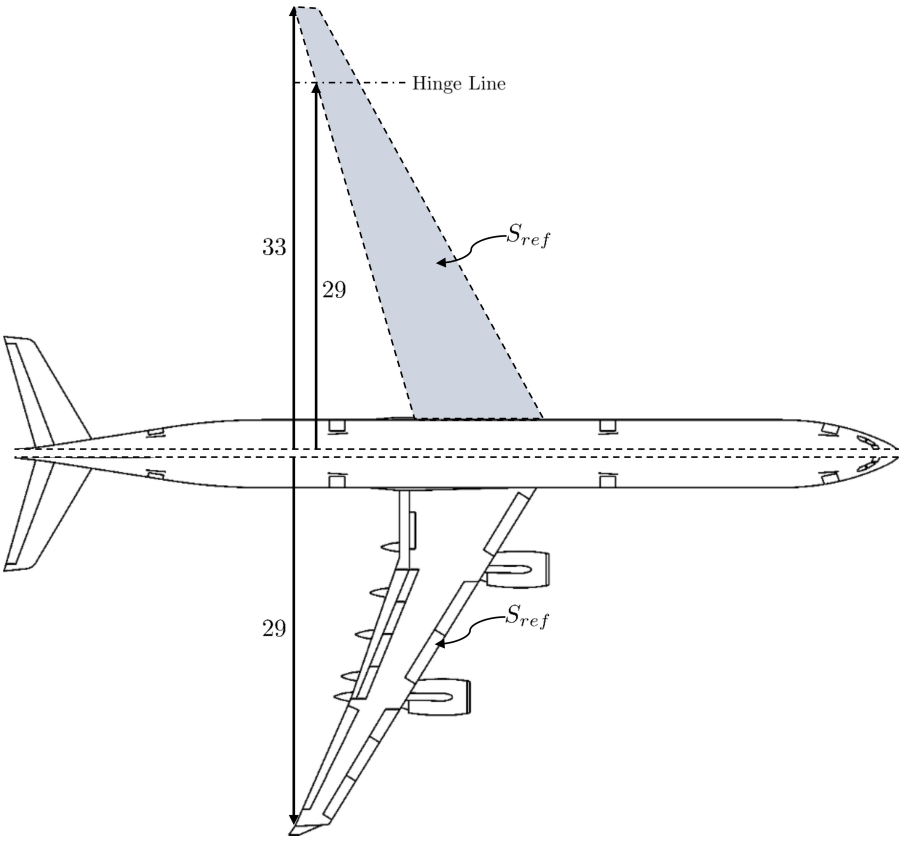

(a)

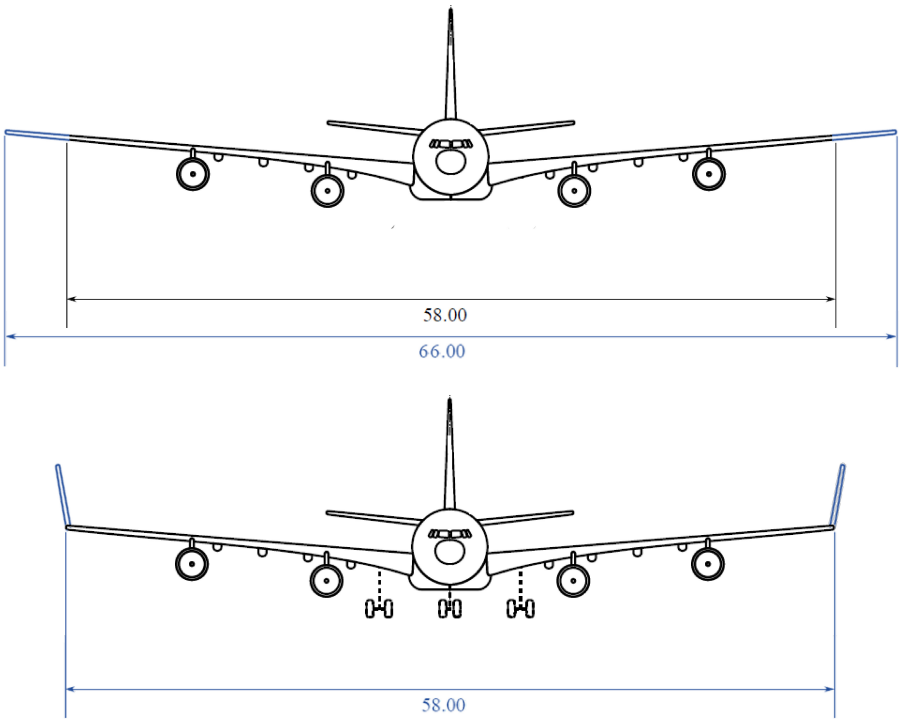

(b)

Figure 9.12: Span extension of Cranfield AX-1 Aircraft Configuration

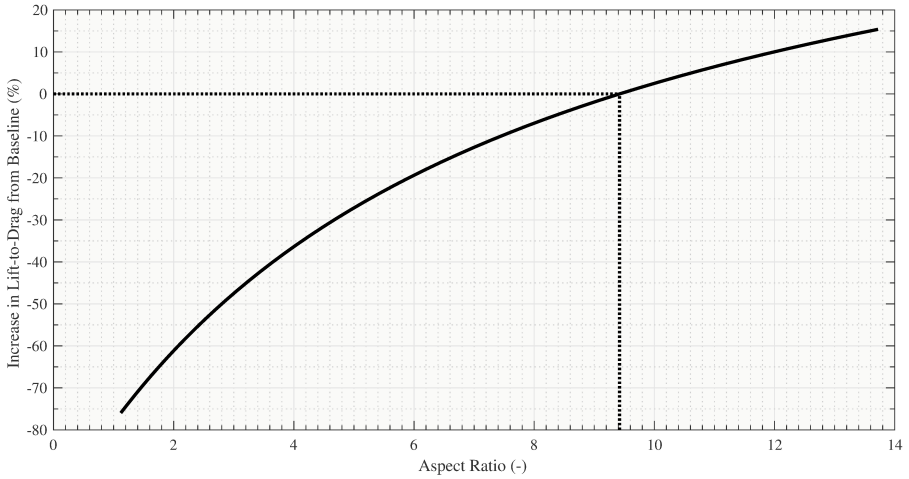

Figure 9.13: Cranfield AX-1 lift-to-drag ratio against increasing aspect ratio (constant S)

The weight penalty is calculated as a function of the aircraft geometry and masses. The initial cruise aircraft weight, W_2, is the sum of the Operational Weight Empty (OWE), W_0, the total of the flight constant payload and fuel reserves, W_1, and the fuel mass burnt off during the cruise flight, W_f, given as

$$W_2 = W_0 + W_1 + W_f$$

The penalised OWE, $\tilde{W}_0$, is increased by a proportion of the baseline OWE, as a function of the increase in wing root bending moment, $L_0 \frac{b_i}{b_0}$, which occurs from the new load distribution. The magnitude of this weight penalty is varied using a weight factor, P_f, where $0 < P_f < 2.0$, giving a penalised initial aircraft weight, $\tilde{W}_2$, as:

$$\tilde{W}_2 = \tilde{W}_0 + W_1 + W_f$$
$$\tilde{W}_0 = W_0 + W_0 P_f \left(L_0 \frac{b_i}{b_0} - 1 \right)$$

9.2.5 *Results and Discussion*

The thermodynamic loss model was therefore run using the exergy metric for two variables; wing aspect ratio and weight penalty factor, where $0 < P_f < 2.0$. The results of four aspect ratios (13.7, 12.6, 11.5 and 10.4) are plotted against the Cranfield AX-1 baseline configuration ($\mathcal{AR} = 9.4$) in Figure 9.14, showing how the assumed mass increase changes the additional exergy input rate required. The following can be concluded from this data:

- For an extended AX-1 aircraft of $\mathcal{AR} = 13.7$, it is feasible that additional structure will be required to support the increase in wing root bending moment. If the additional mass of this structure and the actuator incorporated to morph the wing on the ground is less than 22% of the aircraft OWE there is a benefit to the span extension, shown by the reduction in additional exergy. If the mass is in excess of the 22% threshold the additional mass is more detrimental to the aircraft performance than the increase due to aerodynamic efficiency.
- If there is no additional mass required for the structure and actuator, thus using the penalty factor where $P_f = 0$, a larger performance improvement is found the higher the aspect ratio of the wing. This trend is consistent as the penalty factor increases, thus for lower aspect ratio wings (e.g. $\mathcal{AR} = 10.4$) improvement in aircraft performance is only found if the additional mass does not exceed 5.5% of the OWE.

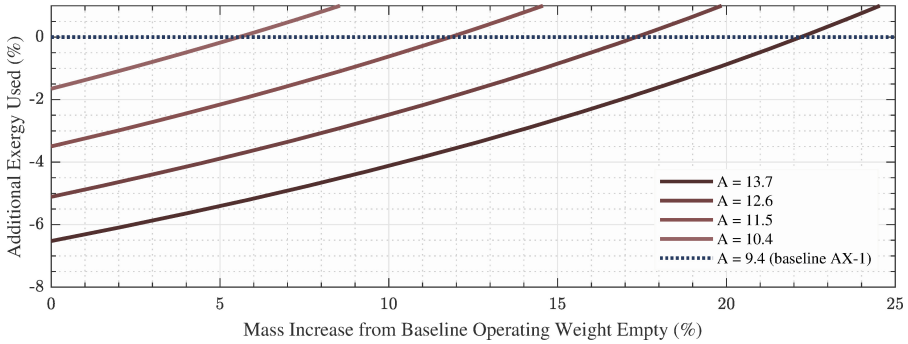

Figure 9.14: Weight penalty requirements generated from the Exergy approach

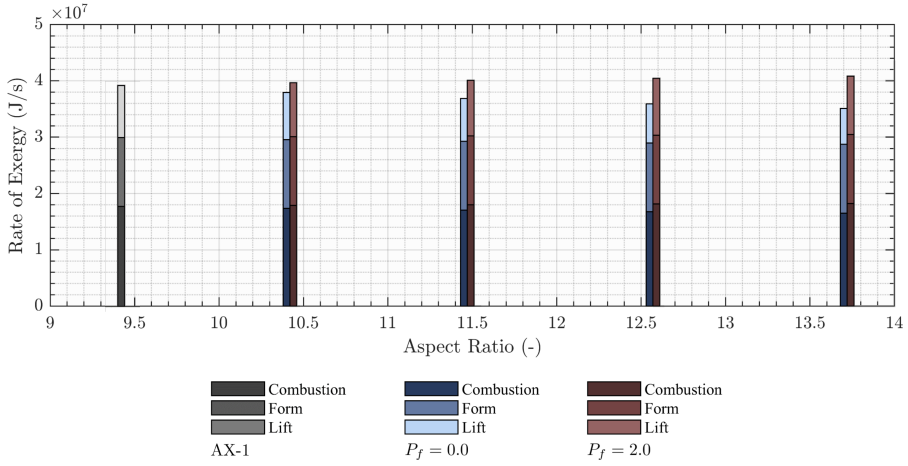

Figure 9.15: Exergy destroyed through different process in aircraft with variable aspect ratios

Figure 9.15 shows the same four aspect ratios (13.7, 12.6, 11.5 and 10.4) which are plotted against the Cranfield AX-1 baseline configuration ($\mathcal{AR} = 9.4$). However in this case they are plotted for the extremes of the weight penalty factor, $P_f = 0$ and $P_f = 2$. In this plot the individual contributions to the total exergy destruction can be seen from the propulsion, form (maintain kinetic exergy) and lift (maintain gravitational potential exergy). Figures 9.16a, 9.16b and 9.16c show EPP plots for $\left[\mathcal{AR} = 13.7 \wedge P_f = 2\right]$, baseline AX-1 and $\left[\mathcal{AR} = 13.7 \wedge P_f = 0\right]$. The following can be concluded from the data on these plots:

- Figure 9.16a represents a configuration over the baseline threshold, as such has a worse performance than the baseline.
- Figure 9.16c represents a configuration under the baseline threshold, as such has a better performance than the baseline.
- As the mass of the aircraft increases (with increasing weight penalty) the amount of lift to be generated increases, and consequently the lift-induced drag increases in value and the proportion of the overall exergy destruction increases.
- The parasitic drag (comparative to the form exergy required to maintain kinetic exergy) as a value has negligible change between the configurations as the overall aircraft external geometry is constant (except wing extension). However, as the total drag decreases (due to reduction in lift-induced) the required thrust reduces, making the proportion of form exergy higher.

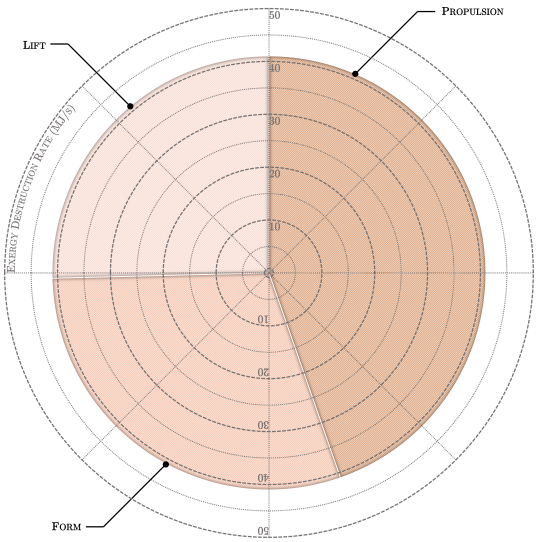

(a) Cranfield AX-1 heavy

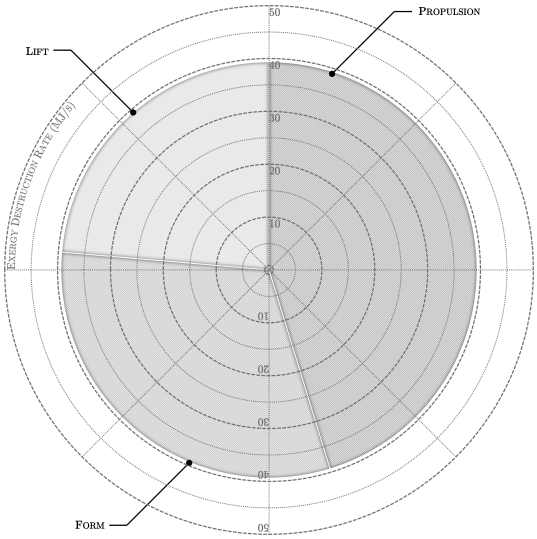

(b) Cranfield AX-1 baseline

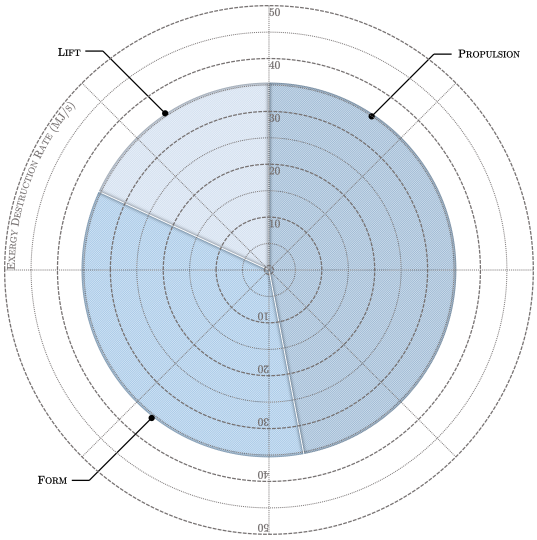

(c) Cranfield AX-1 light

Figure 9.16: Cranfield AX-1 performance assessment

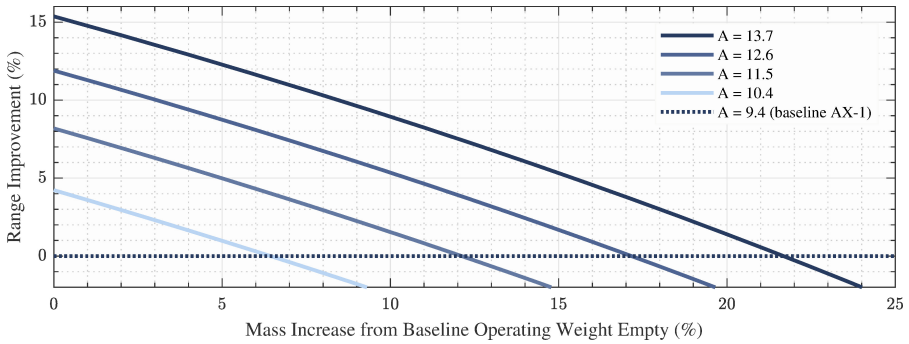

Figure 9.17: Weight penalty requirements generated from the Breguet approach

9.2.6 *Validation Using Breguet Range Equation*

The traditional method used to assess the effectiveness of span extension wing tips is to maximise the range (R) of an aircraft, for a given set of aircraft parameters, utilising the Breguet Range Equation for steady cruise. This section seeks validation of the above analysis by comparing the exergy thermodynamic loss model analysis method to the Breguet Range Equation. The long-established Breguet Range Equation is an implicit energy solver used to maximise the range of an aircraft for a given fuel load based on lumped mass parameters. This provides a comparative range of an aircraft configuration with the extended wingspan against the range of a conventional configuration. Reduced energy intensity provides improved range for a given fuel quantity, which can be achieved by maximising the lift (C_L) to drag (C_D) ratio, as well as the the ratio of initial penalised take off weight ($\tilde{W}_2$) to penalised empty weight ($\tilde{W}_0$) and fixed payload (W_1). If the range is improved for the extended wingspan configuration the design is assumed to be beneficial in terms of energy intensity. For the cruise stage of flight the Breguet variables are assumed constant and these variables are defined using a lumped mass model.

Using the thrust specific fuel consumption, $TSFC$, variable the Breguet Range Equation can be defined in terms of propulsive efficiency (η_p), aerodynamic efficiency (η_a) and the structural efficiency (η_s), as:

$$R = \left(\frac{LCV}{g}\right) \underbrace{\left(\frac{V}{LCV \times SFC}\right)}_{\eta_p} \underbrace{\left(\frac{L}{D\,(M)}\right)}_{\eta_a} \underbrace{\left(\ln \frac{\tilde{W}_2}{\tilde{W}_0 + W_1}\right)}_{\eta_s}$$

The Breguet analysis uses a constant propulsive efficiency, η_p, and a variable aerodynamic, η_a, and structural, η_s efficiency based on the extended wing span and weight penalty. The percentage increase in the range compared to the baseline AX-1 against the OWE percentage mass increase is given for four different aspect ratio aircraft in Figure 9.17. The graph can be used in such a way that if the design of say an aspect ratio 10.4 aircraft has an additional mass increase of less than 6.5% of the baseline OWE, the design will have an improved range. However, if the additional structural and wing mass in greater than the 6.5% threshold the additional mass has a larger detrimental affect on aircraft efficiency than the aerodynamic benefits. With an increase in aspect ratio the improvements in the aerodynamic efficiency are greater and as such, the mass penalty threshold is higher before the cross over to a less efficient design to the baseline.

To compare the exergy results to the Breguet results, Figure 9.18 plots the $\text{Æ}R = 12.6$ data as in Figure 9.17 for the Breguet output, but on the second y-axis the rate of exergy use during cruise is plotted against the weight penalty for the same aspect ratios as the Breguet method. The exergy results show the baseline AX-1 exergy rate

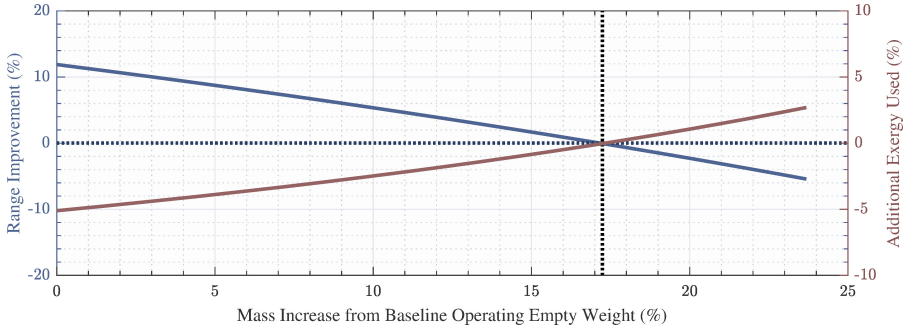

Figure 9.18: Comparison of the Exergy and Breguet results

during cruise, and how with a low weight increase the higher aspect ratios provide a more exergy efficient design. At the same weight increase points as the Breguet method the transition is seen between a more fuel efficient design to a less efficient design against the baseline.

9.2.7 *Comparing the Exergy and Breguet Approaches*

The use of implicit and explicit energy analysis methods for the incorporation of span extended technologies into future aircraft configurations have been studied through analysis performed on a test case. Two approaches have been used: the Breguet Range Equation and the second law based Exergy Analysis. The latter leads to a methodology that can support the design of the complete vehicle as a system of systems in a common mathematical framework. A critical part of this is the development of a decomposition strategy where all the subsystem components can be optimized to a system-level common metric. It has been shown that both the Breguet and the Exergy method provide suitable output to compare different in-flight morphing mechanisms under a single metric. However, the exergy method provides a more detailed analysis method which allows energy losses to be compared to any of the aircraft's subsystems.

One of the key advantages of the Exergy method over the Breguet approach is shown in Figure 9.15, where each energy using process (those modelled are combustion, form and lift) can be compared directly to different configurations under a common design metric of exergy.

9.3 CHAPTER SUMMARY

This chapter has shown a stage by stage development of a thermodynamic loss model that uses an exergy metric to assess the performance of aircraft. The thermodynamic loss model was used to show that from an exergy use perspective, the BEaRDS XB-2 aircraft is more efficient than the Airbus A320, due to the improvement in aerodynamic efficiency and propulsion efficiency from future conceptual engine designs. The chapter concludes by discussing the benefits of incorporating span extension technologies onto long haul commercial aircraft, where the extension morphs on the ground to allow aircraft geometry to meet gate constraints. This method was then compared and validated against the conventional Breguet Range Equation, to provide confidence in the capability of the exergy based approach.

Part IV

CONCLUSIONS

"I may not have gone where I intended to go, but I think I have ended up where I needed to be"

Douglas Adams
The Long Dark Tea-Time of the Soul
1988

10

CONCLUSIONS

10.1 THESIS TECHNICAL OUTPUT

Part i outlined the thesis objective, technical background and the state of exergy analysis for aerospace applications. There is a need to extend the exergy work done primarily in the propulsion, military and hypersonic domains to make the analysis method suitable for commercial aircraft analysis.

Applying exergy to commercial aircraft is an analysis method in it's infancy. With such a large potential scope of study the thesis focused on applying the method to conventional and future HARW aircraft geometries. To facilitate this for flexible aircraft (such as HARW) there was a need to evaluate all nodes of Collar's triangle in terms of exergy. This was the base premise to Part ii of the thesis from which the following can be concluded:

- The BEaR framework developed in Chapter 4 provides a versatile framework to model the structural dynamics of any *slender* system that can be discretised into a series of beams and nodes. Based on Timoshenko mechanics, BEaR provides a capability to produce system state (displacement, velocity and acceleration) output that a post processing routine can perform exergy analysis on. As an open source framework BEaR was written to allow its use in mutliple other programmes, which can be seen by it's use in the BladeSense programme [180] and the continued use of the solver in the BEaRDS programme [134].
- Using the output from the BEaR code on simple toy example mass-spring-damper systems, the concept of exergy was shown to be different than energy for systems with preloaded springs. Here the minimum energy state is the point of zero exergy, yet energy remains in the system, just not energy that can be extracted as useful work. The response of a structural dynamic system was shown to be presented in exergy terms, where the mass, stiffness and damping were associated to the kinetic, potential and dissipation of exergy.
- In considering the aerodynamic forces, exergy analysis on the output fluid state from a CFD analysis allowed the available energy in the system to be quantified. Here the thermal, mechanical and destroyed exergy states can be identified in the wake of the aircraft. This is useful for work on energy harvesting through formation flight, where the exergy analysis shows not all energy in the wake is *useful*, and thus quantifies the maximum amount of work that can be extracted.
- An exergetic efficiency, comparable to a Carnot efficiency, was identified for aircraft, where the efficiency is the exergy destroyed in ideal flight divided by the total exergy destroyed. The ideal energy transfer is defined as the destroyed exergy for a comparable zero volume frictionless lifting surface. This states that the optimal aircraft will generate lift to support the mass of the plane in trimmed cruise flight, yet any losses from the form of the aircraft or inefficiencies in the lift distribution are not-ideal, and thus avoidable.
- Taking an exergy approach to optimal lift distributions, based on the work of Greene, it is shown the circulation distribution that produces minimum induced drag is a parabolic shape in contrast to the well established ellipse defined by Prandtl. This is not to state the ellipse is not the *ideal* lift distribution,

it is just discounted from the exergy approach as it has an infinite circulation gradient at the tip, which defines infinite entropy generation. Thus this distribution is discounted as it disobeys the second law of thermodynamics.

With the technical foundation for exergy analysis of HARW and conventional commercial aircraft, Part iii focuses on the application of exergy to commercial aircraft performance assessment and design. The main conclusions made in this part include:

- Using the minimum exergy destruction derived circulation distribution theory, the BEaRDS XB-2 aircraft is sized to provide the maximum aspect ratio and thus minimum induced drag whilst avoiding negative circulation. It was shown this method derived in the thesis for the unconstrained span, produces a similar result to Prandtl's unconstrained span optimal lift distribution [137]. BEaRDS XB-2 was developed as a HARW version of the short haul Airbus A320. Using the BEaR initialisation script with some assumptions from the similar configuration NASA/Boeing SUGAR, a representative structural model was developed. With the generation of aerodynamic and structural definition, all the exergy based processes developed in Part i can be applied.
- The work package of the BEaRDS programme that this thesis formed a part of, provided a dynamically scaled geometry of the BEaRDS XB-2 aircraft, scaled to fit in the Cranfield 8'x6' wind tunnel. By undertaking an exergy post processing of an aeroelastic analysis of both the full scale and scaled aircraft wings, it was shown why it is difficult to scale up technologies that are shown to work on dynamically scaled models. For a model one sixteenth the geometry of the full scale aircraft, if a technology is shown to work on the scaled model (e.g. folding wing tip), when scaled up to the full size the work input to operate the technology is 5072 times higher. And if one considers the energy and exergy use or savings in the system, they are 20290 times higher for the full size over the scaled aircraft.
- As an introduction to how exergy analysis can be used to analyse the performance of an aircraft a *thermodynamic loss management* model was built allowing the propulsion, aerodynamics, structure and storage systems to all be modelled and compared under the single exergy metric. The test case showed using an exergy based *thermodynamic loss management* model was suitable to assess the performance improvements of increasing the span of the Cranfield AX-1 aircraft, and provides a ceiling mass requirement that the actuation and additional structural mass must be under such that the increased span provides a performance improvement.

10.2 DISSEMINATION OF WORK

The dissemination of work only includes journal papers that have been published. Conference proceeding and invited presentations are listed if they have been presented.

10.2.1 *Journal Papers*

Hayes, D., Lone, M., Whidborne, J. F., Camberos, J., and Coetzee, E., "Adopting exergy analysis for use in aerospace," Progress in Aerospace Sciences, vol. 93, Aug. 2017, pp. 73–94.

10.2.2 *Conference Proceedings*

Pontillo, A., Hayes, D., Dussart, G., Lopez, G., Carrizalez, M., Yusuf, S., and Lone, M., "Flexible High Aspect Ratio Wing: Low Cost Experimental Model and Computational Framework," 56th AIAA Aerospace Sciences Meeting, AIAA SciTech Forum, Orlando, Florida, USA: American Institute of Aeronautics and Astronautics, 2018.

Hayes, D., Lone, M. M., Whidborne, J. F., and Coetzee, E., "Evaluating the Rationale for Folding Wing Tips Comparing the Exergy and Breguet Approaches," 55th AIAA Aerospace Sciences Meeting, AIAA SciTech Forum, Dallas, Texas: American Institute of Aeronautics and Astronautics, 2017.

Weber, S., Ramos Valle, L., Barral, X., Hayes, D., Lone, M. M., and Cooke, A., "Impact of Rotor Blade Aeroelasticity on Rotorcraft Flight Dynamics," AIAA Atmospheric Flight Mechanics Conference, Dallas, Texas: American Institute of Aeronautics and Astronautics, 2017.

Hayes, D., Lone, M. M., and Whidborne, J. F., "Entropy Generation Minimisation and Exergy analysis approaches for aerospace applications - A review," 54th AIAA Aerospace Sciences Meeting, AIAA SciTech Forum, San Diego, California, USA: 2016, pp. 1–18.

10.2.3 *Invited Presentations*

Hayes, D., "An Exergy Approach to Aerodynamic Performance of Flexible Aircraft," Airbus Flight Physics Distributed Partnership R&T (DiPaRT), Bristol, UK: 2017.

Hayes, D., "Developing Generalized Models for Aircraft Thermodynamic Loss Management," International Graduate Summer School (IGSS), Beihang University (BUAA), Beijing, China: 2017.

Hayes, D., "Exergy Methods for Flexible Commercial Aircraft," Airbus PhD Day, Filton, Bristol, UK: 2017.

Hayes, D., "Evaluating the Rationale for Folding Wing Tips Comparing Exergy and Breguet Approaches," Airbus Flight Physics Distributed Partnership R&T (DiPaRT), Bristol, UK: 2016.

Hayes, D., "An Exergy Analysis Approach for Flexible Commercial Aircraft," Airbus Flight Physics Distributed Partnership R&T (DiPaRT), Bristol, UK: 2015.

10.3 CONTRIBUTION TO KNOWLEDGE

Specific contributions to knowledge of each chapter has been highlighted throughout the thesis. Here a summary of the main contributions this thesis has made in the design of aerospace vehicles, is presented:

- The *current* sole journal paper from this thesis, *Adopting exergy analysis for use in aerospace* (based on Chapter 3 of the thesis), provided a detailed review of the literature available on exergy analysis application aerospace systems and showed how it could be made applicable to commercial aircraft. Deriving many novel insights into the application of exergy analysis, this paper provided a review paper not available before, to show how a method applied to propulsion, military and hypersonic systems could be used in commercial aircraft design.
- The large deformations seen in HARW aircraft require non-linear structural analysis. This thesis took the non-linear geometric stiffness matrix developed by Przemieniecki [138] for a 3 DoF system and extended its application for a

generic 6 DoF system. This introduced terms into the non-linear matrix that were not previously available, and made the matrix suitable for integration into the 6 DoF Timoshenko based BEAR framework.

- Using an exergy destruction (proportional to entropy generation) approach, the optimal damping coefficient for any system can be defined based on the initial exergy ratio of kinetic to potential. This is an important finding, as allows designers to develop viscous dampers to return the HARW system to its trimmed condition in as short a time as possible during events such as gusts.
- The previously published exergy coefficient (a measure of the efficiency of an aircraft) was corrected in this thesis from that previously published by Camberos.
- The work of Greene identifying optimal lift distributions from an entropy perspective was extended to compare the work to that of Prandtl for an unconstrained span. This work allowed the development of a HARW based on the minimum exergy destruction principle, the BEARDS XB-2 aircraft.
- Work conducted previously on the dynamic scaling of aircraft to allow wind tunnel testing focused purely on matching the dynamic response, see [144]. This thesis showed if you model a novel technology such as a folding wingtip on a scaled modelled, the reason it is hard to scale the technology up to a full size aircraft is the substantial increases in work required and system energy.
- The premise of a thermodynamic loss management model was based on the framework of Roth [157]. This thesis took the method and applied it to the performance assessment of an aircraft with a morphing wingtip to provide span extension technology. The contribution to knowledge is this application and the validation of the method by comparing it to the well established Breguet Range Equation.

10.4 FURTHER WORK

Given that exergy application to commercial aircraft has been sparsely researched, this thesis had to focus on the specific application of exergy for highly flexible aircraft. There is thus clearly many areas of research that could be undertaken to show the full potential of exergy analyses for commercial aircraft. This future work section will focus on how the work undertaken in this thesis can be expanded and not the wider question of exergy analyses general application to aerospace systems.

- Chapter 5 developed a near-field exergy analysis of the aircraft wake. This is useful for individual aircraft optimisation, however if this is to be extended to model formation flight, a far-field exergy analysis of the wake needs to be done to model the wake roll up into larger vortices and how these can be exploited by trailing aircraft.
- The original parabolic circulation distribution for minimal induced drag of a constrained span wing, developed by Greene [75] was questioned and criticised due to it not conforming to the accepted convention that an ellipse is the optimal lift distribution. The comparison made in this thesis for the unconstrained span optimal lift distribution, shows the Greene method and Prandtl are very similar. As such the same questioning and criticism would not be expected, however this still remains a theoretical derivation. A CFD analysis or wind tunnel testing of the distributions could be done to provide validation data for the hypothesis.

- Linked to the above optimal lift distribution, a multi-parametric optimisation routine could be built to calculate the optimal span accounting for all sources of exergy destruction (not just induced), and also accounting for the effect on the structural dynamics and aerodynamic efficiency linked to deformation shown in Chapter 5.
- When designing transonic aircraft in addition to the minimisation of the induced drag, designers aim to minimise wave drag. Modelling wave drag in the form of exergy destruction would allow a more comprehensive understanding of the true available energy losses due to aerodynamics.
- The studying of the nodes of Collar's triangle focused on only the dynamic response of dynamic aeroelasticity. The unstable phenomena such a flutter and buffeting were not studied as the assumption was made any flexible aircraft still needs to avoid inducing these responses. However, under taking an exergy analysis of flutter could provide an interesting insight, as the concept of negative damping from the exergy perspective suggests negative entropy generation, which clearly cannot be the case, so worthy of looking further into.
- The thermodynamic loss model outlined in Chapter 9 can easily be extended to include more of the aircraft sub-systems such as the environmental control system, APU or to investigate electrical propulsion. Electrical propulsion is especially of interest for exergy analysis as the method cannot use conventional methods such as Breguet. Furthermore with the fuel not being burnt off and instead carried as batteries, there is a clear need to evaluate the efficiency of such aircraft.
- The thesis has only outlined the small part of the BEARDS programme that the thesis feeds directly into. There is further work continuing on this topic at Cranfield University.

Part V

APPENDIX

"No man should escape our universities without knowing how little he knows."

J. Robert Oppenheimer
Partisan Review, Summer issue
1967

A

TECHNICAL FOUNDATION AND FORMULAE EXAMPLES

EXAMPLE 9

The purpose of this thought experiment example is to clarify the difference between energy, entropy and exergy.

There are two closed systems within a defined environment, which has the properties of P_0, T_0 and μ_0. Each system has $1kg$ of a gaseous air, and both are at the same temperature, $T = 293K$, the systems differ in volume, thus System A is at a higher pressure than System B $P_A > P_B$. The internal energy, U, within each system can be calculated as

$$U = \frac{3}{2}nRT$$

given the substance, mass and temperature are the same in both systems, this means both systems have the same internal energy

$$U_A = U_B$$

If a turbine is attached the the closed system work can be extracted. So the question remains, given both systems have the same internal energy, which systems energy is more *useful*? In order to answer the question, the environmental pressure, P_0, must be defined, as required by exergy analysis. Using equation 2.5 with a defined environmental pressure of $P_\infty = 1bar$, a greater amount of work can be extracted by the turbine attached to System A, as the pressure differential between the system and the environment is greater than with System B, thus

$$X_A > X_B$$

The pressure of System B is the same as the environment, thus before the turbine is attached, the system is already in thermodynamic equilibrium with the environment, thus has zero exergy.

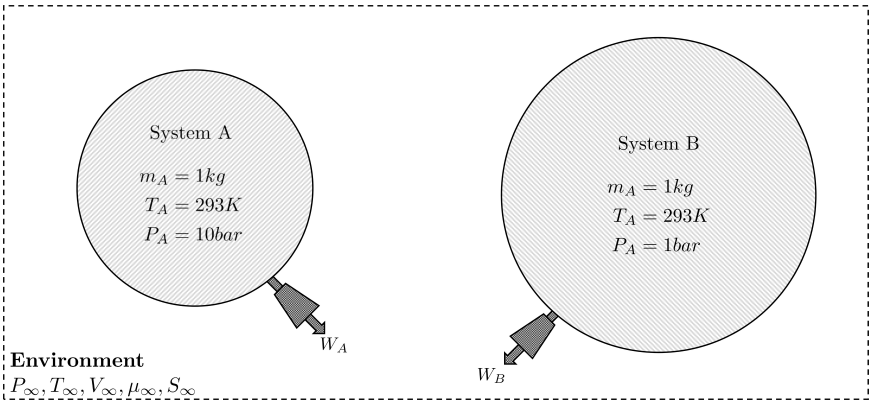

The total exergy that can be extracted from System A is that which brings System A into thermodynamic equilibrium with the environment. However, the maximum amount of work (X_{max}) cannot be extracted as the turbine is not ideal, and due to irreversibilities such as friction, the turbine will transfer energy via heat and generate entropy, in-line with equation 2.2.

EXAMPLE 10

The example will calculate the exergy of a stream of gas, assumed to be ideal such that simplifying methods can be used.

The enthalpy of the stream is defined by Cengel [44] with the thermodynamic relation:

$$dh(s,p) = Tds + vdp$$
$$ds = \frac{dh}{T} - \frac{v}{T}dp$$

Stating the ideal gas assumptions to be made

$$pv = nRT \tag{A.1a}$$
$$h = c_p nkT \tag{A.1b}$$

Substituting equations A.1a and A.1b into 2.4, assuming single mole of substance

$$ds = c_p \frac{dT}{T} - \frac{R}{p}dp \tag{A.2}$$

Taking the integral $\int_1^2 ds$

$$\underbrace{s_1 - s_2}_{\dot{s}} = c_p \ln \frac{T_1}{T_2} - R \ln \frac{P_1}{P_2} \tag{A.3}$$

The time rate of change of exergy in the system can be defined by the stream exergy from Equation 2.7

$$\psi = \dot{X} = \dot{h} - T_\infty \dot{s} \tag{A.4}$$

Introducing the thermodynamic relation of $c_p = \frac{\delta h}{\delta T}$

$$\psi = \dot{X} = c_p (T - T_\infty) - T_\infty \left(c_p \ln \frac{T_1}{T_2} - R \ln \frac{P_1}{P_2} \right) \tag{A.5}$$

Figure shows Equation A.5 as a function of exergy vs temperature for three different pressures

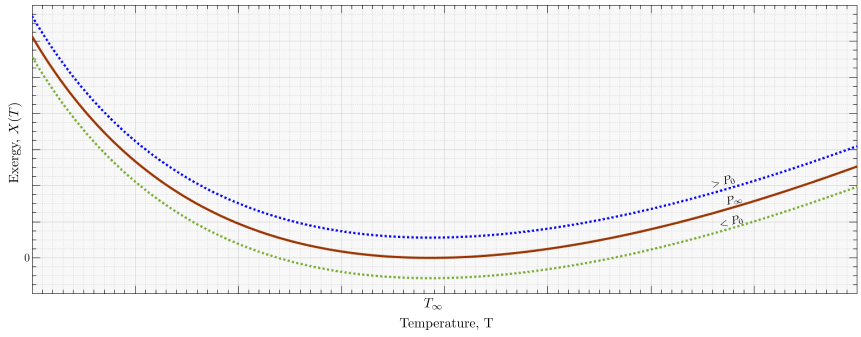

B

AIRCRAFT GEOMETRY

B.1 AIRBUS A320

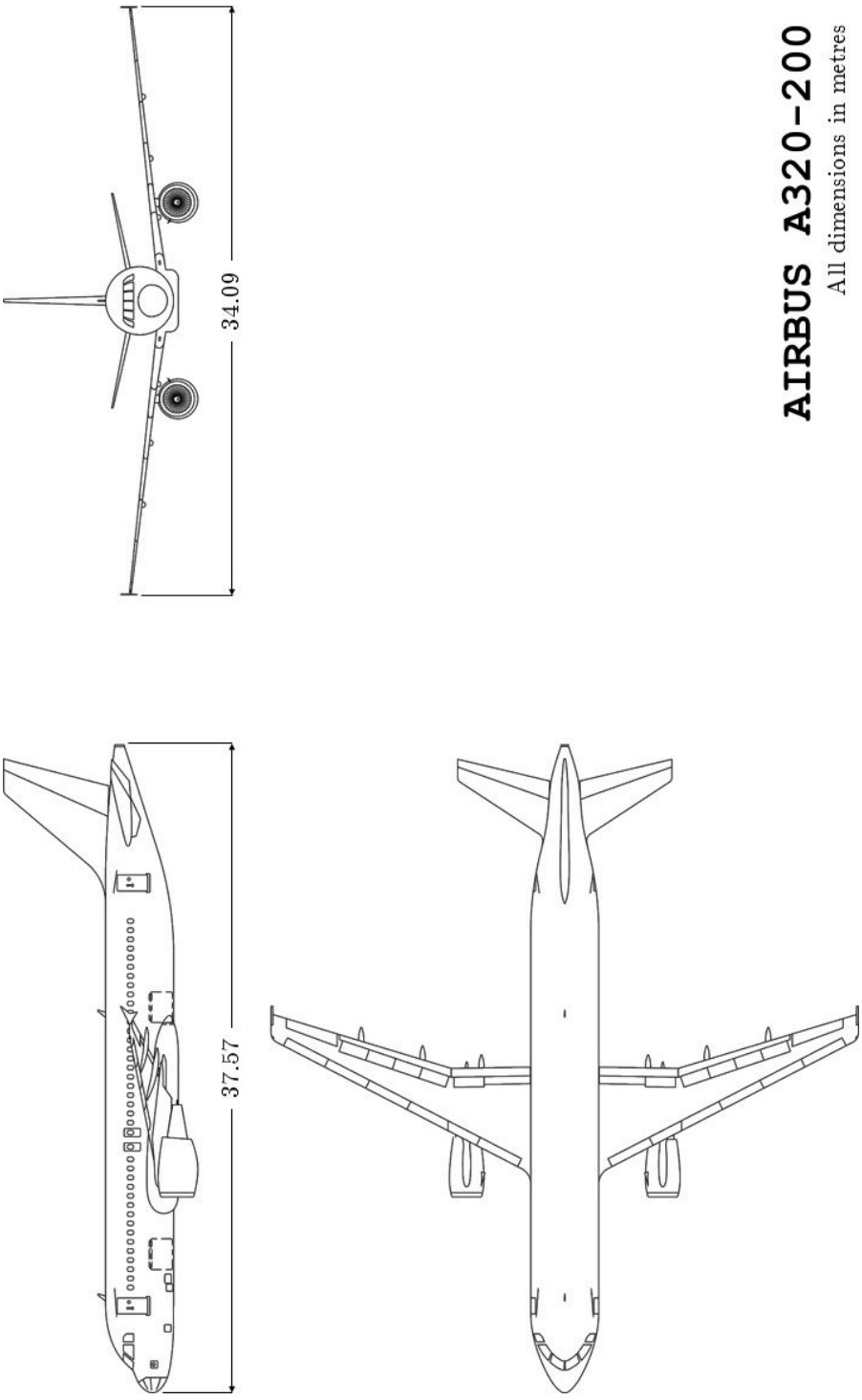

Figure B.1: Airbus A320 drawing

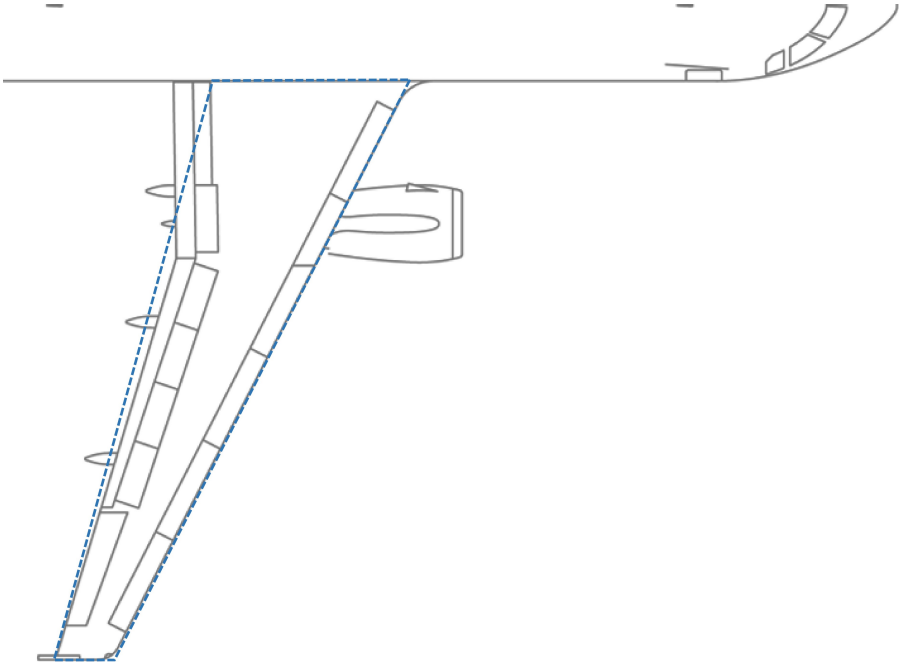

Figure B.2: Airbus A320 equivalent wing

Table B.1: Airbus A320 Aircraft Parameters

	Parameter	Symbol	Units	Value	Ref
Performance	Operating Weight Empty	OWE	kg	42,100	[85]
	Maximum Take-Off Weight	$MTOW$	kg	73,500	[85]
	Maximum Payload Weight	W_{pay}	kg	20,400	[85]
	Cruise Altitude	h	m	11,280	[85]
	Cruise Velocity	u_∞	M	0.78	[85]
	Range (typical)	R	km	4,800	[85]
	Powerplant (x2)	CFM56-5A1			[85]
	Thrust (x2)	T	kN	111.2	[85]
	Specific Fuel Consumption	SFC	$g/kN/s$	16.88	[86]
	Fuel Consumption (cruise)	$\dot{M}_f$	kg/h	2100	[86]
Body	Length	f_l	m	37.57	[85]
	Fuselage height	f_z	m	4.14	[85]
	Fuselage width	f_y	m	3.95	[85]
Aerofoil	Aerofoil	BAC 449 (assumed)			[95]
	Thickness ratio	$\frac{t}{c}$	–	0.113	[184]
	Lift at zero AoA	C_{l_0}	–	0.208	[184]
	Zero lift AoA	α_0	rad	0.031	[184]
Planform	Span	b	m	34.09	[86]
	Aspect Ratio	Æ	–	9.5	[85]
	Reference area	S_{ref}	m^2	122.4	[85]
	Sweep (LE)	Λ_{LE}	rad	0.471	*
	Sweep ($\frac{c}{4}$)	$\Lambda_{\frac{c}{4}}$	rad	0.436	[86]
	Root Chord	c_b	m	6.10	[85]
	Streamwise c_b position	x_b	m	12.55	*
	Tip Chord	c_t	m	1.62	*
	Streamwise c_t position	l_t	m	20.35	*
	Taper Ratio	λ	–	0.240	[86]
	MAC	$\bar{c}$	m	4.29	[86]
	Crank Location	y_1	m	6.47	*
	Crank Chord	c_1	m	3.80	*
Equivalent Planform	Span	b	m	34.09	[81]
	Aspect Ratio	Æ	–	10.9	[81]
	Gross area of wing	S	m^2	115.16	[81]
	Planform area of wing	S_e	m^2	101.82	[81]
	Sweep (LE)	Λ_{LE}	rad	0.4776	[81]
	Sweep ($\frac{c}{4}$)	$\Lambda_{\frac{c}{4}}$	rad	0.4305	[81]
	Sweep ($\frac{c}{2}$)	$\Lambda_{\frac{c}{2}}$	rad	0.3813	[81]
	Sweep (TE)	Λ_{TE}	rad	0.2770	[81]
	Root Chord	c_r	m	5.1363	[81]
	Streamwise c_r position	l_n	m	12.55	[81]
	Tip Chord	c_t	m	1.62	[81]
	Streamwise c_t position	l_t	m	20.35	[81]
	Taper Ratio	λ	–	0.3154	[81]
	geometric mean chord	$\bar{\bar{c}}$	m	3.3781	[81]
	MAC	$\bar{c}$	m	4.0136	[81]

B.2 BOEING SUGAR

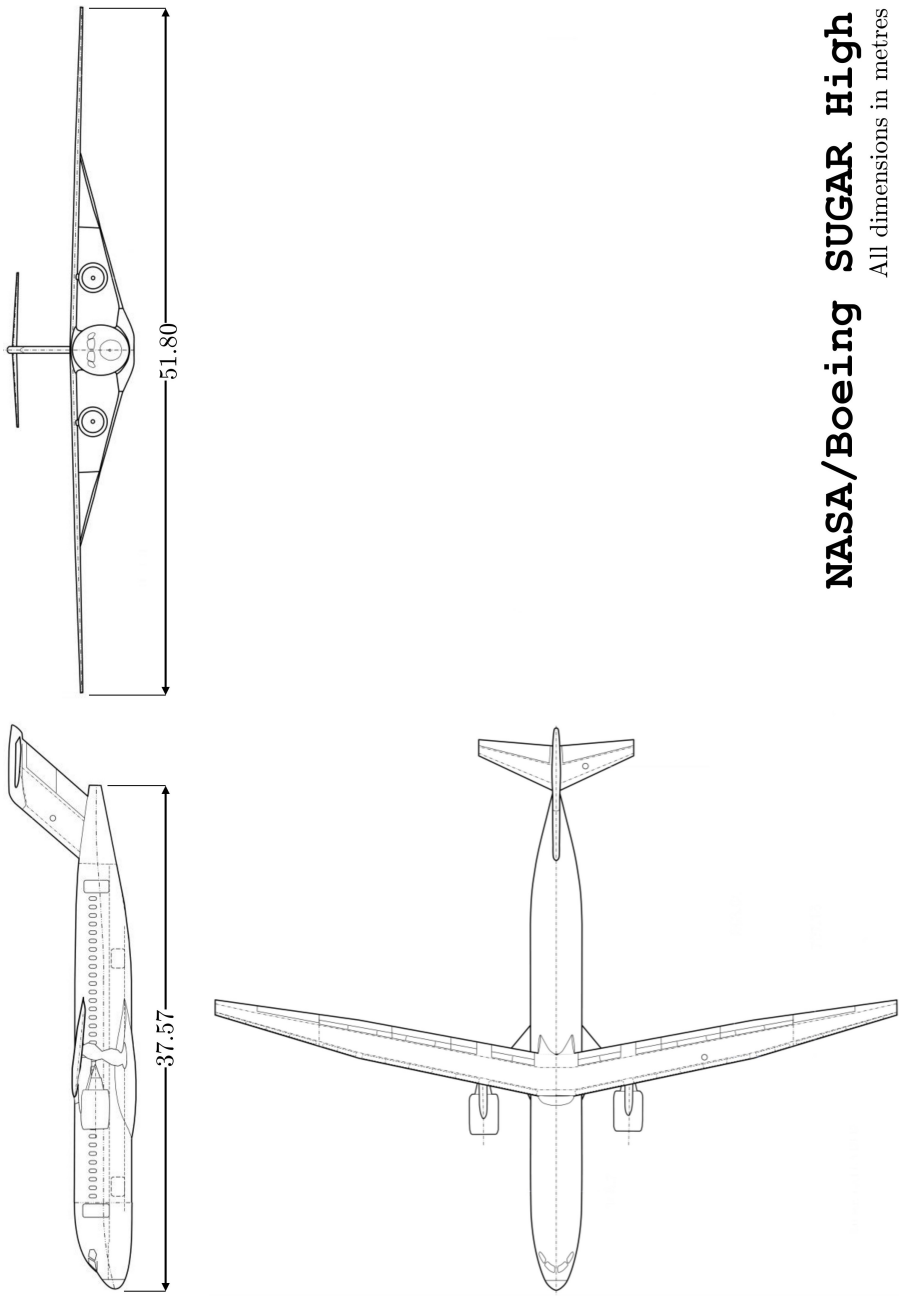

Figure B.3: SUGAR High (765-095-RevD)

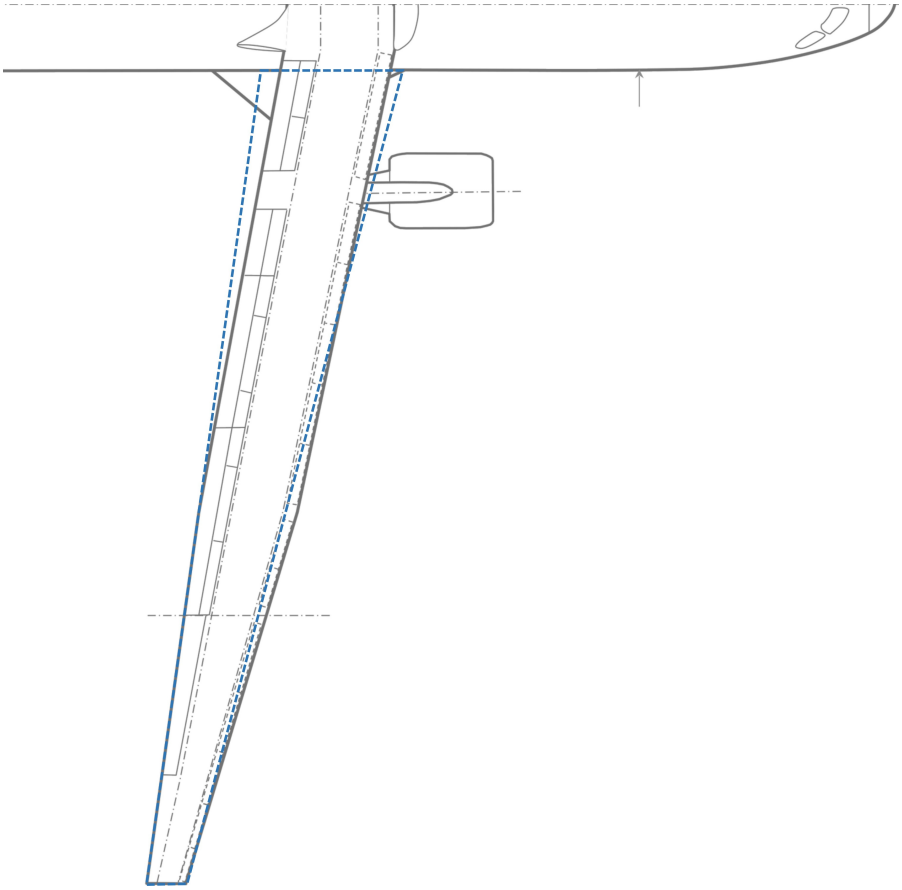

Figure B.4: SUGAR High (765-095-RevD) equivalent wing

Table B.2: NASA/Boeing SUGAR High (765-095-RevD) Parameters

	Parameter	Symbol	Units	Value	Ref
Performance	Operating Weight Empty	OWE	kg	39,599	[30]
	Maximum Take-Off Weight	$MTOW$	kg	68,039	[30]
	Maximum Payload Weight	W_{pay}	kg	13,970	[30]
	Cruise Altitude	h	m	12,436	[30]
	Cruise Velocity	u_∞	M	0.70	[30]
	Range (typical)	R	km	7,889	[30]
	Powerplant (x2)	Ducted Fan Engine gFan +2			[30]
	Thrust (x2)	T	kN	102.3	[30]
	Specific Fuel Consumption	SFC	$g/kN/s$	13.27	[30]
	Fuel Consumption (cruise)	$\dot{M}_f$	kg/h		
Body	Length	f_l	m	38.02	[30]
	Fuselage height	f_z	m	4.23	[30]
	Fuselage width	f_y	m	3.78	[30]
Aerofoil	Aerofoil	Boeing T1 airfoil			[30]
	Thickness ratio	$\frac{t}{c}$	–	0.133	[30]
	Lift at zero AoA	C_{l_0}	–	0.208	*
	Zero lift AoA	α_0	rad	0.031	*
Planform	Span	b	m	51.80	[30]
	Aspect Ratio	$\text{Æ}R$	–	19.55	[30]
	Reference area	S_{ref}	m^2	137.2	[30]
	Sweep (LE)	Λ_{LE}	rad	0.235	[30]
	Sweep ($\frac{c}{4}$)	$\Lambda_{\frac{c}{4}}$	rad	0.219	[30]
	Root Chord	c_b	m	3.31	[30]
	Streamwise c_b position	x_b	m	14.67	*
	Tip Chord	c_t	m	1.15	[30]
	Streamwise c_t position	l_t	m	20.80	*
	Taper Ratio	λ	–	0.346	[30]
	MAC	$\bar{c}$	m	2.80	[30]
	Crank Location	y_1	m	14.93	[30]
	Crank Chord	c_1	m	2.90	[30]
Equivalent Planform	Span	b	m	51.80	[30]
	Aspect Ratio	$\text{Æ}R$	–	19.83	[81]
	Gross area of wing	S	m^2	135.28	[81]
	Planform area of wing	S_e	m^2	125.41	[81]
	Sweep (LE)	Λ_{LE}	rad	0.2717	[81]
	Sweep ($\frac{c}{4}$)	$\Lambda_{\frac{c}{4}}$	rad	0.2433	[81]
	Sweep ($\frac{c}{2}$)	$\Lambda_{\frac{c}{2}}$	rad	0.2144	[81]
	Sweep (TE)	Λ_{TE}	rad	0.1556	[81]
	Root Chord	c_r	m	4.073	[81]
	Streamwise c_r position	l_n	m	14.67	[81]
	Tip Chord	c_t	m	1.15	[81]
	Streamwise c_t position	l_t	m	20.80	[81]
	Taper Ratio	λ	–	0.282	[81]
	geometric mean chord	$\bar{\bar{c}}$	m	2.612	[81]
	MAC	$\bar{c}$	m	3.047	[81]

B.3 CRANFIELD AX-1

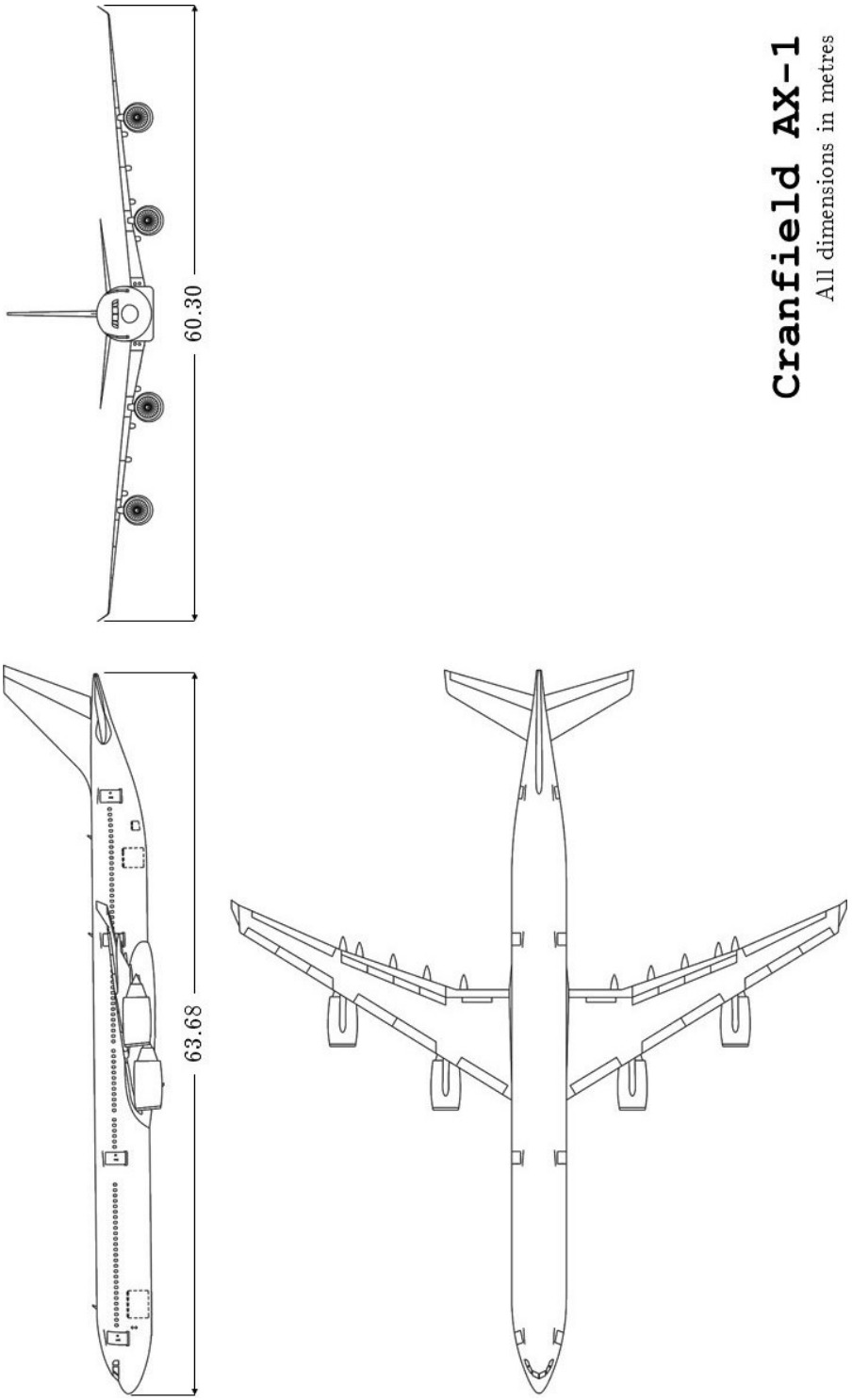

Figure B.5: Cranfield AX-1 drawing

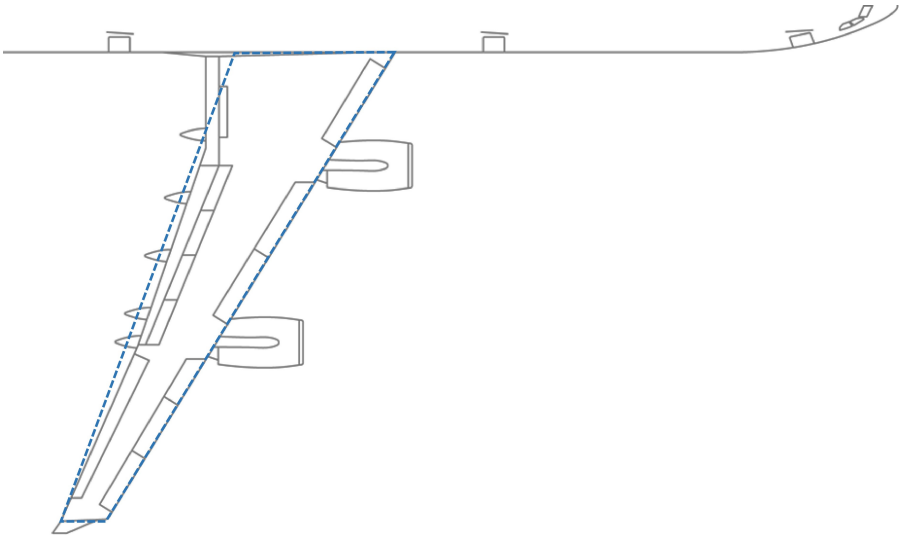

Figure B.6: Cranfield AX-1 equivalent wing

Table B.3: Cranfield AX-1 Aircraft Parameters

	Parameter	Symbol	Units	Value	Ref
Performance	Operating Weight Empty	OWE	kg	129,850	[86]
	Maximum Take-Off Weight	$MTOW$	kg	271,000	[86]
	Maximum Payload Weight	W_{pay}	kg	48,500	[85]
	Cruise Altitude	h	m	10,058	[86]
	Cruise Velocity	u_∞	M	0.74	[86]
	Range (typical)	R	km	10,834	[85]
	Powerplant (x2)	CFM-56-5C2			[86]
	Thrust (x2)	T	kN	138.78	[86]
	Specific Fuel Consumption	SFC	$g/kN/s$	15.43	[86]
	Fuel Consumption (cruise)	$\dot{M}_f$	kg/h	5700	[86]
Body	Length	f_l	m	63.69	[10]
	Fuselage height	f_z	m	5.64	[86]
	Fuselage width	f_y	m	5.64	[85]
Aerofoil	Aerofoil	NASA-SC(2)-0610			[10]
	Thickness ratio	$\frac{t}{c}$	–	0.10	[184]
	Lift at zero AoA	C_{l_0}	–	0.4205	[184]
	Zero lift AoA	α_0	rad	-0.049	[184]
Planform	Span	b	m	58.0	[86]
	Aspect Ratio	Æ	–	9.26	[85]
	Reference area	S_{ref}	m^2	363.1	[86]
	Sweep (LE)	Λ_{LE}	rad	0.5577	[10]
	Sweep ($\frac{c}{4}$)	$\Lambda_{\frac{c}{4}}$	rad	0.518	[86]
	Root Chord	c_b	m	10.553	[10]
	Streamwise c_b position	x_b	m	28.31	*
	Tip Chord	c_t	m	2.480	[10]
	Streamwise c_t position	l_t	m	446.40	[10]
	Taper Ratio	λ	–	0.251	[86]
	MAC	$\bar{c}$	m	7.26	[86]
	Crank Location 1	y_1	m	8.399	[10]
	Crank Chord 1	c_1	m	7.651	[10]
	Crank Location 2	y_2	m	14.422	[10]
	Crank Chord 2	c_2	m	5.923	[10]
	Crank Location 3	y_3	m	23.338	[10]
	Crank Chord 3	c_3	m	3.669	[10]
Equivalent Planform	Span	b	m	58.0	[81]
	Aspect Ratio	Æ	–	10.0	[81]
	Gross area of wing	S	m^2	336.36	[81]
	Planform area of wing	S_e	m^2	303.65	[81]
	Sweep (LE)	Λ_{LE}	rad	0.5577	[81]
	Sweep ($\frac{c}{4}$)	$\Lambda_{\frac{c}{4}}$	rad	0.5108	[81]
	Sweep ($\frac{c}{2}$)	$\Lambda_{\frac{c}{2}}$	rad	0.4612	[81]
	Sweep (TE)	Λ_{TE}	rad	0.3545	[81]
	Root Chord	c_r	m	9.1187	[81]
	Streamwise c_r position	l_n	m	28	[81]
	Tip Chord	c_t	m	2.48	[81]
	Streamwise c_t position	l_t	m	44.33	[81]
	Taper Ratio	λ	–	0.272	[81]
	geometric mean chord	$\bar{\bar{c}}$	m	5.7994	[81]
	MAC	$\bar{c}$	m	6.9371	[81]

B.4 CRANFIELD BEARDS XB-2

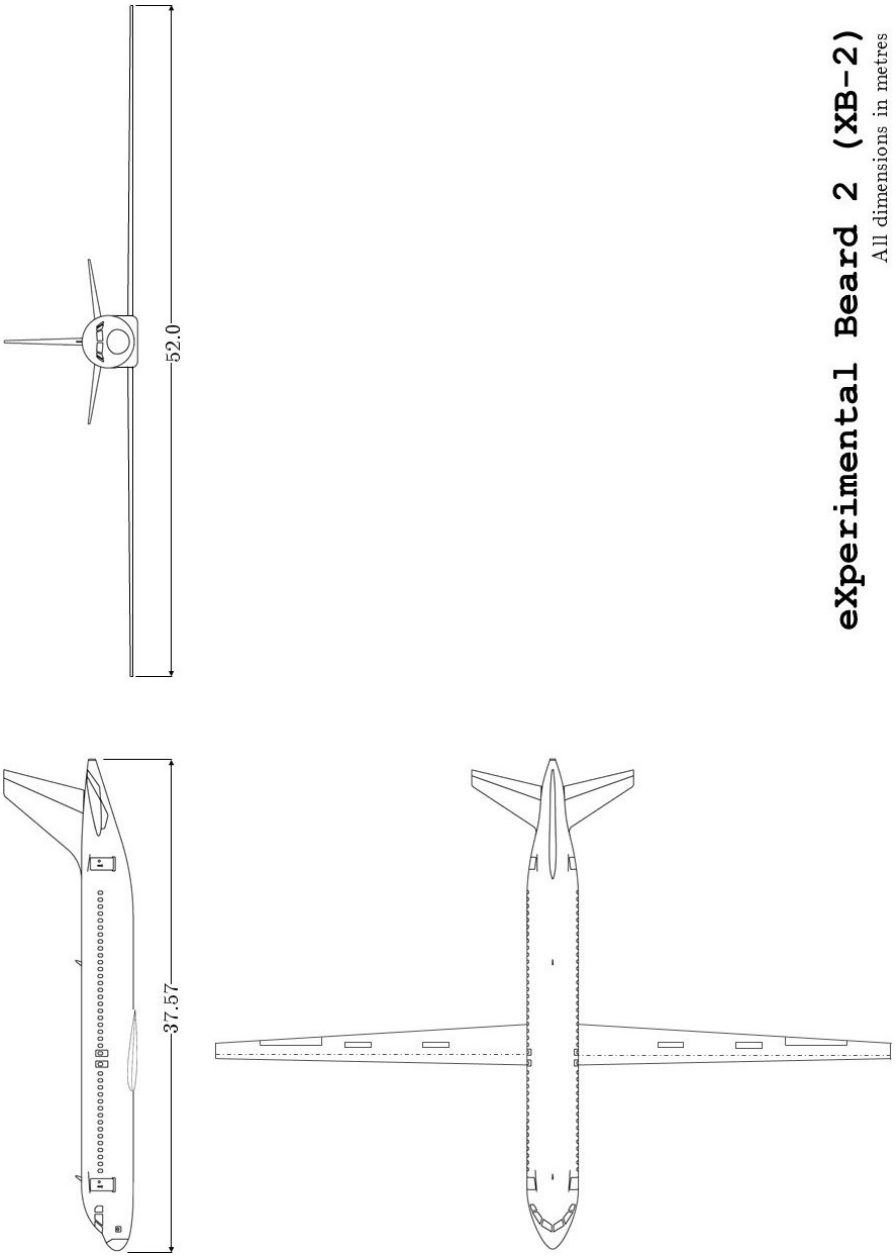

Figure B.7: Cranfield BEARDS XB-2 drawing

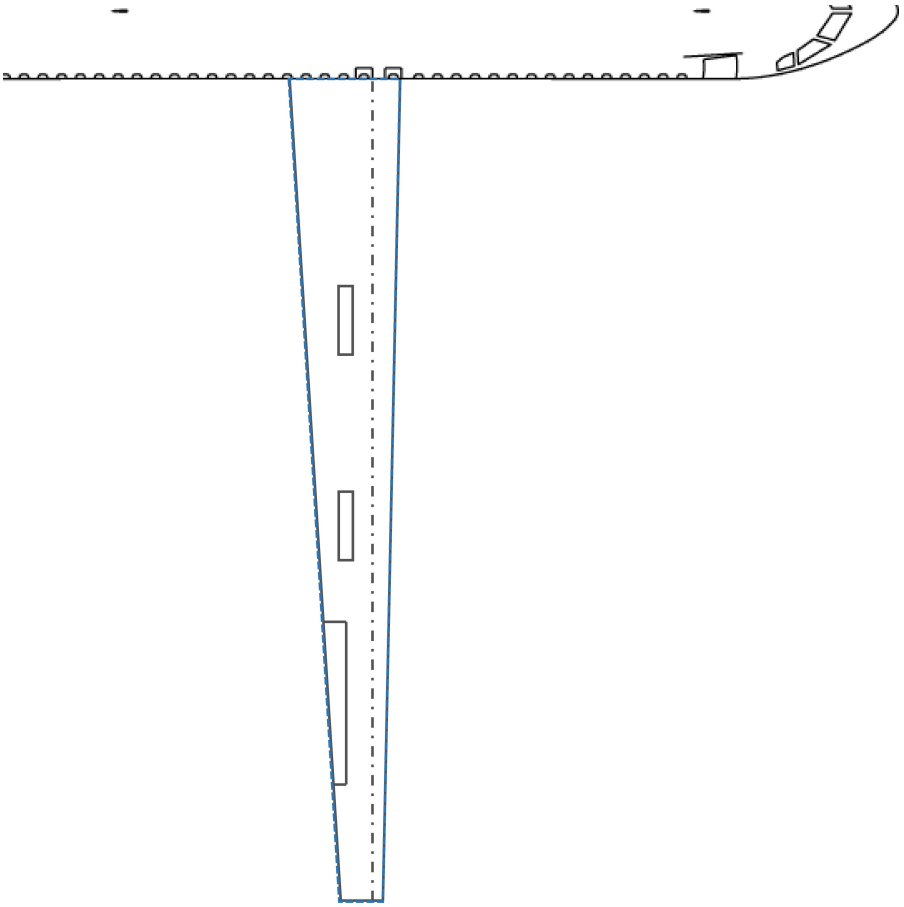

Figure B.8: Cranfield BEARDS XB-2 equivalent wing

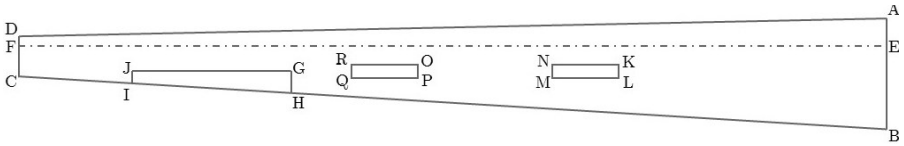

Figure B.9: XB2 wing coordinates

Table B.4: Cranfield eXperimental Beard 2 (XB-2) Parameters

	Parameter	Symbol	Units	XB2
Performance	Operating Weight Empty	OWE	kg	42,100
	Maximum Take-Off Weight	$MTOW$	kg	73,500
	Maximum Payload Weight	W_{pay}	kg	20,400
	Cruise Altitude	h	m	11,280
	Cruise Velocity	u_∞	M	0.6
	Range (typical)	R	km	>4,800
	Powerplant (x2)			gFan+2
	Thrust (x2)	T	kN	102.3
	Specific Fuel Consumption	SFC	$g/kN/s$	13.27
	Fuel Consumption (cruise)	$\dot{M}_f$	kg/h	
Body	Length	f_l	m	37.57
	Fuselage height	f_z	m	4.14
	Fuselage width	f_y	m	3.95
Aerofoil	Aerofoil			NACA
	Thickness ratio	$\frac{t}{c}$	–	0.150
	Lift at zero AoA	C_{l_0}	–	0.125
	Zero lift AoA	α_0	rad	-0.022
Planform	Span	b	m	48.00
	Aspect Ratio	$\mathcal{AR}$	–	18.8
	Reference area	S_{ref}	m^2	122.4
	Sweep (LE)	Λ_{LE}	rad	0.026
	Sweep ($\frac{c}{4}$)	$\Lambda_{\frac{c}{4}}$	rad	0.000
	Root Chord	c_b	m	3.78
	Streamwise c_b position	x_b	m	-
	Tip Chord	c_t	m	1.32
	Streamwise c_t position	l_t	m	
	Taper Ratio	λ	–	0.350
	MAC	$\bar{c}$	m	2.75

Table B.5: eXperimental Beard 2 (XB-2) aerodynamic planform coordinates

Grid	X	Y
A	-0.825	0.000
B	2.475	0.000
C	0.900	26.000
D	-0.300	26.000
E	0.000	0.000
F	0.000	26.000
G	0.747	17.800
H	1.397	17.800
I	1.109	22.550
J	0.747	22.550
K	0.600	8.000
L	1.000	8.000
M	1.000	10.000
N	0.600	10.000
O	0.600	14.000
P	1.000	14.000
Q	1.000	16.000
R	0.600	16.000

C

THE BEAM REDUCTION (BEAR) MODEL

C.1 BEAM THEORIES

For the derivation of the beam theories and the application to the Matlab beam model, the following assumptions have been made. *Note, the validity of each assumption must be assessed for any alternative application and changes to the derivation to be made appropriately.* See Kwon [93]

1. The beam is prismatic and has a straight centroidal (x) axis
2. The beam cross-section has two axis of symmetry in y and z
3. Transverse loading acts in one of the two planes of symmetry (x-y or x-z) or a combination of both
4. The material is elastic, isotropic and homogeneous
5. Plane sections perpendicular to the centroid axis remain plane after deformation
6. Transverse deflections are small

C.1.1 *Euler-Bernoulli Theory*

7. Rotational effects of the beam are neglected, and motion is assumed to be purely translational in the z direction (with a force applied in z axis only)
8. Beam elements remain rectangular during the motion
9. Linear beam theory is valid, such that Hooke's law is valid, given $\sigma_x = E\epsilon_x$

Thus, based on classic *linear* beam theory [82] the bending moment, $M = M(x,t)$, can be defined as a function of the beam deflection, $w = w(x,t)$.

Bending Moment

$$M = EI\frac{\partial^2 w}{\partial x^2} \tag{C.1}$$

From Figure C.1 and using Newtons second law a function can be given for shear loads (V) and the applied load in z ($q(x,t)$)[1].

Force Balance

$$\underbrace{q(x,t)dx + \left[V + \frac{\partial V}{\partial x}dx\right] - V}_{Force} = \overbrace{\rho A dx}^{Mass} \underbrace{\frac{\partial^2 w}{\partial t^2}}_{Acceleration}$$

Simplify

$$q(x,t) + \frac{\partial V}{\partial x} = \rho A\frac{\partial^2 w}{\partial t^2} \tag{C.2}$$

Also taking moments around the centroid axis of the element, gives a function for the bending moment (M). Note this equates to zero as we assume rotary inertia is zero.

1 This assumes small shear deformations, such as those found in long slender beams. This is not valid for compact beams

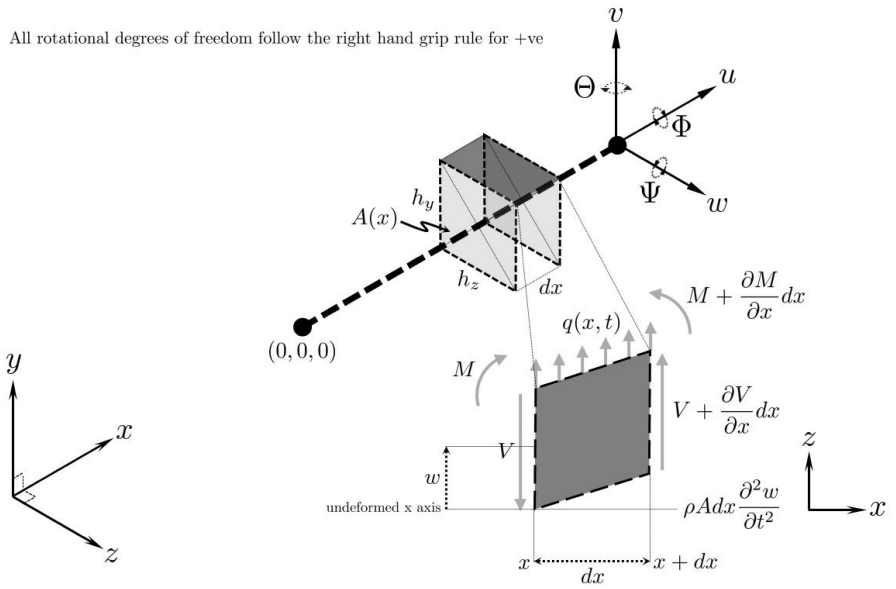

Figure C.1: Beam geometry for derivation

Moments Balance
$$\left[M + \frac{\partial M}{\partial x}dx\right] - M + \left[V + \frac{\partial V}{\partial x}dx\right]dx + [q(x,t)dx]\frac{dx}{2} = 0$$

Simplify
$$\left[\frac{\partial M}{\partial x} + V\right]dx + \left[\frac{\partial V}{\partial x} + \frac{q(x,t)}{2}\right]dx^2 = 0$$

As $dx \ll$, $dx^2 \simeq 0$
$$V = \frac{\partial M}{\partial x} \tag{C.3}$$

Substituting equations C.1 and C.2 into equation C.3 the standard dynamic equation of a Euler-Bernoulli beam is given in equation C.4. This can be sourced in various texts including Thomson [175] and Inman [82].

Dynamic Beam Equation
$$EI\frac{\partial^4 w}{\partial x^4} + \rho A\frac{\partial^2 w}{\partial t^2} = q(x,t) \tag{C.4}$$

C.1.2 *Rayleigh Theory*

The Rayleigh theory refines the Euler-Bernoulli theory by accounting for the rotary motion of the beam elements. In order to form this theory we make the additional assumption that:

10. The angle of rotation, Θ is a small deformation, such that $\Theta \approx \frac{\partial w}{\partial x}$.

Bending Moment (Eq C.1)
$$M = EI\frac{\partial^2 w}{\partial x^2}$$

Force Balance (Eq C.2)
$$q(x,t) + \frac{\partial V}{\partial x} = \rho A\frac{\partial^2 w}{\partial t^2}$$

The place where the rotary motion, i.e., the angular acceleration of beam elements, would be incorporated into the analysis is in the moment equation, see Equation C.3. For Rayleigh theory Equation C.3 becomes Equation C.5.

Moments Balance

$$\left[M+\frac{\partial M}{\partial x}dx\right]-M+\left[V+\frac{\partial V}{\partial x}dx\right]dx+[q(x,t)dx]\,\frac{dx}{2}=\underbrace{\rho I dx\frac{\partial^2\Theta}{\partial t^2}}_{Rotary Inertia}$$

Simplify

$$\left[\frac{\partial M}{\partial x}+V\right]dx+\left[\frac{\partial V}{\partial x}+\frac{q(x,t)}{2}\right]dx^2=\rho I dx\frac{\partial^2\Theta}{\partial t^2}$$

As $dx \ll$, $dx^2 \simeq 0$

$$V-\rho I\frac{\partial^2\Theta}{\partial t^2}=\frac{\partial M}{\partial x}$$

Assume $\Theta \approx \dfrac{\partial w}{\partial x}$

$$V-\rho I\frac{\partial^3 w}{\partial t^2\partial x}=\frac{\partial M}{\partial x} \tag{C.5}$$

Substituting equations C.1 and C.2 into equation C.5 the standard dynamic equation of a Rayleigh beam is given in equation C.6. This can be sourced in various texts including Thomson [175] and Inman [82]. The additional term in Equation C.6 not in Equation C.4, can thus be seen to account for the rotary motion of the element.

Dynamic Beam Equation

$$EI\frac{\partial^4 w}{\partial x^4}+\rho A\frac{\partial^2 w}{\partial t^2}-\rho I\frac{\partial^4 w}{\partial x^2\partial t^2}=q(x,t) \tag{C.6}$$

C.2 BEAM MODELLING

This section will address how to build the Timoshenko model for a simple two node beam (figure 4.2c) where each node is allowed to displace in all six degrees of freedom ($u, v, w, \Phi, \Theta, \Psi$). The beam is based on the method outlined by Przemieniecki [138]. It can be noted that the motion of the beam modelled can be understood with the knowledge of the beam mass and stiffness matrices, $[M]$ and $[K]$ respectively.

C.2.1 *Beam Geometry*

The beam in figure 4.2b is defined with a length (l_x) and discretised into a defined number (N) of elements (e). For this model the elements are assumed to be equal length (l_e), thus the placement of nodes is linearly spaced along the beam at positions, n. A rectangular beam is assumed for simplicity, so the final definition for beam geometry is the beam breadth (h_y) and height (h_z).

With the basic dimensions of the beam defined we can calculate the following properties of the beam:

Effective Shear Area	$A_e = \frac{5}{6} A_{yz}$
Moment of Inertia about the x centroid axis	$I_{xx} = \frac{h_y h_z^3}{12}$
Moment of Inertia about the y centroid axis	$I_{yy} = \frac{h_y^3 h_z}{12}$
Polar Moment of Inertia about the z centroid axis	$J_{zz} = \frac{h_y h_z}{12}\left(h_y^2 + h_z^2\right)$
Torsion constant	$J_T = \frac{h_y h_z^3}{3}$ Where $h_y < h_z$

C.2.2 *Material Properties*

For structural elastic models the material properties required are; material density (ρ), Elastic (Youngs) modulus (E) and Poisson ratio (ν). From these definitions we can calculate the material shear modulus (G).

Shear Modulus	$G = \frac{E}{2(1+\nu)}$

C.2.3 *Mass Matrix [**M**]*

The nomenclature published by Panzer et al [126] for the construction of the individual element matrices will be used. The element connecting a pair of nodes (see Figure 4.2c) effects twelve degrees of freedom in the system (six from each node). We can therefore discretize the element mass matrix $[M_e]$ into the interdependency of each nodes degrees of freedom, $[M_{11}], [M_{22}]$ and the interconnection between the two nodes degrees of freedom (the effect on each other), $[M_{12}], [M_{21}]$.

$$[M_e] = \begin{bmatrix} M_{11} & M_{12} \\ M_{21} & M_{22} \end{bmatrix} \tag{C.7}$$

The mass matrix for discrete elements is derived from the engineering theory of bending and torsion (neglecting shear deformations) as shown in Przemieniecki

[138]. This won't be repeated as the derivation does not contribute to the understanding of the matrix that is required, in place a segment from Przemieniecki [138] is presented below as has an impact when non-linearising the model.

All equations of elasticity for continuous media must be reformatted as matrix equations in the form of concentrated forces, moments, deflections or rotations. For small displacements Przemieniecki [138] presents the relationship as equation C.8, but notes for large deflections no such single relationship can be used in which coefficients of the matrix a are functions of the coordinates only.

$$\{u\} = \{a\}\{U\} \tag{C.8}$$

where

$$\{u\} = \begin{Bmatrix} u_x & u_y & u_z \end{Bmatrix}$$
$$\{U\} = \{U_1 \quad U_2 \quad \cdots \quad u_z\}$$
$$\{a\} = a(x, y, z)$$

Using the coordinate system as given in figure 4.2c, and *node*1 as the origin, the matrix $\{U\}$ for this element consists of twelve displacements, six deflections and six rotations.

$$\{U\} = \{u_1 \quad v_1 \quad w_1 \quad \Phi_1 \quad \Theta_1 \quad \Psi_1 \quad u_2 \quad v_2 \quad w_2 \quad \Phi_2 \quad \Theta_2 \quad \Psi_2\} \tag{C.9}$$

Przemieniecki [138] gives the relation for the mass matrix as equation C.10, for which the transpose $\{a\}$ matrix is given as in equation C.11.

$$[M] = \int_v \rho \{a\}^T \{a\} \, dV \tag{C.10}$$

$$\{a\}^T = \begin{bmatrix} 1-\xi & 0 & 0 \\ 6(\xi-\xi^2)\eta & 1-3\xi^2+2\xi^3 & 0 \\ 6(\xi-\xi^2)\zeta & 0 & 1-3\xi^2+2\xi^3 \\ 0 & -(1-\xi)l\zeta & -(1-\xi)l\eta \\ (1-4\xi+3\xi^2)l\zeta & 0 & (-\xi+2\xi^2-\xi^3)l \\ (-1+4\xi-3\xi^2)l\eta & (\xi-2\xi^2+\xi^3)l & 0 \\ \xi & 0 & 0 \\ 6(-\xi+\xi^2)\eta & 3\xi^2-2\xi^3 & 0 \\ 6(-\xi+\xi^2)\zeta & 0 & 3\xi^2-2\xi^3 \\ 0 & -l\xi\zeta & -l\xi\eta \\ (-2\xi+3\xi^2)l\zeta & 0 & (\xi^2-\xi^3)l \\ (2\xi-3\xi^2)l\eta & (-\xi^2+\xi^3)l & 0 \end{bmatrix} \tag{C.11}$$

Given $\xi = \frac{x}{l} \qquad \eta = \frac{y}{l} \qquad \zeta = \frac{z}{l}$

Matrix $\{a\}$ can then be substituted into equation C.10, and integrated over the volume of the element, to give the four element matrices of equation C.7 and the element mass matrix in equation C.12.

$$[M_{11}] = \rho A l_e \begin{bmatrix} \frac{1}{3} & 0 & 0 & 0 & 0 & 0 \\ 0 & \frac{13}{35} + \frac{6I_z}{5Al^2} & 0 & 0 & 0 & \frac{11l}{210} + \frac{I_z}{10Al} \\ 0 & 0 & \frac{13}{35} + \frac{6I_y}{5Al^2} & 0 & -\frac{11l}{210} - \frac{I_y}{10Al} & 0 \\ 0 & 0 & 0 & \frac{J_x}{3A} & 0 & 0 \\ 0 & 0 & -\frac{11l}{210} - \frac{I_y}{10Al} & 0 & \frac{l^2}{105} + \frac{2I_y}{15A} & 0 \\ 0 & \frac{11l}{210} + \frac{I_z}{10Al} & 0 & 0 & 0 & \frac{l^2}{105} + \frac{2I_z}{15A} \end{bmatrix}$$

$$[M_{22}] = \rho A l_e \begin{bmatrix} M_{11}(1,1) & 0 & 0 & 0 & 0 & 0 \\ 0 & M_{11}(2,2) & 0 & 0 & 0 & -M_{11}(2,6) \\ 0 & 0 & M_{11}(3,3) & 0 & -M_{11}(3,5) & 0 \\ 0 & 0 & 0 & M_{11}(4,4) & 0 & 0 \\ 0 & 0 & -M_{11}(5,3) & 0 & M_{11}(5,5) & 0 \\ 0 & -M_{11}(6,2) & 0 & 0 & 0 & M_{11}(6,6) \end{bmatrix}$$

$$[M_{21}] = \rho A l_e \begin{bmatrix} \frac{1}{6} & 0 & 0 & 0 & 0 & 0 \\ 0 & \frac{9}{70} - \frac{6I_z}{5Al^2} & 0 & 0 & 0 & \frac{13l}{420} - \frac{I_z}{10Al} \\ 0 & 0 & \frac{9}{70} - \frac{6I_y}{5Al^2} & 0 & -\frac{13l}{420} + \frac{I_y}{10Al} & 0 \\ 0 & 0 & 0 & \frac{J_x}{6A} & 0 & 0 \\ 0 & 0 & \frac{13l}{420} - \frac{I_y}{10Al} & 0 & -\frac{l^2}{140} - \frac{I_y}{30A} & 0 \\ 0 & -\frac{13l}{420} + \frac{I_z}{10Al} & 0 & 0 & 0 & -\frac{l^2}{140} - \frac{I_z}{30A} \end{bmatrix}$$

$$[M_{12}] = [M_{21}]^T$$

$$\rho A l_e \begin{bmatrix}
\frac{1}{3} & 0 & 0 & 0 & 0 & 0 & \frac{1}{6} & 0 & 0 & 0 & 0 & 0 \\
0 & \frac{13}{35}+\frac{6I_z}{5Al^2} & 0 & 0 & 0 & \frac{11l}{210}+\frac{I_z}{10Al} & 0 & \frac{9}{70}-\frac{6I_z}{5Al^2} & 0 & 0 & 0 & -\frac{13l}{420}+\frac{I_z}{10Al} \\
0 & 0 & \frac{13}{35}+\frac{6I_y}{5Al^2} & 0 & -\frac{11l}{210}-\frac{I_y}{10Al} & 0 & 0 & 0 & \frac{9}{70}-\frac{6I_y}{5Al^2} & 0 & \frac{13l}{420}-\frac{I_y}{10Al} & 0 \\
0 & 0 & 0 & \frac{J_x}{3A} & 0 & 0 & 0 & 0 & 0 & \frac{J_x}{6A} & 0 & 0 \\
0 & 0 & -\frac{11l}{210}-\frac{I_y}{10Al} & 0 & \frac{l^2}{105}+\frac{2I_y}{15A} & 0 & 0 & 0 & -\frac{13l}{420}+\frac{I_y}{10Al} & 0 & -\frac{l^2}{140}-\frac{I_y}{30A} & 0 \\
0 & \frac{11l}{210}+\frac{I_z}{10Al} & 0 & 0 & 0 & \frac{l^2}{105}+\frac{2I_z}{15A} & 0 & \frac{13l}{420}-\frac{I_z}{10Al} & 0 & 0 & 0 & -\frac{l^2}{140}-\frac{I_z}{30A} \\
\frac{1}{6} & 0 & 0 & 0 & 0 & 0 & \frac{1}{3} & 0 & 0 & 0 & 0 & 0 \\
0 & \frac{9}{70}-\frac{6I_z}{5Al^2} & 0 & 0 & 0 & \frac{13l}{420}-\frac{I_z}{10Al} & 0 & \frac{13}{35}+\frac{6I_z}{5Al^2} & 0 & 0 & 0 & -\frac{11l}{210}+\frac{I_z}{10Al} \\
0 & 0 & \frac{9}{70}-\frac{6I_y}{5Al^2} & 0 & -\frac{13l}{420}+\frac{I_y}{10Al} & 0 & 0 & 0 & \frac{13}{35}+\frac{6I_y}{5Al^2} & 0 & \frac{11l}{210}-\frac{I_y}{10Al} & 0 \\
0 & 0 & 0 & \frac{J_x}{6A} & 0 & 0 & 0 & 0 & 0 & \frac{J_x}{3A} & 0 & 0 \\
0 & 0 & \frac{13l}{420}-\frac{I_y}{10Al} & 0 & -\frac{l^2}{140}-\frac{I_y}{30A} & 0 & 0 & 0 & \frac{11l}{210}-\frac{I_y}{10Al} & 0 & \frac{l^2}{105}+\frac{2I_y}{15A} & 0 \\
0 & -\frac{13l}{420}+\frac{I_z}{10Al} & 0 & 0 & 0 & -\frac{l^2}{140}-\frac{I_z}{30A} & 0 & -\frac{11l}{210}+\frac{I_z}{10Al} & 0 & 0 & 0 & \frac{l^2}{105}+\frac{2I_z}{15A}
\end{bmatrix} \tag{C.12}$$

Single element, two node, mass matrix [**M**]

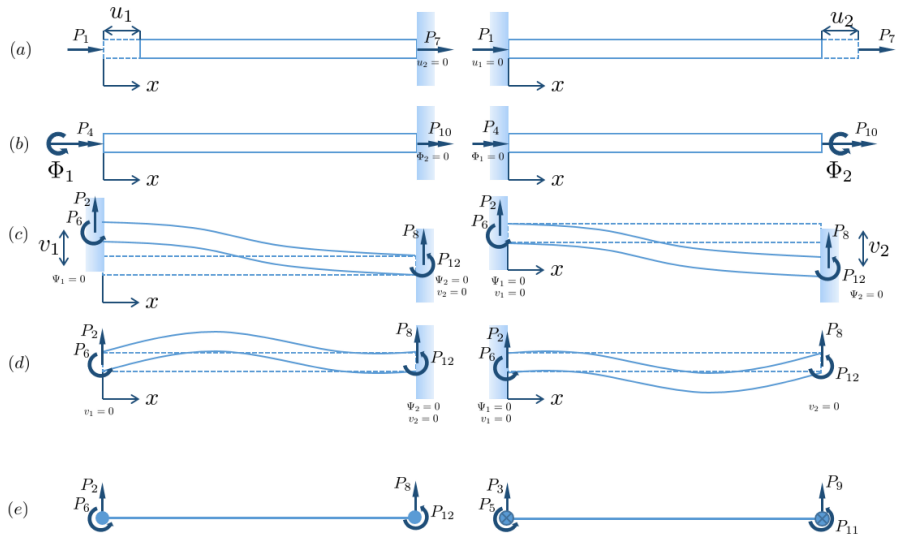

Figure C.2: Axial Forces, P_1 and P_7 acting on a beam element

C.2.4 *Stiffness Matrix [**K**]*

This linear stiffness matrix is constructed using the *stiffness properties of structural elements* approach, see Przemieniecki [138]. To simplify the stiffness matrix thermal stresses due to variations in temperature are neglected. The sign convention outlined in Figure 4.2c is used throughout the derivation.

Given the assumption of a beam that can be displaced in all 6DoF (3 translations and 3 rotations) at each node, the stiffness matrix is built by assessing the displacement of each node in isolation as a reaction to a load applied in one of the DoF, and then the effect one nodes displacement has on the other. Resulting in a [12x12] stiffness matrix, due to two nodes having 6DoF.

Axial Forces, P_1 and P_7

Engineering beam theory defines the normal stress due to axial loading P_1 (see Figure C.2a) as:

$$\sigma_1 = \frac{P_1}{A}$$

Given $\epsilon = \dfrac{du}{dx}$ $\qquad P_1 = -\dfrac{du}{dx}EA$

Integrating $\qquad P_1 x = -uEA + c$

Taking the conditions at $x = 0$, $u = u_1$ and at $x = l$, $u = 0$

$$c = P_1 l$$

Using $x = 0$ condition $\qquad P_1 = \dfrac{EA}{l}u_1$

Given equilibrium $\qquad P_7 = -P_1 = -\dfrac{EA}{l}u_1$

Given the force displacement relationship, $[P] = [K][u]$, the individual stiffness coefficients, k_{ij} can be defined as the element force P_i due to the unit displacement u_j when all other displacements are equal to zero.

Thus
$$k_{1,1} = \frac{P_1}{u_1} = \frac{EA}{l} \tag{C.13}$$
$$k_{7,1} = \frac{P_7}{u_1} = -\frac{EA}{l} \tag{C.14}$$

The same analysis can be performed, with the solutions in Equations C.15 and C.16.

$$k_{7,7} = \frac{P_7}{u_7} = \frac{EA}{l} \tag{C.15}$$
$$k_{1,7} = \frac{P_1}{u_7} = -\frac{EA}{l} \tag{C.16}$$

Twisting Moments, P_4 and P_{10}

Under a torsion load, P_4, beam theory with the definition of torsional stress gives us a rotational displacement, u_4, that is related to the applied load by the identity of torsional stiffness, GJ.

$$P_4 = -GJ\frac{d\theta}{dx}$$
Integrating
$$P_4 x = -GJ\theta + c$$

Taking the conditions as $\theta = 0$ at $x = l$ and $\theta = u_4$ at $x = 0$

$$c = P_4 l$$
Using $x = 0$ condition
$$P_4 = \frac{GJ}{l}u_4$$
Given equilibrium
$$P_{10} = -P_4 = -\frac{GJ}{l}u_4$$

Given the force displacement relationship, $[P] = [K][u]$, the individual stiffness coefficients, k_{ij} can be defined as the element force P_i due to the unit displacement u_j when all other displacements are equal to zero.

Thus
$$k_{4,4} = \frac{P_4}{u_4} = \frac{GJ}{l} \tag{C.17}$$
$$k_{10,4} = \frac{P_{10}}{u_4} = -\frac{GJ}{l} \tag{C.18}$$

The same analysis can be performed, with the solutions in Equations C.19 and C.20.

$$k_{10,10} = \frac{P_{10}}{u_{10}} = \frac{GJ}{l} \tag{C.19}$$
$$k_{4,10} = \frac{P_4}{u_{10}} = -\frac{GJ}{l} \tag{C.20}$$

For commonality I will use the nomenclature published by Panzer et al [126] for the construction of the individual element matrices. The element connecting a pair of nodes (see Figure 4.2c) effects twelve degrees of freedom in the system (six from

each node). We can therefore discretize the element stiffness matrix $[K_e]$ into the inter-dependency of each nodes degrees of freedom, $[K_{11}]$, $[K_{22}]$ and the interconnection between the two nodes degrees of freedom (the effect on each other), $[K_{12}]$, $[K_{21}]$.

$$[K_e] = \begin{bmatrix} K_{11} & K_{12} \\ K_{21} & K_{22} \end{bmatrix} \tag{C.21}$$

$$[K_{11}] = \begin{bmatrix} \frac{EA}{l} & 0 & 0 & 0 & 0 & 0 \\ 0 & \frac{12EI_z}{l^3(1+\Phi_y)} & 0 & 0 & 0 & \frac{6EI_z}{l^2(1+\Phi_y)} \\ 0 & 0 & \frac{12EI_y}{l^3(1+\Phi_z)} & 0 & \frac{-6EI_y}{l^2(1+\Phi_z)} & 0 \\ 0 & 0 & 0 & \frac{GJ}{l} & 0 & 0 \\ 0 & 0 & \frac{-6EI_y}{l^2(1+\Phi_z)} & 0 & \frac{(4+\Phi_z)EI_y}{l(1+\Phi_z)} & 0 \\ 0 & \frac{6EI_z}{l^2(1+\Phi_y)} & 0 & 0 & 0 & \frac{(4+\Phi_y)EI_z}{l(1+\Phi_y)} \end{bmatrix}$$

$$[K_{22}] = \begin{bmatrix} K_{11}(1,1) & 0 & 0 & 0 & 0 & 0 \\ 0 & K_{11}(2,2) & 0 & 0 & 0 & -K_{11}(2,6) \\ 0 & 0 & K_{11}(3,3) & 0 & -K_{11}(3,5) & 0 \\ 0 & 0 & 0 & K_{11}(4,4) & 0 & 0 \\ 0 & 0 & -K_{11}(5,3) & 0 & K_{11}(5,5) & 0 \\ 0 & -K_{11}(6,2) & 0 & 0 & 0 & K_{11}(6,6) \end{bmatrix}$$

$$[K_{21}] = \begin{bmatrix} -K_{11}(1,1) & 0 & 0 & 0 & 0 & 0 \\ 0 & -K_{11}(2,2) & 0 & 0 & 0 & -K_{11}(2,6) \\ 0 & 0 & -K_{11}(3,3) & 0 & -K_{11}(3,5) & 0 \\ 0 & 0 & 0 & -K_{11}(4,4) & 0 & 0 \\ 0 & 0 & K_{11}(5,3) & 0 & \frac{(2-\Phi_z)EI_y}{l(1+\Phi_z)} & 0 \\ 0 & K_{11}(6,2) & 0 & 0 & 0 & \frac{(2-\Phi_y)EI_z}{l(1+\Phi_y)} \end{bmatrix}$$

$$[K_{12}] = [K_{21}]^T$$

Shear Deformation Parameters

$$\phi_y = \frac{12EI_z}{GA_e l_e^2} = 24\,(1+\nu)\,\frac{A}{A_e}\left(\frac{r_z}{l_e}\right)^2$$

$$\phi_z = \frac{12EI_y}{GA_e l_e^2} = 24\,(1+\nu)\,\frac{A}{A_e}\left(\frac{r_y}{l_e}\right)^2$$

6DoF, 2 node stiffness matrix [K]

$$
\begin{bmatrix} P_1 \\ P_2 \\ P_3 \\ P_4 \\ P_5 \\ P_6 \\ P_7 \\ P_8 \\ P_9 \\ P_{10} \\ P_{11} \\ P_{12} \end{bmatrix}
=
\underbrace{\begin{bmatrix}
\frac{EA}{l} & 0 & 0 & 0 & 0 & 0 & \frac{-EA}{l} & 0 & 0 & 0 & 0 & 0 \\
0 & \frac{12EI_z}{l^3(1+\Phi_y)} & 0 & 0 & 0 & \frac{6EI_z}{l^2(1+\phi_y)} & 0 & \frac{-12EI_z}{l^3(1+\phi_y)} & 0 & 0 & 0 & \frac{6EI_z}{l^2(1+\phi_y)} \\
0 & 0 & \frac{12EI_y}{l^3(1+\phi_z)} & 0 & \frac{-6EI_y}{l^2(1+\phi_z)} & 0 & 0 & 0 & \frac{-12EI_y}{l^3(1+\phi_z)} & 0 & \frac{-6EI_y}{l^2(1+\phi_z)} & 0 \\
0 & 0 & 0 & \frac{GJ}{l} & 0 & 0 & 0 & 0 & 0 & \frac{-GJ}{l} & 0 & 0 \\
0 & 0 & \frac{-6EI_y}{l^2(1+\phi_z)} & 0 & \frac{(4+\phi_z)EI_y}{l(1+\phi_z)} & 0 & 0 & 0 & \frac{6EI_y}{l^2(1+\phi_z)} & 0 & \frac{(2-\phi_z)EI_y}{l(1+\phi_z)} & 0 \\
0 & \frac{6EI_z}{l^2(1+\phi_y)} & 0 & 0 & 0 & \frac{(4+\phi_y)EI_z}{l(1+\phi_y)} & 0 & \frac{6EI_z}{l^2(1+\phi_y)} & 0 & 0 & 0 & \frac{(2-\phi_y)EI_z}{l(1+\phi_y)} \\
\frac{-EA}{l} & 0 & 0 & 0 & 0 & 0 & \frac{EA}{l} & 0 & 0 & 0 & 0 & 0 \\
0 & \frac{-12EI_z}{l^3(1+\phi_y)} & 0 & 0 & 0 & \frac{6EI_z}{l^2(1+\phi_y)} & 0 & \frac{12EI_z}{l^3(1+\phi_y)} & 0 & 0 & 0 & \frac{-6EI_z}{l^2(1+\phi_y)} \\
0 & 0 & \frac{-12EI_y}{l^3(1+\phi_z)} & 0 & \frac{6EI_y}{l^2(1+\phi_z)} & 0 & 0 & 0 & \frac{12EI_y}{l^3(1+\phi_z)} & 0 & \frac{6EI_y}{l^2(1+\phi_z)} & 0 \\
0 & 0 & 0 & \frac{-GJ}{l} & 0 & 0 & 0 & 0 & 0 & \frac{GJ}{l} & 0 & 0 \\
0 & 0 & \frac{-6EI_y}{l^2(1+\phi_z)} & 0 & \frac{(2-\phi_z)EI_y}{l(1+\phi_z)} & 0 & 0 & 0 & \frac{6EI_y}{l^2(1+\phi_z)} & 0 & \frac{(4+\phi_z)EI_y}{l(1+\phi_z)} & 0 \\
0 & \frac{6EI_z}{l^2(1+\phi_y)} & 0 & 0 & 0 & \frac{(2-\phi_y)EI_z}{l(1+\phi_y)} & 0 & \frac{-6EI_z}{l^2(1+\phi_y)} & 0 & 0 & 0 & \frac{(4+\phi_y)EI_z}{l(1+\phi_y)}
\end{bmatrix}}_{[K]}
\begin{bmatrix} u_1 \\ v_1 \\ w_1 \\ \Phi_1 \\ \Theta_1 \\ \Psi_1 \\ u_2 \\ v_2 \\ w_2 \\ \Phi_2 \\ \Theta_2 \\ \Psi_2 \end{bmatrix}
\tag{C.22}
$$

C.2.5 *Global beam matrices*

For this note a simple example of a cantilevered beam oscillating in a 2D plane is modelled, as such no coordinate transformations are needed. The global mass and stiffness matrices ($[M], [K]$) can then be built with the knowledge that each node is interlinked to two elements, except the first node, n_1 and the last node, n_{N+1}, see figure 4.2b.

$$[M] = \begin{bmatrix}
M^e_{11} & M^e_{12} & 0 & & & \cdots & & & 0 \\
M^e_{21} & M^e_{11}+M^e_{22} & M^e_{12} & & & & & & \\
0 & M^e_{21} & M^e_{11}+M^e_{22} & M^e_{12} & & & & & \\
 & & M^e_{21} & M^e_{11}+M^e_{22} & M^e_{12} & \ddots & & & \vdots \\
 & & & \ddots & \ddots & \ddots & & & \\
\vdots & & & \ddots & M^e_{21} & M^e_{11}+M^e_{22} & M^e_{12} & & \\
 & & & & & M^e_{21} & M^e_{11}+M^e_{22} & M^e_{12} & 0 \\
 & & & & & & M^e_{21} & M^e_{11}+M^e_{22} & M^e_{12} \\
0 & & & \cdots & & & 0 & M^e_{21} & M^e_{22}
\end{bmatrix}$$

$$[K] = \begin{bmatrix}
K^e_{11} & K^e_{12} & 0 & & & \cdots & & & 0 \\
K^e_{21} & K^e_{11}+K^e_{22} & K^e_{12} & & & & & & \\
0 & K^e_{21} & K^e_{11}+K^e_{22} & K^e_{12} & & & & & \\
 & & K^e_{21} & K^e_{11}+K^e_{22} & K^e_{12} & \ddots & & & \vdots \\
 & & & \ddots & \ddots & \ddots & & & \\
\vdots & & & \ddots & K^e_{21} & K^e_{11}+K^e_{22} & K^e_{12} & & \\
 & & & & & K^e_{21} & K^e_{11}+K^e_{22} & K^e_{12} & 0 \\
 & & & & & & K^e_{21} & K^e_{11}+K^e_{22} & K^e_{12} \\
0 & & & \cdots & & & 0 & K^e_{21} & K^e_{22}
\end{bmatrix}$$

C.2.6 *Boundary Conditions*

The boundary conditions of the beam can be modelled by restraining certain degrees of freedom. For the beam shown in figure 4.2b the following degrees of freedom exist as vector x.

$$x = [u_1\ v_1\ w_1\ \Phi_1\ \Theta_1\ \Psi_1\ u_2\ v_2\ w_2\ \Phi_2\ \Theta_2\ \Psi_2\ \ldots\ u_{N+1}\ v_{N+1}\ w_{N+1}\ \Phi_{N+1}\ \Theta_{N+1}\ \Psi_{N+1}]^T$$

In the case of a cantilevered beam the first node (n_1) has all of its six degrees of freedom restrained (equal to zero). But by zeroing other degrees of freedom it is simple enough to replicate any boundary condition that exists.

$$x = [0\ 0\ 0\ 0\ 0\ 0\ u_2\ v_2\ w_2\ \Phi_2\ \Theta_2\ \Psi_2\ \ldots\ u_{N+1}\ v_{N+1}\ w_{N+1}\ \Phi_{N+1}\ \Theta_{N+1}\ \Psi_{N+1}]^T$$

Part VI

REFERENCE

BIBLIOGRAPHY

[1] Advisory Council for Aviation Research and innovation in Europe. *Realising Europe's vision for aviation Strategic Research & Innovation Agenda - Executive Summary*. Tech. rep. ACARE, 2012.

[2] Air Transport Action Group. *A sustainable flightpath towards reducing emissions*. Tech. rep. November. UNFCCC Climate Talks, Doha: Air Transport Action Group, 2012.

[3] Airbus. *Global Market Forecast - Mapping Demand 2016-2035*. 2016, p. 124. ISBN: 978-2-9554382-1-6.

[4] Kehinde Alabi and Foluso Ladeinde. "Utilizing CFD-based exergy calculations in the design/optimization of a complete aircraft system." In: *Collection of Technical Papers - 45th AIAA Aerospace Sciences Meeting*. Vol. 20. 2007, pp. 13657–13671. ISBN: 1563478900. DOI: 10.2514/6.2007-1130.

[5] Kehinde Alabi, Foluso Ladeinde, David J. Moorhouse, and José A. Camberos. "Assessing CFD modeling of entropy generation for the air frame subsystem in an integrated aircraft design/synthesis procedure." In: *Proceedings of the 44th AIAA Aerospace Sciences Meeting and Exhibit*. January. 2006, pp. 1–19.

[6] Kehinde Alabi, Foluso Ladeinde, David J. Moorhouse, José A. Camberos, and Stony Brook. "A comparison of empirical and CFD based exergy modelling for the airframe." In: *ICAS*. 2006, pp. 1–10.

[7] Kehinde Alabi, Foluso Ladeinde, Michael R. Von Spakovsky, David J. Moorhouse, and José A. Camberos. "The use of the 2nd law as a potential design tool for aircraft air frame subsystems." In: *International Journal of Thermodynamics* 9.4 (2006), pp. 193–205. ISSN: 13019724.

[8] Kehinde Alabi, Foluso Ladeinde, Michael R. Von Spakovsky, David J. Moorhouse, and José A. Camberos. "An advanced exergy and energy simulation tool for large-scale design/optimization of aerospace systems." In: *Collection of Technical Papers - 39th AIAA Thermophysics Conference*. Vol. 1. 2007, pp. 465–481. ISBN: 156347901X.

[9] John D. Anderson. *Aircraft performance and design*. First. WCB/McGraw-Hill, 1999, p. 580. ISBN: 9780070019713.

[10] Stuart P Andrews. "Modelling and simulation of flexible aircraft: handling qualities and active load control [Thesis]." PhD Thesis. Cranfield University, United Kingdom, 2011, p. 284.

[11] Aurélien Arntz and Olivier Atinault. "Exergy-Based Performance Assessment of a Blended Wing–Body with Boundary-Layer Ingestion." In: *AIAA Journal* 53.12 (2015), pp. 3766–3776. ISSN: 0001-1452. DOI: 10.2514/1.J054072.

[12] Aurélien Arntz, Olivier Atinault, Daniel Destarac, and Alain Merlen. "Exergy-based aircraft aeropropulsive performance assessment: CFD application to boundary layer ingestion." In: *32nd AIAA Applied Aerodynamics Conference*. American Institute of Aeronautics and Astronautics Inc., 2014. ISBN: 9781624102882.

[13] Aurélien Arntz, Olivier Atinault, and Alain Merlen. "Exergy-Based Formulation for Aircraft Aeropropulsive Performance Assessment: Theoretical Development." en. In: *AIAA Journal* (2014), pp. 1–13. ISSN: 0001-1452. DOI: 10.2514/1.J053467.

[14] Aurélien Arntz and David Hue. "Exergy-Based Performance Assessment of the NASA Common Research Model." In: *AIAA Journal* 54.1 (2015), pp. 1–13. ISSN: 0001-1452. DOI: 10.2514/1.J054127.

[15] Robert U Ayres, Leslie W Ayres, and K Martinas. "Eco-Thermodynamics: Exergy and Life Cycle Analysis." In: (1996), p. 49.

[16] Peter Baranyi. "Tensor Product Model-Based Control of Two-Dimensional Aeroelastic System." In: *Journal of Guidance, Control, and Dynamics* 29.2 (2006), pp. 391–400. ISSN: 0731-5090. DOI: 10.2514/1.9462.

[17] B Bauer. "Critical remarks on the definition of jet engines propulsive efficiency (in German)." In: *Z. Flugwiss* 18.5 (1970), pp. 158–171.

[18] Adrian Bejan. *Entropy Generation Minimization: The Method of Thermodynamic Optimization of Finite-Size Systems and Finite-Time Processes*. First. CRC Press, 1995, p. 400. ISBN: 9780849396519.

[19] Adrian Bejan. "Role for exergy analysis and optimization in aircraft energy-system design." In: *American Society of Mechanical Engineers, Advanced Energy Systems Division (Publication) AES* 39 (1999), pp. 209–217.

[20] Adrian Bejan. "Fundamentals of exergy analysis, entropy generation minimization, and the generation of flow architecture." In: *International Journal of Energy Research* 26.7 (2002), pp. 545–565. ISSN: 0363-907X. DOI: 10.1002/er.804.

[21] Adrian Bejan. "Constructal theory: Tree-shaped flows and energy systems for aircraft." In: *Journal of Aircraft* 40.1 (2003), pp. 43–48. ISSN: 00218669.

[22] Adrian Bejan. "Entropy Generation Minimization, Exergy Analysis, and the Constructal Law." In: *Arabian Journal for Science and Engineering* 38.2 (2012), pp. 329–340. ISSN: 1319-8025. DOI: 10.1007/s13369-012-0444-6.

[23] Frederick Berg. "Principles for Aircraft Exergy Mapping submitted by." PhD thesis. University of Bath, 2013.

[24] Frederick Berg, Martin Balchin, and Patrick Keogh. *Elucidation of Aircraft Energy Use Through Time-Variant Exergy Analysis*. Tech. rep. 2011. DOI: 10.4271/2011-01-2683.

[25] Frederick Berg, Martin Balchin, and Patrick Keogh. "New Principles for Dynamic Aircraft Exergy Mapping." In: *Journal of Aircraft* 50.4 (2013), pp. 1088–1098. ISSN: 0021-8669. DOI: 10.2514/1.C032040.

[26] P Berry. *Program BEMMODES Beam Element Model MODES*. Tech. rep. Hatfield, HAD.R.GEN.AE.0872: British Aerospace (Commercial Aircraft), 1989, p. 16.

[27] Raymond L. Bisplinghoff, Holt. Ashley, and Robert L. Halfman. *Aeroelasticity*. Dover Publications, 1996, p. 860. ISBN: 0486691896.

[28] Albion H. Bowers and Oscar J. Murillo. *On Wings of the Minimum Induced Drag: Spanload Implications for Aircraft and Birds*. Tech. rep. NASA/TP—2016–219072: Armstrong Flight Research Center, Edwards, California.

[29] Marty K Bradley, Timothy J Allen, and Christopher K Droney. *Subsonic Ultra Green Aircraft Research: Phase II – Volume III – Truss Braced Wing Aeroelastic Test Report*. Tech. rep. April 2014. NASA/CR–2015-218704: National Aeronautics and Space Administration, 2014, p. 87. DOI: 2060/20150017040.

[30] Marty K Bradley, Timothy J. Allen, and Christopher K Droney. *Subsonic Ultra Green Aircraft Research Phase II - Volume I - Truss Braced Wing Design Exploration*. Tech. rep. NASA/CR–2015-218704. Virginia: National Aeronautics and Space Administration, 2015, p. 378.

[31] Marty K. Bradley and Christopher K. Droney. *Subsonic Ultra Green Aircraft Research: Phase II – Volume II – Hybrid Electric Design Exploration*. Tech. rep. NASA/CR–2015-218704: National Aeronautics and Space Administration, 2011, p. 233. DOI: 2060/20150017039.

[32] Keith Merritt Brewer. "Exergy Methods for the Mission-Level Analysis and Optimization of Generic Hypersonic Vehicles." PhD thesis. Virginia Polytechnic Institute and State University, 2006, p. 167.

[33] H Brilliant. "Analysis of scramjet engines using exergy methods." en. In: *31st AIAA/ASME/SAE/ASEE Joint Propulsion Conference and Exhibit*. AIAA, 1995, p. 17.

[34] E. Buckingham. "The Principle of Similitude." In: *Nature* 96.2406 (1915), pp. 396–397. ISSN: 0028-0836. DOI: 10.1038/096396d0.

[35] Jeffrey Butt. "A study of morphing wing effectiveness in fighter aircraft using exergy analysis and global optimization techniques." PhD thesis. Virginia Polytechnic Institute and State University, 2005, p. 129.

[36] Jeremy Cadillon. "Exergy mapping on the AX-1 configuration." Master of Science. Cranfield University, 2017, p. 153.

[37] José A. Camberos. "A review of numerical methods in light of the second law of thermodynamics." In: *Collection of Technical Papers - 39th AIAA Thermophysics Conference*. Vol. 1. 2007, pp. 410–444. ISBN: 156347901X.

[38] José A. Camberos. *Analysis & Design Using Exergy AFRL at a Glance*. Tech. rep. June. 2016.

[39] José A. Camberos and David J. Moorhouse. "Systems engineering in terms of exergy." In: *International Journal of Aerospace Engineering* (2009). DOI: 10.1155/2009/735680.

[40] José A. Camberos and David J. Moorhouse. *Exergy Analysis and Design Optimization for Aerospace Vehicles and Systems*. First. American Institute of Aeronautics and Astronautics, 2011, p. 632. ISBN: 978-1-60086-840-5. DOI: 10.2514/4.868405.

[41] Sadi Carnot. *Réflexions sur la puissance motrice du feu et sur les machines propres à développer cette puissance*. Gauthier-Villars, 1824, p. 102.

[42] A. Castrichini, V. Hodigere Siddaramaiah, D. E. Calderon, J. E. Cooper, T. Wilson, and Y. Lemmens. "Nonlinear folding wing tips for gust loads alleviation." In: *Journal of Aircraft* 53.5 (2016), pp. 1391–1399. ISSN: 0021-8669. DOI: 10.2514/1.C033474.

[43] L. Cavagna, S. Ricci, and L. Riccobene. "Structural Sizing, Aeroelastic Analysis, and Optimization in Aircraft Conceptual Design." In: *Journal of Aircraft* 48.6 (2011), pp. 1840–1855. ISSN: 0021-8669. DOI: 10.2514/1.C031072.

[44] Yunus A Cengel and Michael A Boles. *Thermodynamics: An Engineering Approach*. Seventh. McGraw Hill Education, 2010. ISBN: 9780077366742.

[45] J Chambers. *Modeling Flight NASA Latest Version: The role of dynamically scale Free Flight Models in support of NASA aerospace programs.* 2015.

[46] C.-S. Chang, Dewey H. Hodges, and Mayuresh J. Patil. "Flight Dynamics of Highly Flexible Aircraft." In: *Journal of Aircraft* 45.2 (2008), pp. 538–545. ISSN: 0021-8669. DOI: 10.2514/1.30890.

[47] J M Clarke and J H Horlock. "Availability and propulsion." In: *ARCHIVE: Journal of Mechanical Engineering Science 1959-1982 (vols 1-23)* 17.4 (1975), pp. 223–232. ISSN: 0022-2542. DOI: 10.1243/JMES_JOUR_1975_017_033_02.

[48] Clarence D. Cone. *The theory of induced lift and minimum induced drag of nonplanar lifting systems*. National Aeronautics and Space Administration, 1962, p. 31.

[49] Jonathan Edward Cooper et al. "Design of a Morphing Wingtip." en. In: *Journal of Aircraft* 52.5 (2015), pp. 1394–1403. ISSN: 0021-8669. DOI: 10.2514/1.C032861.

[50] Silvio De Oliveira. *Exergy: Production, Cost and Renewability*. Green Energy and Technology. London: Springer London, 2013, p. 336. ISBN: 978-1-4471-4164-8. DOI: 10.1007/978-1-4471-4165-5.

[51] Silvio De Oliveira. "Exergy method for conception and performance evaluation of aircraft systems." PhD thesis. London, 2013, pp. 237–279. ISBN: 978-1-4471-4164-8. DOI: 10.1007/978-1-4471-4165-5.

[52] Ibrahim Dincer and Marc A Rosen. "Exergy Analysis of Aircraft Flight Systems." In: *Exergy - Energy, Environment, and Sustainable Development*. 2nd Editio. Elsevier, 2013. Chap. 19, pp. 383 –392. ISBN: 978-0-08-097089-9.

[53] John H. Doty and José A. Camberos. "Statistical, modular systems integration using combined energy & exergy concepts." In: *48th AIAA Aerospace Sciences Meeting Including the New Horizons Forum and Aerospace Exposition*. 2010. ISBN: 9781600867392.

[54] John H. Doty, José A. Camberos, and David J. Moorhouse. "Benefits of exergy-based analysis for aerospace engineering applications: Part 1." In: *40th AIAA Thermophysics Conference*. 2008. ISBN: 9781563479427.

[55] John H. Doty, José A. Camberos, and David J. Moorhouse. "Benefits of exergy-based analysis for aerospace engineering applications: Part 2." In: *47th AIAA Aerospace Sciences Meeting including the New Horizons Forum and Aerospace Exposition*. 2009. ISBN: 9781563479694.

[56] John H. Doty, José A. Camberos, and David J. Moorhouse. "Designed experiments: Statistical approach to energy- and exergy-based optimization." In: *39th AIAA Fluid Dynamics Conference*. 2009. ISBN: 9781563479755.

[57] Mark Drela. *Flight vehicle aerodynamics*, p. 279. ISBN: 9780262526449.

[58] Mark Drela. "Power Balance in Aerodynamic Flows." In: *AIAA Journal* 47.7 (2009), pp. 1761–1771. ISSN: 0001-1452. DOI: 10.2514/1.42409.

[59] Gaétan Dussart, Vilius Portapas, Alessandro Pontillo, and Mudassir Lone. "Flight Dynamic Modelling and Simulation of Large Flexible Aircraft." In: *Flight Physics - Models, Techniques and Technologies*. InTech, 2018. DOI: 10.5772/intechopen.71050.

[60] Chris F. Edwards. "Energy Tutorial: Exergy 101." In: Stanford University. GCEP Research Symposium, 2012, p. 26.

[61] M.A. Ehyaei, A. Anjiridezfuli, and Marc A Rosen. "Exergetic analysis of an aircraft turbojet engine with an afterburner." In: *Thermal Science* 17.4 (2013), pp. 1181–1194. ISSN: 0354-9836. DOI: 10.2298/TSCI110911043E.

[62] J Etele and Marc A Rosen. "Exergy losses for aerospace engines - Effect of reference-environments on assessment accuracy." en. In: *38th Aerospace Sciences Meeting and Exhibit*. Reno, Nevada: AIAA, 2000.

[63] European Commission. *Flightpath 2050 Europes Vision for Aviation*. Tech. rep. European Commission, 2011, p. 28. DOI: 10.2777/50266.

[64] European Environment Agency. *Focusing on environmental pressures from long distance transport*. Tech. rep. 7. EEA Report No 7/2014, 2014.

[65] Richard Phillips Feynman. *The Feynman Lectures on Physics: Commemorative Issue*. Vol. 19. Perseus Books Group, 1998, p. 240. ISBN: 0738200077.

[66] J P Fielding and H Smith. "New Models of Innovation for Economic Growth and Sustainability New Concepts for Environmentally Friendly Aircraft." In: (2009), pp. 1–24.

[67] Richard S. Figliola. "Energy-Based Design Methodology for Air Vehicle Systems: Aerodynamic Correlation Study." In: *Air Force Office of Scientific Research* (2005).

[68] Ricardo Gandolfi, Luiz Felipe Pellegrini, Guilherme Araújo Lima Da Silva, and Silvio De Oliveira. "Exergy analysis applied to a complete flight mission of a commercial aircraft." In: *46th AIAA Aerospace Sciences Meeting and Exhibit*. 2008. ISBN: 9781563479373.

[69] Ricardo Gandolfi, Luiz Felipe Pellegrini, and Silvio De Oliveira. "More electric aircraft analysis using exergy as a design comparison tool." In: *48th AIAA Aerospace Sciences Meeting Including the New Horizons Forum and Aerospace Exposition*. 2010. ISBN: 9781600867392.

[70] Louise Gautier. "Aeroelasticity wind tunnel model structural analysis." PhD thesis. Cranfield University, 2016.

[71] Victor Giurgiutiu. "Flight structures fundamental research trends and directions." In: *Aeronautical Journal* 113.1144 (2009), pp. 331–337. DOI: 10.1017/S0001924000003018.

[72] P Glansdorff, A Jaumotte, and J Baland. "Sur la puissance disponible et la rendement de propulsion des moteurs a reaction par jets (in French)." In: *Bull. Acad. Roy. Belg. Cl. des Sc. 5me Serie* 41.12 (1955), pp. 1264–1280.

[73] H. (Hermann) Glauert. *The elements of aerofoil and airscrew theory*. Cambridge University Press, 1983, p. 232. ISBN: 052127494X.

[74] Louis Georges Gouy. "Sur l'énergie utilisable." In: *Journal de Physique Théorique et Appliquée* 8.1 (1889), pp. 501–518. ISSN: 0368-3893.

[75] George C. Greene. *An Entropy Method for Induced Drag Minimization*. Tech. rep. 1989. DOI: 10.4271/892344.

[76] Tomas Grönstedt, Mohammad Irannezhad, Xu Lei, Oskar Thulin, and Anders Lundbladh. "First and Second Law Analysis of Future Aircraft Engines." In: *Journal of Engineering for Gas Turbines and Power* 136.3 (2013), p. 031202. ISSN: 0742-4795. DOI: 10.1115/1.4025727.

[77] Javier Ernesto. Hasbun. *Classical mechanics with MATLAB applications*. Jones and Bartlett Publishers, 2009, p. 548. ISBN: 0763746363.

[78] D. Hayes, M. Lone, J.F. Whidborne, J. Camberos, and E. Coetzee. "Adopting exergy analysis for use in aerospace." In: *Progress in Aerospace Sciences* 93 (2017). ISSN: 03760421. DOI: 10.1016/j.paerosci.2017.07.004.

[79] David Hayes, Mohammad M. Lone, and James F Whidborne. "Entropy Generation Minimisation and Exergy analysis approaches for aerospace applications - A review." In: *54th AIAA Aerospace Sciences Meeting, AIAA SciTech Forum*. AIAA 2016-0866. San Diego, California, USA, 2016, pp. 1–18. DOI: dx.doi.org/10.2514/6.2016-0866.

[80] David Hayes, Mohammad M. Lone, James F Whidborne, and Etienne Coetzee. "Evaluating the Rationale for Folding Wing Tips Comparing the Exergy and Breguet Approaches." In: *55th AIAA Aerospace Sciences Meeting, AIAA SciTech Forum*. Dallas, Texas: American Institute of Aeronautics and Astronautics, 2017. ISBN: 978-1-62410-447-3. DOI: 10.2514/6.2017-0464.

[81] IHS. *IHS ESDU 76003: Cranked and straight tapered wing planform properties*. Tech. rep. 2012. DOI: 9780856791369.

[82] Daniel Inman. *Engineering Vibration*. 2nd. New Jersey: Pearson Education, 2001, p. 619.

[83] International Civil Aviation Organization. *Annex 14 - Aerodromes. Volume I - Aerodrome design and operations. 6th edition.* Tech. rep. International Civil Aviation Organization (ICAO), 2013, p. 336.

[84] International Energy Agency. *Transport, Energy and CO2: Moving toward Sustainability*. Tech. rep. International Energy Agency, 2009, pp. 1–4. DOI: 10.1787/9789264073173-en.

[85] Paul Jackson. *IHS Jane's all the world's aircraft : Development and Production*. 2014-15. IHS, 2015. ISBN: 978 0 7106 3096 3.

[86] Lloyd R. Jenkinson, Paul. Simpkin, and Darren Rhodes. *Civil jet aircraft design*. American Insitute of Aeronautics and Astronautics, 1999, p. 418. ISBN: 9780340741528.

[87] Jessica Jones and Carlos E S Cesnik. "Nonlinear Aeroelastic Analysis of the X-56 Multi-Utility Aeroelastic Demonstrator." In: *15th Dynamics Specialists Conference* January (2016), pp. 1–18. DOI: 10.2514/6.2016-1799.

[88] Robert T Jones. *The Spanwise Distribution Of Lift For Minimum Induced Drag Of Wings Having A Given Lift And A Given Bending Moment*. Tech. rep. December. National Advisory Committee For Aeronautics Technical Note 2249, 1950.

[89] Thomas Jordan, William Langford, and Jeffrey Hill. "Airborne Subscale Transport Aircraft Research Testbed - Aircraft Model Development." In: *AIAA Guidance, Navigation, and Control Conference and Exhibit*. Reston, Virigina: American Institute of Aeronautics and Astronautics, 2005. ISBN: 978-1-62410-056-7. DOI: 10.2514/6.2005-6432.

[90] J. A. Jupp. "The design of future passenger aircraft – the environmental and fuel price challenges." In: 120.1223 (2016), pp. 37–60. ISSN: 00019240. DOI: 10.1017/aer.2015.4.

[91] Joseph Katz and Allen Plotkin. *Low-Speed Aerodynamics*. Cambridge: Cambridge University Press, 2001. ISBN: 9780511810329. DOI: 10.1017/CBO9780511810329.

[92] Ryan C. Kitson, Christopher Lupp, and Carlos E S Cesnik. "Modeling and Simulation of Flexible Jet Transport Aircraft with High-Aspect-Ratio Wings." In: *15th Dynamics Specialists Conference* (2016), pp. 1–21. DOI: 10.2514/6.2016-2046.

[93] Young W. Kwon and Hyochoong Bang. *The Finite Element Method Using MATLAB, Second Edition*. CRC Press, 2000, p. 624. ISBN: 1420041886.

[94] E Lamar. *Vortex-Lattice Fortran program for estimating subsonic aerodynamic characteristics of complex planform*. Tech. rep. February. 1971.

[95] David Lednicer. *http://m-selig.ae.illinois.edu/ads/aircraft.html*. 2010.

[96] J.J. Lee, Stephen P. Lukachko, and Ian A. Waitz. "Aircraft and energy use." In: *Encyclopedia of Energy* 7 (2004), p. 29.

[97] Joosung J. Lee, Stephen P. Lukachko, Ian A. Waitz, and Andreas Schafer. "Historical and future trends in aircraft performance, cost, and emissions." In: *Annual Review of Energy and the Environment* 26.1 (2001), pp. 167–200. ISSN: 1056-3466. DOI: 10.1146/annurev.energy.26.1.167.

[98] T. Lee and J. Pereira. "Nature of Wakelike and Jetlike Axial Tip Vortex Flows." In: *Journal of Aircraft* 47.6 (2010), pp. 1946–1954. ISSN: 0021-8669. DOI: 10.2514/1.C000225. URL: http://arc.aiaa.org/doi/10.2514/1.C000225.

[99] J Lewis. "Propulsive efficiency from an energy utilization standpoint." In: *Journal of Aircraft* 13 (1976), pp. 299–302.

[100] Haipeng Li and Richard S. Figliola. "Exergy based design methodology for airfoil shape optimization." In: *Collection of Technical Papers - 10th AIAA/ISSMO Multidisciplinary Analysis and Optimization Conference*. Vol. 6. 2004, pp. 3700–3707. ISBN: 1563477165.

[101] Haipeng Li, Jason Stewart, and Richard S. Figliola. "Exergy based design methodology for airfoil shape optimization and wing analysis." In: *ICAS-Secretariat - 25th Congress of the International Council of the Aeronautical Sciences 2006*. Vol. 2. 2006, pp. 731–741. ISBN: 9781604232271.

[102] Ruhui Li and Xiaomei Qiu. "Exergy Analysis of Aeroengine and its significance./Journal of Aerospace Power." In: *Journal of Aerospace Power* 7.2 (1992), pp. 169–172.

[103] P.B.S. Lissaman and J.L. Lundry. "A Numerical Solution For The Minimum Induced Drag Of Nonplanar Wings." In: *Journal of Aircraft* 5.1 (1968), pp. 17–21. ISSN: 0021-8669. DOI: 10.2514/3.43901.

[104] W Maltry. "Beitrag zur Anwendung des Zweiten Hauptsatzes auf lufttechnische Prozesse (In German)." In: *Luft- u. Kältetechn* 7 (1971), pp. 227–230.

[105] Kyle Charles Markell. "Exergy Methods for the Generic Analysis and Optimization of Hypersonic Vehicle Concepts." PhD thesis. Virginia Polytechnic Institute and State University, 2005, p. 192.

[106] Kyle Charles Markell, Keith Merritt Brewer, and Michael R. von Spakovsky. "Exergy Methods Applied to the Integrated Mission-Level Analysis and Optimization of Hypersonic Vehicle Concepts." In: *Volume 6: Energy Systems: Analysis, Thermodynamics and Sustainability*. Vol. 6. ASME, 2007, pp. 265–277. ISBN: 0-7918-4300-9. DOI: 10.1115/IMECE2007-42938.

[107] Christopher D. Marley and David W. Riggins. "Exergy Analysis of a Turbojet Engine Modeled as a Lumped Parameter System." In: *50th AIAA Aerospace Sciences Meeting including the New Horizons Forum and Aerospace Exposition*. Reston, Virigina: American Institute of Aeronautics and Astronautics, 2012. ISBN: 978-1-60086-936-5. DOI: 10.2514/6.2012-1122.

[108] Rodrigo Martinez-Val, Emilio Perez, and Jose Palacin. "Historical Perspective of Air Transport Productivity and Efficiency." In: *43rd AIAA Aerospace Sciences Meeting and Exhibit* January (2005), pp. 1–9. DOI: 10.2514/6.2005-121.

[109] Guillermo Maya. "Structural Dynamics Modelling and Simulation." PhD thesis. Cranfield University, 2016, p. 135.

[110] Bonnie McBride, Michael Zehe, and Sanford Gordon. *Coefficients for Calculating Thermodynamic Properties of Individual Species*. Tech. rep. Cleveland, Ohio: National Aeronautics and Space Administration, 2002, p. 291. DOI: NASATP-2002-211556.

[111] Shane McGuire. "Exergy Analysis of the NASA Common Research Model." PhD thesis. Cranfield University, 2016, p. 96.

[112] Muhammad Omar Memon, Kevin Wabick, Aaron Altman, and R. M. Buffo. "Wing Tip Vortices from an Exergy-Based Perspective." en. In: *Journal of Aircraft* 52.4 (2015), pp. 1267–1276. ISSN: 0021-8669. DOI: 10.2514/1.C032854.

[113] L. R. Miranda, R. D. Elliot, and W. M. Baker. "A generalized vortex lattice method for subsonic and supersonic flow applications." In: (1977).

[114] Scott Christopher Monsch. "A study of induced drag and spanwise lift distribution for three-dimensional inviscid flow over a wing." PhD thesis. 2007, p. 53.

[115] Scott Christopher Monsch, Haipeng Li, R. Harris, Jason Stewart, Richard S. Figliola, and José A. Camberos. "Exergy based design methodology for wing shape optimization and analysis." In: *Collection of Technical Papers - 39th AIAA Thermophysics Conference*. Vol. 1. 2007, pp. 455–464. ISBN: 156347901X.

[116] David J. Moorhouse and David M. Pratt. *Methods to Optimize for Energy Efficiency Developed by Presented by : Wright- Patterson AFB ...* Tech. rep. May. 2011.

[117] David J. Moorhouse, Brian Sanders, Michael R. Von Spakovsky, and Jeffrey Butt. "Benefits and design challenges of adaptive structures for morphing aircraft." In: *Aeronautical Journal* 110.1105 (2006), pp. 157–162. ISSN: 00019240.

[118] G. F. Naterer and José A. Camberos. *Entropy Based Design and Analysis of Fluids Engineering Systems*. First. CRC Press, 2008, p. 344. ISBN: 9780849372629.

[119] Nhan T. Nguyen, Eric Ting, Daniel Chaparro, Michael C. Drew, and Sean Shan-Min Swei. "Multi-Objective Flight Control for Drag Minimization and Load Alleviation of High-Aspect Ratio Flexible Wing Aircraft." In: *58th AIAA/ASCE/AHS/ASC Structures, Structural Dynamics, and Materials Conference*. Reston, Virginia: American Institute of Aeronautics and Astronautics, 2017. ISBN: 978-1-62410-453-4. DOI: 10.2514/6.2017-1589.

[120] David Nixon. *A Relationship Between Wave Drag and Induced Drag*. Tech. rep. 2003. DOI: 10.4271/2003-01-3021.

[121] David Nixon. "Simple adaptive planforms for wings." In: *SAE Technical Papers*. 2004.

[122] David Nixon. "Far field effects of wing wakes." In: *Collection of Technical Papers - 45th AIAA Aerospace Sciences Meeting*. Vol. 22. 2007, pp. 15158–15173. ISBN: 1563478900.

[123] David Nixon. *Fundamental Aerodynamics A Different Views*. David Nixon, 2009, p. 246. ISBN: 978-0578032894.

[124] Klaus Oswatitsch. *Contributions to the development of gasdynamics.* Friedr. Vieweg & Sohn Verlagsges GmbH, 1980. ISBN: 3 528 08452 9.

[125] Rafael Palacios, Joseba Murua, and Robert Cook. "Structural and Aerodynamic Models in Nonlinear Flight Dynamics of Very Flexible Aircraft." In: *AIAA Journal* 48.11 (2010), pp. 2648–2659. ISSN: 0001-1452. DOI: 10.2514/1.J050513.

[126] B Panzer, H; Hubele, J; Eid, R; Lohmann. "Generating a parametric finite element model of a 3d cantilever timoshenko beam using Matlab." In: *Technical Reports on Automatic Control* TRAC-4 (2009).

[127] M. J. Patil and Dewey H. Hodges. "On the importance of aerodynamic and structural geometrical nonlinearities in aeroelastic behavior of high-aspect-ratio wings." In: *Journal of Fluids and Structures* 19.7 (2004), pp. 905–915. ISSN: 08899746. DOI: 10.1016/j.jfluidstructs.2004.04.012.

[128] David M. Paulus and Richard A. Gaggioli. "Rational objective functions for vehicles." In: *Journal of Aircraft* 40.1 (2003), pp. 27–34. ISSN: 00218669.

[129] David M. Paulus and Richard A. Gaggioli. "The Exergy of Lift and Aircraft Exergy Flow Diagrams." In: *International Journal of Thermodynamics* 6.4 (2003), pp. 149–156. ISSN: 13019724.

[130] Luiz Felipe Pellegrini, Ricardo Gandolfi, Guilherme Araújo Lima Da Silva, and Silvio De Oliveira. "Exergy analysis as a tool for decision making in aircraft systems design." In: *Collection of Technical Papers - 45th AIAA Aerospace Sciences Meeting*. Vol. 23. 2007, pp. 16485–16496. ISBN: 1563478900.

[131] Vijayamand Periannan. "Investigation of the Effects of Various Energy and Exergy-Based Objectives / Figures of Merit on the Optimal Design of High Performance Aircraft System." PhD thesis. 2005.

[132] Vijayamand Periannan, Michael R. von Spakovsky, and David J. Moorhouse. "Investigation of the Effects of Various Energy and Exergy-Based Figures of Merit on the Optimal Design of a High Performance Aircraft System." In: *Advanced Energy Systems*. Vol. 2006. ASME, 2006, pp. 337–347. ISBN: 0-7918-4764-0. DOI: 10.1115/IMECE2006-14186.

[133] Vijayamand Periannan, Michael R. Von Spakovsky, and David J. Moorhouse. "A study of various energy- And exergy-based optimisation metrics for the design of high performance aircraft systems." In: *Aeronautical Journal* 112.1134 (2008), pp. 449–458. ISSN: 00019240.

[134] Alessandro Pontillo, David Hayes, Gaetan Dussart, Guillermo Lopez, Martin Carrizalez, Sezsy Yusuf, and Mudassir Lone. "Flexible High Aspect Ratio Wing: Low Cost Experimental Model and Computational Framework." In: *56th AIAA Aerospace Sciences Meeting, AIAA SciTech Forum*. Orlando, Florida, USA: American Institute of Aeronautics & Astronautics, 2018.

[135] Andrei V. Popov, Lucian T. Grigorie, Ruxandra M. Botez, Mahmood Mamou, and Youssef Mébarki. "Real Time Morphing Wing Optimization Validation Using Wind-Tunnel Tests." In: *Journal of Aircraft* 47.4 (2010), pp. 1346–1355. ISSN: 0021-8669. DOI: 10.2514/1.47431.

[136] Prandtl and L. *Applications of Modern Hydrodynamics to Aeronautics. [in Two Parts]*. United States. National Advisory Committee for Aeronautics: Volume 116 of Report (United States. National Advisory Committee for Aeronautics), 1923.

[137] Ludwig Prandtl. *Essentials of Fluid Dynamics: With Applications to Hydraulics, Aeronautics, Meteorology and Other Subjects*. Blackie, 1960, p. 452.

[138] J. S. Przemieniecki. *Theory of Matrix Structural Analysis*. Dover, 1985, p. 468. ISBN: 0486649482.

[139] Jon Ramba and Tyler Mccall. *Airbus A380 Design Scope*. Tech. rep. Airbus Group, 2005.

[140] Diego F. Rancruel. "A Decomposition Strategy Based on Thermoeconomic Isolation Applied to the Optimal Synthesis / Design and Operation of an Advanced Fighter Aircraft System A Decomposition Strategy Based on Thermoeconomic Operation of an Advanced Fighter Aircraft System." PhD thesis. 2003.

[141] Diego F. Rancruel and Michael R. Von Spakovsky. "Advanced fighter aircraft sub-systems optimal synthesis/design and operation: Airframe integration using a thermoeconomic approach." In: *Collection of Technical Papers - 10th AIAA/ISSMO Multidisciplinary Analysis and Optimization Conference*. Vol. 6. 2004, pp. 3403–3415. ISBN: 1563477165.

[142] Rayleigh. "The Principle of Similitude." In: *Nature* 95.2368 (1915), pp. 66–68. ISSN: 0028-0836. DOI: 10.1038/095066c0.

[143] Daniel P. Raymer. *Aircraft design : a conceptual approach*. Fourth Edi. Reston, Virginia: American Institute of Aeronautics and Astronautics, 1989, p. 729. ISBN: 0930403517.

[144] Anthony P. Ricciardi, Robert A. Canfield, Mayuresh J. Patil, and Ned Lindsley. "Nonlinear Aeroelastic Scaled-Model Design." In: *Journal of Aircraft* 53.1 (2015), pp. 1–13. ISSN: 0021-8669. DOI: 10.2514/1.C033171.

[145] Anthony P. Ricciardi, Robert A. Canfield, Mayuresh J. Patil, and Ned Lindsley. "Nonlinear Aeroelastic Scaled-Model Design." In: *Journal of Aircraft* 53.1 (2016), pp. 20–32. ISSN: 0021-8669. DOI: 10.2514/1.C033171.

[146] Anthony P. Ricciardi, Charles A. G. Eger, Robert A. Canfield, and Mayuresh J. Patil. "Nonlinear Aeroelastic-Scaled-Model Optimization Using Equivalent Static Loads." In: *Journal of Aircraft* 51.6 (2014), pp. 1842–1851. ISSN: 0021-8669. DOI: 10.2514/1.C032539.

[147] David W. Riggins. *Evaluation of performance loss methods for high-speed engines and engine components*. 1997.

[148] David W. Riggins. "Thrust losses in hypersonic engines part 2: Applications." In: *Journal of Propulsion and Power* 13.2 (1997), pp. 288–295. ISSN: 07484658.

[149] David W. Riggins, José A. Camberos, Mitch Wolff, and Kevin Bowcutt. "Mission-Integrated Exergy Analysis for Hypersonic Vehicles: Methodology and Application." In: *Journal of Propulsion and Power* 29.3 (2013), pp. 610–620. ISSN: 0748-4658. DOI: 10.2514/1.B34733.

[150] David W. Riggins, C. R. McClinton, and P. H. Vitt. "Thrust losses in hypersonic engines part 1: Methodology." In: *Journal of Propulsion and Power* 13.2 (1997), pp. 281–287. ISSN: 07484658.

[151] David W. Riggins, Trent M. Taylor, and David J. Moorhouse. "The second-law based analysis of aerospace vehicle performance." In: *Collection of Technical Papers - 44th AIAA Aerospace Sciences Meeting*. Vol. 6. 2006, pp. 4020–4040. ISBN: 1563478072.

[152] David W. Riggins, Trent M. Taylor, L. Terhune, and David J. Moorhouse. "Methods for the design of energy efficient high speed aerospace vehicles." In: *Aeronautical Journal* 111.1119 (2007), pp. 297–309. ISSN: 00019240.

[153] Gordon Rogers and Yon Mayhew. *Engineering Thermodynamics: Work and Heat Transfer*. 4th ed. Longman, 1992, p. 736. ISBN: 9780582045668.

[154] Bryce Alexander Roth. "A Theoretical Treatment of Technical Risk in Modern Propulsion System Design A Theoretical Treatment of Technical Risk in Modern Propulsion System Design." PhD thesis. Georgia Institute of Technology, 2000.

[155] Bryce Alexander Roth. "Work potential perspective of engine component performance." In: *Journal of Propulsion and Power* 18.6 (2002), pp. 1183–1190. ISSN: 07484658.

[156] Bryce Alexander Roth. "Work transfer analysis of turbojet and turbofan engines." In: *Proceedings of the 40th Joint Propulsion Conference, ...* (2004).

[157] Bryce Alexander Roth and Dimitri N. Mavris. "Generalized model for vehicle thermodynamic loss management." In: *Journal of Aircraft* 40.1 (2003), pp. 62–69. ISSN: 00218669. DOI: 10.2514/2.3058.

[158] Bryce Alexander Roth and Dimitri N. Mavris. "Method for propulsion technology impact evaluation via thermodynamic work potential." In: *Journal of Aircraft* 40.1 (2003), pp. 56–61. ISSN: 00218669.

[159] Mohammad H. Sadraey. *Aircraft Design: A Systems Engineering Approach*. First Edit. Chichester, UK: John Wiley & Sons Ltd, 2013. ISBN: 9781119953401.

[160] Salim M Salim and S C Cheah. "Wall y + Strategy for Dealing with Wall-bounded Turbulent Flows." In: *International MultiConference of Engineers and Computer Scientists (IMECS)* II (2009), pp. 1–6. DOI: 10.1.1.149.722.

[161] Oliver Schmitz and Mirko Hornung. "Unified Applicable Propulsion System Performance Metrics." In: *Journal of Engineering for Gas Turbines and Power* 135.11 (2013), p. 111201. ISSN: 0742-4795. DOI: 10.1115/1.4025066.

[162] Enrico Sciubba and Göran Wall. "A brief commented history of exergy from the beginnings to 2004." In: *International Journal of Thermodynamics* 10.1 (2007), pp. 1–26. ISSN: 13019724.

[163] Leonid Shaikhet. *Lyapunov Functionals and Stability of Stochastic Functional Differential Equations*. Heidelberg: Springer International Publishing, 2013. ISBN: 978-3-319-00100-5. DOI: 10.1007/978-3-319-00101-2. URL: http://link.springer.com/10.1007/978-3-319-00101-2.

[164] Adam P. Simpson and Chris F. Edwards. "An exergy-based framework for evaluating environmental impact." In: *Energy* 36.3 (2011), pp. 1442–1459. ISSN: 03605442. DOI: 10.1016/j.energy.2011.01.025.

[165] Robert J. Simpson, Rafael Palacios, Henrik Hesse, and Paul Goulart. "Predictive Control for Alleviation of Gust Loads on Very Flexible Aircraft." In: *55th AIAA/ASME/ASCE/AHS/ASC Structures, Structural Dynamics, and Materials Conference*. Reston, Virginia: American Institute of Aeronautics and Astronautics, 2014. ISBN: 978-1-62410-314-8. DOI: 10.2514/6.2014-0843.

[166] Kenneth Smith. "Morphing Wing Fighter Aircraft Synthesis / Design Optimization." PhD thesis. Virginia Polytechnic Institute and State University, 2009, p. 185.

[167] Kenneth Smith, Jeffrey Butt, Michael R. Von Spakovsky, and David J. Moorhouse. "A study of the benefits of using morphing wing technology in fighter aircraft systems." In: *Collection of Technical Papers - 39th AIAA Thermophysics Conference*. Vol. 2. 2007, pp. 1497–1508. ISBN: 156347901X.

[168] Yasin Sohret, Selcuk Ekici, Önder Altuntas, Arif Hepbasli, and T. Hikmet Karakoç. "Exergy as a useful tool for the performance assessment of aircraft gas turbine engines: A key review." In: *Progress in Aerospace Sciences* 83 (2016), pp. 57–69. ISSN: 03760421. DOI: 10.1016/j.paerosci.2016.03.001.

[169] Jason Stewart and Richard Figliola. "A unified methodology for aerospace systems integration based on entropy and the second law of thermodynamics." In: May 2004 (2005).

[170] Aurel Stodola. *Steam and Gas Turbines*. 6th (Trans. New York: Peter Smith, 1945, p. 1356.

[171] Jan Szargut, D Morris, and F Steward. *Exergy analysis of thermal, chemical, and metallurgical processes*. 1st Editio. Hemisphere Publishing Corporation, 1988, p. 332. ISBN: 0-89116-574-6.

[172] Jingfeng Tang, Wen Bao, and Daren Yu. "The Theoretical Treatment of Comparison of Performance between two scramjet engines with Energy-bypass based on Exergy Method." In: *46th AIAA Aerospace Sciences Meeting and Exhibit*. 2008. ISBN: 9781563479373.

[173] T Theodorsen. *General theory of aerodynamic instability and the mechanism of flutter*. Tech. rep. NASA, 1949.

[174] T Theodorsen and IE Garrick. "Nonstationary flow about a wing-aileron-tab combination including aerodynamic balance." In: (1942).

[175] William Thomson and Marie Dahleh. *Theory of Vibration with Applications*. 5th. New Jersey: Prentice Hall, 1998, p. 519. ISBN: 0-13-651068-X.

[176] Stephen Timoshenko and J. N. Goodier. *Theory of elasticity*. Third. McGraw-Hill, 1970, p. 567. ISBN: 0070858055.

[177] Benson Tongue. *Principles of Vibration*. 2nd. Oxford: Oxford University Press, 2002, p. 518.

[178] Onder Turan. "Some Exergetic Measures of a JT8D Turbofan Engine." In: *Journal of Automation and Control Engineering* 2.2 (2014), pp. 110–114. ISSN: 23013702. DOI: 10.12720/joace.2.2.110-114.

[179] Michael R. Von Spakovsky. *The Use of Exergy and Decomposition Techniques in the Development of Generic Analysis and Optimization Methodologies Applicable to the Synthesis/Design of Aircraft / Aerospace Systems*. Tech. rep. Virginia Tech, 2003, p. 73.

[180] Simone Weber, Laura Ramos Valle, Xavier Barral, David Hayes, Mohammad M. Lone, and Alastair Cooke. "Impact of Rotor Blade Aeroelasticity on Rotorcraft Flight Dynamics." In: *AIAA Atmospheric Flight Mechanics Conference*. Dallas, Texas: American Institute of Aeronautics and Astronautics, 2017. ISBN: 978-1-62410-448-0. DOI: 10.2514/6.2017-0021.

[181] J Weissinger. *The lift distribution of swept-back wings*. Tech. rep. NASA, 1947.

[182] John E. Yates and Coleman duP. Donaldson. *A fundamental study of drag and an assessment of conventional drag-due-to-lift reduction devices*. Tech. rep. September. NASA Contractor Report 4004, 1986.

[183] Farshid Zabihian. "Educating Undergraduate Mechanical Engineering Students about Exergy Analysis." In: *122nd ASEE Annual Conference & Exposition*. Seattle, Washington: American Society for Engineering Education, 2015, pp. 26.570.1 –26.570.12. DOI: 10.18260/p.23908.

[184] *http://airfoiltools.com*.